UNIVERSIDAD NACIONAL AUTÓNOMA DE MÉXICO

POSGRADO EN CIENCIAS DE LA TIERRA

INSTITUTO DE GEOFÍSICA

Slow Slip Events and Tectonic Tremor in the Mexican Subduction Zone: Implications for Seismic Hazard

T E S I S

QUE PARA OPTAR POR EL GRADO DE:

DOCTOR EN CIENCIAS DE LA TIERRA

PRESENTA:

Carlos David Villafuerte Urbina

Director de Tesis:
Dr. Víctor Manuel Cruz Atienza

Instituto de Geofísica

Ciudad Universitaria Cd. México, Mayo 2021

Abstract

Since the discovery of slow slip events (SSE), several investigations worldwide indicate their connection with the occurrence of large earthquakes, making this subject in recent years a leading research field with large implications in the assessment of seismic hazard. This dissertation focuses on characterizing the aseismic slip processes occurring in the Mexican subduction zone, their interaction with tectonic tremors (TT) and their influence on the seismic potential. To address these objectives, the present work is divided into two parts.

In the first part we study the physical processes in the vicinity of the plate interface that give rise to the interaction between SSEs and TTs. By analyzing the evolution of the deformation fields associated with the 2006 SSE in Guerrero, we show that the causal relationship between the TTs and SSEs depends on the stressing rate induced by the slip velocity of SSEs occurring around the asperities of TTs. Furthermore, complex processes such as tremor migrations, which are manifestations associated with aseismic slip transients, can be explained by secondary slow slip pulses generated by pore pressure waves traveling at velocities similar to the migrations observed in Guerrero due to nonlinear diffusion processes and pre-existing pore pressure gradients at the plate interface.

In the second part of the thesis, we analyze in detail the 2017 Tehuantepec (Mw 8.2) and Puebla-Morelos (Mw 7.1) earthquakes in 2017, the 2018 Pinotepa (Mw 7.2) earthquake and the Huatulco (Mw 7.4) earthquake, together with the unusual sequence of aseismic slip events between 2017-2020 in the states of Guerrero and Oaxaca. For this purpose, we developed ELADIN (ELastostatic ADjoint Inversion), an inversion method that allows to simultaneously determine regions at the plate contact that are under loading stress regimes (coupled) or relaxing stress regimes in the form of SSEs and afterslip, for instance. The analysis of the aseismic evolution and its associated stresses during this sequence suggests that the earthquakes and slow slip events can be explained as a chain of events interacting with each other on a regional scale due to quasi-static and/or dynamic perturbations. Such interaction seems to be conditioned by the transient memory of earth materials subjected to the "traumatic"deformation induced by the seismic waves of the great Mw8.2 Tehuantepec earthquake, which strongly perturbed the aseismic beat along the 650 km length of the plate interface and may have transiently altered the mechanical properties of the fault zone facilitating this bidirectional (slow and fast) interplay of events.

The results and the analyses presented in this thesis suggest that aseismic processes at the plate interface are part of a large subduction system that should be continuously evaluated to estimate more accurately the conditions giving rise to large earthquakes in Mexico.

Resumen

Desde el descubrimiento de los eventos de deslizamiento lento (SSE, por sus siglas en inglés) en 2001, diversas investigaciones han sugerido su conexión con la ocurrencia de grandes terremotos. Estos eventos producen relajaciones lentas de la corteza acompañadas de tremor tectónico (TT), compuesto de múltiples sismos pequeños con baja y muy baja frecuencia dominante. El estudio de los SSEs y TTs en los últimos años ha resultado entonces fundamental para la re-evaluación del peligro sísmico en fallas activas y muy particularmente en zonas de subducción. Esta disertación se enfoca en caracterizar los procesos de deslizamiento asísmico que ocurren en la zona de subducción mexicana (i.e., de los SSEs y del acoplamiento interplaca) y su interacción con los TTs con el fin de dilucidar su influencia en el potencial sísmico a lo largo del Pacifico mexicano. Para alcanzar estos objetivos, este trabajo se divide en dos partes.

En la primera parte se estudian los procesos físicos en la vecindad de la interfaz de placas que dan origen a la interacción entre SSEs y TTs. Mediante el análisis de la evolución de los campos de deformación asociados con el SSE de 2006 en Guerrero, demostramos que la relación causal que existe entre la ocurrencia de TTs y SSEs depende de la tasa de esfuerzos inducida por la velocidad de deslizamiento de los SSEs alrededor de las asperezas causantes de los TTs. Asimismo, investigamos procesos más complejos como las migraciones rápidas de tremor, que son manifestaciones extraordinarias asociadas a deslizamientos lentos transitorios, y que pueden ser explicadas por la propagación de pulsos de presión de poro en la interfaz de placas con velocidades similares (en dirección y módulo) a las de migración de TT en Guerrero como resultado de procesos de difusión no lineales en el contacto de placas y gradientes de presión de poro preexistentes.

En la segunda parte de la tesis se analiza en detalle los terremotos de Tehuantepec (Mw 8.2) y Puebla-Morelos (Mw 7.1) en 2017, Pinotepa (Mw 7.2) en 2018 y Huatulco (Mw 7.4) en 2020, junto con la inusual secuencia de SSEs que tuvo lugar en los estados de Guerrero y Oaxaca entre 2017 y 2020 (i.e., seis SSEs, tres en Guerrero y tres en Oaxaca en sólo tres años). Para ello, hemos desarrollado ELADIN (ELastostatic ADjoint Inversion), un método de inversión que, a partir de datos geodésicos, permite determinar simultáneamente las regiones de la interfaz de placas que están bajo regímenes de esfuerzos acumulativos (i.e., regiones acopladas) y de esfuerzos relajantes en forma de SSEs. El análisis de la evolución del deslizamiento asísmico, de los esfuerzos asociados y de las ondas sísmicas radiadas durante esta secuencia sugiere que los terremotos y los SSEs fueron el resultado de interacciones mutuas a escala regional a través de perturbaciones quasi-estáticas y/o dinámicas. Dicha interacción parece estar condicionada por la memoria transitoria de los materiales terrestres sometidos a la deformación inducida por las ondas sísmicas del gran terremoto de Tehuantepec, Mw 8.2, que perturbó fuertemente los ciclos de SSEs en un segmento de la interfaz de placas con 650 km de longitud que abarca ambos estados del país. Dicha condición parece haber alterado las propiedades mecánicas de las zonas de falla facilitando esta interrelación bidireccional entre los eventos (lentos y rápidos). Los resultados y análisis presentados en este trabajo también sugieren que los procesos de deslizamiento asísmico (en régimen de acoplamiento y de relajación) en la interfaz de placas son parte de un gran sistema dinámico que deben de ser

evaluados de manera continua para estimar con mayor verosimilitud las condiciones que dan lugar a la ocurrencia de grandes sismos en México.

Contents

Chapter 1

Introduction

Large earthquakes in subduction zones represent one of the greatest threats to communities around the world. These phenomena can be devastating due to the strong motion they can produce at the surface or the generation of tsunamis if they occur close to the seabed. According to the simplest traditional perspective, the seismic cycle has been regarded as three successive phases. An interseismic period in which stresses accumulate over tens of years in regions where the tectonic plates are locked due to the friction at the plate interface; a co-seismic slip event where the accumulated stresses are suddenly released giving rise to an earthquake; and a latter phase where the stress co-seismic perturbations are aseismically accommodated through interplate slip and viscoelastic response of the solid earth.

Advances in geodetic observation networks have made possible to delimit the coupled portions of the plate interface that allow stress accumulation and where future large earthquakes might occur. In addition, different seismo-geodetic observations in the last 20 years have led to a more realistic and complex understanding of the seismic cycle that integrates a significant diversity of slow slip processes during the interseismic period with different spatiotemporal characteristics. These interplate aseismic slip processes can be classified kinematically in relation to the relative plate velocity (V_{pl}). If the slip velocity is greater than V_{pl}, the crust undergoes a stress-relaxing slip (i.e., slow slip events or afterslip). If the slip velocity is less than V_{pl}, then the crust is loaded due to the interface creeping under a coupling regime. These two aseismic slip conditions have a major bearing on how stresses accumulate and release at the plate interface.

As mentioned above, among the slip processes that relax the crust are the slow slip events (SSEs), which are transients with durations of days to months located mainly in the downdip and updip segments surrounding the seismogenic zone (Dragert et al., 2001; Beroza and Ide, 2011; Saffer and Wallace, 2015; Schwartz and Rokosky, 2007; Obara, 2011). These events are located in regions where there is a transition in the mechanical properties of the plate interface (i.e., from highly-locked to free slip) and where pore pressures close to lithostatic have been inferred (Audet and Kim 2016 and references therein). The SSEs distinguish themselves by their slow slip velocity and propagation, which are several orders of magnitude smaller compared to regular earthquakes and therefore do not produce detectable seismic signals. However, these events are regularly accompanied by tectonic tremors (TT, Obara 2002; Obara et al. 2004; Bartlow et al. 2011; Rogers and Dragert 2003; Obara and Hirose 2006; Wech et al. 2009), which are sustained, low amplitude and non-impulsive seismic signals consisting of low (LFE) and very-low (VLF) frequency earthquakes whose radiation comes from unstable dislocations of small asperities at the plate contact (Shelly et al., 2006, 2007b; Ide et al., 2007; Ito et al., 2007).

Thanks to several observations in subduction zones, we now know that much of the activity of TT is modulated by aseismic slips that occur around the unstable asperities. Thus, TTs, LFEs and VLFs can be used as guides to detect the occurrence of small SSEs that cannot be geodetically observed at the surface. Although most large SSEs propagate simultaneously with tremors preferentially in the along-strike direction of the interface, different catalogs of TTs have revealed the existence of tremor migrations that disclose more complex secondary slip processes during the propagation of SSEs (Ghosh et al., 2010; Houston et al., 2011; Peng et al., 2015; Bletery et al., 2017). These migrations have been identified in two preferential directions in different parts of the world: in the opposite direction to the SSE propagation front, with velocities up to 10-40 times faster than the dislocation front (Houston et al., 2011; Peng et al., 2015; Royer et al., 2015); and along the SSE propagation front with velocities up to 100 times faster than that of propagating SSE (Ghosh et al., 2010; Shelly et al., 2007a) . In addition, these tremors that are part of the so-called slow earthquake family are highly sensitive to dynamic perturbations produced by the passage of seismic waves (Rubinstein et al., 2009; Miyazawa and Mori, 2006; Miyazawa and Brodsky, 2008; Peng and Chao, 2008; Chao et al., 2019), as well as small tidal-induced stresses (Thomas et al., 2012; Houston, 2015; Royer et al., 2015; Yabe et al., 2015) that suggest weak fault strength regions as a consequence of small values of effective stresses associated with the existence of pressurized fluids (Audet et al., 2009; Peacock et al., 2011; Katayama et al., 2012).

Although SSEs by themselves do not generate a hazard at the surface, the scientific community systematically investigates whether these events are capable of triggering large earthquakes due to their proximity to potentially seismogenic regions (Obara and Kato, 2016). While not all SSEs are accompanied by large earthquakes, some evidence from recent large subduction earthquakes such as the 2011 Mw9.0 Tohoku earthquake in Japan and the 2014 Mw8.1 Iquique earthquake in Chile suggest that SSEs preceded and interacted with these events through two possible mechanisms: by gradually decoupling the location where the rupture initiated (Kato et al., 2012; Schurr et al., 2014), or by stress loading the earthquake nucleation zone (Ruiz et al., 2014; Ito et al., 2013). Other investigations discuss this kind of interactions in different subduction zones (e.g., Radiguet et al. 2016; Uchida et al. 2016; Socquet et al. 2017; Voss et al. 2018). In addition to these observations, several theoretical and experimental models have explored the conditions and mechanisms that allow SSEs to trigger large earthquakes (e.g., Matsuzawa et al. 2010; Segall and Bradley 2012; Uchida et al. 2016).

Many studies have focused on the effects that SSEs may have in the occurrence of large earthquakes. However, the interaction can also occur the other way around. Static and dynamic stresses from seismic waves produced by large Earthquakes can be responsible for triggering SSEs (Wallace et al., 2017), modifying their evolution (Zigone et al., 2012) as well as increasing TT activity (Rubinstein et al., 2009; Miyazawa and Brodsky, 2008; Husker et al., 2019). Moreover, effects of an earthquake in the SSE activity could unchain a new interaction between upcoming SSEs and earthquakes thus having important implications on the seismic hazard. Despite these observations and models, the physical processes governing the interaction between SSEs and earthquakes remain not fully understood and is an area of ongoing research.

Due to its tectonic configuration, where the coast is only 65 km away from the oceanic trench, the Mexican subduction zone is an ideal place to study the evolution of aseismic slip processes and

their possible interaction with large earthquakes. In this region, interplate earthquakes of Mw 7+ have a recurrence of 30-50 years (Singh et al., 1981). The great majority of these earthquakes occur just below the coast and inland (i.e., between 10 and 30 km depth), which provides an excellent opportunity to have better observations and to develop models of the tectonic processes involved in the generation of large earthquakes.

In the Mexican subduction zone, SSEs occur in the deep segment of the plate interface between 30-50 km depth mainly beneath the states of Oaxaca and Guerrero. In Guerrero, SSEs occur approximately every 3.5 years (Cotte et al., 2009) and are the largest reported events in the world with an equivalent magnitude Mw 7.5 and durations of approximately 6 months (Vergnolle et al., 2010; Radiguet et al., 2012). In Oaxaca, SSEs are smaller (Mw 6.5) and have shorter durations with average recurrence of about 1.5 years (Graham et al., 2016). In both regions, SSEs are accompanied by TTs that exhibit migration characteristics very similar to those observed in other subduction zones (Payero et al., 2008; Kostoglodov et al., 2010; Brudzinski et al., 2010; Husker et al., 2012; Frank et al., 2014). Although nowadays it is well stablished that TTs and SSEs in Guerrero are concomitant in space and time, their spatial correlation was not clear until recently because persistent TTs and the regions of maximum slow slip appeared to be spatially separated, supporting the idea that TTs were triggered by the stress increased generated downdip the plate interface by the SSEs.

The last four Mw 7+ interplate earthquakes in Mexico have been preceded by SSEs in the downdip interface zone adjacent to the ruptures: the Papanoa earthquake (Mw 7.4) in Guerrero in 2014 (Radiguet et al., 2016), and three more earthquakes in Oaxaca, the Ometepec earthquake (Mw 7.5) in 2012 (Graham et al., 2014a) and, as we will see in the following chapters, the Pinotepa earthquake (Mw 7.2) in 2018 (Cruz-Atienza et al., 2021) and the Huatulco earthquake (Mw 7.5) in 2020 (Villafuerte et al., 2021). These observations suggest an interaction between SSEs and the seismogenic, shallower interface regions of the Mexican subduction zone, whose physical processes should be understood to improve our seismic hazard assessment.

Recently, four earthquakes with magnitude Mw greater than 7 occurred in the south-central part of Mexico in a period of only 3.5 years. This sequence began on September 8, 2017, with the largest earthquake ever recorded in the country (Mw 8.2) that took place within the subducted Cocos slab southeast of the Mexican subduction zone, in the Tehuantepec seismic gap (Suárez et al., 2019; Melgar et al., 2018). Eleven days later, another intraslab earthquake, the Puebla-Morelos event (Mw 7.1) occurred on September 19, 2017, only 127 km from Mexico City causing great devastation in the capital and its surroundings (Singh et al., 2018; Mirwald et al., 2019). Given the very short time between the two events, the scientific community wondered if the Puebla-Morelos rupture could have been affected in some way by the Tehuantepec earthquake despite the almost 500 km that separate them. Five months later, an interplate thrust earthquake of magnitude 7.2 occurred on February 16, 2018, south of the state of Oaxaca near the municipality of Pinotepa Nacional. The sequence culminated with the Huatulco interplate earthquake (Mw 7.5), southeast of the coast of Oaxaca, on June 23, 2020. During the occurrence of all these events, SSEs were taking place in the states of Guerrero and Oaxaca in an unusual way in terms of their recurrence times and magnitudes, suggesting that they could have played a role in this devastating earthquake sequence.

All these observations in different subduction zones including Mexico rise different questions that

have motivated the realization of this thesis: What are the physical mechanisms explaining the spatiotemporal correlation of SSEs and TTs? What role do fluids play in the plate interface to generate the migration of tremors and aseismic slip transients? Are all large earthquakes preceded by SSEs in Mexico? What are the mechanisms and mechanical conditions at the interface that would establish a causal relationship (i.e., an interaction) between SSEs and large earthquakes in the Mexican subduction zone? Are the Tehuantepec, Puebla-Morelos, Pinotepa and Huatulco earthquakes related in any way? If so, what role do SSEs play in this possible link? What happens to the interplate coupling during the evolution of SSEs and during the inter-SSE period? Is it constant in time? How important are these slow slip processes (SSEs and coupling changes) in the stress accumulation of the seismogenic zone during the seismic cycle? Do all these processes tell us anything about earthquake potential and forecasting?

To answer these questions in the best possible way, this dissertation is divided in two main parts. In the first part, which includes Chapters 1 and 2, we seek to understand the physical mechanisms and conditions at the interface behind the spatiotemporal correlation of SSEs and tectonic tremors in Mexico, including the much more complex processes that give rise to rapid tremor migrations. In Chapter 1 (Villafuerte and Cruz-Atienza, JGR, 2017) we perform extensive high-resolution TT locations in Guerrero and analyze them along with LFEs and the evolution of the crustal deformation produced by the 2006 SSE to better understand the causal relationship between SSEs and TTs. Furthermore, we use the TT occurrence rate to find the actual location of short-term SSEs in Guerrero. In Chapter 2 (Cruz-Atienza, Villafuerte and Bhat, Nature Communications, 2018) we investigate how pressurized fluids at the interface are able to produce secondary slow slip pulses during SSEs due to non-linear pore pressure waves that propagate with velocities and directions similar to the rapid tremor migrations observed in different subduction zones, including those we discovered in Guerrero by using our TT high-resolution locations.

In the second part of the thesis, which includes Chapters 3, 4 and 5, we explore the interaction between SSEs and earthquakes in the Mexican subduction zone starting with the great Mw 8.2 Tehuantepec event of September 8, 2017 and ending with the Mw 7.5 Huatulco earthquake in June 23, 2020. To achieve this purpose, in Chapter 3 (Tago, Cruz-Atienza, Villafuerte et al., Geophysical Journal International, 2021; accepted) we introduce the ELastostatic ADjoint INversion (ELADIN) method for imaging slip processes at the plate interface from geodetic observations and whose main practical capability is to determine simultaneously the regions of the interface that are under coupling regime and those that experience crustal-relaxing slip (i.e., SSEs and afterslip). In Chapter 4 (Cruz-Atienza, Tago, Villafuerte et al., Nature Communications, 2021) we study regionally how the sequence of SSEs and earthquakes can be explained as a causal cascade of events through quasi-static and/or dynamic interaction in the states of Guerrero and Oaxaca. Besides, we also document the large, unprecedented disruption of the SSEs cycle in both states (i.e., an extreme reduction of both their recurrence periods and magnitudes) due to the great Tehuantepec-earthquake seismic waves, and propose that fault gouge materials (e.g., at the plate interface) underwent abnormal non-linear elastic changes that brought them to a metastable state facilitating the initiation of SSEs and earthquakes. Finally, in Chapter 5 (Villafuerte et al., AGU Advances, 2021; under review), we analyze in greater detail the evolution of the slip velocity at the interface in Oaxaca including the pre-seismic, co-seismic and post-seismic phases of the 2020 Huatulco earthquake to elucidate how

these slip processes contributed to the accumulation of stresses and the way interplate coupling at seismogenic depths changed with time during the SSEs cycle, leading to a more realistic picture of the seismic potential in the region than long-term coupling models.

Chapter 2

Insights into the Causal Relationship between Slow Slip and Tectonic Tremor in Guerrero, Mexico

Contents

This chapter has been modified from its associated article: **Villafuerte, C**. and Cruz-Atienza, V. M. (2017). Insights into the causal relationship between slow slip and tectonic tremor in Guerrero, Mexico. *Journal of Geophysical Research: Solid Earth*, 122(8):6642-6656. doi:10.1002/2017JB014037

Abstract

Similar to other subduction zones, tectonic tremors (TT) and slow slip events (SSE) take place in the deep segment of the plate interface in Guerrero, Mexico. However, their spatial correlation in this region is not as clear as the Episodic Tremor and Slip observed in Cascadia and Japan. In this study we provide insights into the causal relationship between TTs and SSEs in Guerrero by analyzing the evolution of the deformation fields induced by the long-term 2006 SSE together with new locations of TTs and low-frequency earthquakes (LFE). Unlike previous studies we find that the SSE slip rate modulates the TT and LFE activity in the whole tremor region. This means that the causal relationship between the SSE and the TT activity directly depends on the stressing rate history of the tremor asperities that is modulated by the surrounding slip rate. We estimated that the frictional strength of the asperities producing tremor downdip in the sweet spot is around 3.2 kPa, which is 2.3 times smaller than the corresponding value updip in the transient zone, partly explaining the overwhelming tremor activity of the sweet spot despite that the slow slip there is smaller. Based on the LFE occurrence-rate history during the inter-long-term SSE period we determined that the short-term SSEs in Guerrero take place further downdip (about 35 km) than previously estimated, with maximum slip of about 8 mm in the sweet spot. This new model features a continuum of slow slip extending across the entire tremor region of Guerrero.

2.1 Introduction

Recent advances in seismological and geodetic observatories have enabled recognizing a new class of slow tectonic phenomena occurring on the plate interface of different subduction zones worldwide (Schwartz and Rokosky, 2007; Peng and Gomberg, 2010). Among these manifestations, slow-slip events (SSE) release aseismically part of the strain accumulated on the transitional segments of the interface (updip and downdip of the seismogenic zone) and can last from days to several months (Beroza and Ide, 2011; Obara, 2011; Schwartz and Rokosky, 2007). SSEs are very often accompanied by tectonic tremors (TT) (Obara, 2002), which are sustained low-amplitude seismic signals more likely composed by the summation of low frequency earthquakes (LFEs) produced by small shear dislocations near the plate interface (Shelly et al., 2007a; Ide et al., 2007). Each one of these seismic signals has a characteristic frequency content and represents an individual manifestation of a larger-scale tectonic release process (Beroza and Ide, 2011). The clearest example of the spatio-temporal correlation between SSEs and TTs is the so-called Episodic Tremor and Slip (ETS) observed in Nankai and Cascadia (Rogers and Dragert, 2003; Obara and Hirose, 2006). Whereas in Cascadia and Nankai TTs occur within the zones of maximum slip rate of the SSEs (i.e., behind the slip front) (Bartlow et al., 2011; Hirose and Obara, 2010), in other subduction zones such as Bungo Channel in Japan, Hikurangi in New Zealand and Guerrero in Mexico, TTs appear to be located apart in space supporting the idea that they are triggered by the increase of shear stress outside the slipping regions (Hirose et al., 2010; Kostoglodov et al., 2010; Bartlow et al., 2014).

We focus on the Guerrero subduction zone, Mexico, where long-term SSEs occur approximately every 3.5 years (Cotte et al., 2009; Radiguet et al., 2012) and represent the largest aseismic events in the world, with moment magnitude up to 7.6 (Kostoglodov et al., 2003, 2010). In this region, the TT and LFE activity takes place in the horizontal segment of the plate interface beneath the continent (Payero et al., 2008; Kostoglodov et al., 2010), almost always concomitant with slow slip transients (Kostoglodov et al., 2010; Husker et al., 2012; Frank et al., 2015b). However, the spatial correlation between tremor and long-term SSEs is not as clear, because the highest TT activity is shifted downdip about 50 km from the maximum slip of long-term SSEs (Figure 2.1a) (Kostoglodov et al., 2010; Husker et al., 2012).

Different studies of TTs and LFEs in Guerrero (Payero et al., 2008; Kostoglodov et al., 2010; Husker et al., 2012; Cruz-Atienza et al., 2015; Frank et al., 2014; Maury et al., 2016), show that these events concentrate in two main source regions of the horizontal plate interface: the so-called sweet spot, downdip between 200-240 km from the trench, and the transient zone, located updip and close to the slab kink where it becomes horizontal, between 150 to 175 km from the trench (Figure 2.1) (Husker et al., 2012; Frank et al., 2014). Unlike the transient zone, TTs and LFEs take place persistently in the sweet spot even in the absence of long-term events (Kostoglodov et al., 2010; Husker et al., 2012; Frank et al., 2014). For this reason, Husker et al. (2012) suggested that the sweet spot represents an interface segment with the optimal conditions of temperature, pressure and fluid content to generate frequent tectonic tremor. In contrast, most of the tremor updip in the transient zone occurs during short episodes activated only during SSEs and, in some cases, during the passage of teleseismic waves (Zigone et al., 2012).

During the inter-long-term SSE periods there are TT and LFE episodes occurring approximately every 3 months in both the transient zone and the sweet spot (Kostoglodov et al., 2010; Husker et al., 2012; Frank et al., 2015b). This activity takes place simultaneously with very-low amplitude displacements in the GPS records that have been associated with short-term SSEs (Vergnolle et al., 2010). The source inversion of these signals indicates that they are produced by moment magnitude 6.4 SSEs located in the interface segment separating both tremor regions (i.e., the transient zone and the sweet spot) (Frank et al., 2015b). Current evidence of SSEs and tremor in Guerrero has thus led previous authors to propose different models to explain the activity of TTs in the sweet spot. Kostoglodov et al. (2010) suggested that given the spatial offset between the sweet spot and the 2006 SSE, the activity of TTs in the sweet spot is driven by the increase of shear stresses downdip of the SSE. Endorsing this argument, Frank et al. (2015a) concluded that variations in the LFE activity during the 2006 SSE were not associated with the slip rate at the interface, but rather with the increase of shear stresses in the sweet spot and the transient change of pore pressure close to the interface. In this study we report new high-resolution TT locations in Guerrero and analyze, along with a previously reported LFE catalog, their detailed spatio-temporal correlation with the strain field produced by the 2006 SSE to better elucidate both the causal relationship between slow slip transients and tremor in the whole region, and the actual location of short-term SSEs in Guerrero.

2.2 Tectonic tremor location in Guerrero

We relocated TTs in Guerrero by means of the Tremor Energy and Polarization method (TREP) (Cruz-Atienza et al., 2015) from broadband seismic data of the high-resolution Meso-American Subduction Experiment (MASE, green squares in Figure 2.1a) (Caltech, 2007) recorded between the beginning of 2005 and mid-2007. During this period, a long term SSE (6 months duration) took place, providing us the opportunity to analyze the activity of TTs during the evolution of such a large aseismic transient. The tremor episodes were automatically detected using the spectral threshold method proposed by Husker et al. (2010) and correspond to those analyzed by Husker et al. (2012).

The TREP method determines TT hypocentral locations from the spatial distribution of the tremor energy, its spatial derivative and the azimuth of the particle motion polarization ellipsoid. According to the source mechanisms reported for LFEs and VLFEs in the region (Frank et al., 2013; Maury et al., 2016), the method assumes horizontal fault planes and determine both the slip direction (i.e. the rake angle) and the source location that best explain the three above-mentioned observables. This technique performs a grid search in a 3D lattice with possible hypocenters beneath the study region. To do so, a synthetic Green's function database is pre-computed for double-couple point dislocations. The Green's functions are calculated considering the 1D layered velocity model proposed by Campillo et al. (1996) for the Guerrero province and the anelastic effects given by an attenuation relationship determined for the region (García et al., 2004). The comparison between synthetic and observed data, as well as the uncertainty of the locations, are discussed in detail by Cruz-Atienza et al. (2015).

Unlike the TTs locations reported by Cruz-Atienza et al. (2015) using the TREP method, for this

work we implemented a time-scan strategy along the entire tremor bursts using 1-minute windows with 20 seconds overlap and considering theoretical move-outs for the S-wave arrivals. We obtained 15,222 locations (Figure 2.1) with uncertainties smaller than 10 km assuming a grid increment of 5 km in the three Cartesian directions. This strategy allows us to analyze in detail the spatial variation of tremor sources during the observational period. Our final locations share features with those of previous studies, such as the concentration of TT sources downdip in the sweet spot and some activity with smaller density updip in the transient zone (Figure 2.1b). Depth of most tremors is well constrained around the plate interface at 42 km and below, within the oceanic slab, up to a depth of 50 km as can be seen in the histogram on the left of Figure 2.1b. The comparison with the LFE locations by (Frank et al., 2014) is remarkable in both the trench-perpendicular and vertical directions (compare Figures 2.1b and 2.1c), supporting the idea that tremor is composed of LFE swarms (Shelly et al., 2006). In contrast with the LFEs catalog (Frank et al., 2014), our tremor locations using the TREP method have good resolution in the along-strike direction (i.e., in the array-perpendicular axis). As shown by (Cruz-Atienza et al., 2015), resolution lengths in that direction are similar to those in the trench-perpendicular direction. This allows us to analyze the occurrence of TTs along dip and along strike over the horizontal plate interface during the propagation of the SSE.

Figure 2.1a shows both our TT locations and the final slip distribution of the 2006 SSE determined by Radiguet et al. (2011). The slip propagation of this event does not exhibit a simple unilateral trend (see rupture times with white contours). It nucleates at the downdip portion of the interface, and simultaneously spreads updip and bilaterally in the trench-parallel direction. The sweet spot (maroon rectangle) is located in the downdip limit of the maximum slip, as previously discussed by Kostoglodov et al. (2010). Although the maxima of slip are updip and do not coincide with the sweet spot, there is a small amount of slip (around 5 cm) that accommodates in the main TT source area (i.e., in the sweet spot). It could be argued though that such small slip may be an artifact due to the smoothing procedure involved in the source inversion. However, since the sweet spot lies in a region with highest confidence for the inverted slip according to the resolution matrix reported by Radiguet et al. (2011), the slip mapped there is very likely to be real.

2.3 Elastic fields induced by the 2006 SSE

To investigate the causal relationship between the 2006 SSE and the associated TTs in Guerrero, following Rivet et al. (2011, 2013) we used a three-dimensional (3D) finite difference code for solving the velocity-stress formulation of elastodynamic equations (Olsen et al., 2009) to track the quasi-static evolution of the stress field induced by the slow slip history inverted by Radiguet et al. (2011) considering 20-day time steps. Our velocity model, which is the same used by Rivet et al. (2011), integrates a trench-perpendicular tomographic structure (Iglesias et al., 2010) extended in the trench-parallel direction and takes into account the geometry of the plate interface and the elastic properties of the upper oceanic crust inferred by previous studies (Pérez-Campos et al., 2008; Kim et al., 2010).

Using this numerical model we obtained the stress tensor and the volumetric changes (i.e., the trace

of the stress tensor) at every point of our 3D domain associated with every slip increment of the SSE. We thus solved for the normal and shear stresses acting on fault planes parallel to the plate interface, that we have assumed horizontal in the tremor region according to its geometry (Pérez-Campos et al., 2008) and recent observations of TTs (Cruz-Atienza et al., 2015), LFEs (Frank et al., 2013) and very low frequency earthquakes (VLFs) (Maury et al., 2016) in Guerrero, which have focal mechanisms with zero or very low dipping angles. We then estimated pore pressure changes from the volumetric strain field assuming undrained conditions as:

$$\triangle p = -B\frac{\triangle \sigma_{kk}}{3} \tag{2.1}$$

where σ_{kk} is the change of dilatancy and B represents the Skempton coefficient ranging from 0 to 1, where the rock is fluid-saturated for B close to 1. This relation implies that changes of dilatancy every 20 days are instantaneously translated into changes of pore pressure. Since the permeability is low within the oceanic crust (Audet et al., 2009; Peacock et al., 2011; Perry et al., 2016) where fluids are likely to be present in Guerrero (Song et al., 2009; Kim et al., 2010), fluid diffusion is slow enough to make our approach valid for the time span of the SSE. To confine fluids within the top 5 km of the subducted slab we considered B= 0.9 in that layer and B= 0 elsewhere.

To quantify the combined effect of the normal and shear stresses along with the pore pressure, we computed the Coulomb Failure Stresses (CFS). Assuming a fault friction coefficient, μ, the CFS indicates how prone is a rock to failure on a specific fault orientation following the relation:

$$\triangle CFS = \triangle \tau + \mu(\triangle \sigma_N + \triangle p) \tag{2.2}$$

where $\triangle\tau$ represents the change of shear stress on the fault plane in the slip direction, $\triangle\sigma_N$ is the change of the fault normal stress (positive for tension) and $\triangle p$ is the change of pore pressure that counteracts the effect of $\triangle\sigma_N$. Since $\triangle\tau$ induced by the SSE is almost an order of magnitude larger than the corresponding values for $\triangle\sigma_N$ and $\triangle p$, the CFS do not significantly change for different friction coefficients. We have though assumed a friction coefficient of 0.2, which is in general agreement with recent estimates in regions where slow phenomena occur (Thomas et al., 2009, 2012; Houston, 2015).

2.4 Spatio-temporal correlation between TTs and the 2006 SSE

Figures 2.1b and 2.1c show that TTs and LFEs are remarkably well confined to depths close to the plate interface. Since we are interested in the along-dip and along-strike variations of tremor activity, and how they are correlated with the elastic fields induced by the SSE near by the interface, for the analysis we only considered TT locations between 40 and 50 km depth (i.e., at the interface and within the subducted slab), the slip on the plate interface and the $\triangle CFS$ over a horizontal plane 2 km below the plate interface. Figure 2.2 shows the evolution of both the 2006 SSE and the associated CFS, along with the occurrence of TTs in the corresponding time windows. CFS (right column)

is only shown where it is numerically well resolved by our finite difference method (i.e., in the volume containing the horizontal segment of the plate interface). We notice that $\triangle CFS$ at parallel planes within the first 5 km below the plate interface are essentially the same, so the solution at the chosen depth is representative of the deformations taking place within the upper oceanic crust. When estimating the pore pressure we assumed that fluids are uniformly distributed along the slab, which may be not necessarily true considering possible dehydration pulses in specific slab segments as inferred from mineralogical phase transformations and thermal modeling (Manea and Manea, 2011). However, given the large uncertainties in the fluid content, for the sake of simplicity and to identify first order correlations with the TT activity we kept our hypothesis in the analysis.

In order to identify the parameter that actually triggers tremor in the whole SSE region, as a first approach we analyzed the spatio-temporal consistency of tremor activity with (1) slipping regions of the plate interface and (2) with interface region where $\triangle CFS$ is positive. To do so, for each 20-day window of the SSE we quantified the percentage of TTs in each window occurring over regions with slip increments larger than 5 mm and $\triangle CFS$ higher than 5 kPa. Figure 2.3 summarizes the results of this exercise, where we find that there is a much higher spatio-temporal consistency of TT activity with slip (red bars) than with $\triangle CFS$ (blue bars) during the most intense phase of the SSE (i.e., between May and August, where the green line depicts the SSE source time function, STF). The trend is different at the beginning and the end of the SSE, where the STF starts growing and falls to zero, respectively. At those stages, TT activity is more consistent with increments of CFS.

Histograms in Figure 2.3 essentially give us an integrated idea of the temporal correlation between the SSE-induced elastic fields and tremor activity in the whole region. Thus, to generate detailed maps showing their spatio-temporal correlation, we divided our horizontal domain into bins of 3 x 3 km. In each bin we extracted the time series of the SSE-induced fields (i.e., the slip rate and $\triangle CFS$ time series) and the TT counts during the whole duration of the SSE. Figure 2.4 shows some examples of those series in three representative bins with locations shown in Figure 2.5 (small squares). Whereas there is no visual correlation between the TT activity and the evolution of $\triangle CFS$ (upper panels) at these bins, the correlation between the TT activity and the slip rate is remarkable (lower panels). To quantify the similarity of the time series in the whole region, for each bin we computed the correlation coefficient (CC) between the TT time series and those associated with both SSE-induced fields. Values of CCs for the series of Figure 2.4 are reported inside each panel, where positive high values are only found for the slip rate time series (lower panels).

Figure 2.5 presents the resulting spatial distributions of CCs in the study region. These maps allow delineating the regions where there is (or there is not) a significant spatio-temporal correlation between the TT activity and the evolution of both the SSE slip rate (top panel) and the associated $\triangle CFS$ (bottom panel). As previously shown in Figure 2.4, the evolution of $\triangle CFS$ has very low, if any, positive correlation with the activity of TTs during the SSE in the entire study region. In contrast, the slip rate correlates very well with the tremor activity in both the transient zone and the sweet spot, the latter being a region where previous studies found difficult to conciliate the tremor rate with the slip evolution of the SSE (e.g., (Kostoglodov et al., 2010; Frank et al., 2015a)). To quantify the statistical significance of the estimated CCs, we performed a goodness-of-fit test under the null hypothesis that the slip rate and the occurrence of TTs are not temporally correlated. Figure A.1b shows that regions where we found high CCs values present low p values (p <0.05), implying

that our correlation estimates there provide a significant result and that the null hypothesis can be rejected at the 95 % confidence level.

In addition, we calculated the CC between the evolution of the pore pressure and the occurrence of TTs and found a good correlation in the sweet spot (Figure A.2, left panel). However, the occurrence of TTs and the evolution of the normal stress are highly anticorrelated in the same region (Figure A.2, right panel), which implies that both fields, the pore pressure and the normal stress, counteract each other making difficult to associate the evolution of pore pressure with variations in the activity of TTs. We can only conclude then that pore pressure inhibits the clamping effect of the normal stress to maintain very low effective stresses in the sweet spot.

2.5 Correlation between LFEs and SSEs

We now compare the evolution of the SSE-induced fields with the long-term activity of LFEs. The large amount of events detected and located almost continuously by Frank et al. (2014) brings us the opportunity to do such comparison not only during the 2006 SSE but also during the preceding inter-SSE period, where short-term SSEs have been identified (Vergnolle et al., 2010; Frank et al., 2015b).

Following Frank et al. (2015a), we first obtained the LFE rate from their cumulative count in different segments of the plate interface with increasing distance from the trench (Figure A.3a). To make an appropriate comparison with the SSE-induced fields that have a time resolution of 20 days, we filtered the LFE occurrence-rate time series in every segment for periods longer than 40 days (Figures A.3sb and c). The black curves of Figure 2.6 show the averages of the time series along both the transient zone (left) and the sweet spot (right). As previously noticed by Frank et al. (2015a), two main features arise from the analysis: (1) the LFE rates in both the transient zone and the sweet spot largely increases during the 2006 long-term SSE; and (2) there exist isolated peaks of LFEs activity in both regions during the inter-SSE period associated with short-term SSEs (Frank et al., 2015b). Figure 2.6 also shows that the rate of LFEs in the sweet spot during the short-term SSEs is as high as the maximum rate observed during the 2006 long-term SSE. This last feature is not present in the transient zone, where bursts of LFEs during the short-term SSEs are only one fifth of the maximum rate observed during the 2006 SSE. To compare the rate of LFEs with the SSE-induced fields, we subtracted from the time series (Figures A.3b and c) the secular seismicity rate in each region (i.e., the minimum value of the time series) to preserve only the changes of activity associated with the short- and long-term SSEs. We then computed, for every 20-day increment, the average of the 2006 SSE-induced fields along the transient zone and the sweet spot (i.e., the average of each field inside the rectangles shown in Figure 2.5). Tests for different geometries and sizes for the rectangular regions gave essentially the same results.

To make possible the comparison of the LFEs time series with the evolution of the SSE-induced fields including the inter-long-term SSE period, we approximated the slip distribution of the short-term SSEs found by Frank et al. (2015b)with a two-dimensional (2D) Gaussian function by taking care of fitting the best possible each slip contour (please notice in Figure A.4 how close is our

approximation for values larger than 2 mm to the slip distribution reported in Figure 2.1a of Frank et al. (2015b)). To validate the elliptical slip approximation, which neglects some small values (<2 mm) close to the shore and downdip, we compared the associated surface displacements (computed with our 3D finite difference model) with the corresponding GPS measurements reported by Frank et al. (2015b) (Figure A.4). Although our displacement predictions slightly differ from those of Frank et al. (2015b), they explain fairly well the observations, especially in the closest three stations where displacements are larger than 1 mm and the data errors are smaller than the actual displacements. Given the small duration of the short-term events, we assumed a 7-days-width (Gaussian) slip rate function that corresponds to the maximum duration of the LFE bursts reported by Frank et al. (2014) in the same period. The times for the maxima of the slip rate functions were chosen to coincide with the times of the maxima of the LFE rate history during the inter-long-term SSE period. This procedure allows us to quantify also the average of the elastic fields induced by the short-term SSEs reported by Frank et al. (2015b)in both the transient zone and the sweet spot (rectangles of Figure 2.5) in the same way we did for the 2006 long-term SSE (i.e., by solving the 3D elastodynamic equations for the slow slip distribution).

Figure 2.6 shows the resulting comparison, where $\triangle CFS$ (blue curves) does not correlate (positively) with the LFE rate (black curves) neither in the sweet spot nor the transient zone. During the 2006 long-term SSE, $\triangle CFS$ is anticorrelated with the activity of LFEs in the transient zone, and its maximum in the sweet spot is delayed more than two months from the corresponding LFE rate maximum. In contrast, the slip rate in both regions during the long-term SSE is well correlated with the occurrence-rate of LFEs. These results are consistent with our findings of Section 4 regarding the TT activity, where we concluded that tremor is better correlated in space and time with the long-term SSE slip rate than with the associated $\triangle CFS$.

During the inter-long-term SSE period (i.e., outside the shaded areas of Figure 2.6), while the slip rate (red curves) amplitudes in the transient zone (left panel) follow pretty well the observed rates of LFEs associated with the short-term SSEs, in the sweet spot (right panel) they are much smaller (more than 60 %) than expected (compare black and red curves). One possible reason for this discrepancy is that the short-term slip distribution inverted by Frank et al. (2015b) is located in the wrong place. We notice that given the extremely small GPS amplitudes associated with these events, Frank et al. (2015b) had to stack GPS time series from different short-term SSEs getting uncertainties much larger than most of their observations (see Figure A.4). They found, however, that the short-term slip patches are located south (i.e., trenchward) of the sweet spot (see Figures 2.7a and A.4).

2.6 Finding the actual location of the short-term SSEs

Our results of Sections 4 and 5 show that the slip rate on the plate interface is the parameter that better correlates with tremor activity during the most active phase of the long-term 2006 SSE in both the transient zone and the sweet spot. It is thus reasonable to think that the slip rate modulates the LFE rate, as suggested by Frank et al. (2015b) when interpreting LFEs activity in terms of deep slip transients in the same region. We then should expect the slip rate function to

mimic the tremor (and LFEs) rate evolution during the short-term SSEs in the same way we have shown to be the case during the long-term 2006 event. By using this expectation as an observational constraint, we can infer the slip distribution of the short-term SSEs that best explain the rate of LFEs in both source regions.

The slip rate functions shown in Figure 2.6 during the inter-long-term SSE period (red curves outside the shaded areas) were computed from our elliptical approximation of the short-term slip distribution proposed by Frank et al. (2015b) (Figure A.4). The fit with the LFE rate (black curves) is far from satisfactory in the sweet spot. We then performed a grid search to look for the size and position of the elliptical slip patch, both in the along-dip direction, that best explain the LFE rate in the two tremor regions (i.e., in the sweet spot and the transient zone). We define the size of the slip patch along both ellipse axes as the distance between the slip contours limiting 0.99 cumulative probability of the Gaussian distributions, which correspond approximately to the distance separating the slip contours with 5 % of the maximum slip. The patch size in the along-strike direction was fixed to 130 km because this value minimizes the error function defined below to evaluate the goodness of the slip models. The grid search then explored slip patches with different along-dip dimensions and positions, so that all patches have the same moment magnitude equal to 6.4, reported as the upper limit for the short-term SSEs by Frank et al. (2015b). Since the slip distributions are given by 2D Gaussian functions, to match the chosen magnitude, the method automatically adapts the maximum slip values at the center of the ellipses.

The most prominent difference between the transient zone and the sweet spot is the relative amplitudes of the LFE rate functions (black curves in Figure 2.6) during the short- and long-term SSEs. While the amplitude ratio in the sweet spot between most short-term SSEs and the long-term SSE is nearly one, in the transient zone the average ratio is about five. We thus define the goodness of a given slip model as the average error of the slip-rate amplitude ratio in both tremor regions. If the observed LFEs ratio is defined as r_o and the predicted slip-rate ratio as r_p, the model error in each region is then given by $(r_o - r_p)/r_o$. Figure 2.7b shows the goodness of all slip models explored in the grid search. Although the resolution for the slip patch location is better (vertical axis) than the patch size (horizontal axis), the optimal slip model is clearly located 215 km away from the trench (i.e., right in the sweet spot and thus 35 km farther downdip from the position determined by Frank et al. (2015b)) and has 170 km length (white start) with maximum slip of 8.0 mm. The optimal slip model is shown in Figure 2.7a, where we also compare the observed GPS displacements determined by Frank et al. (2015b) for the short-term SSEs with the displacements predicted by the model. Considering the very large GPS data uncertainties (circles in Figure 2.7a), we did not use the GPS displacements to resolve the inversion because many different slip distributions may formally explain the geodetic observations in the same way, providing no useful information. In this sense, our displacement predictions are as good as those reported by Frank et al. (2015b) for their slip distribution. The difference between both models is that our slip distribution also explains the LFE rates in both tremor regions. This can be seen in Figures 2.7c and 2.7d where we show that, unlike Frank et al.'s model (red curves in Figure 2.6), the slip-rate functions predicted by our slip distribution satisfy the expected behavior in both tremor regions (i.e., the relative slip-rate amplitudes during both short- and long-term SSEs) when compared with the rate of LFEs (black lines).

The along-dip extension of our slip model indicates that the short-term SSEs are likely to take place mainly in the sweet spot, although they also reach the transient zone. In the transient zone (i.e., at 170 km from the trench), a slip larger than 2 mm is required for the slip-rate to match the observational condition imposed by the LFE rate. Figure 2.8 shows an overview of the SSEs in Guerrero (blue and red curves) along with our tectonic tremor locations (color shades) and LFEs (gray curves). Unlike previously suggested, we can see that most of the TT and LFE activity taking place in the sweet spot coincides with the plate interface segment where the short-term SSEs occur according with our analysis.

2.7 Discussion

The comparison of the SSE-induced fields with independent observations of TTs and LFEs in Guerrero suggests that the SSEs slip rate in the plate interface is the parameter that controls the occurrence rate of these seismic events in the whole tremor region (i.e., updip in the transient zone and downdip in the sweet spot). During the long-term 2006 SSE, the rate of LFE sources is similar in both regions (Frank et al., 2015a). However, the maximum slip rate in the sweet spot is approximately half of the maximum value observed in the transient zone (see Figures 2.7c and 2.7d). This implies that there is a significant difference between both regions in terms of frictional properties that could be interpreted as variations of the tremor-asperities yielding strength. To estimate the strength level of the tremor asperities, we calculated the peak to residual stress drop associated with the maximum slip rate in the two tremor regions. To do so we considered a simple relationship for anti-plane shear cracks stating that the ratio of the slip-front propagation speed, V_{prop}, and the slip rate, V_{slip}, can be approximated as the ratio of the elastic shear modulus, G, and the peak-to-residual stress drop, $\triangle\tau$, in the slipping front as (Ida, 1973; Shibazaki and Shimamoto, 2007; Rubin, 2011; Rubin and Armbruster, 2013)

$$\frac{V_{slip}}{V_{prop}} = \frac{1}{\alpha}\frac{\triangle\tau}{G} \tag{2.3}$$

where α is a geometric constant that depends on the spatial distribution of the stress drop behind the slip front. For slow dislocations such as shown in Figure 2.2 or those observed in Cascadia during the ETS, the length of the slip front, W, is much larger than the distance between the front and the place where the slip has reached its final value, L (i.e., $W >> L$). In these cases, $\alpha = 1/\pi$ is the more appropriate choice for a uniform stress drop distribution (Rubin and Ampuero, 2009; Hawthorne et al., 2016). Assuming a shear modulus of 18 GPa (Royer et al., 2015) and a constant SSE propagation speed of 0.8 km/day (Radiguet et al., 2011), by taking the average of the maximum slip rates as 1 and 0.45 mm/day for the transient zone and the sweet spot (see Figures 2.7c and 2.7d), respectively, the corresponding stress drops for these regions are 7 and 3 kPa. Such values depend on the relatively unconstrained choices for G and α. However, values twice as large for these constants (i.e., G = 30 GPa and $\alpha = 0.6$), that are valid for cases where $W \approx L$, would affect the estimated stress drops by a factor of 1.5 to 3, that still are in good agreement with the peak stresses of tens of kPa dynamically induced by the surface waves of the 2010 Maule earthquake, which

triggered a large number of tremors in Guerrero during the 2009-2010 SSE (Zigone et al., 2012). Spatial variations in the stress drop during the SSE suggest that tremor asperities updip in the transient zone can support higher stresses (i.e., around 2.3 times larger) than those downdip in the sweet spot. Such variations, that can be interpreted as changes of the yielding levels in both regions, may be associated either with variations of the asperities density in the plate interface (Yabe and Ide, 2014) or changes in the distribution of sources of fluids, which would translate into variations of pore pressure and thus of the effective stresses along the interface. We point out that the second hypothesis seems more plausible in Guerrero considering that thermal modeling of the subducted Cocos plate predicts mineralogical phase transformations in the slab releasing large amounts of fluids right in the sweet spot (Manea and Manea, 2011).

Our results imply that the $\triangle CFS$ induced around the SSEs slipping regions might not be enough to break the tremor asperities. Typical values of $\triangle CFS$ in the sweet spot during the main phase of the SSE are of the order of few kPa (e.g., up to 2.5 kPa in Figure 2.4b), which are clearly not large enough to trigger tremor as suggested by Figure 2.5b, where no overall correlation is found between the TT activity and the regions with positive values of $\triangle CFS$. However, during the late phase of the 2006 SSE (i.e., the last three months) this is not true, as revealed by the higher consistency between the TT activity and $\triangle CFS$ than with the slip (Figure 2.3). One possible explanation for the low consistency with slip in that period is that tremor bursts in September and November (see black line in Figure 2.3) correspond to reactivated slip transients not resolved in the SSE inversion by Radiguet et al. (2012). Another possibility is that stronger tremor asperities were loaded during the passage of the SSE front and then broken by trailing increments of the CFS, as suggested by the last snapshot of the right column in Figure 2.2. Our findings then suggest that the causal relationship between SSEs and TTs primarily depends on the stressing rate history of tremor asperities, which in turn is modulated by the slip rate surrounding the asperities. Figure 2.9 illustrates this idea. Once the SSE approaches the TT source region, it induces an increase of the shear stress (or $\triangle CFS$) ahead of the slip front (panel a). At this point, the stress concentration does not exceed the strength level of the asperities. As soon as the slip front reaches the tremor region, the slip rate surrounding the locked asperities keeps stressing them till they break (panel b), increasing thus the TT occurrence rate behind the slip front (panel c). This mechanism has also been suggested to explain the tremor genesis in Cascadia (Wech and Bartlow, 2014). As discussed before, the strength of the asperities in the sweet spot is significantly lower (about 2.3 times lower) than in the transient zone, which makes the former region much more sensitive to tiny stress perturbations due to small dislocations associated with short-term SSEs that we have shown take place in the sweet spot.

TTs and LFEs are sensitive to small stress perturbations induced by tides in different subduction zones. Recent studies found that the tremor rate and the tidal stress changes obey an exponential relationship (Thomas et al., 2012; Houston, 2015; Yabe et al., 2015). Houston (2015) observed that tremor rate during the late stage of the ETS is an exponential function of the $\triangle CFS$. Since our results point out that the $\triangle CFS$ is not linearly related with the occurrence rate of TTs and LFEs, i.e., they have very low correlation coefficients (top panels of Figure 2.4 and Figure 2.5b), we explored the possibility that changes in the rate of these events follow an exponential function of the $\triangle CFS$ induced by the SSEs. We performed several tests in different TT regions where we computed the $\triangle CFS$ using different values of the friction and Skempton coefficients and compared with the

associated tremor rates. However, we did not find a convincing exponential trend as observed for tidal stresses.

The spatial-temporal correlation between tremor activity and the slip rate during the 2006 long-term SSE is clear from our results. However, other SSEs should be analyzed to generalize our conclusions. We performed the same analysis for the 2009-2010 SSE in Guerrero using the slip rate imaging determined by Radiguet et al. (2012). During such event, the MASE array was not longer in operation so we generated a TT catalog using five to seven broadband stations deployed in Guerrero during the G-Gap project. However, the sparsity of the array and the limited time span of the data, which did not cover the complete duration of the SSE, prevented us obtaining exhaustive TT locations to generate consistent correlation maps such as those of Figure 2.5.

2.8 Conclusions

High-resolution tremor locations obtained with the TREP method allowed us to make a detailed analysis of the occurrence rate of TTs during the long-term 2006 SSE. Results from the analysis revealed a consistently high spatial-temporal correlation between the SSE slip rate and the occurrence rate of TT along both the transient zone (updip) and the sweet spot (downdip). The absence of correlation with the SSE-induced $\triangle CFS$ leads us to discard the hypothesis advanced by previous authors that the stress transferred from the updip slipping regions acts as the main mechanism triggering tremor downdip in the sweet spot. Our quantitative results strongly suggest that the SSE slip rate is the main parameter modulating the TT activity in the whole Guerrero region. This conjecture implies that the causal relationship between SSEs and the TT activity directly depends on the stressing rate history of the tremor asperities, which in turn is modulated by the slip rate in the surrounding regions (Figure 2.9). Such conclusion supports the idea that TT can be used as a monitoring tool to infer the occurrence of slow slip on the plate interface (e.g., (Wech et al., 2009; Frank et al., 2015b; Frank, 2016)). However, care should be taken with the long-term SSEs in Guerrero because the location of the maximum slip does not coincide with the regions of maximum TT activity. A clear example of this is that despite tremor activity dominates in the sweet spot, where we found the highest correlation coefficients with the slip rate, the amount of slip there (3 to 7 cm, Figure 2.1) is about three times smaller than updip in the transient zone. We have estimated that the strength of the asperities radiating tremor in the sweet spot is around 3.2 kPa, which is 2.3 times smaller than the corresponding value updip in the transient zone, and which makes the former region more sensitive to tiny stress perturbations such as those induced by teleseismic surface waves and short-term SSEs. In addition, we used the LFE rate history during the 2006 SSE and inter-long-term SSE periods to constrain the slip distribution of the short-term SSEs in Guerrero. Our results show that these events take place further downdip (about 35 km) than previously estimated by Frank et al. (2015b) (Figure 2.7a) with maximum slip of about 8 mm in the sweet spot (Figure 2.8). This new model features a continuum of slow slip regions covering the entire tremor zone. Although further analysis of different SSEs is still necessary to confirm that the slip rate is the parameter that systematically controls the tremor rate in the region, this study provides the first quantitative insights into the causal relationship between TTs and SSEs in Guerrero, Mexico.

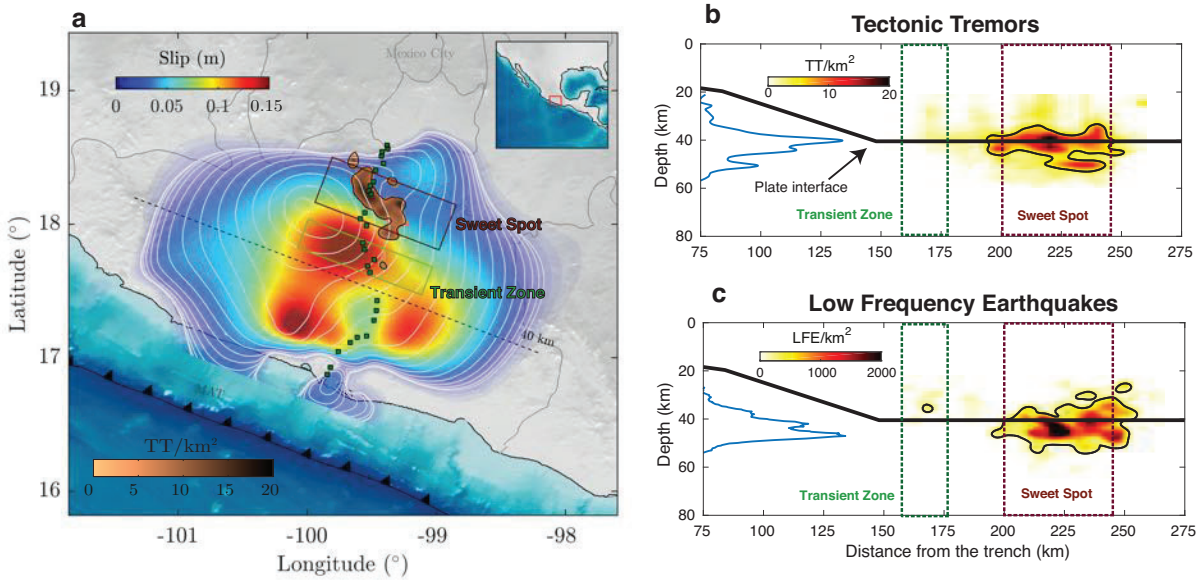

Figure 2.1. TT (this study) and LFE (Frank et al., 2014) locations in Guerrero, and slip distribution of the 2006 SSE (Radiguet et al., 2011). The green and maroon rectangles in the three panels indicate the transient zone and the sweet spot, respectively. (a) The blue-red colored region represents the cumulative slip of the 2006 SSE. White contours show the rupture times for 2 cm cumulative slip every 20 days. Green squares indicate the location of the MASE array stations used to locate the TTs. The beige-black colors represent the cumulative TT density and the black contour encloses the regions containing densities higher than 5 TT/ km2. The dashed line indicates where the plate interface becomes horizontal. (b and c) Cumulative TT and LFE densities projected onto a vertical trench-perpendicular section. The blue curves show normalized histograms for the TTs and LFEs hypocenters. Note that most of the tremor activity occurs between 40 and 45 km depth (i.e., at the plate interface and/or within the top 5 km of the oceanic crust).

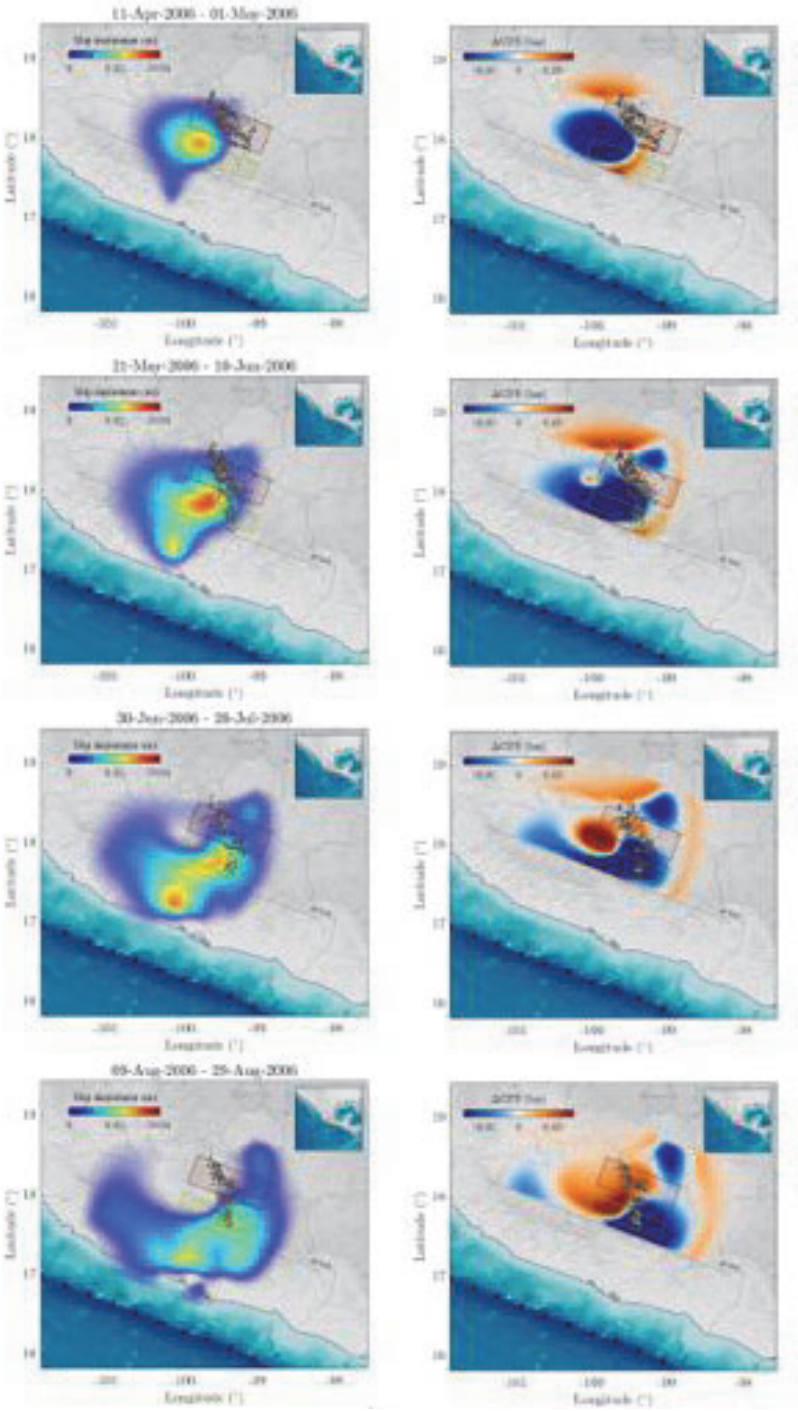

Figure 2.2. Snapshots of the slip increment for the 2006 SSE (left column) and the associated $\triangle CFS$ computed over a horizontal plane 2 km below the plate interface (right column). The black dots indicate the associated TTs occurring during the corresponding time window. Green and maroon rectangles represent the transient zone and the sweet spot, respectively. The dashed line indicates where the plate interface becomes sub-horizontal.

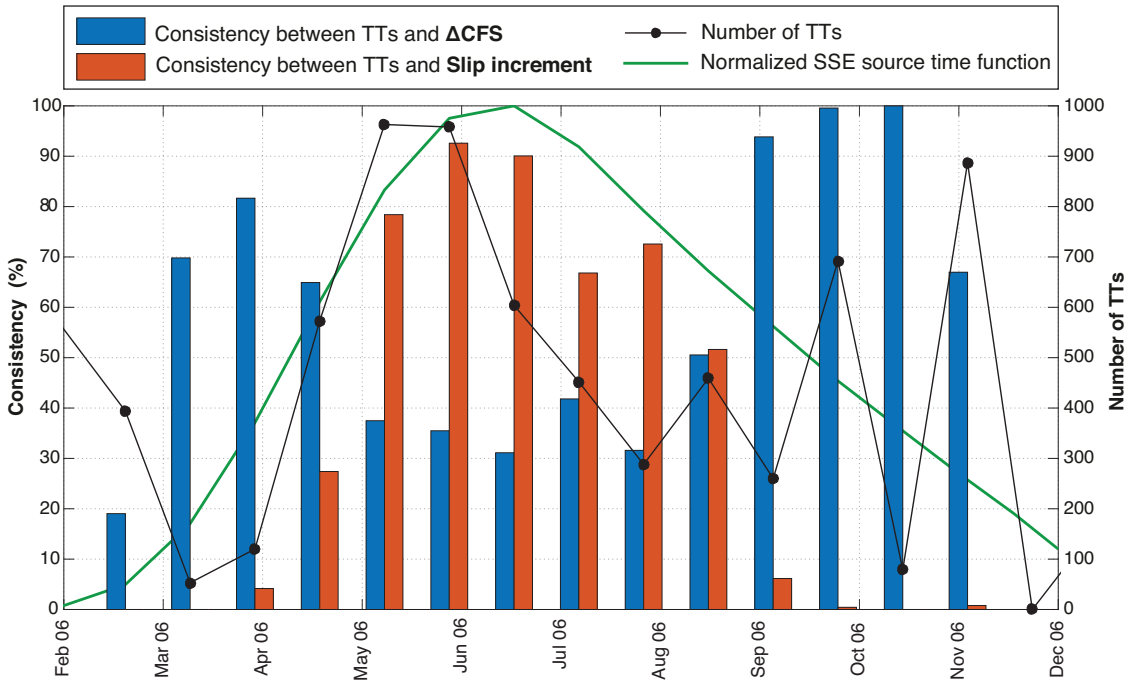

Figure 2.3. Consistency between the TT occurrence and the 2006 SSE-induced elastic fields. The bars represents the percentage of TTs in each time window located within regions with values of $\triangle CFS$ larger than 5 kPa (blue bars) and within regions with slip increments larger than 5 mm (red bars) for every 20-day slip increment of the 2006 SSE (left axis). The black line shows the number of TTs associated with each window (right axis). The green line shows the normalized source time function (STF) of the SSE along the horizontal segment of the plate interface.

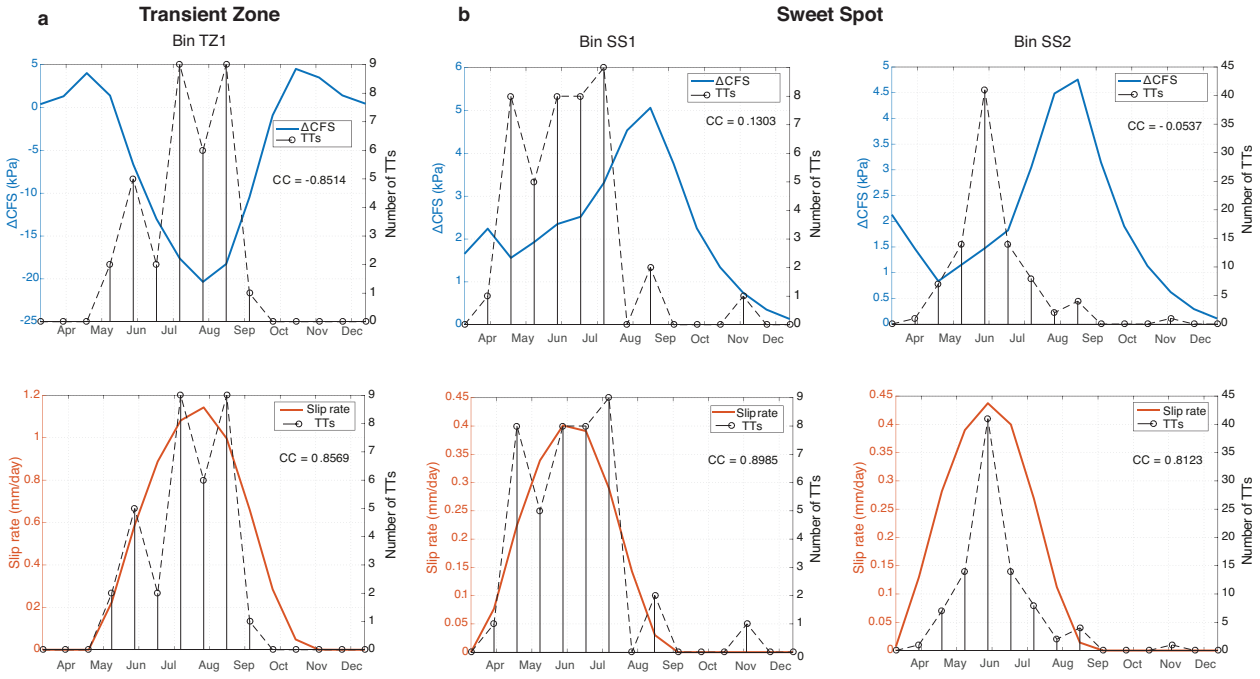

Figure 2.4. Comparison between the activity of TTs and the evolution of the SSE-induced fields in three representative spots of the plate interface (columns). Correlation coefficients (CC) between the TTs time series (black) and the evolution of the $\triangle CFS$ (blue) and the slip rate (red) are shown inside each panel. The 3x3 km spots are located in the Transient zone (a) and the sweet spot (b), as shown in Figure 5a.

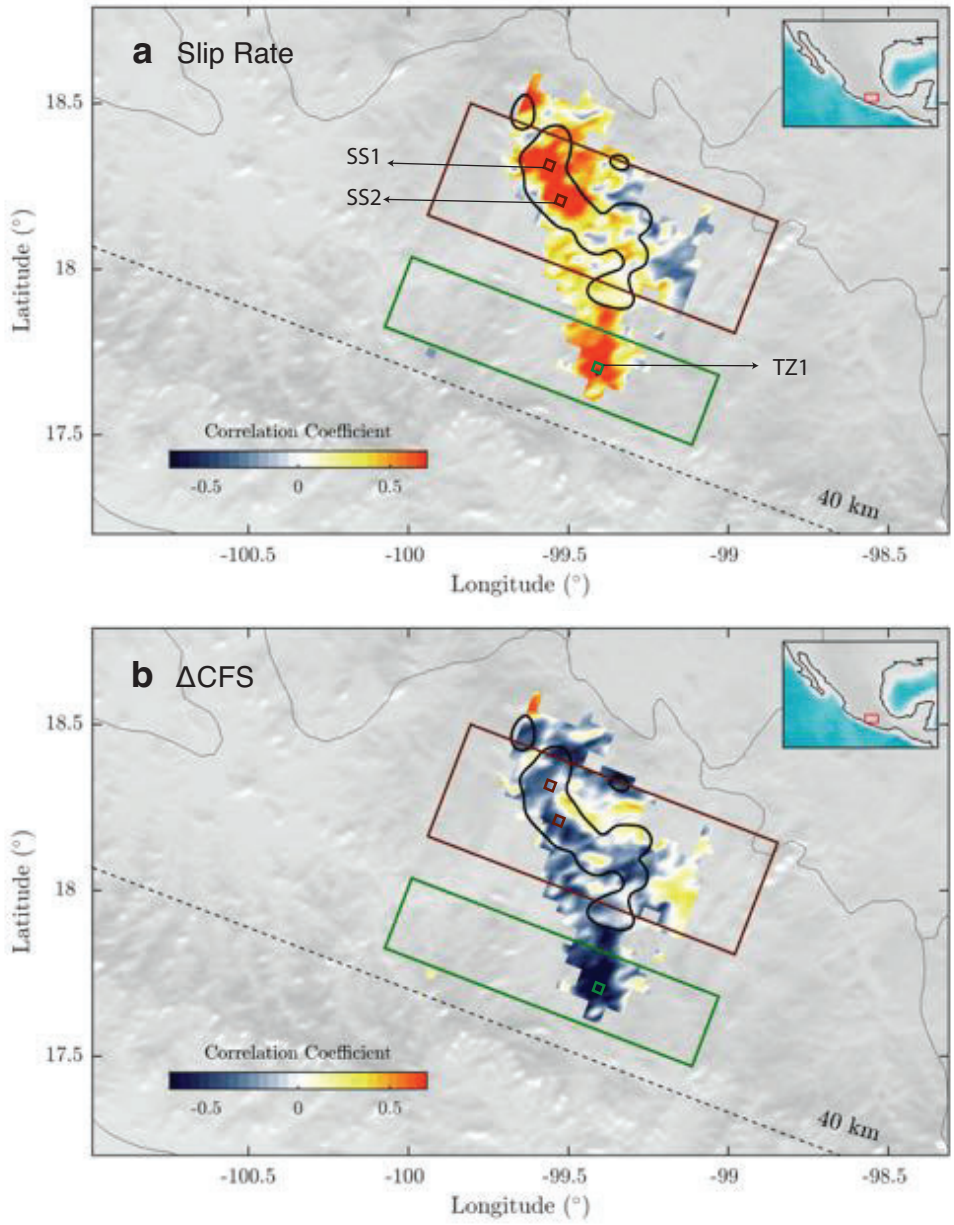

Figure 2.5. Correlation coefficients between the activity of TTs and the evolution of the slip rate (a) and the $\triangle CFS$ (b) during the 2006 SSE. The black contours indicate the regions with the highest occurrence of TTs. Squares indicate the 3x3 km bins where the time series shown in Figure 4 were extracted for the TT and SSE-induce fields. Green and maroon boxes indicate the transient zone and the sweet spot, respectively.

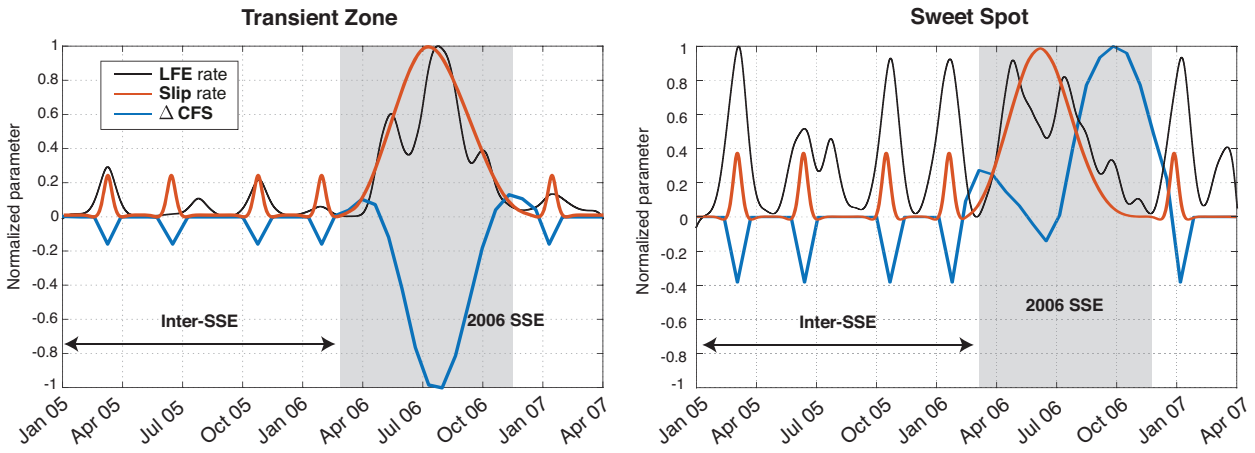

Figure 2.6. Comparison between the evolution of the SSE-induced fields and the occurrence-rate of LFEs (black lines) in the transient zone (left) and the sweet spot (right). The evolution of the $\triangle CFS$ and the slip rate is represented by the blue and red curves, respectively, during the 2006 SSE (shaded area) and the inter-SSE period.

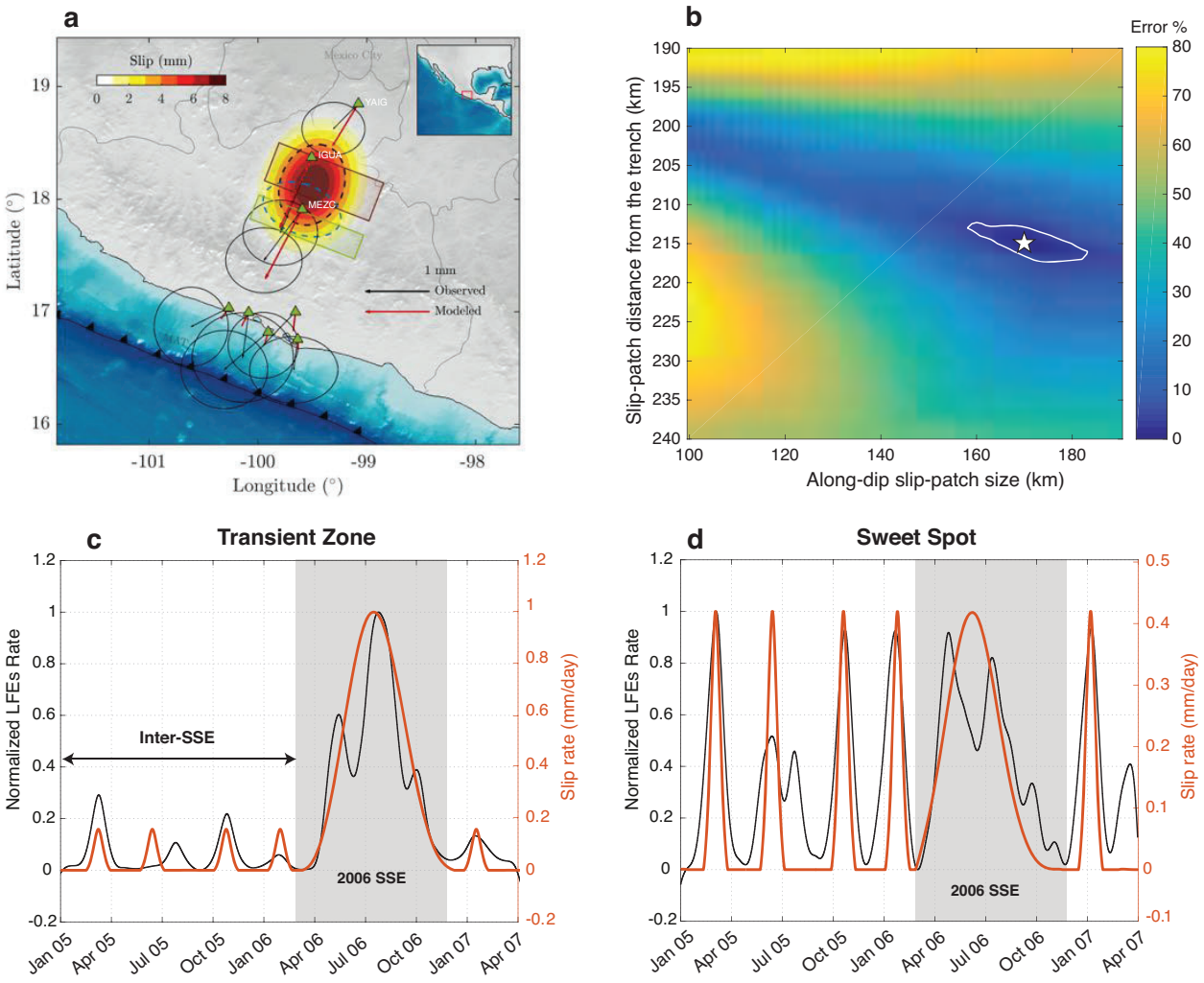

Figure 2.7. Location of the short-term SSEs and evolution of the slip rate in the tremor regions. (a) Slip distribution (color map) determined for the short-term SSEs that best explains the LFEs occurring rate in both transient zone and sweet spot during the inter-SSE period. The dashed blue ellipse approximates the 4 mm isoslip contour of the short-term SSE found by Frank et al. (2015b) (see Figure S4). The black dashed ellipse delineates the same isoslip contour for our model. Green triangles represent the local GPS stations and black arrows the observed GPS displacement vectors with their respective error ellipses. The red vectors correspond to the displacement predicted by our slip distribution obtained from the grid search. Green and maroon rectangles represent the transient zone and the sweet spot, respectively. (b) Cost function for the slip models explored in the grid search. White star indicates the slip model that present the best fit and the white contour encloses the models with errors smaller than 5 %. (c) and (d) show the fits between the slip rate (red curve) and the LFE rate (black curve) in the transient zone and the sweet spot, respectively, including our preferred short-term slip model.

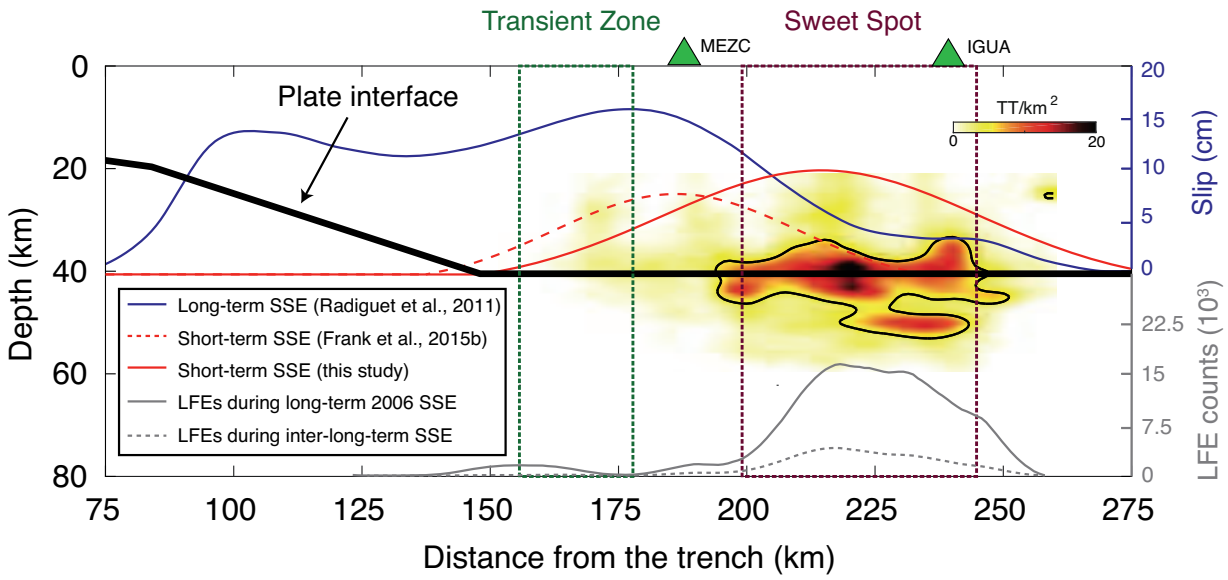

Figure 2.8. Overview of the slow earthquakes activity in Guerrero. Final slip distribution for the 2006 SSE (blue curve) below the MASE array Radiguet et al. (2011). Slip distributions for the short-term SSEs determined in this study (red curve) and by Frank et al. (2015b) (red dashed curve) are multiplied by a factor of 30 for comparison purposes with the long-term 2006 slip distribution. The thick black line sketches the geometry of the plate interface. The green and maroon dashed boxes indicate the location of the transient zone and the sweet spot. The green triangles represent the local GPS stations. The density of TTs shown in color shades (this study) is the same as in the Figure 1b and the gray curves show the LFEs histograms during both the long-term 2006 SSE (solid) and the inter-long-term SSEs period (dashed).

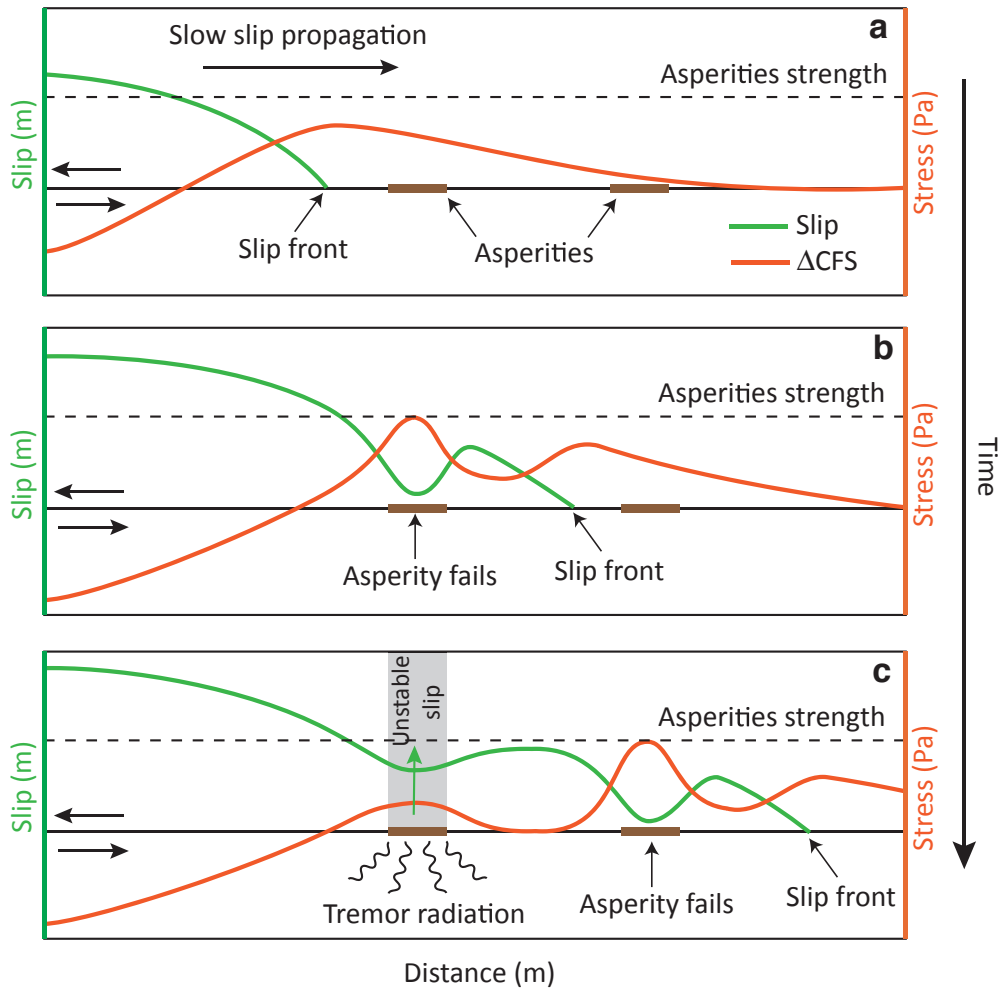

Figure 2.9. Cartoon illustrating the causal relationship between the SSEs and the TTs as suggested by our analysis. The stress ahead of the slip front does not break tremor asperities. It is the stable slip surrounding the asperities that brings them to failure behind the slip front. See text for more details.

Chapter 3

Rapid Tremor Migration and Pore-Pressure Waves in Subduction Zones

Contents

This chapter has been modified from its associated article: Cruz-Atienza, V. M., **Villafuerte, C.**, and Bhat, H. S. (2018). Rapid tremor migration and pore pressure waves in subduction zones. *Nature Communications*, 9(1):1?13. doi.org/10.1038/s41467-018-05150-3

Abstract

Rapid tremor migration (RTM) in subduction zones is a manifestation of complex fault-zone processes on the plate interface. Recent observations have revealed a large diversity of RTM patterns that are always associated with aseismic, shear strain at the interface. Small unstable asperities embedded in the stable shear zone are thus believed to originate tremor radiation during migration. Tectonic tremors have been recognized to occur where overpressured fluids exist. Spatial variations of fluid pressure may lead to non-linear diffusion processes with potentially large implications in tremor generation. Here we show that pore-pressure waves are likely to exist in the plate interface, propagating with speeds and pathways similar to RTMs observed in different subduction zones including Guerrero, Mexico, where we introduce new high-resolution tremor locations and a RTM source physical model. These waves may explain the whole hierarchy of RTM patterns by producing transient reductions of the fault strength and thus secondary slip fronts triggering tremor during slow earthquakes.

3.1 Introduction

Slow slip events (SSE) in subduction zones (Dragert et al., 2001) have been recognized as the main driving mechanism triggering tectonic tremors (TT) (Rogers and Dragert, 2003; Obara et al., 2004) and low frequency earthquakes (LFE) (Shelly et al., 2006) in the vicinity of the plate interface (Brown et al., 2009). A clear spatio-temporal correlation exists between the propagating slow slip and tremor in different subduction zones, such as Cascadia and Nankai (Wech et al., 2009; Obara, 2010). Known as Episodic Tremor and Slip (Rogers and Dragert, 2003) (ETS), this coupled phenomenon mostly propagates along-strike of the interface at speeds of 10 [km d^{-1}] (Wech et al., 2009; Obara, 2010; Wech and Bartlow, 2014). However, much faster tremor migrations have also been recognized in two other preferential directions. During the ETS propagation, localized tremor sources may migrate faster for tens of kilometers opposite to the ETS-front propagation (often along-strike) direction, with speeds from 100 to 400 km d^{-1} (i.e., 7-17 km h^{-1}) (Houston et al., 2011; Obara et al., 2012). These Rapid Tremor Reversals (RTR) may travel up to 45 km backward initiating in the active ETS front (Peng and Rubin, 2016). The second rapid migration pattern is characterized by propagating streaks at even faster speeds ranging from 25 to 150 km h^{-1} along the slip-parallel (i.e. along-dip) direction (Shelly et al., 2007a; Ghosh et al., 2010). Recently, high-resolution tremor locations in Cascadia and Mexico have revealed a more complex behavior of Rapid Tremor Migrations (Peng et al., 2015; Peng and Rubin, 2017) (RTM), where they also occur in directions other than the along-dip and along-strike axes, especially after the main ETS front has moved away.

Observations in different subduction zones show that tremor radiation is always accompanied by slow slip in the plate interface. This is true for the ETS main front (Rogers and Dragert, 2003; Obara et al., 2004; Bartlow et al., 2011) and the secondary RTMs (including RTR (Hawthorne et al., 2016)). Such observations suggest that tremor sources are triggered, in all cases, by the stress concentration over unstable asperities surrounded by the slow slipping fault (Bartlow et al., 2011; Ito et al., 2007; Yabe et al., 2015; Villafuerte and Cruz-Atienza, 2017). For explaining the origin of RTM, the problem then reduces to understand the conditions allowing different slip patterns during an SSE (Bletery et al., 2017). Understanding the physics of Secondary Slip Fronts (SSF) propagating accordingly with the hierarchical RTM patterns has been a major research topic in the last years. Different works have tackled this problem based on fault constitutive models either under the rate-and-state (R&S) friction framework (Hawthorne and Rubin, 2013; Rubin, 2011; Colella et al., 2012; Yingdi and Ampuero, 2017) or by integrating brittle-ductile rheological considerations (Ando et al., 2012). Although a few of these models can explain most of the RTM patterns, none of them integrates a potentially critical element that seems to be always present in the ETS environment: overpressured fluids.

Regions of the globe where ETS occurs are systematically located at depths of the plate interface (30-45 km) where there is strong evidence of overpressured fluids in the oceanic crusts (OC) (Shelly et al., 2006; Audet et al., 2009; Peacock et al., 2011; Katayama et al., 2012). Fluid pressurization is the result of prograde metamorphic dehydration reactions producing large amounts of hydrous fluids from subducted materials (Saffer and Tobin, 2011). Overpressured fluids has been widely evoked in the literature suggesting possible implications they may have in the generation of SSEs and tremor (Katayama et al., 2012; Liu and Rice, 2007; Segall et al., 2010). Different investigations

have shown that composite faults characterized by a stable frictional matrix (i.e. dominated by velocity-strengthening (VS) constitutive parameters in the R&S friction law (Dieterich, 1994)) may undertake dynamic instabilities in embedded, velocity-weakening (VW) asperities (Yabe and Ide, 2017; Lui and Lapusta, 2016) provided that the contrast in frictional strength between the matrix and the asperities is large enough. In those models, the steady-state frictional strength is proportional to the effective normal stress acting on the fault plane (given by $(a-b)\sigma_e$, where a and b are R&S parameters and σ_e is the effective stress (Rubin and Ampuero, 2005)), so that the contrast required to produce seismic radiation from the asperities during an SSE, and thus LFEs, is likely to be induced by spatial and/or temporal variations of pore pressure (p). Furthermore, experimental evidence supported by R&S friction models also show that reductions of the effective stresses during stable sliding may produce transitions from VS condition to fully unstable (VW conditions) waves radiation (Liu and Rice, 2007). Understanding how fluids may behave in the slow-earthquakes environment affecting the effective stresses could thus shed light into the actual mechanisms governing tremor generation and migration. Here we explore a physical model capable to explain the diversity of RTM patterns as a result of transient perturbations of p traveling at the expected speeds and pathways along the fluid-saturated plate interface.

3.2 Results

3.2.1 Pore-pressure waves in the plate interface

Fluid transport in porous media may explain seismicity migration patterns due to diffusion processes (Nur and Booker, 1972; Miller et al., 2004). The driving force for fluid diffusion is the gradient of p (∇p_0), which can induce pressure fronts traveling with typical speeds ranging from 0.002 to 0.04 km h^{-1} in borehole injection tests (Shapiro et al., 2002). Laboratory studies of rock mechanics since the late sixties have shown that permeability (k) is a strongly decreasing function of the effective pressure (i.e., of $P_e = P_c - p$, where P_c is the confining pressure). Experiments in granite rock protoliths, fault-damaged zones and fault-core samples under elevated confining pressures systematically show an exponential decrease of k as the effective pressure increases of the form (Evans et al., 1997):

$$k(P_e) = k_0 e^{-\gamma P_e}, \tag{3.1}$$

where k_0 is the rock permeability for P_e=0, and γ is a constant dictating the sensitivity of permeability to a given change of P_e. Such a nonlinear behavior of k leads to the general diffusion equation for fluid-saturated porous rocks given by

$$\frac{\partial p}{\partial t} = \frac{1}{\phi \eta_f (\beta_f + \beta_n)} \nabla \cdot [k(P_e) \nabla p], \tag{3.2}$$

where ϕ is the rock porosity, β_f and β_n are the compressibilities of the fluid and the porous matrix, respectively, and η_f is the fluid viscosity (see Methods). Equation (3.2) is a nonlinear partial

differential equation that admits soliton-like solutions traveling as single pore pressure waves (Rice, 1992). Solitary pressure waves have been evoked to explain different geophysical phenomena (Miller et al., 2004; Bourlange and Henry, 2007). Conditions for these waves to exist depend on two main parameters. These are ∇p_0 and γ. To explore the physical conditions where pressure waves propagate within the RTM speed range, we have developed a finite volume scheme in two dimensions for solving equation (3.2) (see Methods and Appendix B). Figure 3.1a shows a solution of the equation where a solitary pore-pressure wave propagates for several kilometers with an average speed of 42.6 km h^{-1} (Figure 3.1b). Unlike linear diffusion processes, which exhibit instantaneous pressure effects in the whole saturated medium, this perturbation travels in space while producing a transient reduction of P_e. Behind the pressure wave, absolute p values decrease below their initial level inducing higher final values of P_e.

Borehole measurements and indirect estimates based on temperature and flow meters logs in different subducted OCs indicate permeability values from 10^{-16} and up to 10^{-11} [m^2] (Fisher, 1998). As the confining pressure increases down into depths where most SSEs and TTs take place (30-45 km), porosity (ϕ) in the OC and the serpentinized mantle wedge decreases down to 2-4.5 % (Peacock et al., 2011), with estimated permeabilities ranging between 10^{-17} and 10^{-22} [m^2] (Peacock et al., 2011; Katayama et al., 2012). However, large-scale stepwise changes in permeability at the onset of slip are produced due to the strong fault-zone-cracks aperture dependence of permeability, where earthquake-induced increases in rock mass permeability may reach values of 10^{-13} [m^2] (Miller, 2015). The aperture of fault-zone cracks or veins due to tectonic processes is supported by geological evidence in exhumed subduction-zone rocks and can vary from 10^{-6} to 10^{-3} m (Fagereng et al., 2014; Angiboust et al., 2015; Plümper et al., 2017), which implies permeability values of $10^{-13} < k < 10^{-8}$ m^2 across fault-zone fluid pathways from the relationship $k = b^2/12$, where b is the vein aperture in meters (Miller, 2013). Overpressured fluids subject to the plate-motion strain field (e.g. SSEs) may also increase k up to several orders of magnitude due to hydrofracturing processes and preexistent fault-zone cracks unclamping that may produce prominent fluid-migration channel networks (Miller, 2015; Plümper et al., 2017; Angiboust et al., 2014). Observations in exhumed rocks of plate-interface shear zones (Fagereng et al., 2014) and fluid-flow experiments in sheared serpentinite rocks (Kawano et al., 2011) also reveal a large anisotropy of permeability that enhances fluid transport along the plate-interface direction within the fault damage-zone. Since k in that direction is about two orders of magnitude larger than its value along the interface-perpendicular axis, we neglect fluid transport in the later direction within the RTMs time scale. In the following we thus assume that diffusion takes only place in the damage zone along the two dimensions that are parallel to the plate interface.

We carried out a parametric study of equation (3.2) to identify the physical conditions leading to pore-pressure waves traveling with the RTM speeds considering laboratory-observed and estimated values for k_0, γ, ϕ and ∇p_0(see Methods). For each combination of these parameters we solved equation (3.2) assuming values for the remaining constants shown in Table 3.1, and searched for propagating pressure waves in the simulation domain. In case a wave was detected, we quantified its average propagation speed along 15 km by tracking the front where p reaches a threshold of 3 kPa (circles in Figures 3.1a and 3.1b), value that implies a similar drop of P_e and thus of the fault strength. The threshold corresponds to a representative mean value of global TT sensitivity

to terrestrial tides (Yabe et al., 2015).

Figure 3.1c shows, for $k_0 = 1$ x 10^{-12} m^2 and $\phi = 2\,\%$, the propagation speeds of pressure waves for different combinations of ∇p_0 and γ. Predicted speeds range from 20 to 120 km h^{-1} within the model-space lying between the black contours. As a reference, the red square delineates the range of γ values measured in the laboratory and ∇p_0 corresponding to those induced by the 2006 SSE in Guerrero (see next section) as the lower limit, and an arbitrary upper limit. The parametric analysis revealed that soliton-like solutions dominate the pore-pressure evolution provided that there is also a preexisting gradient of P_e. Following equation (3.1), spatial variations of P_e set up heterogeneous initial values of k. Figure 3.2b illustrates this condition, where k is significantly larger in the region where p is close to the confining pressure, P_c, that we have assumed constant here because of the horizontal configuration of the Cocos plate in Guerrero (Figure 3.2a, see next section), but that may also change in space (e.g. with depth) producing similar results (see Supplementary Figure 3.3 for a Cascadia-like example). In all cases, solitary waves propagate from higher to lower pore-pressure regions as shown, for instance, in Figures 3.1a and 3.2c.

3.2.2 Rapid tremor migration in Guerrero, Mexico.

Similarly to other subduction zones, such as Nankai, Cascadia, Alaska, Costa Rica and Hikurangi, sinking of the Cocos plate underneath the North American plate in central Mexico produces a diversity of slow earthquakes. Among them, the largest SSEs in the globe taking place in Guerrero every 3.5 years with moment magnitude around 7.5 (Kostoglodov et al., 2003). Additionally, tectonic tremor (Payero et al., 2008), low frequency earthquakes (Frank et al., 2014) and very low frequency earthquakes (Maury et al., 2016) have also been observed in that province. Figure 3.3a shows the final slip produced by a long-term SSE occurred between March and December 2006 (Radiguet et al., 2012), where the dashed line indicates the distance from the trench where the plate interface becomes horizontal at 40 km depth (Pérez-Campos et al., 2008). Here, we carefully analyzed a high-resolution TT catalog recently introduced (Villafuerte and Cruz-Atienza, 2017) to search for RTMs in Guerrero. TT hypocentral locations have 5 km uncertainties in the three components and were obtained using the Tremor Energy and Polarization (TREP) method (Cruz-Atienza et al., 2015) from broadband seismic data recorded in the MASE array (Caltech, 2007) (green squares) between January 2005 and March 2007. Most of hypocenters lie close to the horizontal plate interface (Villafuerte and Cruz-Atienza, 2017), so we only considered TT sources between 40 and 45 km depth for the analysis. We found 54 RTMs in the catalog; each one associated with an individual tremor burst. Figures 3.3b-3.3d and Supplementary Figure 23.2 show some representative examples of these rapid migration patterns.

Projected horizontal locations into the migration directions (black arrows) allowed us to estimate the tremor migration speeds and distances (insets). Migration directions correspond to the azimuth that maximizes the speed after projection. The wind-rose diagram of Figure 3.3a summarizes the whole RTM directions and speeds, from which 26 RTMs occurred during the 2006 long-term SSE. The remaining 28 migrations occurred during inter-SSE tremor bursts associated with short-term slow earthquakes (Peng and Rubin, 2017; Frank et al., 2014). For example, Figure 3.4a shows the RTMs found between May and June during the long-term 2006 SSE, while Figure 3.4b shows the

RTMs produced by a short-term SSE in January 2007, months later the long-term SSE has passed through that region. Almost 90 % of the RTMs are located close to the downdip limit of the long-term slow slip, in the so-called sweet spot (Husker et al., 2012) (Figure 3.3a), where tremor activity dominates in the region. There is a preferential trench-perpendicular (i.e. slip-parallel) migration pattern with speeds ranging from 30 to 90 km h^{-1}, which is consistent with recent estimates in Guerrero (Peng and Rubin, 2017; Frank et al., 2014) and with the tremor streaks found in Nankai and Cascadia. There are also RTMs in the along-strike (and updip) directions with even faster speeds (60-120 km h^{-1}), which may probably correspond to RTRs.

Figure 3.1d presents the whole RTM catalog (color lines) bounded by lower and upper speed limits predicted by Equation (2) for pore-pressure gradients of 0.05 and 0.37 MPa km^{-1} (black dashed lines). These bounding models correspond to the white circles in Figure 3.1c, for which values of k_0, ϕ, and γ are 10^{-12} m^2, 2 % and 10^{-7} Pa^{-1}, respectively. Other physical conditions may also produce pressure waves with speeds similar to those of the RTM catalog. Supplementary Figure 3.3 show the parametric results for three other values of k_0, where pressure waves barely propagate for k_0 equal or less than 10^{-14} m^2 and very high-pressure gradients (i.e. $\nabla p_0 > 4$ MPa km^{-1}).

Migration speeds for different porosities (1 % and 2 %) and wave front thresholds (1-10 kPa) are also presented in Supplementary Figure 3.4, from where we concluded that plausible ranges for the model parameters producing pressure waves in the plate interface with speeds between 1 and 200 km h^{-1} are those reported in Table 3.2. Notice that these speed limits enclose not only our RTMs in Guerrero but also observed values in other subduction zones worldwide.

3.2.3 SSFs and RTMs associated with pore-pressure waves.

Recent high-resolution TT locations have revealed unprecedented observations of the RTM spatio-temporal behaviors in Cascadia and Mexico (Peng et al., 2015; Peng and Rubin, 2017). Rapid migration patterns evolve as the main slow-slip front passes through the tremor region. Initially, RTMs are more frequent, mostly follow the main SSE front geometry and have larger migration speeds (Peng and Rubin, 2017). This can partly be appreciated in Figure 3.4a, where most RTMs are parallel to the SSE front. As the front moves away, RTMs recurrence times become longer and tidally modulated, while their migration speeds decrease (Peng and Rubin, 2017; Yabe et al., 2015; Houston, 2015). Figure 3.4b shows, for instance, that once the SSE front is far away, the RTMs preferential direction is reoriented along dip.

Fault-zone pressure waves may control the plate-interface effective normal stresses (σ_e) and thus the fault strength that, as mentioned earlier, has strong implications in the slip velocity under the R&S friction law. In the condition of variable effective stress, the fault state variable changes according to the jump of σ_e (Dieterich, 1994). For constant shear (τ) and normal (σ) tractions, a change in the effective stress from the initial, ${\sigma_e}^i = (\sigma - p_i)$, to the final, ${\sigma_e}^f = (\sigma - p_f)$, states, produces a response in the slip velocity given by (Liu and Rice, 2007)

$$\frac{v_f}{v_i} = \left(\frac{{\sigma_e}^f}{{\sigma_e}^i}\right)^{(\alpha/a)} \exp\left[\frac{\tau}{a}\left(\frac{1}{{\sigma_e}^f} - \frac{1}{{\sigma_e}^i}\right)\right], \tag{3.3}$$

where α is about 0.2 for slow slip rates, and v_i and v_f are the initial and final slip velocities, respectively, due to the change in pore pressure $\Delta p = p_f - p_i$ For tractions $\tau = 8.5$ MPa and $\sigma = {\sigma_e}^i = 2$MPa, which are reasonable values for the SSE plate interface environment (Audet et al., 2009; Fagereng et al., 2014), small values of Δp (i.e. between 1 and 20 kPa, that correspond to the typical stress perturbation of a pressure wave as shown in Figure 3.2c) may produce v_f up to two orders of magnitude higher than v_i (Supplementary Figure 3.5). Such slip accelerations are consistent with estimates for the slip velocity of SSF as compared with the typical velocities of the SSE main fronts (Hawthorne et al., 2016; Bletery et al., 2017). The effective-stress transient reduction induced by pressure waves may thus potentially lead to SSFs triggering RTMs via the stress transfer from the stable fault matrix to embedded unstable asperities (Villafuerte and Cruz-Atienza, 2017; Yingdi and Ampuero, 2017; Ando et al., 2012; Lui and Lapusta, 2016). However, a critical condition for these waves is the existence of pore-pressure gradients in the fault zone where the SSEs take place. Pressure gradients in tremor zones may result from dilation changes induced by ongoing or past SSEs, localized dehydration reactions in the subducted slab, variations in the geometry of the slab and/or the plate interface, or different combinations of these mechanisms.

Our observations of RTMs in Guerrero show a dominant migration direction away from the trench (Figure 3.3a). We thus explored whether the residual (static) trench-perpendicular pore-pressure gradient induced by the 2006 SSE in the oceanic crust could explain this observation. However, as shown in Supplementary Figure 3.6, although p decreases in the sweet spot with distance from the trench, the maximum gradient (2 kPa km^{-1}) is significantly smaller (about one order of magnitude) that those required to produce pressure waves with the expected speeds (Table 3.2). Though the residual strain field from cumulative SSEs may lead to larger ∇p_0, an additional preexistent gradient seems necessary in Guerrero to meet the physical conditions producing such waves.

Prominent gradients of pore pressure (as large as 3 MPa km^{-1}) in subducted OCs have been inferred from tomographic P-wave imaging (Tsuji et al., 2014) and thermomechanical slab modeling (Faccenda et al., 2009). Those preexistent gradients represent the pumping force driving fluids into the mantle and through inslab normal faults. Metamorphic dehydration reactions in the OC depend on both, local pressure/temperature conditions, and the composition of the subducted materials. In Guerrero, tremor activity concentrates in the sweet spot over separated along-strike patches (Maury et al., 2016). This observation suggests that mechanical and/or fluid pressure conditions in those patches are different from the neighboring segments, as supported by mineralogical phase diagrams and thermal modeling of the subducted Cocos plate, which indicate that the largest dehydration pulse take place in the top of the slab right in the sweet spot (Manea and Manea, 2011). These arguments are certainly valid for other subduction zones, where overpressure fluids should also be confined in space (Plümper et al., 2017). As we move from the optimal dehydration zones, pore pressure should decrease due to diffusion processes and lower fluid production rates (Figure 3.5a). This mechanism seems a reasonable candidate for setting preexistent conditions promoting pressure waves in Guerrero and thus SSFs in the down-dip direction. Since most tremor migrations are parallel to the SSEs main-front (Peng and Rubin, 2017), there should be a dominant pore-pressure reduction across the sweet spot (inset of Figure 3.5a) with distance from the trench.

When the SSE main front passes through a region with high-enough ∇p (approximately larger than 20 kPa km^{-1}, Table 3.2) and nearly zero effective pressure, the permeability increases along

the front channelizing the pathway for pressure waves and RTMs. Large localized increments of k (i.e. of several orders of magnitude) due to shear slip in the fault zone have been recognized in borehole injection tests (Miller, 2015) and suggested to have implications for tremor generation (Peng and Rubin, 2017). The inset of Figure 3.5a illustrates this, where pressure waves propagate driven by the p gradient following the highly-permeable SSE front. We numerically explored this idea by solving equation (2) over a plane laying 1 km below the plate interface taking, as initial conditions for p, the final distribution of the pore-pressure induced by the 2006 SSE in the sweet spot (Supplementary Figure 3.6) plus a constant preexistent gradient (along-dip reduction of p) of 20 kPa km^{-1}. The model assumes that permeability is high in the slow-slip active front that we approximated, according to previous authors, as a 5 km width trench-perpendicular region (Peng and Rubin, 2017) (Figure 3.6a). In this region, k_0 gradually increases from 10^{-16} m^2 in its surroundings (i.e. outside the front), to 1 x 10^{-12} m^2 in the middle of the region. A cross section of the problem initial conditions in terms of p, P_e and k are shown in Figure 3.6b. The resulting pore-pressure evolution reveals a solitary wave propagating with an average speed of 50 km h^{-1} and down-dip direction similar to those observed for the dominant RTMs in Guerrero (compare with Figures 3.3b-3.3d).

3.3 Discussion

While RTMs along the main SSE front are naturally associated with the most-active slip region, understanding tremor migrations in the front-perpendicular direction such as the RTRs is not as intuitive. These migrations, which are less frequent, can happen either in the forward or backward SSE propagation direction (Houston et al., 2011; Obara et al., 2012; Peng et al., 2015). In general, RTM speeds decrease and become less frequent as the main SSE front moves away the tremor region. This observation can be explained by a drop of pore-pressure in the active SSE front due to the host-rock transient dilation induced by the shear slip (Peng and Rubin, 2017). Such mechanism, known as the dilatant strengthening process (Marone et al., 1990; Segall and Rice, 1995; Liu and Rubin, 2010), increases the effective normal stresses in the shear zone producing stable slip (i.e. slow earthquakes) even in velocity-weakening fault regions (Segall et al., 2010). An outstanding consequence of this process is the generation of pore-pressure gradients behind the propagating SSE front. Figure 3.5b illustrates this condition, where two opposite, front-perpendicular gradients are set as a consequence of the transient dilation (Segall et al., 2010). In region A, p decreases with distance from the front as the slip-rate develops to reach its maximum value. Further behind, in region B, pore-pressure recovers as the rock returns to its original undilated state producing a gradual increase of p. Numerical investigations of the dilatant strengthening process show that the associated ∇p may be of the order of 80 [kPa km^{-1}] (Liu and Rubin, 2010). Although it is difficult to quantify from the available results whether the corresponding meet the conditions producing pressure waves, since gradients between 20 and 5000 kPa km^{-1} induce waves propagating with the expected RTM speeds (Table 3.2), the dilatant strengthening process may potentially set suitable conditions for the existence of pressure pulses. The pore-pressure gradient in region A could thus potentially be the driving force for pulses (and the associated SSFs) triggering RTRs, while the gradient in region B, could promote RTMs in the opposite forward direction, as observed in nature. Since preexistent

gradients in the OC may be highly variable in space it is possible that, in some regions, the dominant gradients are those induced by the dilatant strengthening process thus promoting pressure pulses triggering RTRs and forward RTMs. In Guerrero, transient reductions of the crustal wave speed have been observed during SSEs (Rivet et al., 2011). This extraordinary observation, which may be explained by the non-linear dilatant-strengthening response of the deep crust (Rivet et al., 2013), suggest that some RTMs we reported for the 2006 SSE could be produced by the physical mechanism illustrated in Figure 3.5b.

In addition to the fault-zone dilatant process that seems to be a plausible mechanism explaining the speed and recurrence evolution of RTMs as the SSE propagates (Peng and Rubin, 2017), pore-pressure waves also produce a trailing drop of p as they sweep the RTM pathway (Figure 3.1a). The result of this process is a reduction of ∇p_0 in the tremor zone. Figure 3.1c shows that migration speed of pressure waves decreases with reductions of ∇p_0 (e.g. along a vertical path joining both white circles). Thus, successive waves, propagating across similar paths, will slow down with recurrence time. Besides this, since overpressured fault spots where pressure waves are expected to born would also experience an increment of P_e, the origin time of the next wave would be delayed (i.e. the recurrence time would increase) as the SSE strain field evolves in a similar way RTM behave. The pressure gradient reduction depends on the healing and resealing of the fault zone behind the associated SSF as P_e grows during the trailing drop of p. Future work should certainly integrate these mechanical processes into the model to identify other factors controlling the evolving nature of RTMs during an SSE episode.

Our modeling results also suggest another explanation for the RTM speed reduction with recurrence time. The parametric study we carried out assumed, for each parameters combination, the same frictional strength for tremor asperities (Figures 3.1c and B.3). However, the larger the strength, the slower is the pressure front. This can be seen in Figure B.4 (solid curves), where the front speed slows down by a factor of three for strength increments of the same order (i.e. from 1 to 5 kPa). In a fault where tremor asperities with different strengths are randomly distributed, the front of a pressure wave triggering weaker asperities will travel faster and manifest earlier than the slower trailing front triggering stronger asperities. This mechanism would translate into successive RTMs with decreasing speeds.

Our observations of RTMs in Guerrero (Figures 3.3 and B.2) reveal that tremor migrates as 5 to 10 km width source packages, which is consistent with results using different TT location methods in Guerrero and Cascadia (Peng et al., 2015; Peng and Rubin, 2017; Bletery et al., 2017). One possible explanation of this migration pattern is that the active slip region associated with the SSFs describes a pulse-like perturbation responding to some self-healing frictional process. Our pore-pressure wave model also predicts propagating pulse-like perturbations of the fault-zone effective pressure (e.g. Figures 3.1a and 3.2c). Nevertheless, their widths and migration speeds are significantly larger and smaller, respectively, than those observed for RTMs. The actual fault response to such pressure transients (e.g. its slip rate) may not be as intuitive though. In other terms, the associated SSF may not necessarily mimic the evolution of p along the fault that, in a R&S friction model coupled with a time varying evolution of p, strongly depends on the temporal derivative of p (i.e. on dp/dt). Modeling results for fluid injection tests next to faults subject to such friction law show that slip instabilities occur, in fact, where is close to its maximum value and p grows monotonically (Okubo,

2014). For our pore-pressure wave model and its implications in tremor generation this means that the associated SSFs could take place well before reaching the maximum value of p in the fault zone, so that the pressure pulse does not necessarily depicts the shape of the associated SSF, which may be significantly narrower and have faster migration speed. This, of course, deserves further analysis of the non-linear diffusion problem (Equation 2) coupled with R&S friction laws in the fault plane, which goes beyond the scope of this work but represents the current direction of our investigations.

There also exists the possibility that the RTM pulse width may be significantly narrower than the SSF. This can be seen considering that tremor asperities radiating waves during the same RTM are expected to have similar strengths (Peng and Rubin, 2017; Yabe et al., 2015). As the SSF propagates and successively surrounds the (locked) tremor asperities, it charges the asperities until they break at the moment their instability condition is reached no matter that the slip front continues developing behind the broken asperities (Villafuerte and Cruz-Atienza, 2017). This simple principle suggests that pressure pulses, which presumably induce SSFs with even wider active regions than the RTM front, are likely to trigger pulse-like tremor migrations as observed in Guerrero and other places. In other words, pressure pulses should not be as narrow as the RTM fronts to be consistent with observations.

In summary, observational and theoretical evidence worldwide strongly suggest that tectonic tremor is always triggered by small unstable asperities embedded in a slow-sliding (stable) fault zone saturated with overpressures fluids. Such mechanism is also valid to explain RTMs due to much faster, SSFs propagating along the fault. Here we show that pore-pressure waves are likely to propagate across the plate-interface fault zone with the expected RTM speeds and pathways provided that moderate pore pressure gradients ($\gtrsim 20$ kPa km^{-1}) exist in the SSE region. Those gradients can be generated either by preexisting and localized dehydration processes in the oceanic crust, variations of the interface geometry and the SSE-induced strain field (i.e. through the dilatant strengthening processes). During propagation, pore pressure waves produce transient reductions of the effective fault-normal stresses that may lead to SSFs triggering tremor via the stress transfer into the asperities. Although this idea should be rigorously explored by means of a R&S friction model coupled with the non-linear fluid-diffusion equation, rapid pressure waves in that framework seem a plausible mechanism capable to explain the hierarchical diversity of RTMs patterns observed in different subduction zones including Guerrero, Mexico, where cutting-edge seismogeodetic instrumentation, offshore and onshore, has been recently deployed to improve the characterization of slow earthquakes and constrain our RTM model (Cruz-Atienza et al., 2018a). The model we propose opens a new area of research that may help to better understand the fault system in different geophysical conditions such as volcanic systems, geothermal fields and production wells with induced seismicity, where the seismic hazard is high and should be assessed by means of physic-based modeling considerations.

3.4 Methods

3.4.1 Non-Linear Diffusion Equation with Variable Permeability.

The spatio-temporal evolution of pore pressure in fluid-saturated media is given by the hydraulic diffusion equation. To deduce this equation for a given function of permeability such as Equation 1, let us start by the equation of mass conservation,

$$\frac{\partial m}{\partial t} + \nabla \cdot \underline{q}(\underline{x}) = 0, \tag{3.4}$$

where m represents the fluid mass for unit volume of porouse medium, $\underline{q}(\underline{x})$ is the fluid-discharge velocity vector, t is time and $\underline{x}$ is a general position vector. From Darcy's law, the fluid discharge may be expressed as

$$\underline{q}(\underline{x}) = -\frac{\rho_f}{\eta_f} k(\underline{x}) \nabla p(\underline{x}), \tag{3.5}$$

where ρ_f and η_f are the fluid density and viscosity, respectively, $k(\underline{x})$ is a general function of permeability and p is the pore pressure. Given that the total fluid mass can be expresses in terms of porosity, ϕ, and the fluid density as $m = \phi\rho_f$, then

$$\frac{\partial m}{\partial t} = \phi \frac{\partial \rho_f}{\partial t} + \rho_f \frac{\partial \phi}{\partial t}, \tag{3.6}$$

Ignoring thermal and anelastic effects, the temporal derivatives of the right-hand term are given by

$$\frac{\partial \rho_f}{\partial t} = \rho_f \beta_f \frac{\partial p(\underline{x})}{\partial t} \tag{3.7}$$

and

$$\frac{\partial \phi}{\partial t} = \phi \beta_n \frac{\partial p(\underline{x})}{\partial t}, \tag{3.8}$$

where β_f and β_n are the fluid and porous matrix compressibilities, respectively. Substituting (3.7) and (3.8) into equation (3.6), we have

$$\frac{\partial m}{\partial t} = \phi \rho_f (\beta_n + \beta_f) \frac{\partial p(\underline{x})}{\partial t}. \tag{3.9}$$

Inputting (3.5) and (3.9) into equation (3.4), we finally obtain the diffusion equation for a general function of permeability

$$\frac{\partial p(\underline{x})}{\partial t} = \zeta \nabla \cdot [k(\underline{x}) \nabla p(\underline{x})] \tag{3.10}$$

where

$$\zeta = \frac{1}{\phi \eta_f (\beta_f + \beta_n)}.$$

If permeability varies with effective pressure (i.e. with $P_e(\underline{x}) = P_c(\underline{x}) - p(\underline{x})$) following the exponential form given by Equation 1 Evans et al. (1997), then equation (3.10) states the non-linear problem we are interested in this investigation:

$$\frac{\partial p(\underline{x})}{\partial t} = \zeta \nabla \cdot [k(P_c(\underline{x}) - p(\underline{x})) \nabla p(\underline{x})]. \tag{3.11}$$

As mentioned early in the manuscript, besides predicting the linear fluid diffusion, this partial differential equation admits soliton-like solutions traveling as single pore pressure waves under certain conditions[41].

3.4.2 2D Finite Volume Method for Solving the Non-Linear Diffusion Equation.

To solve the nonlinear partial differential equation (1) in two dimensions (2D) we applied the finite volume (FV) method. We choose this method because it is conservative and stable when solving diffusion problems, which is an important property to study pressure waves propagation avoiding numerical dispersion. Our 2D FV method decomposes the domain into $N \times M$ rectangular elements (or control volumes) in the $x - z$ plane with sizes $\triangle x \times \triangle z$, as illustrated in Figure B.7.

Assuming the general case for anisotropic and variable permeability (i.e. $k(x, z, t)$), we have that

$$\underline{\underline{k}} = \begin{bmatrix} k_{xx} & k_{xz} \\ k_{zx} & k_{zz} \end{bmatrix}. \tag{3.12}$$

Since the fluid diffusivity is given by $\underline{\underline{K}} = \zeta \underline{\underline{k}}$, then equation (1) may be written as

$$\frac{\partial p}{\partial t} = \nabla \cdot \left[\underline{\underline{K}} \cdot \nabla p \right], \tag{3.13}$$

where the pore pressure, $p(x, z, t)$, is also a function of space and time. Developing equation (3.13) and integrating both terms in a given volume ($\triangle V$),

$$\int_{\triangle V} \frac{\partial p}{\partial t} dV = \int_{\triangle V} \frac{\partial}{\partial x} \left[K_{xx} \frac{\partial p}{\partial x} + K_{xz} \frac{\partial p}{\partial z} \right] dV + \int_{\triangle V} \frac{\partial}{\partial z} \left[K_{zx} \frac{\partial p}{\partial x} + K_{zz} \frac{\partial p}{\partial z} \right] dV. \tag{3.14}$$

Since K_{xx} is constant within a control volume and considering the indexes shown in Figure B.7, the first integral of the right-hand term may be expressed as

$$\begin{aligned}\int_{\triangle V} \frac{\partial}{\partial x}\left[K_{xx}\frac{\partial p}{\partial x}\right] dV &= \int_{z_{j-1/2}}^{z_{j+1/2}} \int_{x_{i-1/2}}^{x_{i+1/2}} \frac{\partial}{\partial x}\left[K_{xx}\frac{\partial p}{\partial x}\right] dxdz \\ &= \int_{z_{j-1/2}}^{z_{j+1/2}} \left[K_{xx}\frac{\partial p}{\partial x}\right]\Bigg|_{x_{i-1/2}}^{x_{i+1/2}} dz \\ &= \int_{z_{j-1/2}}^{z_{j+1/2}} \left[K_{xx_{i+1/2}}\left(\frac{\partial p}{\partial x}\right)_{i+1/2} - K_{xx_{i-1/2}}\left(\frac{\partial p}{\partial x}\right)_{i-1/2}\right] dz \\ &= \triangle z K_{xx_{i+1/2}}\left(\frac{\partial p}{\partial x}\right)_{i+1/2} - \triangle z K_{xx_{i-1/2}}\left(\frac{\partial p}{\partial x}\right)_{i-1/2}. \end{aligned} \tag{3.15}$$

Following the same procedure for the remaining integrals of the right-hand term of equation (3.14), we have that

$$\int_{\triangle V} \frac{\partial}{\partial x}\left[K_{xz}\frac{\partial p}{\partial z}\right] dV = \triangle z K_{xz_{i+1/2}}\left(\frac{\partial p}{\partial z}\right)_{i+1/2} - \triangle z K_{xz_{i-1/2}}\left(\frac{\partial p}{\partial z}\right)_{i-1/2} \tag{3.16}$$

$$\int_{\triangle V} \frac{\partial}{\partial z}\left[K_{zx}\frac{\partial p}{\partial x}\right] dV = \triangle x K_{zx_{j+1/2}}\left(\frac{\partial p}{\partial x}\right)_{j+1/2} - \triangle x K_{zx_{j-1/2}}\left(\frac{\partial p}{\partial x}\right)_{j-1/2} \tag{3.17}$$

$$\int_{\triangle V} \frac{\partial}{\partial z}\left[K_{zz}\frac{\partial p}{\partial z}\right] dV = \triangle x K_{zz_{j+1/2}}\left(\frac{\partial p}{\partial z}\right)_{j+1/2} - \triangle x K_{zz_{j-1/2}}\left(\frac{\partial p}{\partial z}\right)_{j-1/2}. \tag{3.18}$$

We approximate the spatial derivatives of pore pressure along the element boundaries using a

second-order finite difference scheme, so that

$$\begin{aligned}
\left(\frac{\partial p}{\partial x}\right)_{i+1/2} &\approx \frac{p_{i+1,j} - p_{i,j}}{\triangle x} \\
\left(\frac{\partial p}{\partial z}\right)_{i+1/2} &\approx \frac{p_{i+1/2,j+1/2} - p_{i+1/2,j-1/2}}{\triangle z} \\
\left(\frac{\partial p}{\partial x}\right)_{j+1/2} &\approx \frac{p_{i+1/2,j+1/2} - p_{i-1/2,j+1/2}}{\triangle x} \\
\left(\frac{\partial p}{\partial x}\right)_{i-1/2} &\approx \frac{p_{i,j} - p_{i-1,j}}{\triangle x} \\
\left(\frac{\partial p}{\partial z}\right)_{i-1/2} &\approx \frac{p_{i-1/2,j+1/2} - p_{i-1/2,j-1/2}}{\triangle z} \\
\left(\frac{\partial p}{\partial x}\right)_{j-1/2} &\approx \frac{p_{i+1/2,j-1/2} - p_{i-1/2,j+1/2}}{\triangle x} \\
\left(\frac{\partial p}{\partial z}\right)_{j+1/2} &\approx \frac{p_{i,j+1} - p_{i,j-1}}{\triangle z} \\
\left(\frac{\partial p}{\partial z}\right)_{j-1/2} &\approx \frac{p_{i,j} - p_{i,j-1}}{\triangle z}.
\end{aligned} \tag{3.19}$$

Values of pore pressure in the element corners are approximated as the average of p in the four elements sharing the same node. For example, pore pressure at the $(i + 1/2, j + 1/2)$ node is given by

$$p_{i+1/2,j+1/2} = \frac{1}{4}(p_{i,j} + p_{i,j+1} + p_{i+1,j} + p_{i+1,j+1}) \tag{3.20}$$

in such a way that the integrals from (3.15) to (3.18) may be approximated as

$$\begin{aligned}
\int_{\triangle V} \frac{\partial}{\partial x}\left[K_{xx}\frac{\partial p}{\partial x}\right] dV &\approx K_{xx_{i+1/2,j}}(p_{i+1,j}-p_{i,j}) - K_{xx_{i-1/2,j}}(p_{i,j}-p_{i-1,j}) \\
\int_{\triangle V} \frac{\partial}{\partial x}\left[K_{xz}\frac{\partial p}{\partial z}\right] dV &\approx \frac{1}{4}K_{xz_{i+1/2,j}}(p_{i,j+1}+p_{i+1,j+1}+p_{i,j-1}+p_{i+1,j-1}) \\
&\quad - \frac{1}{4}K_{xz_{i-1/2,j}}(p_{i-1,j+1}+p_{i-1,j-1}+p_{i,j-1}+p_{i,j+1}) \\
\int_{\triangle V} \frac{\partial}{\partial z}\left[K_{zx}\frac{\partial p}{\partial x}\right] dV &\approx \frac{1}{4}K_{zx_{i,j+1/2}}(p_{i-1,j+1}+p_{i-1,j}+p_{i+1,j+1}+p_{i+1,j}) \\
&\quad - \frac{1}{4}K_{zx_{i,j-1/2}}(p_{i-1,j}+p_{i-1,j-1}+p_{i+1,j}+p_{i+1,j-1}) \\
\int_{\triangle V} \frac{\partial}{\partial z}\left[K_{zz}\frac{\partial p}{\partial z}\right] dV &\approx K_{zz_{i,j+1/2}}(p_{i,j+1}-p_{i,j}) - K_{zz_{i,j-1/2}}(p_{i,j}-p_{i,j-1}).
\end{aligned} \tag{3.21}$$

Discretizing now the left-hand term of equation (3.14) in space, we obtain

$$\int_{\triangle V} \frac{\partial p(x,z,t)}{\partial t} dV = \frac{\partial}{\partial t}\int_{z_{j-1/2}}^{z_{j+1/2}}\int_{x_{i-1/2}}^{x_{i+1/2}} p(x,z,t)dxdz = \triangle x \triangle z \frac{\partial p_{i,j}}{\partial t}.$$

Equating both discretized terms of equation (3.14), we finally get the discrete form of equation (3.13):

$$\begin{aligned}
\triangle x \triangle z \frac{\partial p_{i,j}}{\partial t} \approx\ & a_0 p_{i,j} + a_1 p_{i-1,j+1} + a_2 p_{i,j+1} + a_3 p_{i+1,j+1} + a_4 p_{i-1,j} \\
& + a_5 p_{i+1,j+1} + a_6 p_{i-1,j-1} + a_7 p_{i,j-1} + a_8 p_{i+1,j-1}
\end{aligned} \tag{3.22}$$

where coefficients a are defined as

$$\begin{aligned}
a_0 &= -(K_{xx_{i+1/2,j}} + K_{xx_{i-1/2,j}} + K_{zz_{i,j+1/2}} + K_{zz_{i,j-1/2}}) \\
a_1 &= \left(\frac{K_{zx_{i,j+1/2}} - K_{xz_{i-1/2,j}}}{4}\right)
\end{aligned}$$

$$
\begin{aligned}
a_2 &= \left(\frac{K_{xz_{i+1/2,j}} - K_{xz_{i-1/2,j}}}{4} + K_{zz_{i,j+1/2}} \right) \\
a_3 &= \left(\frac{K_{xz_{i+1/2,j}} + K_{zx_{i,j+1/2}}}{4} \right) \\
a_4 &= \left(K_{xx_{i-1/2,j}} + \frac{K_{zx_{i,j+1/2}} - K_{zx_{i,j-1/2}}}{4} \right) \\
a_5 &= \left(K_{xx_{i+1/2,j}} + \frac{K_{zx_{i,j+1/2}} - K_{zx_{i,j-1/2}}}{4} \right) \\
a_6 &= -\left(\frac{K_{xz_{i-1/2,j}} + K_{zx_{i,j-1/2}}}{4} \right) \\
a_7 &= \left(\frac{K_{xz_{i+1/2,j}} - K_{xz_{i-1/2,j}}}{4} + K_{zz_{i,j-1/2}} \right) \\
a_8 &= \left(\frac{K_{xz_{i+1/2,j}} - K_{zx_{i,j-1/2}}}{4} \right)
\end{aligned}
\tag{3.23}
$$

Boundary Conditions.

To complete the scheme (3.22) we need update formulae also for the boundary points of the domain. This means setting values $p_{i,0}, p_{i,N}, p_{0,j}$ y $p_{N,j}$, where N represents the total number of elements per dimension, derived by taking the boundary conditions into account.

To this purpose we impose Neumann conditions (i.e., no-flux) along the boundaries. This means that pore-pressure derivatives in the boundary-perpendicular directions are set to zero for all t. At boundary points, spatial derivatives are approximated with a second-order finite difference scheme considering ghost elements beyond the boundaries, so that the condition for any j at $i = 0$ (see Figure B.7) is given by

$$
\frac{\partial p_{0,j}}{\partial z} \approx \frac{p_{0,j} - p_{-1,j}}{\triangle x} = 0,
$$

which implies that

$$
p_{-1,j} = p_{0,j}. \tag{3.24}
$$

By imposing this condition into scheme (3.22) for $p_{i,j} = p_{0,j}$, we obtain p values for the left-hand edge of the domain as

$$
\begin{aligned}
\triangle x \triangle z \frac{\partial p_{0,j}}{\partial t} \approx (a_1 + a_2) p_{0,j+1} + a_3 p_{1,j+1} + (a_4 + a_0) p_{0,j} \\
+ a_5 p_{1,j} + (a_6 + a_7) p_{0,j-1} + a_8 p_{1,j-1}.
\end{aligned}
\tag{3.25}
$$

Similarly, for the rest of the domain boundaries we obtain

$$\begin{aligned}
\triangle x\triangle z\frac{\partial p_{N,j}}{\partial t} &\approx a_1 p_{N-1,j+1} + (a_2+a_3)p_{N,j+1} + a_4 p_{N-1,j} + (a_5+a_0)p_{N,j} \\
&\quad + a_6 p_{N-1,j-1} + (a_7+a_8)p_{N,j-1} \\
\\
\triangle x\triangle z\frac{\partial p_{i,0}}{\partial t} &\approx a_1 p_{i-1,1} + a_2 p_{i,1} + a_3 p_{i+1,1} + (a_4+a_6)p_{i-1,0} \\
&\quad + (a_5+a_8)p_{i+1,0} + (a_7+a_0)p_{i,1} \\
\\
\triangle x\triangle z\frac{\partial p_{i,N}}{\partial t} &\approx (a_1+a_4)p_{i-1,N} + (a_2+a_0)p_{i,N} + (a_3+a_5)p_{i+1,N} \\
&\quad + a_6 p_{i-1,N-1} + a_7 p_{i,N-1} + a_8 p_{i+1,N-1}.
\end{aligned} \tag{3.26}$$

For the elements located at the domain corners we set both spatial derivatives to zero getting

$$\triangle x\triangle z\frac{\partial p_{0,0}}{\partial t} \approx (a_1+a_2)p_{0,1} + a_3 p_{1,1} + (a_4+a_6+a_7+a_0)p_{0,0} + (a_5+a_8)p_{1,0}$$

$$\triangle x\triangle z\frac{\partial p_{N,0}}{\partial t} \approx a_1 p_{N-1,1} + (a_2+a_3)p_{N,1} + (a_4+a_6)p_{N-1,0} + (a_5+a_0+a_7+a_8)p_{N,0}$$

$$\triangle x\triangle z\frac{\partial p_{0,N}}{\partial t} \approx (a_1+a_2+a_4+a_0)p_{0,N} + (a_3+a_5)p_{1,N} + (a_6+a_7)p_{0,N-1} + a_8 p_{1,N-1}$$

$$\triangle x\triangle z\frac{\partial p_{N,N}}{\partial t} \approx (a_1+a_4)p_{N-1,N} + (a_2+a_3+a_5+a_0)p_{N,N} + a_6 p_{N-1,N-1} + (a_7+a_8)p_{N,N-1}, \tag{3.27}$$

Expressions (3.22), (3.25), (3.26) and (3.27) represent a system of Ordinary Differential Equations (ODEs) that may be expressed in the general form

$$\frac{d\underline{p}}{dt} \approx \frac{1}{\triangle x\triangle z}\underline{\underline{A}}\underline{p}, \tag{3.28}$$

where $\underline{p}$ represents a $N \times N$ matrix while $\underline{\underline{A}}$ is a $N^2 \times N^2$ matrix. To solve system (3.28) in time we used the MATLAB function edo15s, which yields robust solutions for stiff systems of ODEs by considering time-adaptive steps. We provide a verification of the FV method by comparing numerical predictions with analytical solutions in the Supplementary Methods and in the Figure B.8.

Model Parameter	**Value**
Fluid viscosity (η)	9.54 $\times 10^{-5}$ Pa s
Porous matrix compresibility (β_n)	6.5 $\times 10^{-10}$ Pa
Fluid compresibility (β_f)	6.4$\times 10^{-10}$ Pa

Table 3.1. Constant parameters assumed in all simulations presented of this work.

Model Parameter	**Range of values**
Permeability (k_0)	$10^{-14} - 10^{-11}$ m^2
Porosity (ϕ)	$0.01 - 0.02$
Pore pressure gradient (∇p_0)	0.02 - 5 MPa km^{-1}
Sensitivity (γ)	$1 \times 10^{-8} - 5 \times 10^{-7}$ Pa^{-1}
Pore pressures threshold	$1 - 10$ kPa

Table 3.2. Ranges of the model parameters where soliton pore-pressure waves may propagate with speeds between 1 and 200 km h^{-1} under plausible conditions for subduction zones where RTMs are observed.

3.4.3 Parametric analysis of the non-linear poroelastic equation.

We performed a parametric analysis of Equation 2 to identify the physical conditions leading to pore-pressure waves traveling with the observed RTM speeds. We considered values of $10^{-10} < k_0 < 10^{-16}$ m^2 and pore pressure gradients (∇p_0) ranging between 10^{-1} and 10^{1} MPa km^{-1}. For γ parameter, we explored values around those derived from experimental tests, between 10^{-8} and 10^{-5} Pa^{-1} [40], and estimated porosities (ϕ) for the Cascadia subducted slab, between 1 % and 2 % [28]. For each combination of the parameters we solved Equation 2 assuming values for the remaining constants shown in Table 3.1 and track the pressure-wave front along 15 km for threshold values of p ranging between 1 and 10 kPa. Results obtained in the parametric analysis are summarized in Figures 3.1c, B.3 and B.4, from which we determined the ranges of the model parameters (Table 3.2) producing pressure waves in the plate interface with speeds between 1 and 200 km/h.

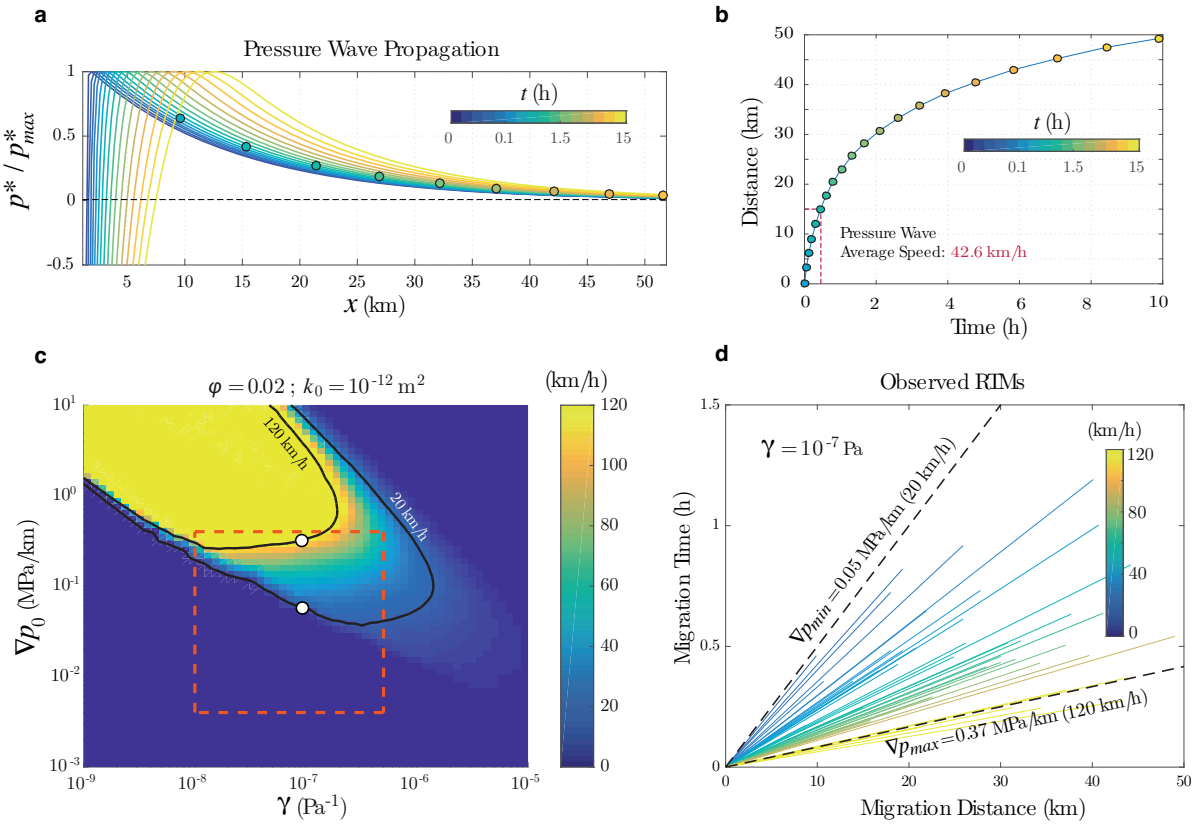

Figure 3.1. Analysis of the non-linear diffusion equation under plausible conditions for the Guerrero subduction zone. (a) Pore-pressure wave propagation predicted by equation (2), where $p* = p - p_0$. Circles show the position of the wave front for a pore-pressure threshold of 3 kPa and color shaded the time in hours. (b) Wave front propagation (circles in panel a) and average speed after 15 km. (c) Parametric study of equation (2) in terms of wave speeds for a threshold of 3 kPa (see Supplementary Figure 3 for different permeabilities). Speed values between the black curves include those observed for RTMs in Guerrero. Red box delineates γ values observed in laboratory experimentsEvans et al. (1997) and the maximum pore-pressure gradient induced by the 2006 SSE (lower limit). (d) Guerrero RTM speeds bounded by the two theoretical limits indicated with white circles in panel c.

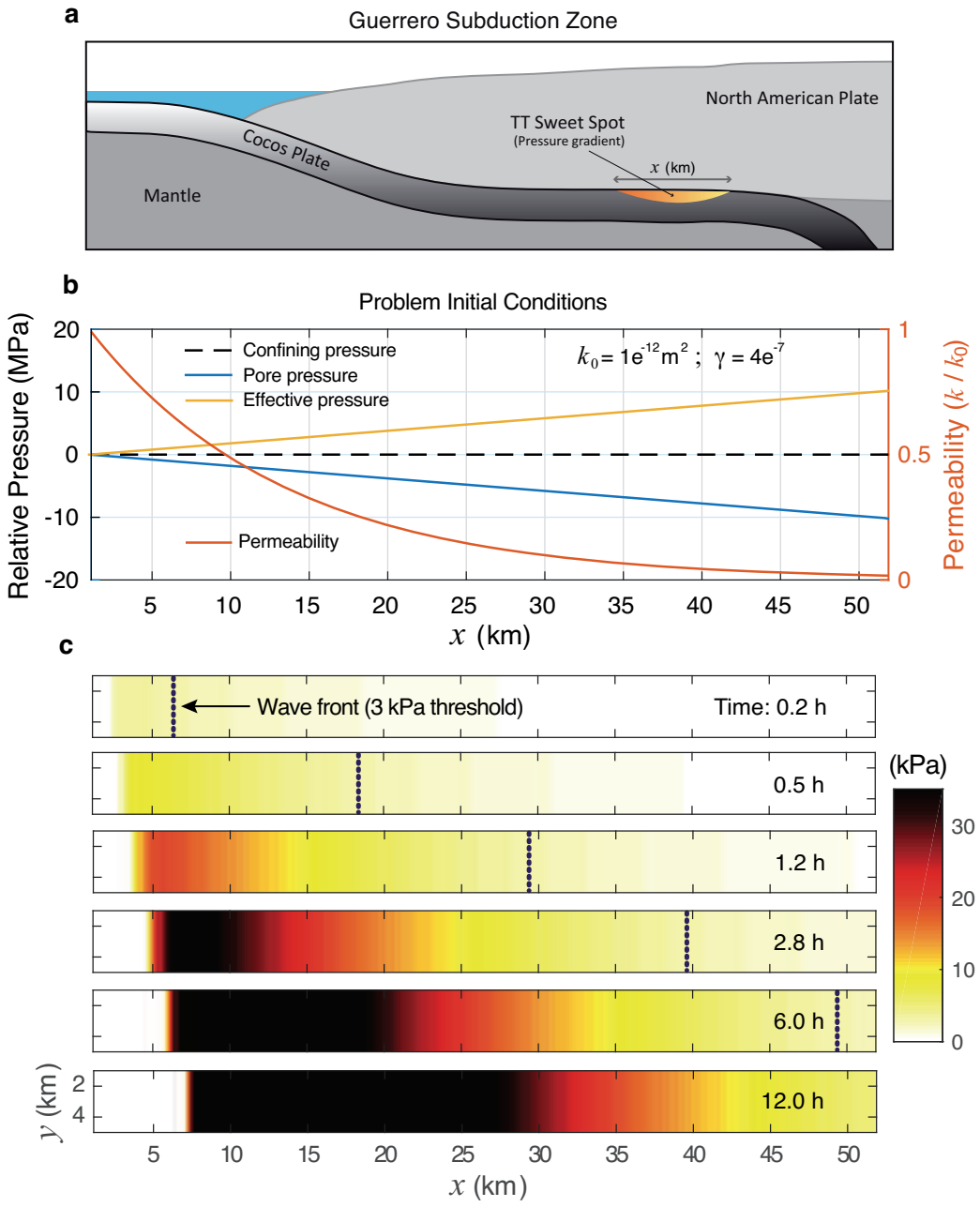

Figure 3.2. Downdip pore-pressure wave solution under plausible conditions for the Guerrero subduction zone. (a) Cartoon showing the geometry of the oceanic Cocos plate under the continent. Gradient of gray colors illustrate the lithostatic pressure in the subducted slab, while color gradient illustrate local pore pressure changes in the sweet spot. (b) Initial conditions and parameter values for the simulation presented in Figures 1a and 1b. (c) Resulting pore-pressure wave propagation in the 2D domain. The dashed black line depicts the wave front for a pressure threshold of 3 kPa.

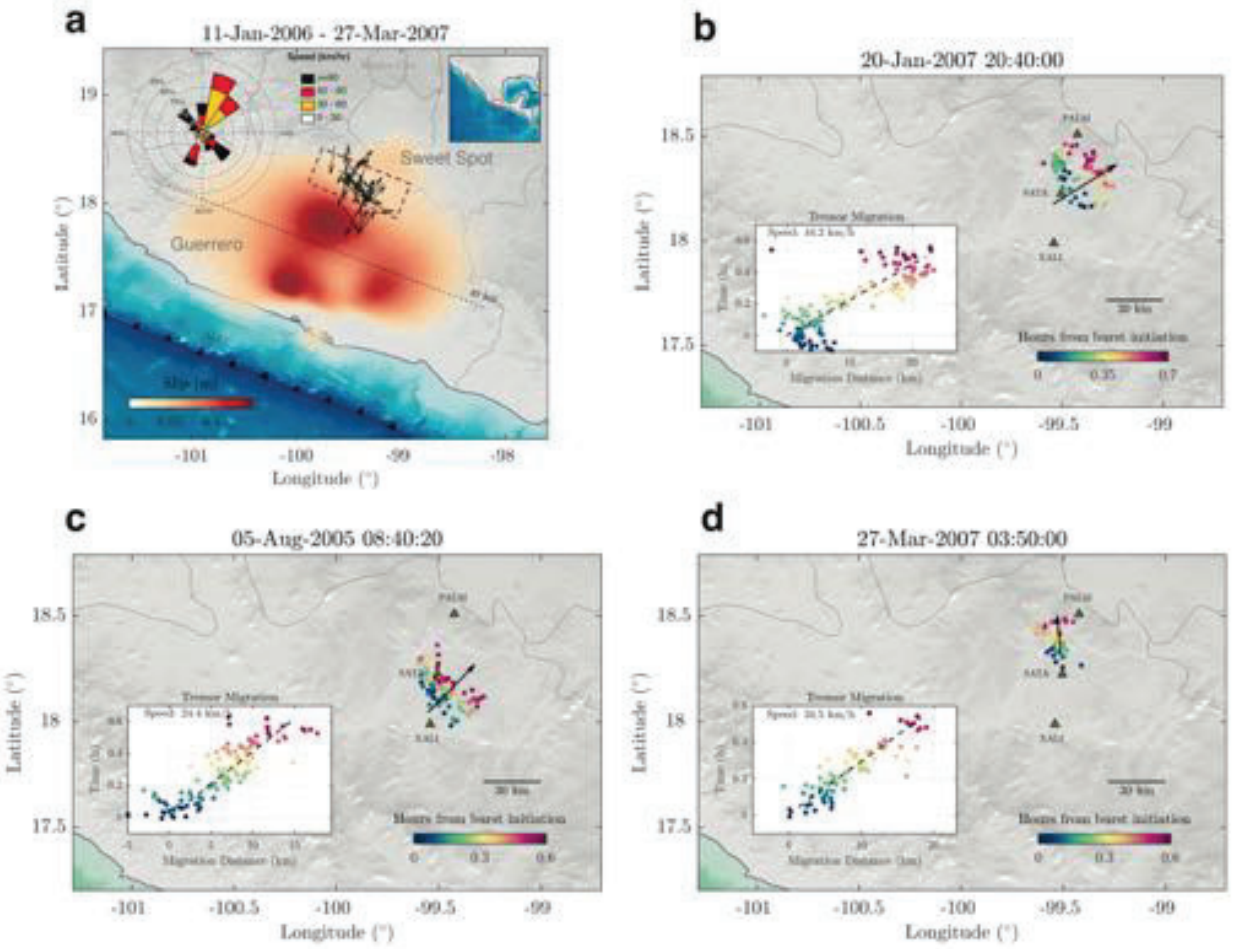

Figure 3.3. Rapid tremor migrations observed in Guerrero. (a) Migration direction and position (black arrows) of the 54 RTMs determined from seismic records in the MASE array of stationsCaltech (2007) (green squares) using the TREP methodCruz-Atienza et al. (2015). The wind-rose histogram shows the directions and speeds of the whole RTM catalog. As a reference, color shaded shows the final slip of the 2006 SSERadiguet et al. (2012). The dashed line indicates where the subducted Cocos plate becomes horizontal at 40 km depth, and the wine rectangle the positions of the sweet spot. (b-d) Examples of RTMs for one-minute moving windows with 20 s overlap. Hypocentral projections onto the migration directions (black arrows) are show in the insets, where migration speeds are reported (see Figure A5 for more RTM examples). The basemaps were created using SRTM15+ data.

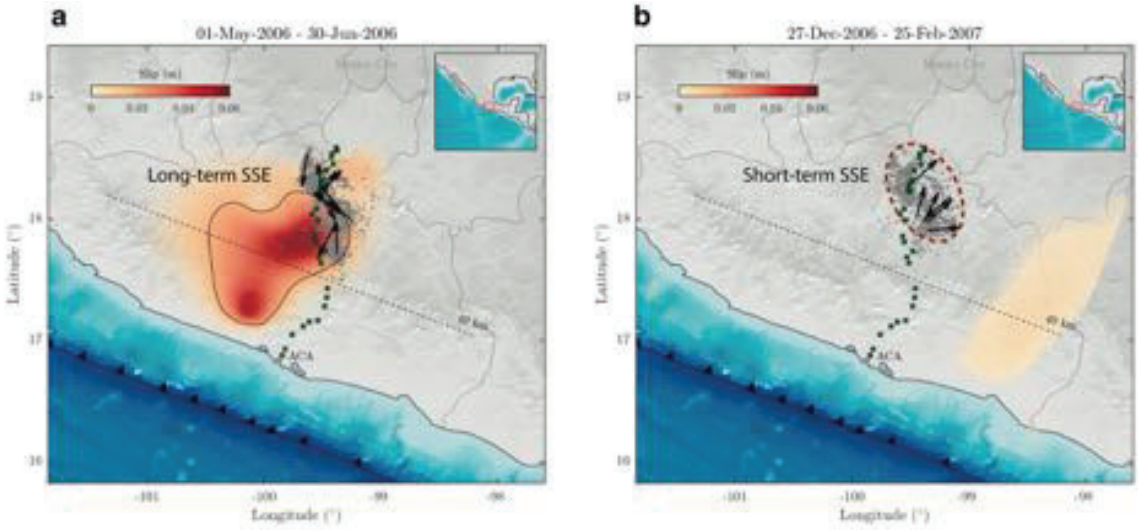

Figure 3.4. Slip increments of the 2006 SSE for the periods indicated on top of each panel. Tremor epicenters and RTMs associated with each period are shown in gray dots and black arrows, respectively. TTs and RTMs in panel b are related to a slip reactivation (i.e. a short-term SSE, wine dotted line) months later the long-term SSE has moved away the tremor region.

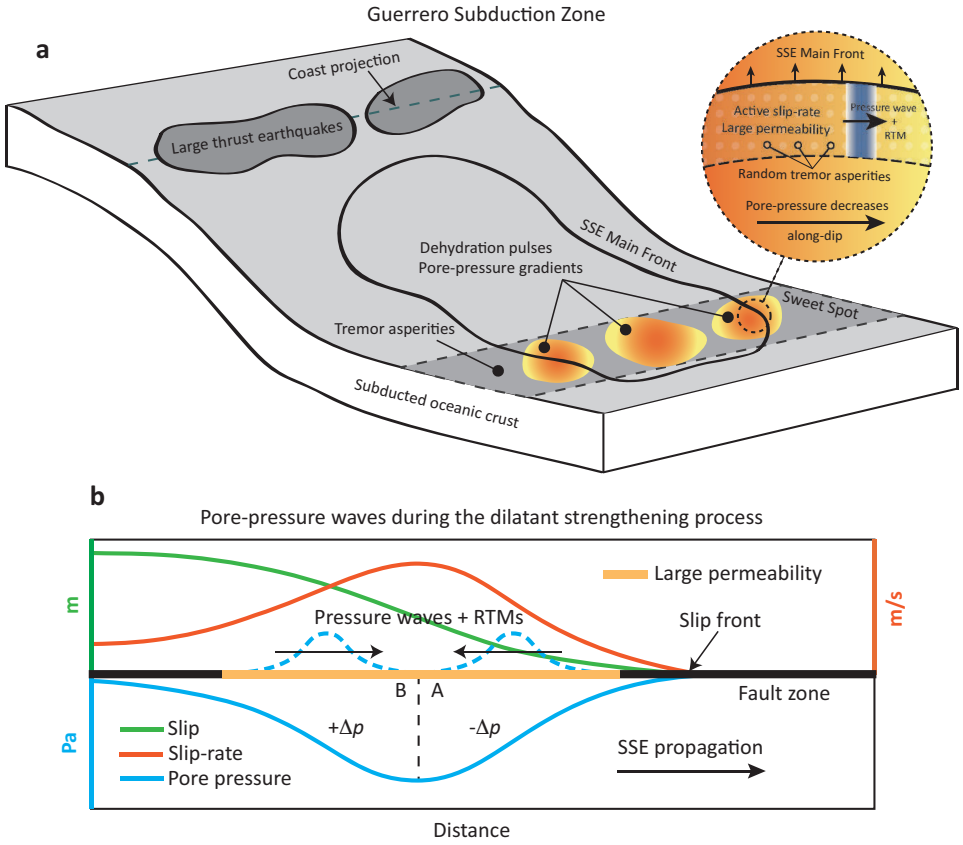

Figure 3.5. Cartoons illustrating the mechanisms we propose to explain the existence of pore-pressure waves in the plate interface and the associated generation of RTMs. (a) The Cocos plate interface during a SSE experiences tremor radiation due to the propagation of a pressure wave, which is driven by a preexistent ∇p_o associated with a localized dehydration pulse in the oceanic crust. A highly permeable zone associated with the active SSE front channelizes the wave. This mechanism is likely to explain RTMs following the SSE front (e.g. tremor streaks). (b) Plate interface conditions set by the dilatant strengthening mechanism during a SSE. Two opposite pore-pressure gradients are generated in the SSE front-perpendicular direction where permeability is increased. This mechanism is likely to explain both the rapid tremor reversals (RTRs) and RTMs in the SSE propagation direction.

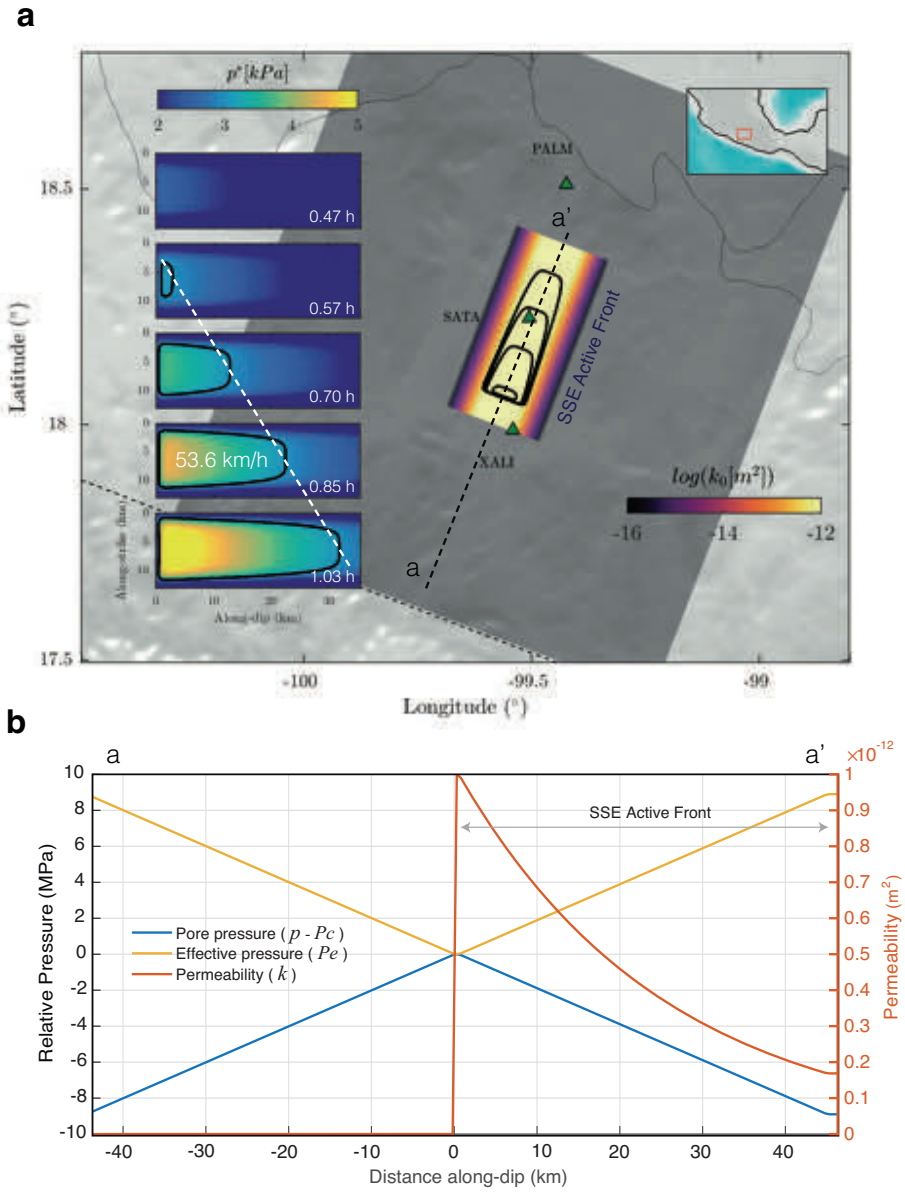

Figure 3.6. Two-dimensional pore-pressure wave simulation in Guerrero (blue-yellow shaded in panel a, where $p* = p - p_0$). In this model, permeability k_0 gradually increases (black-yellow shaded in panel a) inside an elongated trench-perpendicular region that we assume correspond to the most active SSE front (i.e. where slip-rate is significantly large). The black contours indicate the position of the wave-front for a pressure threshold of 3 kPa. Compare with Figure 3. Panel b shows the initial conditions for the simulation along the cross-section a-a'depicted with a dashed black line in panel a.

Chapter 4

Adjoint Slip Inversion under a Constrained Optimization Framework: Revisiting the 2006 Guerrero Slow Slip Event

Contents

This chapter has been modified from its associated article: Tago, J., Cruz-Atienza, V. M., **Villafuerte, C.**, Nishimura, T., Kostoglodov, V., Real, J., and Ito, Y. (2021). Adjoint slip inversion under a constrained optimization framework: Revisiting the 2006 Guerrero slow slip event. *Accepted at Geophysical Journal International.*

Abstract

To shed light on the prevalently slow, aseismic slip interaction between tectonic plates, we developed a new static slip inversion strategy, the ELADIN (ELastostatic ADjoint INversion) method, that uses the adjoint elastostatic equations to compute the gradient of the cost function. ELADIN is a 2-step inversion algorithm to efficiently handle plausible slip constraints. First it finds the slip that best explains the data without any constraint, and then refines the solution by imposing the constraints through a Gradient Projection Method. To obtain a selfsimilar, physically-consistent slip distribution that accounts for sparsity and uncertainty in the data, ELADIN reduces the model space by using a von Karman regularization function that controls the wavenumber content of the solution, and weights the observations according to their covariance using the data precision matrix. Since crustal deformation is the result of different concomitant interactions at the plate interface, ELADIN simultaneously determines the regions of the interface subject to both stressing (i.e., coupling) and relaxing slip regimes. For estimating the resolution, we introduce a mobile checkerboard analysis that allows to determine lower-bound fault resolution zones for an expected slip-patch size and a given stations array. We systematically test ELADIN with synthetic inversions along the whole Mexican subduction zone and use it to invert the 2006 Guerrero Slow Slip Event (SSE), which is one of the most studied SSEs in Mexico. Since only 12 GPS stations recorded the event, careful regularization is thus required to achieve reliable solutions. We compared our preferred slip solution with two previously published models and found that our solution retains their most reliable features. In addition, although all three SSE models predict an upward slip penetration invading the seismogenic zone of the Guerrero seismic gap, our resolution analysis indicates that this penetration might not be a reliable feature of the 2006 SSE.

4.1 Introduction

An elegant and powerful mean to solve geophysical inverse problems is the adjoint method (*AM*) since it provides a robust theoretical framework for constrained optimization problems. Given an objective function, $\mathbb{C}$, measuring the difference between data and a model prediction (i.e., a forward problem), to determine the model parameters that minimize $\mathbb{C}$, the *AM* allows computing efficiently the derivative of $\mathbb{C}$ with respect to the parameters by combining the forward problem and the solution of an adjoint equation (i.e., of an adjoint problem) (Fichtner et al., 2006; Tromp et al., 2005; Tarantola, 1984; Gauthier et al., 1986). Thus, the inverse problem can be solved by using any optimization method that exploits that derivative to find the minimum of $\mathbb{C}$. The *AM* provides a robust theoretical framework for constrained optimization problems that has been used in many geophysical inverse problems. The *AM* has been successfully used to solve full-waveform inverse problems in seismology, either to determine the elastic properties of the earth (Tromp et al., 2005; Askan et al., 2007; Fichtner et al., 2010; Krischer et al., 2018) or the kinematic history of earthquake sources (Sánchez-Reyes et al., 2018; Somala et al., 2018). For geodetic data, Kano et al. (2015) used the *AM* to estimate frictional parameters during the afterslip of an earthquake.

The longterm deformation of the Earth's crust close to the tectonic boundaries may be often explained in terms of the aseismic slip occurring between the plates. Depending on whether the interplate slip rate is larger or smaller than the relative plate motion, the plate interface experiences a relaxing slow slip event (SSE) (Dragert et al., 2001) or a stressing coupling regime (i.e., creeping or full locking) (Simpson et al., 1988), respectively. In the first case, a slip dislocation may predict the associated displacement field. In the later, the crustal deformation could be explained through the backslip formulation (Savage, 1983). The surface displacement is the summation of all contributions from the interface points experiencing either a coupling regime or an SSE. In the present work, to determine the plate interface aseismic slip history in these terms from continuous GPS (or any other geodetic) measurements, we introduce and solve a constrained optimization problem based on the adjoint elastostatic equations with a Tikhonov regularization term (Calvetti et al., 2000; Asnaashari et al., 2013) and a projection operator built with the von Karman autocorrelation function (Mai and Beroza, 2002; Amey et al., 2018). The new method, called ELADIN (ELastostatic ADjoint INversion), simultaneously determines the distribution of the interplate coupling and slow slip from surface displacements.

In those cases where the crustal strain field corresponds to a quasi-static seismotectonic process, the surface displacement is linearly related to the fault slip. However, determining the slip over an extended buried fault from such displacement remains an ill-posed problem. Underdetermination of the model parameters, i.e., the slip distribution, arises from the sparse sampling of the displacement field and the rapidly decreasing sensitivity of displacement to slip with distance from the fault (Nocquet, 2018). One rigorous framework to overcome this problem and to determine the uncertainty of such an inverse problem solution are the Bayesian approaches. The incorporation of prior information through probability density functions (pdf) allows determining the posterior model covariance and pdfs, as well as imposing model restrictions by means of truncated prior pdfs (Tarantola and Valette, 1982; Nocquet, 2018; Minson et al., 2013; Yabuki and MatsuÚra, 1992; Amey et al., 2018; Nocquet et al., 2014; Nishimura et al., 2004). For instance, Minson et al. (2013)

samples the posterior pdf using a Monte Carlo Markov Chain that enables to apply non-negativity constraints and any prior pdf. Dettmer et al. (2014) even showed how the optimal slip parametrization can be estimated from the data. Although Bayesian approaches are widely used and powerful, one important limitation that most have is the large computational load required to determine stochastically the posterior pdfs and thus the uncertainty of the model parameters. Yet, a proper selection of the prior pdf can overcome these issues making the sampling of the posterior pdf much faster through analytical or semi-analytical evaluations (Nocquet, 2018; Benavente et al., 2019).

An alternative to solve the elastostatic inverse problem is by introducing model regularizations and physically consistent restrictions. To prevent unrealistic oscillatory slip distributions, the most common regularization approach is to smooth the solution by applying a Laplacian operator (i.e., penalizing the second derivative of the slip) (McCaffrey et al., 2007; Wallace and Beavan, 2010). Usually, the hyperparameter controlling the smoothing is chosen subjectively by finding a satisfactory compromise between the data fit and the smoothing of the slip distribution. One common strategy to determine the hyperparameter is through an L-curve analysis that looks for an optimal value that keeps the data fitted with the strongest possible regularization (Radiguet et al., 2011). From a statistical approach, the hyperparameter can be determined using objective methods such as the Akaike Bayesian Information criterion (ABIC) (Yabuki and MatsuÚra, 1992; Miyazaki et al., 2006) or fully Bayesian techniques (Fukuda and Johnson, 2008). Although the Laplacian operator reduces unphysical and rough slip solutions (and thus unreliable large stress drops), this is not the most convenient regularization strategy to preserve the real nature of the fault slip, which has a self-similar spectral signature (Mai and Beroza, 2002). Recently, Amey et al. (2018) proposed to use the von Karman autocorrelation function to build the model covariance matrix such that the penalization term should lead to self-similar slow-slip solutions.

When designing ELADIN, our goal was to introduce a regularization approach that would preserve the above-mentioned nature of faulting and, at the same time, allow a spectral control of the problem solution that guaranties a given resolution criterion. To this purpose we use a von Karman autocorrelation function that reduces the model space to a domain where the wavenumber content of all possible solutions satisfies a minimum slip characteristic length previously determined through robust resolution tests. In our approach, we do not build a model covariance matrix, as proposed by Amey et al. (2018), but we convolve the von Karman correlation function with the slip to project it into a reduced model space. We illustrate the capabilities of the method by inverting GPS data for the 2006 Guerrero SSE, which has been widely investigated in the literature, and describe several benefits that our solution has in comparison with some previous models. Systematic inversion of GPS data along the entire Mexican subduction zone applying the ELADIN method is presented in an associated work (Cruz-Atienza et al., 2021) where we analyzed the aseismic slip history of the plate interface between 2017 and 2019, and its interaction with large earthquakes.

4.2 The ELADIN Method

In this section, we first introduce the forward model that allows us to compute the synthetic displacements produced by a slip over the fault. Then, we formulate the inverse problem in a constrained

optimization framework, reducing the solution space to control its spectral content with a von Karman autocorrelation function. We also include a Tikhonov term to penalize regions where slip is not expected to occur and to impose slip magnitude constraints. Finally, we present a 2-step algorithm that first solves the inverse problem without slip constraints using the adjoint equations for the gradient computation, and then projects the resulting solution into the feasible solution space which is later improved by means of a Gradient Projection method that imposes the desired physically-consistent slip constraints.

4.2.1 Forward model

The elastostatic representation theorem for the displacement field, $\underline{u}(\underline{x})$, due to a slip, $\underline{d}(\underline{\xi})$, produced at a fault, Σ, is

$$u_j(\underline{x}) = \int_\Sigma T_k(S_{ij}(\underline{\xi},\underline{x}),\hat{\underline{n}}(\underline{\xi}))d_k(\underline{\xi})d\Sigma, \qquad i,j,k \in \{x,y,z\}, \tag{4.1}$$

where $T_i(\cdot,\cdot)$ is the i-component of the traction vector on the fault computed through the Somigliana tensor, $S_{ij}(\underline{\xi},\underline{x})$, and the fault normal vector $\hat{\underline{n}}(\underline{\xi})$. It is a common practice to compute the Somigliana tensor considering a half-space homogeneous medium. However, Williams and Wallace (2015) have shown that neglecting the medium heterogeneities can result in slip overestimates of $\sim 20\,\%$ for deeper events, and underestimates up to $42\,\%$ for shallow earthquakes. For this reason, we adopted the AXITRA method (Bouchon and Aki, 1977; Coutant, 1990) for the calculation of the Somigiliana tensor, which allows us to consider heterogeneous layered media.

If the traction and the slip are projected along the plate convergence direction, c-, and the complementary perpendicular direction, $p-$direction, eq. (4.1) can be written in matrix form as

$$\begin{aligned}
\begin{bmatrix} u_1(\underline{x}) \\ u_2(\underline{x}) \\ u_3(\underline{x}) \end{bmatrix} &= \int_\Sigma \begin{bmatrix} T_p(S_{i1}(\underline{\xi},\underline{x}),\hat{\underline{n}}(\underline{\xi})) & T_c(S_{i1}(\underline{\xi},\underline{x}),\hat{\underline{n}}(\underline{\xi})) \\ T_p(S_{i2}(\underline{\xi},\underline{x}),\hat{\underline{n}}(\underline{\xi})) & T_c(S_{i2}(\underline{\xi},\underline{x}),\hat{\underline{n}}(\underline{\xi})) \\ T_p(S_{i3}(\underline{\xi},\underline{x}),\hat{\underline{n}}(\underline{\xi})) & T_c(S_{i3}(\underline{\xi},\underline{x}),\hat{\underline{n}}(\underline{\xi})) \end{bmatrix} \begin{bmatrix} d_p(\underline{\xi}) \\ d_c(\underline{\xi}) \end{bmatrix} d\Sigma, \qquad i \in \{x,y,z\} \\
\underline{u}(\underline{x}) &= \int_\Sigma \underline{\underline{T}}(\underline{\xi};\underline{x})\underline{d}(\underline{\xi})d\Sigma.
\end{aligned} \tag{4.2}$$

Then, the fault is discretized in M subfaults such that the integral can be approximated as

$$\underline{u}(\underline{x}) \simeq \sum_{i=1}^{M \text{ subfaults}} A^i \underline{\underline{T}}(\underline{\xi}^i;\underline{x})\underline{d}(\underline{\xi}^i), \tag{4.3}$$

where A^i is the $i-$subfault area. Finaly, if we want to compute the displacement for N receivers, we can order the displacements in a single vector such that the entire computation is reduced to a simple matrix-vector product as

$$\begin{bmatrix} \underline{u}(\underline{x}^1) \\ \underline{u}(\underline{x}^2) \\ \vdots \\ \underline{u}(\underline{x}^N) \end{bmatrix} = \begin{bmatrix} A^1\underline{\underline{T}}(\underline{\xi}^1;\underline{x}^1) & A^2\underline{\underline{T}}(\underline{\xi}^2;\underline{x}^1) & \cdots & A^M\underline{\underline{T}}(\underline{\xi}^M;\underline{x}^1) \\ A^1\underline{\underline{T}}(\underline{\xi}^1;\underline{x}^2) & A^2\underline{\underline{T}}(\underline{\xi}^2;\underline{x}^2) & \cdots & A^M\underline{\underline{T}}(\underline{\xi}^M;\underline{x}^2) \\ \vdots & \vdots & \ddots & \vdots \\ A^1\underline{\underline{T}}(\underline{\xi}^1;\underline{x}^N) & A^2\underline{\underline{T}}(\underline{\xi}^2;\underline{x}^N) & \cdots & A^M\underline{\underline{T}}(\underline{\xi}^M;\underline{x}^N) \end{bmatrix} \begin{bmatrix} \underline{d}(\underline{\xi}^1) \\ \underline{d}(\underline{\xi}^2) \\ \vdots \\ \underline{d}(\underline{\xi}^M) \end{bmatrix},$$

$$\underline{U} = \underline{\underline{\mathcal{T}}}\,\underline{D}, \tag{4.4}$$

where $\underline{U} \in \mathbb{R}^{3N}$, $\underline{\underline{\mathcal{T}}} \in \mathbb{R}^{3N\times 2M}$ and $\underline{D} \in \mathbb{R}^{2M}$.

4.2.2 Inverse problem

The inverse problem consists in recovering the slip at each subfault of a known interface that produces displacements observed at geodetic stations. Due to the linearity of the forward model, eq. (4.4), we construct a quadratic cost function to formulate a convex inverse problem as

$$\mathbb{C}(\underline{D}) = \frac{1}{2}\left[\underline{U} - \underline{U}_o\right]^T\left[\underline{U} - \underline{U}_o\right], \qquad \text{subject to} \quad \underline{U} = \underline{\underline{\mathcal{T}}}\,\underline{D}, \tag{4.5}$$

where $\underline{U}_o \in \mathbb{R}^{3N}$ are the displacements observed at the N geodetic stations stored in a single ordered vector, as we did with $\underline{U}$ in eq. (4.4). Since real data are sparse and may have significant noise, the inverse problem (4.5) is ill-conditioned. In order to face these issues, a problem regularization and realistic physical constraints are introduced next.

4.2.2.1 Problem Regularization

Most often, the problem regularization is done by means of two elements: a model precision matrix and/or Tikhonov terms. The model precision matrix is the inverse of the model covariance matrix which controls how sensitive is the slip in a given subfault to the slip on its neighbor subfaults. Radiguet et al. (2011) proposed a subfault correlation that follows a decreasing exponential function according to a defined correlation length. The problem we found with this approach is that the precision matrix for different correlation lengths does not have significantly different effects due to the fast decay of that function. For different types of correlation functions we tested, e.g., gausian and linear correlation functions, the model covariance matrix starts to become ill conditioned when the subfaults size becomes smaller than the correlation length. So, the precision matrices that could be computed were useless.

Tikhonov terms added to the cost function are used to penalize the roughness of the solution. Generally, the penalization is applied to the first or second spatial derivatives of the slip. However, when penalizing the derivatives, the norm of the slip solution is reduced as well. Besides, these two

alternatives involve hyperparameters that need to be optimally determined because they control the tradeoff between the misfit of the data and the strength of the regularization.

These inconveniences lead us to propose a new approach that reduces the solution space so that the wavenumber content of the solution (i.e., the minimum characteristic length of the slip patches) can be controlled. The main idea is to apply a filter, projection operator, $\underline{\underline{F}}$, to the slip $\underline{D}$. Then, the cost function (4.5) can be formulated as

$$\mathbb{C}(\underline{D}) = \frac{1}{2}\left[\underline{U} - \underline{U}_o\right]^T \underline{\underline{C}}_d^{-1}\left[\underline{U} - \underline{U}_o\right], \qquad \text{subject to} \quad \underline{U} = \underline{\underline{\mathcal{T}}}\,\underline{\underline{F}}\,\underline{D}, \tag{4.6}$$

where $\underline{\underline{C}}_d$ is the data covariance matrix to weight the data according to their quality or proximity to the slip.

Recently, Amey et al. (2018) build a model covariance matrix with the von Karman autocorrelation function and showed that it is a good strategy to guarantee the slip self-similar properties (Mai and Beroza, 2002) that cannot be achieved with a common Laplace regularization. The spatial von Karman autocorrelation function is

$$vk(r) = \frac{r^H K_H(r)}{(1e^{-10})^H K_H(1e^{-10})}, \tag{4.7}$$

where H is the Hurst exponent, $K_H(\cdot)$ is the modified Bessel function of second kind of order H, r is the correlation length that can be computed as

$$r = \sqrt{\frac{s^2}{a_s^2} + \frac{d^2}{a_d^2}}, \tag{4.8}$$

where (s, d) are the coordinates in the along-strike and along-dip directions on the fault, and (a_s, a_d) are the correlation lengths in those directions. Instead of using the von Karman autocorrelation function, eq. (4.7), to build a model covariance matrix, we propose to construct a linear operator K which, convolved with the slip D, controls the wavenumber content of the output function along both the strike and dip component. This convolution can be formulated as a matrix-vector product where the projection matrix, $\underline{\underline{F}}$, applies the convolution of the linear operator K to the slip, $\underline{D}$, as was done in eq. (4.6) (see Appendix C for further details). That is, $\underline{\underline{F}}$ projects the slip, $\underline{D}$, into a reduced solution space bounded by a chosen wavenumber.

4.2.2.2 Slip constraints

The model regularization we introduced guarantees that an optimal slip solution can be found. However, this solution may violate some expected physically-consistent restrictions, such as the full-coupling regime limit or slip rakes consistent with the plate convergence direction. Thus, slip

constraints need to be imposed according to the available geological information. The cost function (4.6) can then be reformulated as

$$\mathbb{C}(\underline{D}) = \frac{1}{2}\left[\underline{U}-\underline{U}_o\right]^T \underline{\underline{C}}_d^{-1}\left[\underline{U}-\underline{U}_o\right] + \frac{\beta}{2}\left[\underline{\underline{W}}(\underline{\underline{F}}\underline{D}-\underline{D}_p)\right]^T\left[\underline{\underline{W}}(\underline{\underline{F}}\underline{D}-\underline{D}_p)\right], \tag{4.9}$$

$$\text{subject to} \quad \underline{U} = \underline{\underline{\mathcal{T}}}\,\underline{\underline{F}}\,\underline{D}, \tag{4.10}$$

$$D_i^{j,l} \leq (\underline{\underline{F}}\underline{D})_i \leq D_i^{j,u}, \qquad i \in \{p,c\} \wedge j \in \{\text{SSE, Coupling}\}\,\text{regime}, \tag{4.11}$$

where β is a hyperparameter, $\underline{\underline{W}}$ is a model-weight diagonal matrix that penalizes the slip per subfaults, $\underline{D}_p$ is an *a priori* slip solution and $(D_i^{j,l}, D_i^{j,u})$ are the lower and upper limits of the i-component of the slip in the j-regime. The slip is either in the SSE regime if its c-component is opposite to the plate convergence direction or in the coupling regime otherwise. If we have an *a priori* slip solution, $\underline{D}_p$, we can force the solution to be as close as possible to it by accepting only model changes that improve the data fit. In that case, the weight matrix should be the identity matrix, $\underline{\underline{W}} = \underline{\underline{I}}$. If no *a priori* slip information is available, we simply set $\underline{D}_p = 0$ and, to obtain the minimum norm solution, we make again $\underline{\underline{W}} = \underline{\underline{I}}$. Since we are not interested in getting the minimum norm solution in the present study, we thus set $\underline{\underline{W}} = 0$ everywhere except in the subfaults where we assume free slip (i.e., no coupling or SSE regime). The bigger the weighting value, the bigger is the subfaults slip penalization. The hyperparameter β controls the tradeoff between the fit of the data and the Tikhonov regularization term. Its value only guarantees that the solution does not contain significant slip in the penalized regions. On the other hand, if an *a priori* slip solution ($\underline{D}_p \neq 0, \underline{\underline{W}} = \underline{\underline{I}}$) is used or a minimal norm solution ($\underline{D}_p = 0, \underline{\underline{W}} = \underline{\underline{I}}$) is desired, then β must be determined following an optimal strategy as an L-curve analysis (e.g., Radiguet et al. (2011)) or the ABIC criterion (e.g., Miyazaki et al. (2006)).

4.2.2.3 Gradient computation: Adjoint method

To solve the inequality-constrained inverse problem (eqs. (4.9)-(4.11)), first we address the gradient of the cost function without considering the inequality constraints, eq. (4.11). In the framework of constrained inverse problems, the Lagrangian can be computed as

$$\mathcal{L}(\underline{D}, \underline{U}, \underline{\lambda}) = \mathbb{C}(\underline{D}) + \underline{\lambda}^T\left[\underline{U} - \underline{\underline{\mathcal{T}}}\,\underline{\underline{F}}\,\underline{D}\right], \tag{4.12}$$

where $\underline{\lambda}$ are the Lagrange multipliers. The Lagrangian total derivative with respect to the slip, $\underline{D}$, is

$$D_{\underline{D}}\mathcal{L} = \nabla_{\underline{D}}\mathcal{L} + \nabla_{\underline{U}}\mathcal{L}\cdot\nabla_{\underline{D}}\underline{U} + \nabla_{\underline{\lambda}}\mathcal{L}\cdot\nabla_{\underline{D}}\underline{\lambda}. \tag{4.13}$$

To simplify the computation of the gradient, we follow the adjoint method strategy (Fichtner et al., 2006). We start forcing $\nabla_{\underline{\lambda}}\mathcal{L} = 0$ by solving a forward model $\underline{\tilde{U}} = \underline{\underline{\mathcal{T}}}\,\underline{\underline{F}}\,\underline{D}$. Then, we use the predicted displacement, $\underline{\tilde{U}}$, to compute the adjoint source as $\underline{\tilde{\lambda}} = \underline{\underline{C}}_d^{-1}\left[\underline{U}_o - \underline{\tilde{U}}\right]$ which implies $\nabla_{\underline{U}}\mathcal{L} = 0$. As a result, the Lagrangian total derivative is the solution of the adjoint problem plus a term related with the slip constraints as

$$\begin{aligned} D_{\underline{D}}\mathcal{L} &= \nabla_{\underline{D}}\mathcal{L} \\ &= -(\underline{\underline{\mathcal{T}}}\,\underline{\underline{F}})^T\underline{\tilde{\lambda}} + \beta\left[\underline{\underline{F}}^T\underline{\underline{W}}^T\underline{\underline{W}}\left(\underline{\underline{F}}\,\underline{D} - \underline{D}_p\right)\right]. \end{aligned} \tag{4.14}$$

Once the gradient of the cost function has been evaluated, we can follow any numerical optimization strategy to find the set of model parameters that minimize that function.

4.2.2.4 Gradient Projection Method

To avoid dealing with inequality constraints, it is often convenient to bring the current solution into the physically-consistent space after each iteration of the inversion procedure. However, for the slip inversion we realized that such procedure is not convenient because the gradient direction is often orthogonal to the slip constraints making the algorithm to stop. For large scale problems with lower and upper bounds for the variables, Nocedal and Wright (2006) propose the Gradient Projection Method (GPM) as an efficient strategy to deal with inequality restrictions. The GPM consists of two stages per iteration. In the first stage, the steepest descent direction is followed until a bound, i.e., the limit of an inequality constraint, is encountered and needs to be bent to stay feasible. Then, along the resulting piecewise-linear path, a local minimizer, called *Cauchy point*, is found (see Appendix C for details). For the second stage, a new optimal point is searched in the face of the feasible box on which the Cauchy point lies, i.e., those slip constraints that have reached a limit are changed to equality constraints. It implies that those inequality constraints are now part of the active set. This subproblem is usually not solved exactly since the remaining inequality constraints are usually not considered.

For the slip inversion, we do not follow exactly the GPM to avoid the subproblem of the second stage. This is because we expect that many subfaults in the coupling regime achieve its slip limit and that the number of iterations required was difficult to define. So, after computing the Cauchy point, we directly take it as a new iteration point where the gradient is computed again. Thus, our approach is essentially a steepest descent algorithm that respects the inequality constraints. Our GPM version is slow, so to achieve a fast convergence we then propose an algorithm that is explained in the next section.

4.2.2.5 2-step inversion algorithm

In order to increase the convergence speed, we developed a 2-step inversion algorithm. The purpose of the first step is to get an optimal initial solution for the GPM. In this step, we solve the unconstrained

slip inverse problem using the adjoint method to compute the gradient of the cost function. Once the gradient is obtained, any iterative optimization algorithm can be used to find the optimal solution, e.g., the Conjugate Gradient method, the l-BFGS method, etc. In this work, we use the SEISCOPE optimization toolbox, which is a friendly and powerful optimization library developed in FORTRAN 90 with many available optimization strategies (Métivier and Brossier, 2016). After some performance trials, we decided to use the l-BFGS method. In the second step, we first project the solution into the physically-consistent domain and then we solve the constrained slip inverse problem with a slight modification of the GPM. As explained above, after computing the Cauchy point, instead of reformulating the inverse problem according to the new active set incorporating some inequality constraints, we use it as the new iteration of the slip. This is not a fast strategy, but since we start from a slip distribution that is close to the optimal solution, only a few iterations of the GMP are required (about 200). The pseudcode is described in Algorithm 1.

Algorithm 1: 2-Step Algorithm

1^{st} Step: Unconstrained slip inverse problem (Adjoint method)
Data: GPS Data
Initialize the slip $\underline{D}_0 = 0$;
while Convergence is not achieved **do**

1. Compute a forward problem
$$\underline{U}_k = \underline{\underline{\mathcal{T}}}\,\underline{\underline{F}}\,\underline{D}_k.$$
2. Compute the adjoint source
$$\underline{\lambda}_k = \underline{\underline{C}}_d^{-1}\left[\underline{U}_o - \underline{U}_k\right].$$
3. Compute the adjoint problem to get the gradient
$$\nabla_{\underline{D}}\mathcal{L} = -(\underline{\underline{\mathcal{T}}}\,\underline{\underline{F}})^T\underline{\lambda}_k + \beta\left[\underline{\underline{F}}^T\underline{\underline{W}}^T\underline{\underline{W}}\left(\underline{\underline{F}}\,\underline{D}_k - \underline{D}_p\right)\right]$$
4. With the gradient use any iterative optimization algorithm to find an update step $\Delta\underline{D}_k$
5. Update the slip
$$\underline{D}_{k+1} = \underline{D}_k + \Delta\underline{D}_k.$$

end

2^{nd} Step: Constrained slip inverse problem (Gradient Projection Method)
Data: Optimal solution of 1^{st} step, $\underline{D}^*$
Project $\underline{D}^*$ into the physically-consistent domain to get the initial solution $\underline{D}_0$;
while Convergence is not achieved **do**

1. From $\underline{D}_k$ compute the Cauchy point $\underline{D}_k^c$ (details in Appendix C)
2. Update the slip
$$\underline{D}_{k+1} = \underline{D}_k^c.$$

end

4.3 Resolution

Resolution of our inverse problem essentially depends on the geometry configuration of the problem. This is, on the fault geometry and the distribution of observation sites, i.e., on the displacement field sampling and its sensitivity to dislocations at the fault. For a given problem discretization, synthetic inversions are a powerful mean to quantify how well an inverse method performs. If well-conceived, these tests may lead to very useful resolution information under realistic conditions, i.e., if they include data uncertainties and minimize the dependence on the target model. In the following, we present comprehensive exercises where the restitution of the target model is systematically quantified. To this purpose, for a given slip solution we define the restitution index, r_i as

$$r_i = 1 - \left| \frac{d_i^T - d_i^I}{d_i^T} \right|, \tag{4.15}$$

where d_i^T and d_i^I are the slip of the target and inverted models at the i-subfault, respectively. The slip component used to determine the restitution index can be either the plate convergence or its perpendicular direction. We also introduce the average restitution index, ari, which is the mean of the restitution indexes over the M subfaults that discretize the 3D subduction interface between the Cocos and the North American plates in central Mexico (Cruz-Atienza et al., 2021). r_i is one if the inverted slip equals the target slip and zero if the difference between them equals the target value. We have discretized the plate interface with subfaults whose surface projection is a square of 10×10 km^2. To compute the static traction vectors along the interface due to single body forces at the stations, eq. (4.1), we assumed a four-layer 1D structure suitable for the region (Campillo et al., 1996) and used the AXITRA method (Bouchon and Aki, 1977; Coutant, 1990). For the analysis, we have considered all available permanent GPS stations (66 sites) in central Mexico (Cruz-Atienza et al., 2021) and 5 ocean bottom pressure gauges (OBP) deployed in the Guerrero seismic gap since November 2017 (Cruz-Atienza et al., 2018a), where only the vertical displacements were considered.

4.3.1 Mobile checkerboard

A widely used strategy to quantify an inverse problem resolution is the checkerboard (CB) test. However, this test is intrinsically linked to the arbitrary choice of the target CB model, which means to the CB unit size, its positions and the absolute model-properties periodically attributed. For this reason, we performed comprehensive mobile checkerboard (M-CB) tests for different patch sizes (PS). Based on previous GPS data inversions in central Mexico (Radiguet et al., 2012; Cruz-Atienza et al., 2021), we set up the checkerboards by alternating patches with 30 cm of slip (a typical value for SSEs in the region) and -10 cm of back slip (a cumulative value of slip deficit over 20 months in a fully coupled regime assuming a plate convergence rate of 6 cm/year). It should be noted that this type of checkerboard tests, where the resolution of the slip and coupling can be evaluated simultaneously, is not common practice because most of the available inversion methods can only handle these two quantities separately.

Figure 4.1 shows the inversion results for three CBs with different PS, [60, 80 and 100 km], and the same correlation length, $L = 20$ km. As we shall see, this value of L maximizes the average restitution index (*ari*) in these cases where no slip restrictions were imposed (i.e., no gradient projection method was used) and no data uncertainly was considered (i.e., the precision matrix was the identity matrix). Although the data fit is almost perfect in all three cases, it is clear that the target model restitution strongly depends on PS, the slip model characteristic length. As expected, the larger PS the better is the restitution. This is quantified in the right column, where the restitution index, r, is displayed for all subfaults. Besides, two more conclusions stand out: (1) restitution is better in SSE patches than in coupling patches, and (2) the inversion scheme cannot resolve the unrealistic slip discontinuity along the boundary of the CB patches. Both conclusions were expected because the backslip is one third of the positive slip, and because of both the imposed model regularization and the limited sensitivity of displacements with distance to the fault.

Previous results do not provide a reliable estimate of the problem resolution when facing real data because in that case we do not know the actual slip producing the observed displacements. A M-CB test consists in multiple CB inversions so that all possible model positions are explored. Results from the test may be translated into the mobile checkerboard restitution index (*mcri*) per subfault, which corresponds to the average of the r values estimated for each inversion. The *mcri* is a quantity that eliminates the resolution dependence on the CB configuration. For a given PS, we performed 6 M-CB tests, one without regularization, $L = 0$ km and the rest with different correlation lengths, $L = 10, 20, 30, 40$ and 50 km. Five different PS of 40, 60, 80, 100 and 120 km were considered so each case required a different number of CB inversions to complete the associated M-CB test. Since the horizontal projection of subfaults is 10 km per side and we shifted the CBs with a 20 km jump along the dip and strike directions to complete all possible configurations, the total number of CB inversions in a M-CB test for an given PS in km is $(\mathrm{PS}/10)^2$.

Figure 4.2 presents an overview of three M-CB tests for PS of 60, 80 and 100 km (those considered in Figure 4.1). As expected, in the top row, we see that the *mcri* increases with the PS, reaching values close to 0.8 in some regions close to the coast where there is the largest density of stations, and where the plate interface is closest to them. In deeper interface regions, between 30 and 50 km depth, *mcri* falls up to about 0.2 for PS of 60 km and over 0.5 for PS of 100 km along the whole subductions zone. As clearly seen in the right column of Figure 4.1, the unrealistic slip discontinuities along the patches edges makes the resitution very difficult, so we can considerer the *mcri* maps of Figure 4.2 (first row) as a lower resolution bound. Isocontours of these maps for different PSs and optimal correlation lengths thus define reliable fault regions where the inversions should resolve the unknown target slip above the *mcri* isocontour value (e.g., above 40 % of the target slip if *mcri* equals 0.4).

The M-CB tests also allow to identify the optimum correlation length per subfault that maximizes the *ari*. This is shown in the second row of Figure 4.2, where we find that (1) the optimal L decreases for all PSs where the fault is well illuminated (i.e., in regions with high density of stations relative to the interface depth), and that (2) the optimal L increases as the PS decreases in places with sparse stations coverage, as it happens offshore near the subduction trench, for instance. Based on this multiscale analysis we built optimal solutions for the same CBs of Figure 4.1 by integrating the best inverted slip per subfault that corresponds to the associated optimal correlation length. Resolution

improvements for the multiscale models ranged between 10 % and 20 % as shown in the third row of the figure (compare with the right column of Figure 4.1). However, something unexpected came out when comparing whole-interface average *mcri* values for all M-CB tests. Figure 4.3 shows this metric along with the average data-misfit error (i.e., the L2 norm of the difference between target and inverted displacements) for all tested PSs as a function of L, the correlation length. Although the spatial distribution of the optimal L depends on the slip characteristic length PS, the best average regularization was the same for all PSs and equal to 20 km. Such independency of the average *mcri* on L for different PSs is determined by the unrealistic slip jumps of the checkerboards slip values that sweep the whole interface no matter the PS. However, as we shall see latter, the optimal regularization length actually increases with PS if both the data uncertainty (the precision matrix) and the slip restrictions (the GPM step) are considered in the inversions. What is remarkable and was indeed expected in Figure 4.3 is that (1) the maximum restitution values increased with PS, (2) the restitution function for a given PS displayed a concave behavior and (3) the best fitting models are not the best solutions (i.e., those with the highest restitution). Regularization is thus critical to achieve physically acceptable and reliable slip models.

4.3.2 Gaussian slip

The analysis of the previous section did not consider the uncertainty in geodetic measurements that may be significantly large, especially in the vertical component where atmospheric noise and non-tectonic physical signals are particularly present. Nor did the analysis incorporate slip restrictions that are essential to guaranty tectonic expectations in our slip solutions such as backslip smaller than expected for a full-coupled interface regime and slip rake angles close to the plate convergence direction. For this reason, we now study three synthetic exercises in which the target slip corresponds to truncated Gaussian slip distributions (to SSE-like functions) with different spatial supports, surrounded by a fully coupled plate interface. The associated surface displacements (i.e., the inverted data) are strongly and randomly perturbed according to a normal probability distribution given by the data variance per component, which we took as 2.1, 2.5 and 5.1 mm in the north, east and vertical directions, respectively (Radiguet et al., 2011).

Figure 4.4 shows the target slip models and both, the associated exact displacements (blue arrows) and the perturbed ones (red arrows). The data uncertainty is represented by the gray ellipses at the tips of the perturbed vectors, the semiaxes corresponding to the standard deviation of the normal distribution used to perturb the data per component. The interplate coupling corresponds to three-months cumulative backslip assuming a 6 cm/yr plate convergence (i.e., 1.5 cm), and the geometry and position of the three Gaussian slip patches were inspired by recent SSE solutions found in the region (Cruz-Atienza et al., 2021). Please notice how large are the perturbations.

Inversions for the three Gaussian slip models were done for both the exact and perturbed data. Each set of data was inverted without regularization, $\underline{\underline{F}} = \underline{\underline{I}}$, and with correlation lengths of 10, 20, 30, 40, 50 and 60 km. In all cases backlip restrictions were applied by means of the GPM so the interplate coupling could never overcome the value of one. Figure 4.5A shows some slip solutions for the largest-Gaussian exact data together with the associated restitution maps. Although the

data fit is excellent in all cases, acceptable solutions are only retrieved when model regularization is applied. For L = 30 km, the *ari* is above 0.9 so that the slip solution is almost perfect, except along the Gaussian contour where there is an unrealistic slip discontinuity in the target model (the same situtation as for the checkeboard tests).

When random noise is added to the theoretical observations and the inverse problem is solved by integrating the data uncertainty by means of the precision matrix, the model regularization becomes even more critical to achieve a reliable solution. This can be seen in Figure 4.5B, where the restitution is very poor around the Gaussian slip area when no regularization is applied as compared with that for L = 40 km, where the *ari* is also above 0.9 and thus the slip solution is surprisingly good. Also astonishing, results for the other two, smaller Gaussian slip models were very similar (see Figures **??** and **??**). A summary of the 42 inversions (14 per Gaussian model) is shown in Figure 4.6, where we see that although the data-fitting errors for the noisy inversions are roughly four times larger than those obtained from the exact data, the *ari* in all cases is above 0.9 for the best solutions (i.e., for the optimal L) even for the smallest and circular Gaussian case, which has a slip characteristic length smaller than 80 km centered at 38 km depth (Figure 4.4A).

4.4 The 2006 Guerrero SSE

During the 20 years preceding the devastating 2017 Mw8.2 Tehuantepec earthquake that took place offshore the Oaxaca state, Mexico, long term SSEs in Guerrero occurred almost every four years (i.e., six events between 1998 and 2017) and had remarkably large moment magnitudes (Mw>7.5) (Kostoglodov et al., 2003; Radiguet et al., 2012; Cruz-Atienza et al., 2018a). After the earthquake, the regional plate-interface SSE beating has strongly changed so that two other SSEs took place in that state in the next two years (in 2018 and 2019) with much smaller magnitudes (Mw $\sim$ 7.0) (Cruz-Atienza et al., 2021). Among all Mexican SSEs, the 2006 Guerrero event has been the most investigated despite the poor GPS instrumentation on that time (Kostoglodov et al., 2010; Vergnolle et al., 2010; Radiguet et al., 2011, 2012; Cavalié et al., 2013; Bekaert et al., 2015; Villafuerte and Cruz-Atienza, 2017). One of its most interesting features is that, unlike adjacent subduction segments, the slow slip seems to have penetrated the updip seismogenic region of the plate interface up to 15 km depth in the Guerrero seismic gap. In this section we perform a thorough analysis of the inverse problem resolution for that event and provide what we think are its most reliable features as compared with previous results reported in the literature.

4.4.1 Resolution

In previous sections we found that the problem resolution depends on two main parameters: (1) the slip characteristic length (PS) and (2) the inverse-problem correlation length (L). This is true for a given problem geometry (i.e., for a stations array and plate interface geometry). For this reason, we can determine fault regions where resolution (i.e., the restitution index) is high enough for a given L and PS, which means that the inverted slip in those regions is valid within the wavenumber bandwidth associated to the von Karman spectrum for that L. Since only 12 significant GPS stations

registered the 2006 SSE, we performed three different M-CB tests considering only the location of these sites and CB periodic *c*-slip values of -8 and 25 cm. The tests were done for checkerboard unit lengths (PS) of 80, 100 and 120 km, and for L = 0 (no regularization), 10, 20, 30, 40, 50 and 60 km. These resolution exercises assumed reasonable backslip and rake angle restrictions so that the *c*-slip component ranges within $[-8, 32]$ cm and the angle within $[20, -20]^\circ$ with respect to the *c*-direction, which implies the admissible range of $[-3, 3]$ cm for the *p*-slip component.

Plate-interface resolution maps (i.e., for the *mcri* metric) are shown in Figure 4.7 as a function of PS and L. As expected, overall *mcri* values increase with PS for a given L. Although less evident, they also increase with L for a given PS up to a certain correlation value. However, supplementary results not shown reveal that, in the latter case, the high-resolution regions stop expanding for L above 30 km for all three PS cases. The maps show isocontours for $mcri = 0.6$, which delineate fault regions where the slip solutions are likely to resolve the actual slip within 40 % error. As explained previously, these maps represent a lower resolution bound because the M-CB tests assume unrealistically sharp slip discontinuities that strongly penalize the restitution index along the boundaries of the square slip patches (e.g., see Figure 4.1). For this reason, we expect the resolution within the regions to be higher than the *mcri* isocontours value. Either way, even in the M-CB test for the maximum PS and L values, the high resolution region does not extend across the whole expected SSE area, as claimed by previous authors using different inversion techniques (Radiguet et al., 2011). Our resolutions maps represent the key piece allowing us to tell something reliable (to some point) about the 2006 SSE.

Figure 4.8 summaries the results from all M-CB tests in terms of the average mcri and data-misfit L2 error. Although errors are similar for all slip characteristic lengths PS, the maximum average mcri value increase with PS and follow a concave trajectory with L as previously noticed from Figure 4.7. However, unlike the previous M-CB exercises considering all currently available geodetic stations (Figures 4.2 and 4.3), the optimal correlation lengths (i.e., those maximizing the restitution) increase with PS. This remarkable and reasonable result is due to both the slip restrictions and the sparsity of the stations. It tells us that, depending on the characteristic size of the SSE patch we want to solve best, the regularization of the problem must be adapted. For instance, if we are interested in SSE patches with a characteristic length of 80 km, then L = 10 km is the optimal choice. Of course, such small value is detrimental to the extent of the acceptable resolution region, as seen in Figure 4.7. If L = 20 km, then patches with characteristic length of 100 km will be optimally solved in a larger fault region.

4.4.2 2006 SSE Inversions

The next inversions we present were done using the same GPS data as Radiguet et al. (2011). This means that the displacement time series were carefully pre-processed (Vergnolle et al., 2010) and then corrected for inter-SSE deformations by subtracting the linear trends from the period 2003-2005 per station. Thus, the resulting time series are supposed to show the deviations from the long-term steady motion during the 2006 Guerrero SSE.

Since the inter-SSE displacement trends per station are significantly different in Guerrero (Radiguet

et al., 2012), it is important to emphasize that the removal of these individual (usually linear) trends from the data for SSE imaging is an incorrect practice for two reasons: (1) the resulting displacement (or velocity) guesstimates no longer correspond to the initial reference system (e.g., fixed tectonic plate), often leading to overestimated deformation values and thus unrealistically high SSE moment magnitudes; and (2) the non-linear transformation implied by the corrections removes the common reference frame between GPS stations, which makes the resulting data set not strictly comparable and therefore its inversion meaningless. The fact that this correction is common practice does not make it acceptable. Either way, for the sake of comparison with previous solutions using this dataset, we have inverted the corrected time series from January 30 (2006) to January 15 (2007) for four different correlations lengths (L = 10, 20, 30 and 40 km) considering slip restrictions, so that the backslip could not overcome the full-coupling regime in that period and the rake vector could vary +/- 20° from the *c*-direction.

Figure 4.9 shows the inversion results for two optimal correlation lengths (L = 20 and 30 km). Since the data is almost perfectly explained in both cases, the preferred solution will depend on both the scale at which we are interested in for interpretations and reasonable physical considerations. Taking the 1 cm slip contour as the effective SSE area, then the moment magnitude of the 2006 event is consistent for both inversions and equal to Mw7.4. For estimating Mw, we considered a typical crustal rigidity $\mu = 32 \times 10^9$ Pa.

As shown in the last section, given the poor GPS coverage during the 2006 SSE, the inverse problem regularization plays a critical role to have some confidence in the slip solutions. In the absence of resolution analysis, it is difficult to justify any conclusion, especially between distant stations. For instance, the absence of data along most of the north-west Guerrero seismic gap (NW-GGap) (i.e., between ZIHP and CAYA) (UNAM, 2015) and the Guerrero Costa Chica (i.e., between CPDP and PINO) is unfortunate and obliges us to be cautious in the interpretations. Previous investigations concluded that SSEs behave differently between these two Guerrero subduction segments so that, unlike the Costa Chica, the slow slip in the NW-GGap reaches the updip seismogenic interface zone (i.e., up to 15 km depth) (Radiguet et al., 2011; Cavalié et al., 2013) releasing aseismically a significant part of the accumulated inter-SSE strain (Radiguet et al., 2012; Bekaert et al., 2015).

Figure 4.10 shows a comparison between our preferred solution (model A) (i.e., for L = 30 km) and two previously published solutions, one from the simultaneous inversion of both GPS and InSAR data (Model B by Cavalié et al. (2013)) and the other from GPS data only (model C by Radiguet et al. (2011)). Our solution is shown together with the associated 60 % resolution regions (regions where the average *mcri* is higher than 0.6), which are taken from Figure 4.7 according to the optimal solutions of Figure 4.8. Confidence contours thus delineate the fault regions where solutions should disagree with the actual slip by less than 40 % in different wavenumber bandwidths depending on L. The red contours delineate the 60 % confidence regions for a slip characteristic length of 80 km, while the green contours depict the same regions for a 120 km characteristic length. Although the three slip solutions are in general consistent, there are clear differences among them. The most visible are (1) the concentration of separated patches in model C (i.e., one of them far from the coast and below 40 km depth, and another one to the east) which may be artifacts due to a lack of regularization (Bekaert et al., 2015), which are consistent north of the CAYA and COYU stations, and (2) the peak slip values that range between 20 and 25 cm. Moment magnitudes are also slightly

different (i.e., 7.4 and 7.6 for models A and C, respectively). However, all three models coincide on the updip SSE spreading west of station CAYA, where our model has resolution higher than 60 % up to a distance no more than 30 km west of that station. This region is of critical importance because it extends along the NW-GGap, where recent onshore and offshore observations show that slow earthquake indeed happen in a particular way, and thus where the mechanical properties of the plate interface could be different (Cruz-Atienza et al., 2021; Plata-Martínez et al., 2021). Models B and C are remarkably different between stations ZIHP and CAYA, where the InSAR data used for model B does not play any significant role. West of this region, model B predicts a very large shallow penetration of the SSE across the mechanically stable zone where M7+ earthquakes occur every ∼35 years (see past rupture areas)(UNAM, 2015). For this reason, model C, which is consistent with our model A, is the most plausible solution for that zone. Besides, our resolution close to the ZIHP station is higher than 60 % as well. In conclusion, our preferred ELADIN solution has the most reliable features of both previously published slip models.

4.5 Conclusions

We have introduced the ELADIN method, a new fault-slip inversion technique based on the adjoint elastostatic equations under a constrained optimization framework. The method main characteristics are the projection operator built with the von Karman autocorrelation function to control the spectral content of the solution, i.e, the problem regularization, and the gradient projection method to impose physically-consistent slip restrictions (e.g., interplate coupling smaller than any given value and rake angles consistent with the relative plate motion). To account for the data uncertainty, the method weights the observations according to their individual variances through the precision matrix. Synthetic slip inversions from strongly perturbed data show that the model restitution across the plate interface is surprisingly high (for both SSE and coupled interface regions) when this uncertainty is taken into account. The ELADIN method thus allows determining the aseismic slip on any 3D plate interface (or any fault surface) by simultaneously inverting relaxing slip and coupled fault areas with a spectral control of the problem solution that guaranties a given resolution criterion. We defined this criterion by means of the mobile checkerboard restitution index ($mcri$), which allows determining fault regions where the resolution (i.e., the slip restitution index) is high enough for a given von Karman autocorrelation length, L. This means that the inverted slip in those regions is valid (to some desired extent) within the wavenumber bandwidth associated to the von Karman spectrum for that L.

After a thorough resolution analysis of the study region, we inverted the 2006 Guerrero SSE. Our preferred slip model (Model A), obtained for L = 30km, was compared with two previously published solutions and found that it retains the most reliable features of these two models. On one hand, our model is consistent with the solution of Cavalié et al. (2013) (Model B) in that it places the maximum slip region above 40 km depth (i.e., downdip from stations CAYA and COYU), where this solution is well constrained by the InSAR data. On the other, although all solutions predict the SSE shallow penetration along a large part of the NW-GGap segment (west of CAYA), our resolution analysis clearly shows that this penetration might not be a reliable feature of the 2006

SSE. However, our Model A is much closer to the solution of Radiguet et al. (2011) (Model C) close to station ZIHP, where only GPS data is available. In this sense and considering also that M7+ earthquakes occur every ∼35 years east from that station (see previous rupture areas in Figure 4.10), which implies that the plate interface is mechanically unstable, then the extremely large updip SSE penetration predicted by Model B (Cavalié et al., 2013) between stations ZIHP and CAYA seems unrealistic.

A systematic application of the ELADIN method has been made in two associated works (Cruz-Atienza et al., 2021; Villafuerte et al., 2021) to invert recent GPS and InSAR data from the large array shown in Figure 4.1, in the period 2016-2020, where four major earthquakes and multiple SSEs occurred throughout the Mexican subduction zone.

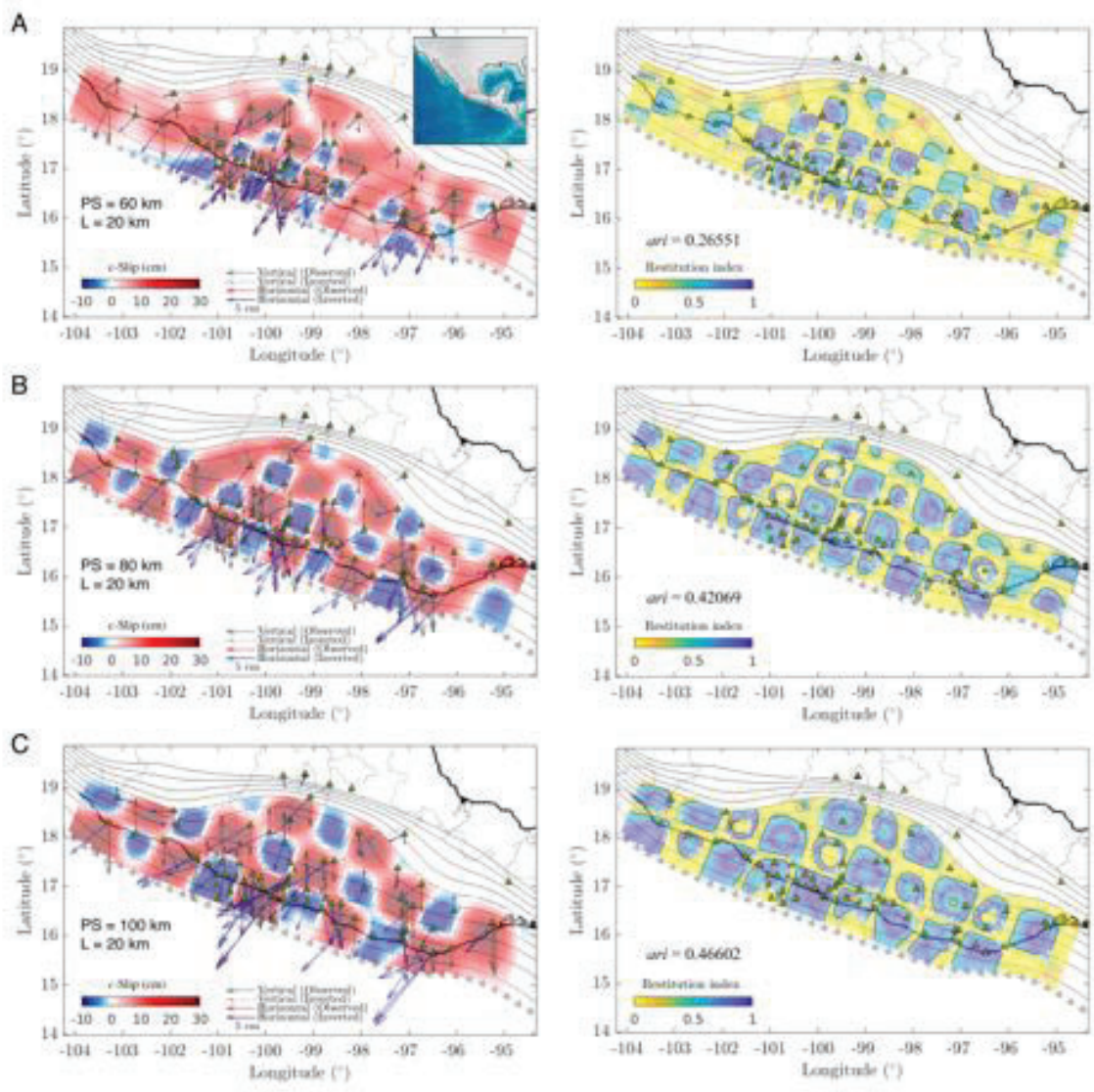

Figure 4.1. Checkerboard inversions for PS of (A) 60, (B) 80 and (C) 100 km, and correlation length, L, of 20 km. The inverted slip along the plate convergence direction, *c*-slip, with the surface displacement fits (left column) and the associated restitution index (right column) are displayed on the 3D plate interface (gray contours). Green triangles are the GPS stations.

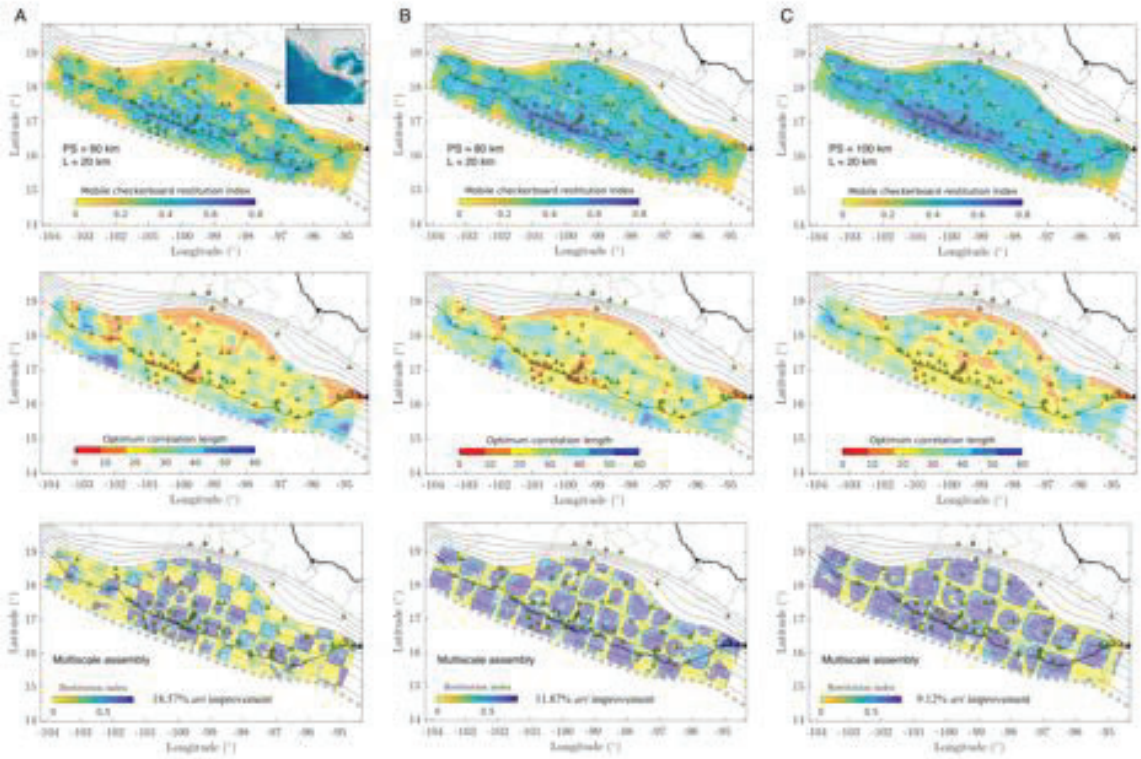

Figure 4.2. M-CB tests for PS of (A) 60, (B) 80 and (C) 100 km and correlation length, L, of 20 km. Distributions of *mcri* (first row), the optimal correlation length (second row) and the multiscale assembly of the restitution index (computed from the assembly of the best slip solutions for the CBs shown in Figure 1), all of them computed with the *c*-slips inverted and displayed on the 3D plate interface (gray contours). Green triangles are the GPS stations.

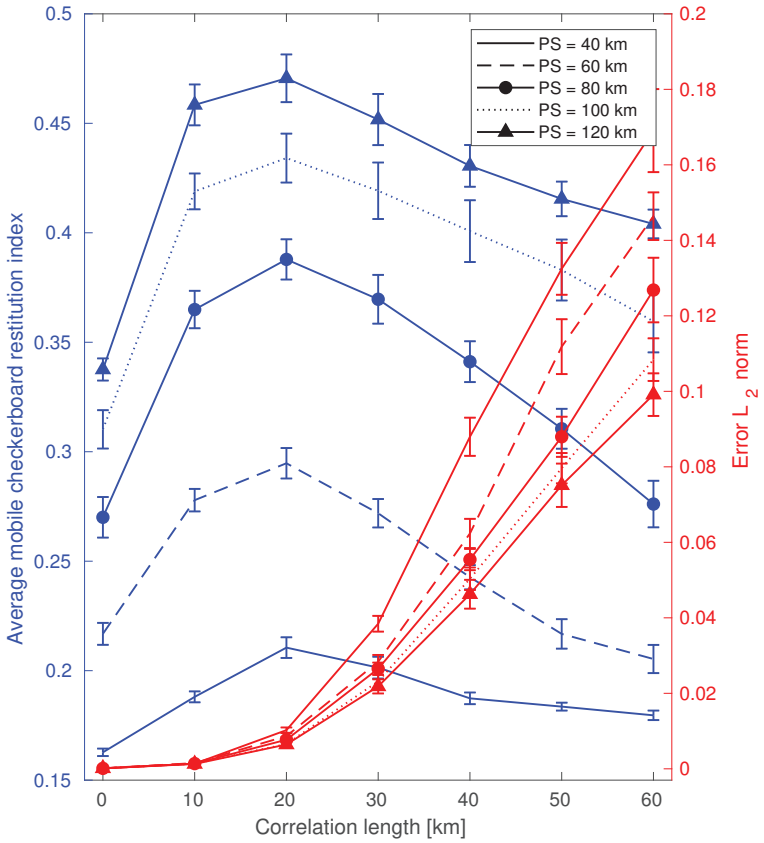

Figure 4.3. Results from all M-CB tests in terms of the whole-interface average *mcri* (blue) and the average data-misfit error (red), as a function of the inversions correlation length L for PS of 40, 60, 80, 100 and 120 km.

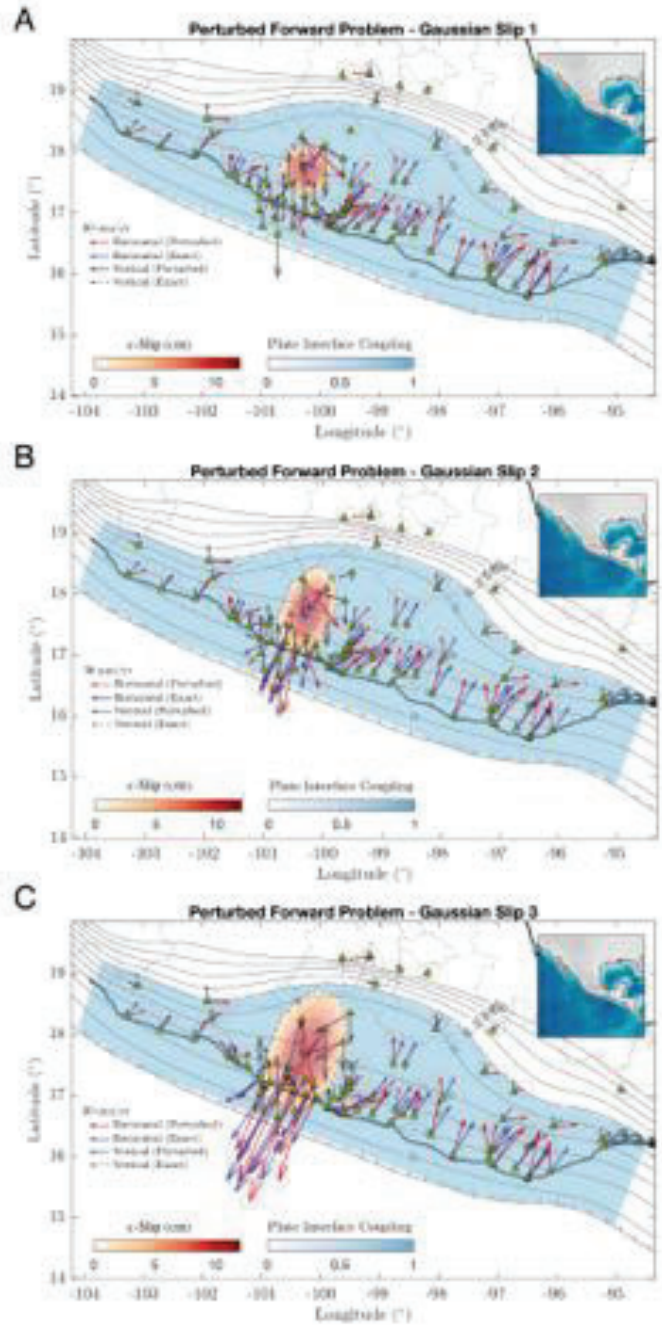

Figure 4.4. Slip models along the c-direction on the plate interface (background colors) and the associated model displacement predictions (arrows) for three Gaussian-like slip patches with different characteristic lengths. Blue and black-solid arrows show the exact surface displacements while red and black-dashed arrows show the same predictions but stochastically perturbed according to the normal distributions given by the data variance per component.

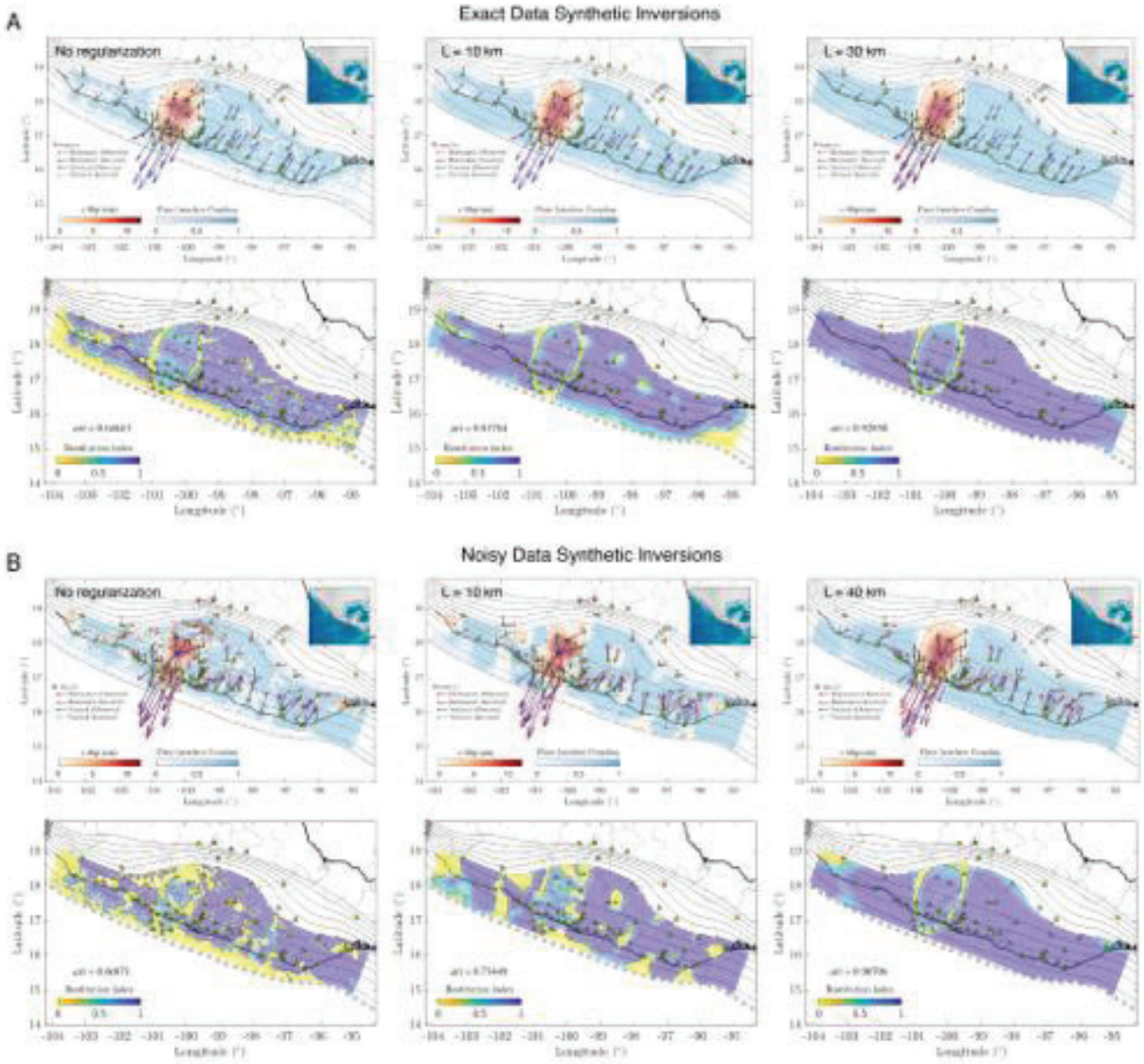

Figure 4.5. Synthetic inversion results for the *c*-slip model shown in Figure 4C from the exact target displacements (panel A) and from the perturbed (noisy) displacements (panel B). The second row of each panel shows the distribution of the restitution index for the *c*-slip over the plate interface without regularization and for different values of the correlation length, L.

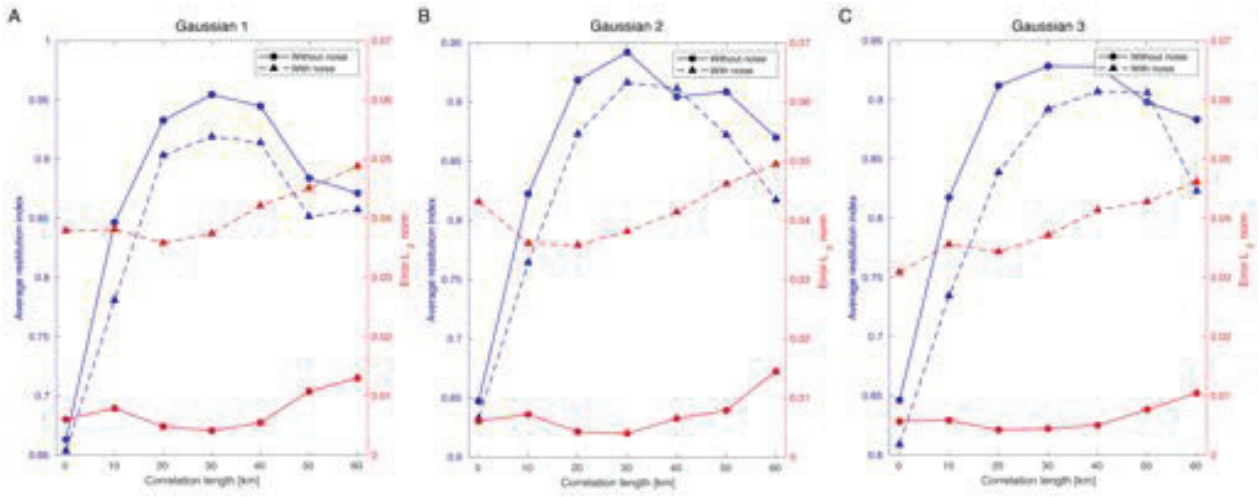

Figure 4.6. Synthetic inversion results for the three Gaussian-like slip functions shown in Figure 4.4 in terms of the whole-interface average restitution index, *ari*, and average data-misfit error (red) as a function of the inversions correlation length L. Solid lines correspond to the inversions using the exact data while dashed lines to the inversions with noisy data (see Figure 4). Notice that in all cases the maximum restitutions, *ari*, are above 0.9.

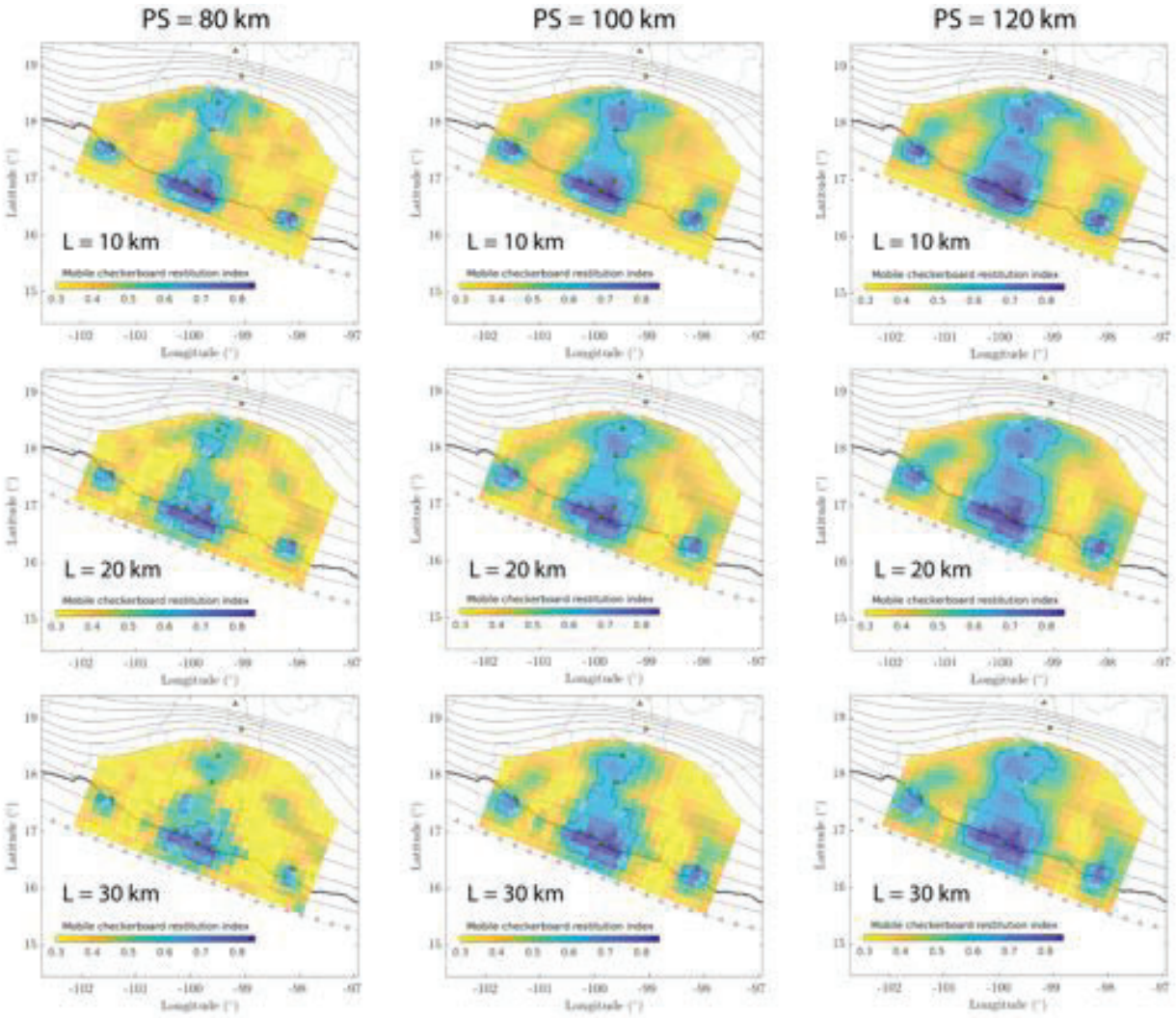

Figure 4.7. Plate interface distribution of the mobile checkerboard restitution index, *mcri*, of the *c*-slip inverted from M-CB tests corresponding to patch sizes (PS) of 80, 100 and 120 km and correlation lengths L = 10, 20 and 30 km for the 2006 SSE stations configuration. Black contours correspond to *mcri* values of 0.6 (i.e., slip resolution of 60 %).

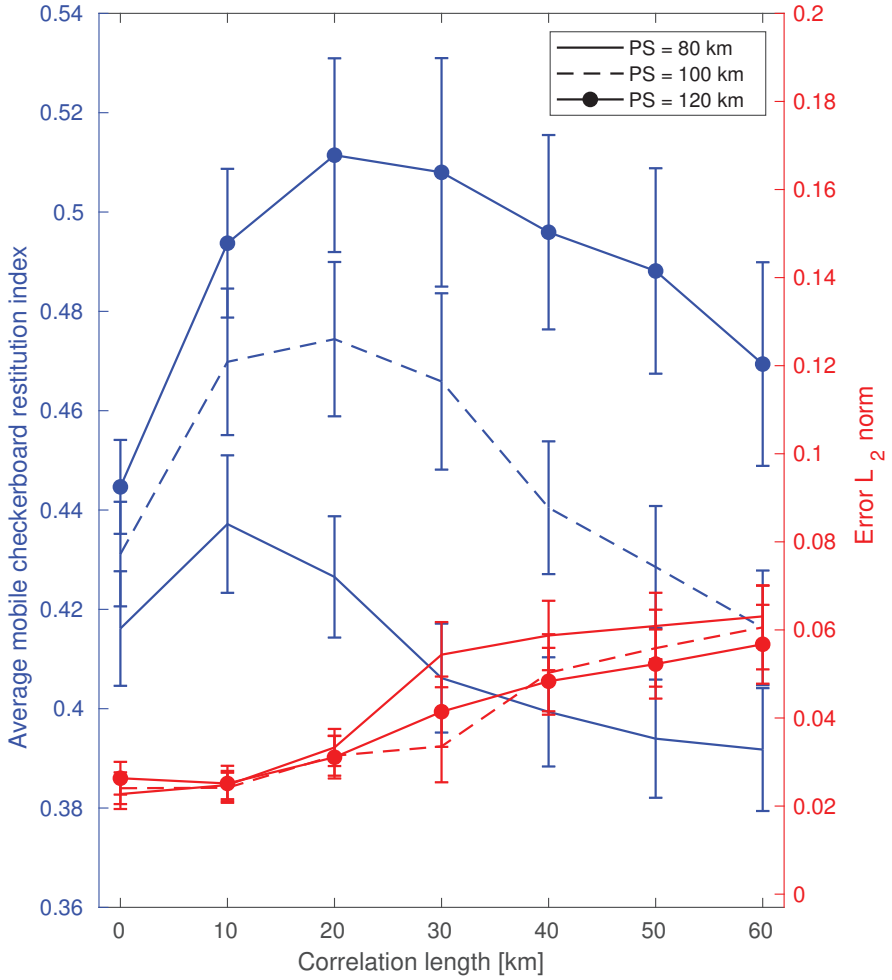

Figure 4.8. Results from all M-CB tests for the 2006 SSE stations configuration in terms of the whole-interface average *mcri* (blue) and the average data-misfit error (red), as a function of the inversions correlation length L and PS of 80, 100 and 120 km.

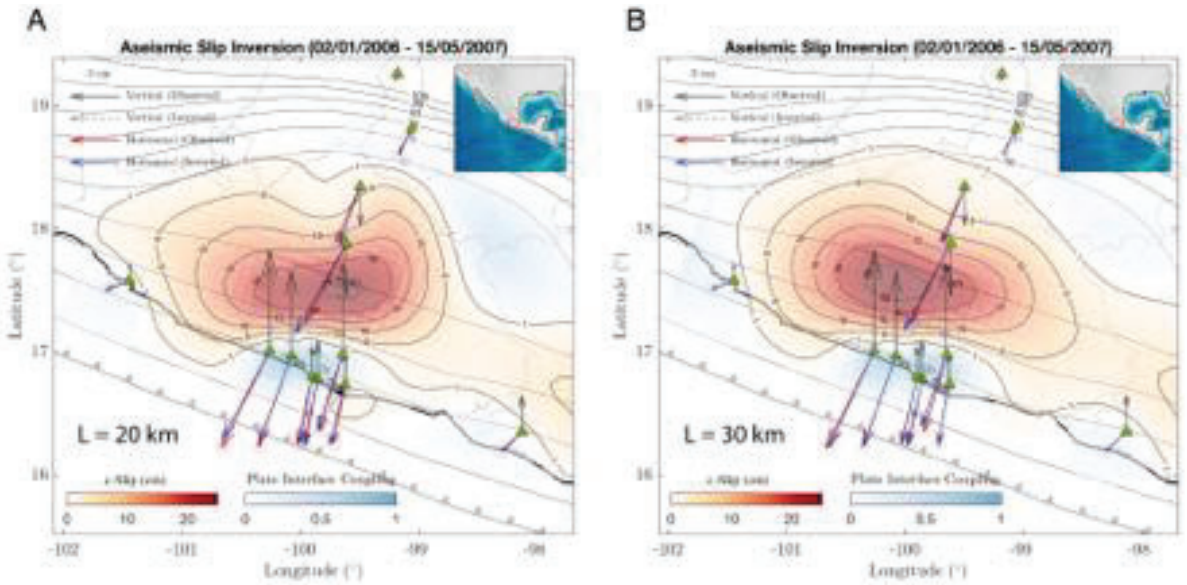

Figure 4.9. Aseismic slip inversions, in the plate convergence direction, of the 2006 Guerrero SSE for correlation lengths L = 20 km (A) and L = 30 km (B). The plate interface coupling is determined from the ratio between the back slip and the cumulative slip in the inverted period given a plate convergence rate of 6 cm/yr.

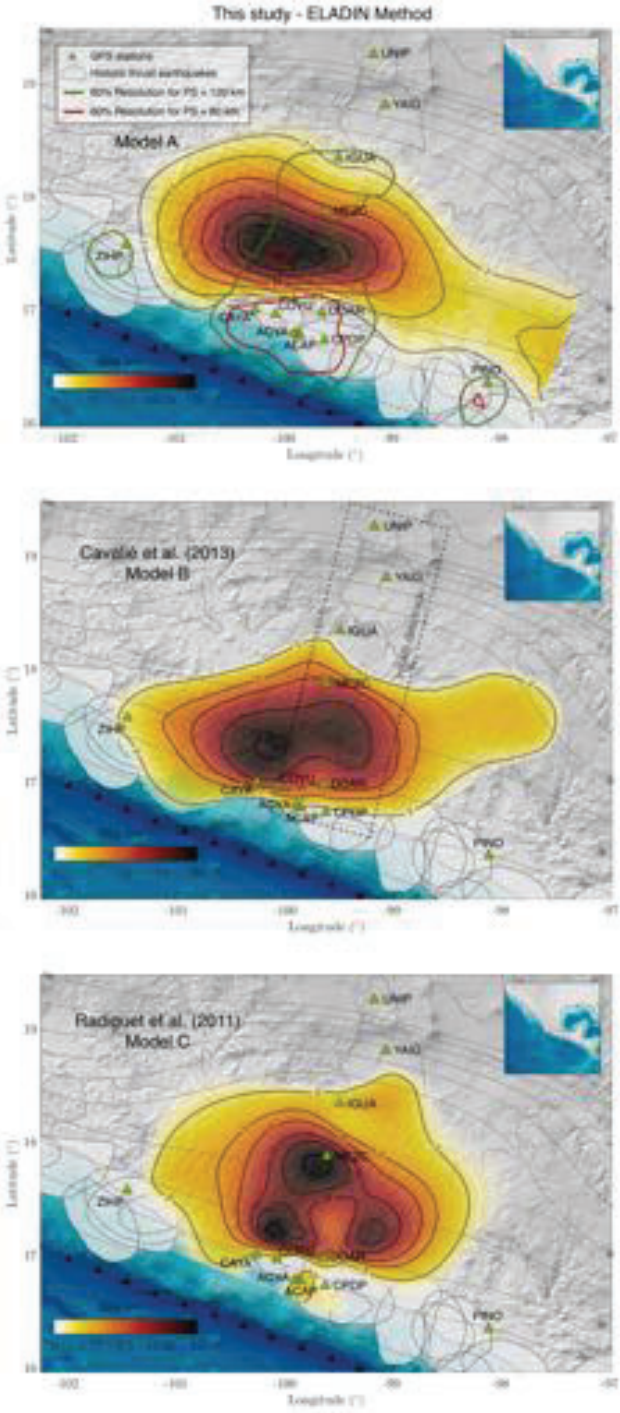

Figure 4.10. Comparison of our preferred solution (model A - for L = 30 km, Figure 4.9) with two previously published models for the 2006 Guerrero SSE, model B from Cavalié et al. (2013) and model C from Radiguet et al. (2011). 60 % resolution contours for slip-patch (PS) characteristic lengths of 80 and 120 km are shown over model A.

Chapter 5

Short-Term Interaction between Silent and Devastating Earthquakes in Mexico

Contents

This chapter has been modified from its associated article: Cruz-Atienza, V., Tago, J., **Villafuerte, C.**, Wei, M., Garza-Girón, R., Dominguez, L., Kostoglodov, V., Nishimura, T., Franco, S., and Real, J. (2021). Short-term interaction between silent and devastating earthquakes in Mexico. *Nature communications*,12, 2171, doi.org/10.1038/s41467-021-22326-6

Abstract

The triggering of large earthquakes on a fault hosting aseismic slip or, conversely, the triggering of slow slip events (SSE) by passing seismic waves involves seismological questions with important hazard implications. Just a few observations plausibly suggest that such interactions actually happen in nature. In this study we show that three recent devastating earthquakes in Mexico are likely related to SSEs, describing a cascade of events interacting with each other on a regional scale via quasi-static and/or dynamic perturbations across the states of Guerrero and Oaxaca. Such interaction seems to be conditioned by the transient memory of Earth materials subject to the "traumatic"stress produced by seismic waves of the great 2017 (Mw8.2) Tehuantepec earthquake, which strongly disturbed the SSE cycles over a 650 km long segment of the subduction plate interface. Our results imply that seismic hazard in large populated areas is a short-term evolving function of seismotectonic processes that are often observable.

5.1 Introduction

Seismicity rate varies over time and depends on changes in both the state of stress and properties of the solid Earth. The diversity of earthquakes discovered in recent years, together with new observations of very small transient variations in the crustal properties, offer an unprecedented perspective for exploring causality between different seismotectonic processes. Inferred effects of slow slip events (SSE, also called silent earthquakes) on large and devastating earthquakes have led to critical questions closely related to seismic hazard. The role of SSEs in the seismic cycle seems to have been preponderant in the initiation of some megathrust earthquakes (Kato et al., 2012; Ruiz et al., 2014; Obara and Kato, 2016; Uchida et al., 2016; Radiguet et al., 2016). Observations also show that transient waves from teleseismic or regional earthquakes may trigger SSEs and tectonic tremor (Miyazawa and Mori, 2006; Rubinstein et al., 2009; Zigone et al., 2012; Wallace et al., 2017; Tymofyeyeva et al., 2019), which are two closely related phenomena in active faults. Highly pressurized fluids where slow earthquakes happen (Audet and Kim, 2016) make frictional conditions very sensitive to small stress or strain perturbations (Cruz-Atienza et al., 2018b; Warren-Smith et al., 2019), thus playing an important role in the generation of SSEs and, certainly, in their interaction with devastating events.

Recently, three major earthquakes took place in southcentral Mexico causing more than 480 deaths and losses of 1,6 billion dollars. The earthquake sequence initiated with the great Mw8.2 Tehuantepec event on September 8, 2017, the largest earthquake ever recorded in Mexico, which may have broken the whole subducted Cocos lithosphere (Melgar et al., 2018; Suárez et al., 2019) (Fig. 5.1). Eleven days later and 480 km northwest, on September 19, the Mw7.1 Puebla-Morelos normal-faulting (57 km depth) event delivered a deadly shock to Mexico City (Singh et al., 2018), where 44 buildings collapsed and 600 were seriously damaged despite its remarkably slow, dissipative rupture (Mirwald et al., 2019). The sequence ended five months later on February 16, 2018, with a Mw7.2 thrust event below Pinotepa Nacional, Oaxaca (hereafter Pinotepa), more than 250 km away from both previous earthquakes, causing damage where similar ruptures have severely harmed local infrastructures in the past. Besides damaging earthquakes, the Mexican subduction zone is prone to very large SSEs and persistent tectonic tremor, especially in the Guerrero and Oaxaca states, which extend along the epicentral regions of the earthquake sequence (Kostoglodov et al., 2003; Radiguet et al., 2012; Villafuerte and Cruz-Atienza, 2017; Graham et al., 2016; Maury et al., 2016; Husker et al., 2019; Maubant et al., 2020). At the time of the Tehuantepec and Puebla-Morelos events, two separate SSEs were taking place in Guerrero and Oaxaca (Husker et al., 2019; Maubant et al., 2020; Cruz-Atienza et al., 2018a). As we will discuss later on, other SSEs also happened in both states in an unusual way during and after the five-month earthquake sequence, featuring a unique story that deserves to be told and understood. In this work we investigate possible interactions between such SSEs and the three devastating earthquakes, and found that most of our observations can be explained as a regional cascade of causally related events through short-term, quasi-static and dynamic interactions that have strongly perturbed the regional SSE cycles in the states of Guerrero and Oaxaca.

5.2 Results

5.2.1 Aseismic Slip History of the Plate Interface

In the Mexican subduction zone, slow surface displacement can be explained in terms of the aseismic slip between the subducted Cocos plate and the overriding North American plate. Such slip can be understood either as SSEs, post-seismic relaxations or plate interface coupling (PIC, i.e., $1 - v/b$, where v is the interplate slip rate, b is the plate convergence rate and $v \leq b$). For imaging the spatial evolution of the aseismic slip in those terms, we inverted continuous displacement records at 57 permanent GPS stations from November 2016 to October 2019, the largest dataset ever analyzed in Mexico, making use of ELADIN, a recently developed and powerful technique (Tago et al., 2021) (Methods, Figure D.1). Careful examination of the GPS time series revealed several transient deformations in the Guerrero and Oaxaca states. Figure 5.2 presents the aseismic-slip inversion results for the whole analyzed period, where we find: (Fig. 5.2A) an almost typical inter-seismic deformation period; (Fig. 5.2B) the 2017 Mw6.9 Guerrero SSE (G-SSE1) that reached shallow interface regions (up to 10 km depth, Figure D.2) and the initiation of the 2017 Oaxaca SSE (O-SSE1) before the onset of the earthquake sequence; (Fig. 5.2B-5.2D) the evolution of the Mw6.9 O-SSE1; (Fig. 5.2E-5.2F) the Mw7.2 post-seismic slip of the Pinotepa earthquake (PE-afterslip) that lasted at least until November 2018, together with a neighboring but separated, 200 km length, Mw6.9 SSE in Guerrero (G-SSE2, second one); and (Fig. 5.2G-5.2H) the concomitant evolution of the 2019 Mw7.0 Guerrero (G-SSE3, third one) and Mw6.9 Oaxaca (O-SSE2, second one) SSEs (Table 5.1). The aseismic slip evolution for all time windows is summarized in Figure 5.3A and integrated in the Supplementary Movie 1, where we display the whole space-time evolution of the events interpolated linearly every 30 days. Considering only the slip areas encompassed by 1 cm contours (Figs. 5.1 and 5.3A), the aseismic moment released during this three-year period is equivalent to a magnitude Mw7.5 earthquake (M0 = 2.32 x 1020 Nw m), where only 31 % of M0 corresponds to the afterslip of the Mw7.2 Pinotepa rupture (Table 5.1).

Figure 5.4 shows the aseismic slip evolution (for events with Mw >6) throughout the period of the earthquake sequence. For the analysis, we separated the slip history in two parts; one before (Fig. 5.4A) and the other after (Fig. 5.4B) the Pinotepa earthquake. The second part includes the previous inverted window as a reference. Panel A (and the GPS time series at the ARIG station in panel B, left) shows that the G-SSE1 basically ended with the occurrence of the devastating Mw8.2 Tehuantepec and Mw7.1 Puebla-Morelos earthquakes. Only a few minor slip patches were imaged in the following three months (Fig. 5.2C). We further see that the O-SSE1, which also initiated months before the earthquakes, developed bilaterally during the five months that followed the sequence initiation. More interestingly, examination of the GPS time series in the southern stations reveals a sudden reversal of the displacement direction from north to south (green circles, left) when the great Tehuantepec event took place. In contrast, northern stations (green circles, right) feature a slow, typical SSE initiation well before, around May-June 2017. The sharp change of the deformation regime in the south suggests that the Tehuantepec earthquake modified the ongoing Oaxaca SSE. The question also arises as to whether the Guerrero and Oaxaca SSEs could have promoted the rupture of the Puebla-Morelos and Pinotepa events, respectively, as proposed

for other earthquakes in Mexico (Radiguet et al., 2016; Graham et al., 2016).

The GPS displacements in panel B show a similar effect over the ongoing Oaxaca SSE to that inferred for the Tehuantepec earthquake, but in this case produced by the Mw7.2 Pinotepa event. While displacements in the eastern stations show either an ongoing or a smooth, spontaneously initiated SSE before this earthquake (green circles, right), some stations to the west exhibit again an abrupt change of displacements from north to south, right when the earthquake happened (green circles, left). All reported SSEs (i.e., three in Guerrero and two in Oaxaca) and the PE-afterslip overlap one another outlining a 650 km long, trench-parallel band of aseismic stress release (Figs. 5.1 and 5.3A). Effects of the earthquakes on the SSE activity or, inversely, of the SSEs on the earthquakesínitiation may have occurred due to static and/or dynamic stress/strain perturbations. In the following we examine these possibilities.

5.2.2 Stress Transfer and Seismicity

Stress transfer to active faults has long been recognized as a preponderant factor in earthquake occurrence (Stein, 1999). Although fault failure depends on the absolute stress level, changes of the Coulomb Failure Stress (CFS) can explain rupture sequences and seismicity-rate variations remarkably well. CFS changes smaller than 50 kPa are often spatially well correlated (above 65 %) with triggered seismicity and significantly larger (one order of magnitude) than values required for triggering slow earthquakes in subduction zones (Nakata et al., 2008).

The 1 cm slip contour of the G-SSE1 stopped about 80 km from the Puebla-Morelos intraslab earthquake hypocenter (Fig. 5.2B). The CFS on the seismogenic fault (i.e., within a 20 km radius from the hypocenter) due to the plate-interface aseismic slip evolution (SSE + PIC) reveals a rise of 35 kPa around the earthquake hypocenter in the 40 days preceding the rupture (Figs. D.3A-D and D.3E, Methods). Albeit this increment is in the upper part of the 10-50 kPa earthquake triggering range commonly referred in the literature (Stein, 1999) and similar to the one believed to have triggered the Mw7.3 (2014) Papanoa earthquake by a SSE in Guerrero (Radiguet et al., 2016), interestingly, it occurred in the late stage of the SSE, when the PIC near the rupture area experienced a recovery certainly affected by the neighboring SSE evolution. This unexpected behavior of the interface coupling during a SSE has also been observed in the last three SSEs in Oaxaca (6), the last one only two months before the recent Huatulco earthquake (Mw7.4) of June 23, 2020, suggesting that an interaction exists between different interface regions experiencing either stress-release or stress build-up. As we will discuss later, the strong shaking produced in the seismogenic fault by the great Tehuantepec earthquake eleven days earlier, could significantly reduce the intraslab fault strength (Delorey et al., 2015; Van Den Abeele et al., 2000) and thus anticipate the Mw7.1 Puebla-Morelos rupture initiation (Johnson and Jia, 2005) driven by the CFS induced by the aseismic slip at the plate interface (i.e., by the SSE and the associated PIC changes) (Fig. 5.3B). To our knowledge, this is the first evidence that an SSE-related process in the plate interface could promote the initiation of a devastating intraslab rupture such as the Puebla-Morelos earthquake.

Five months later, the Mw7.2 Pinotepa thrust earthquake took place at the Cocos-North American plate boundary (Fig. 5.1) while the O-SSE1 was unfolding (Fig. 5.4A). The detailed aseismic slip

and CFS evolution on the plate interface preceding the earthquake is shown in Fig. D.4. Around the hypocentral region there is a clear rise of CFS reaching cumulative values close to 400 kPa (Fig. 5.5A). During the five months following the Mw8.2 Tehuantepec rupture and within a radius of 20 km from the Pinotepa earthquake hypocenter, the CFS experienced a sustained growth of 200 kPa due to the SSE development to the north (Fig. 5.5B). During the same period, GPS inversions show that the interplate slip rate, which always remained in a coupling regime (i.e., smaller than the plate convergence rate), decreased until the initiation of the earthquake (i.e., the PIC increased from 0.1-0.2 up to 0.65). However, the area north of the hypocenter, where the maximum seismic moment was released during the Pinotepa earthquake (between 20 and 30 km depth) (Li et al., 2020), was indeed pervaded by the O-SSE1 with a slip of 1 to 3 cm (Fig. 5.4A). To better elucidate the mechanical process leading to the Pinotepa earthquake nucleation, we carefully analyzed the seismicity in the hypocentral region during the year preceding the event using two complementary template matching techniques (Methods, Figs. 5.5 and 5.6).

Figure 5.5C shows 21-days event counts with magnitude larger than 2.1 and foci within a 30 km radius from the hypocenter. Notice the outstanding spatial correlation between the CFS concentration and the precursor seismicity next to the earthquake hypocenter (inset of Figure 5.5A). Our seismic catalog has 431 % more detections (5,977 earthquakes) than those reported by the Servicio Sismológico Nacional (SSN) above the completeness magnitudes for the same period and hypocentral distance. One clear characteristic stands out from the temporal evolution of our earthquake catalog: seismicity raised steadily after the Mw8.2 Tehuantepec event until the Mw7.2 Pinotepa earthquake, especially during the two previous months (up to 50 % increase), when the O-SSE1 induced the largest CFS increment in the hypocentral region (see also Fig. D.4F).

The increase in CFS, PIC and seismicity rate in the hypocentral region before the Pinotepa earthquake strongly suggests that the dominant mechanism that led to the onset of rupture corresponds to an asperity model; i.e., a heterogeneous initial stress in the source region was loaded at a mesoscale by the development of the SSE to the north until an overloaded nucleation patch, the asperity (e.g., subducted seamount), overcame the plate interface strength. Despite the increasing coupling of the plate interface (and CFS) during the preparedness of the earthquake, seismicity also increased next to the hypocenter. This scenario disfavors the putative widespread idea of a SSE-induced aseismic slip acceleration around the nucleation patch, observed for other large earthquakes (Kato et al., 2012; Ruiz et al., 2014), as the main triggering mechanism for this event (Fig. 5.3B). The small magnitude precursor seismicity reveals small-scale processes that cannot be resolved by our GPS inversions. However, this activity can be explained by a cascading rupture of small, neighboring asperities loaded by the mesoscale effect of the SSE evolution north of the hypocenter.

In addition, except for the large PE-afterslip area and the very east portion of the O-SSE1, static CFS perturbations produced by the earthquake sequence seems not to have had major bearing on the SSE activity as can be appreciated in Figures 5.6B and 5.6D, where positive stress values in most areas of the subsequent SSEs (green contours) are negligible.

5.2.3 Plate Interface Dynamic Perturbations

Abrupt changes in the slow crustal deformation pattern after the Tehuantepec and Pinotepa earthquakes (Fig. 5.4) suggest an effect of both events on the interplate aseismic slip that cannot be explained by static stress transfers, as shown in the last section. However, dynamic stress or strain perturbations produced by seismic waves may have important implications in the elastic properties of fault zone materials (e.g., transient reduction of the bulk modulus) and the slip behavior, especially where slow earthquakes take place (Miyazawa and Mori, 2006; Rubinstein et al., 2009; Wallace et al., 2017; Delorey et al., 2015; Johnson and Jia, 2005; Johnson et al., 2012). For instance, long-period surface waves from the 2010 Mw8.8 Maule earthquake triggered deep tremor in Guerrero and likely reactivated an ongoing SSE (Zigone et al., 2012).

We estimated dynamic perturbations at the plate interface for both earthquakes of the sequence (Methods). Figure 5.6A shows the CFS peak values produced by the Rayleigh waves (25 s period) of the Mw8.2 Tehuantepec event (Figs. D.7 and D.8) beneath strong motion stations in south-central Mexico. Dynamic perturbations around the O-SSE1 region lasted about 80 s and are characterized by three major wave cycles with CFS values ranging between 75 and 200 kPa, and absolute dilations between 1.4-6.0 microstrain (Fig. D.9). Albeit the dynamic triggering of slow earthquakes also depends on the (uncertain) preexistent fault condition, dynamic dilations from the Tehuantepec event are two orders of magnitude larger than those produced in Japan by the great Sumatra-Andaman 2004 earthquake, which triggered widespread tremor in Shikoku and Tokai regions (Miyazawa and Mori, 2006) and CFSs about eight times larger (Miyazawa and Brodsky, 2008). The earthquake triggered tremor in Oaxaca (Husker et al., 2019) and a SSE in the San Andreas fault (Tymofyeyeva et al., 2019), 3,000 km northwest from the source. Since the O-SSE1 initiated before the earthquake and considering that tremor sensitivity increases as the slow slip develops (Houston, 2015), it is plausible that such dynamic perturbations were responsible of the large SSE enhancement and thus of the sudden change of the crustal deformation pattern in the region (Figs. 5.4A and 5.3B).

Given that the Mw7.2 Pinotepa earthquake is a much smaller event that occurred closer to the (presumably) triggered G-SSE2 (Figs. 5.2B), shorter-period body waves could also affect the SSE that was unfolding in Oaxaca at the moment of rupture. Figure 5.6C shows the complete-wavefield CFS maximum values simulated on the plate interface for the earthquake using the DGCrack numerical platform (Tago et al., 2012) (Methods, Fig. D.10). Values range between 100 and 150 kPa within the G-SSE2 slip area, where prestress increments were already above 400 kPa due to the O-SSE1 (Fig. 5.5A), and overcome 400 kPa in the post-seismic slip region downdip from the epicenter. In contrast, the co-seismic static CFS change produced by the earthquake is at least two orders of magnitude smaller in the same SSE region (Fig. 5.6D). This indicates that seismic waves of the Pinotepa earthquake could also be responsible for triggering the second SSE in Guerrero (G-SSE2) and therefore the change in the regional deformation pattern at the time of the event (Figs. 5.4B and 5.3B).

5.2.4 Mechanics of SSEs Dynamic Triggering

To assess whether seismic waves from the Tehuantepec and Pinotepa earthquakes could explain the abrupt changes of the crustal deformation pattern, we conducted numerical simulations of SSEs in the framework of rate-and-state (R&S) friction models subject to the stress dynamic perturbations estimated for both earthquakes. Previous studies with similar methods (Tymofyeyeva et al., 2019; Wei et al., 2018) focused on dynamically triggered SSEs when the perturbation occurs in the inter-SSE period. However, the Tehuantepec and Pinotepa earthquakes happened during the large O-SSE1 (Fig. 5.4), making this a unique opportunity to better understand the mechanics of SSEs when seismic waves from M7+ and larger regional earthquakes perturb them in a tectonic environment where both phenomena are frequent.

Following Wei et al. (2018), we developed a 2D R&S SSE model for the Oaxaca region (Fig. 5.7A) (Methods, Fig. D.11). Figure 5.7C shows the model response to dynamic stresses estimated for the Tehuantepec earthquake at the plate interface under station YOIG, which is located above the O-SSE1 slip area (Fig. 6refFig5.4A and Fig. D.9). Final slip due to the stress perturbation is about twice the value of the reference, spontaneous SSE. Figure 5.7B shows the .[a]seismic slip jumpïnduced by this perturbation, where the propagation speed of the SSE front experiences an abrupt acceleration which, in turn, implies a change of the same order in the surface displacements. The higher the CFS peak value of the perturbation, the larger are both the final slip and the SSE front and slip accelerations. The same happens with the perturbations estimated for the Pinotepa earthquake (Fig. 5.7D). However, despite that peak values over the O-SSE1 region are significantly larger than those induced by Rayleigh waves from the Tehuantepec event (>250 kPa, Fig. 5.6C), they overcome the SSE triggering threshold for a much shorter time (intense phase durations for the Mw8.2 and Mw7.2 events are 75 s and 13 s, respectively). Consequently, the slip increment associated with each wavelet exceeding the threshold is smaller. This is clear in the insets of Figures 5.7C and 5.7D, where the slip rate response and cumulative slip increment due to several waves from the Pinotepa earthquake is comparable to the increment of a single phase of the Tehuantepec event. Therefore, the dominant period of seismic waves also controls its SSE triggering potential and thus the effective fault response (Fig. D.11D).

Since our model considers only along-dip SSEs propagation and the actual slip in Oaxaca and Guerrero migrated predominantly along-strike, it is clear that seismic waves from both earthquakes could produce a much longer SSE evolution than theoretically predicted by our simple model, explaining thus the observed crustal rebounds initiated with both ruptures (Fig. 5.4).

5.3 Discussion

During two years, between June 2017 and July 2019, in addition to the devastating earthquake sequence, five large SSEs (Mw >6.9) occurred in southcentral Mexico over a trench-parallel continuous band of 650 km in length with a cumulative moment magnitude Mw7.4 (Figs. 5.1 and 5.3A, Table 5.1). Three of them in Guerrero, and the other two in Oaxaca interspersed by the Pinotepa earthquake post-seismic slip with Mw7.2 (Fig. 5.3B). Among all aseismic events, only the 2017 Guerrero

and Oaxaca SSEs (G-SSE1 and O-SSE1) initiated before the earthquake sequence, so that 87 % of the total aseismic moment was released during the 1.7 years following the great Mw8.2 Tehuantepec rupture, when the earthquake sequence started. Although the three Guerrero SSEs nucleated in different regions (Fig. 5.2), all of them overlap downdip of the Northwest Guerrero seismic gap with a slip larger than 5 cm each (Figs. 5.1, 5.3 and Fig. D.2). Unlike the last 20 years, during which all SSEs occurred every 4 years in Guerrero (six events between 1998 and 2017) (Radiguet et al., 2016), the last two events reported here had much smaller recurrence periods, of 0.25 and 0.5 years for the G-SSE2 and G-SSE3, respectively. Figure 5.8 shows a detailed comparison of displacement time series at different GPS sites in Guerrero, including the longest record in Mexico, from CAYA station, since 1997. A simple inspection of that record reveals the clear disruption of the SSE cycle in that province after the Mw8.2 Tehuantepec event.

Something unusual also happened in Oaxaca; the plate interface slipped (aseismically) continuously for the whole two years period with at least two reactivations, one during the post-seismic relaxation of the Mw7.2 Pinotepa earthquake, and the other one around December 2018, when the O-SSE2 initiated. Figure 5.8 further shows the long record at PINO station, where we appreciate how the return period of SSEs in Oaxaca was also reduced after the Mw8.2 earthquake. This is clear when comparing the 8 months between O-SSE2 and O-SSE3, the later event (not studied here) starting two months before the Mw7.4 Huatulco earthquake of June 23, 2020 (Chapter 6), and the 1.5 years that typically elapse between the silent events in Oaxaca (Graham et al., 2016). It is worth mentioning that despite the data scarcity at PINO station between 2007 and 2012, the SSEs indicated in the figure (vertical blue bars) are exactly those documented for Oaxaca in the literature (Graham et al., 2016). M7+ events similar to the Pinotepa earthquake had occurred in Oaxaca and Guerrero (Radiguet et al., 2016; Graham et al., 2016), but none were followed by an SSE during their post-seismic relaxation (i.e., only nine months later). After the Mw7.5 Ometepec earthquake of March 2012, for example, the next SSE took place almost two years later and once the interseismic deformation regime had already recovered (Fig. 5.8). All these observations strongly suggest that, in addition to the dynamic effect of the seismic waves from the Tehuantepec and Pinotepa earthquakes on the dynamics of the ongoing SSEs, the elastic and frictional properties of the plate interface across the entire Mexican subduction zone underwent a change due to the extremely large, unprecedented ground shaking on September 8, 2017.

When seismic waves exceed a certain strain threshold, fault gouge materials undergo abnormal non-linear elastic changes that can bring them to a metastable state facilitating the initiation of earthquake and SSEs (Delorey et al., 2015; Johnson and Jia, 2005; Johnson et al., 2012). Transient changes in both the elastic properties of the crust and the regional seismicity rate have been observed after local and regional earthquakes (Delorey et al., 2015; Brenguier et al., 2008). The greater the damage in the fault core and the lower its effective pressure (e.g., in presence of overpressured fluids), then the non-linear effects of seismic waves will produce a greater drop of the elastic modulus of granular fault gouges (i.e., a material modulus softening triggered from a lower strain threshold) assisting the unstable interplate slip initiation (Van Den Abeele et al., 2000; Johnson and Jia, 2005). Although these effects have not yet been observed at the scale of the fault-zone in subduction zones, large seismic waves can affect the continental crust down to its root for several years (Wang et al., 2019). It is thus reasonable that the Mw8.2 Tehuantepec earthquake is responsible for the

extraordinary disruption of the SSE cycle observed at the regional scale, and even for facilitating the dynamic triggering of the SSEs that we report here. The same hypothesis is valid for the Puebla-Morelos and Pinotepa earthquakes, triggered by the 2017 Guerrero and Oaxaca SSEs (G-SSE1 and O-SSE1), respectively, where the loss of rigidity on both seismogenic fault zones could occur on September 8 (2017) assisting their rupture initiation (Johnson and Jia, 2005).

As recently discussed by an international community of earthquake modelers (Dunham et al., 2020), this anomalous non-linear behavior of fault-gouge materials should have important implications in friction that are not yet incorporated into R&S fault models. A fault constitutive model that integrates the state laws of both the contact surface and the damaged zone volume subject to these non-linear effects under pressurized fluid conditions, could better explain the interaction between different kinds of dynamic slip instabilities (slow and rapid) and even the sudden regional disruption of the SSE cycles, discussed in this study, after the great Tehuantepec earthquake.

Figure 5.2 and Supplementary Movie 1 clearly show how the interface coupling, PIC, continuously changes over time. Recent laboratory experiments and theoretical fault models strongly suggest that friction is a (very) sensitive function of the interplate slip-rate where SSEs occur (Im et al., 2020; Ikari and Saffer, 2011). Slow-slip dynamic instabilities therefore depend on the velocity field discontinuity at the interface, which is zero only where both plates are completely locked (i.e., in seldom cases). Large temporal variations of the blue areas in Figure 5.2 imply large changes in the slip-rate (below the plate convergence velocity), which must therefore have significant implications in the stability of the megathrust not only because of their frictional counterparts, but also due to the associated stress changes as recently observed in the hypocentral region of the 2020 Mw7.4 Huatulco earthquake in Oaxaca as we will see in the next chapter.

Continuous monitoring of both the deformation and the seismic properties of the crust is therefore essential to evaluate the possibility of large earthquakes in the future and to have a clearer idea of the temporal evolution of seismic hazard in subduction zones.

5.4 Methods

5.4.1 Elastostatic adjoint inversion

The method used to invert the GPS time series, ELADIN (ELastostatic ADjoint INversion) (Tago et al., 2021), simultaneously determines the distribution of coupling and SSEs in the plate interface to explain the surface displacements. To this purpose, the method solves a constrained optimization problem based on the adjoint elastostatic equations with Tikhonov regularization terms, a von Karman autocorrelation function and a Gradient Projection method to guarantee physically-consistent slip restrictions. The main parameters governing the inversions are the correlation length of the von Karman function, L, which controls the wavenumber content of the solution, and the precision matrix, which weights the data according to its confidence. We assumed a von Karman Hurst exponent of 0.75 and L = 40 km. Comprehensive resolution tests show that, given the problem geometry (i.e., the 3D plate interface and the available stations, Fig. 5.1), these values maximize the restitution

index for slip patches larger than 80 km length and minimize the data misfit error in the whole plate interface (Tago et al., 2021).

Although GPS data has been carefully processed to generate the displacement time series (see next section), there always remain trailing errors and physical signals that do not correspond to tectonic processes (Fig. D.1). The precision matrix allows to minimize the effect of such noise in the inversion results and corresponds to the inverse of the data variance per station and time window. To do this, especially in the vertical component, numerous synthetic and real data inversions lead us to adjust the precision matrix (i.e., the data weights) to ensure that, at least, polarities of the vertical-displacement are well explained by the inverted models, while maintaining the best horizontal-displacement fits (Tago et al., 2021). The data variance for each component and time window is computed from the differences between daily displacement values and a moving, locally weighted LOESS function (i.e., 2nd order polynomial regressions with a half-window time support).

For the inversions we removed the coseismic displacements produced by the three large earthquakes and improved the 3D plate interface geometry introduced by Radiguet et al. (2016) based on the work of Ferrari et al. (2012)., which compiles relocated seismicity, receiver functions and tomography studies in southern Mexico. We refined the final geometry beneath Oaxaca based on recent magneto-telluric and receiver function analysis (Arzate-Flores et al., 2016; Rodríguez-Domínguez et al., 2019) (Fig. 5.1) and assumed a suitable 1D four-layer regional structure (Campillo et al., 1996). The slip vector is decomposed in the plate-convergence (pc) and pc-perpendicular directions, which vary along the plate interface (DeMets et al., 2010). Restrictions were imposed to meet reasonable plate coupling constraints (i.e., backslip smaller than the cumulative plate motion in the associated time window) and moderate pc-perpendicular slip by means of an iterative Gradient Projection method (Tago et al., 2021)., so that the slip rake could only vary 30 degrees with respect to the plate convergence direction.

5.4.2 GPS data processing

We used continuous records in 57 permanent GPS stations spread across central Mexico (Fig. 5.1). The stations belong to three different networks: the Mexico-Japan SATREPS-UNAM project (Cruz-Atienza et al., 2018a), the National Seismological Service (SSN-UNAM) and Tlalocnet (Cabral-Cano et al., 2018). GPS data was processed using two different methods: Gipsy 6.4 (Lagler et al., 2013) and Gamit/Globk 10.7 (Herring et al., 2010). For the period between October 23 (2016) to November 22 (2018), after carefully comparing both displacement time series in all stations, we selected those with better signal to noise ratio and consistency with nearby stations (Fig. D.1A). For the period from November 22 (2018) to October 8 (2019), we only considered selected time series calculated using Gipsy 6.4 (Fig. D.1B).

The GIPSY displacement time series are estimated with a Precise Point Positioning strategy. The station positions are defined in the International Terrestrial Reference Frame, year 2014 (ITRF 2014). For daily processing we used the Jet Propulsion Laboratory final and non-fiducial products (orbits and clocks). We generated observables using 2 model categories: (1) Earth models and (2) observation models. The Earth models include tidal effects (i.e., solid tides, ocean loading and tide

created by polar motion), Earth rotation (UT1), polar motion, nutation and precession. Observation models, on the other hand, are related with phase center offsets, tropospheric effects and timing errors (i.e., relativistic effects). The troposphere delay is estimated like a random walk process. This effect is broken into wet and dry components. The azimuthal gradient and the dry component are estimated using GPT2 model and mapping function (TGIPSY1). The antennas phase center variations are considered through antenna calibration files. For receiver antennas, the correction is estimated taking the International GNSS Service (IGS) Antex file. We also applied a wide-lane phase bias to account for the ambiguity resolution and removed outliers.

The GAMIT displacement time series are estimated using a double difference method that calculates the between-station and satellites differences. It reduces satellite clock and orbit errors, localized atmospheric errors and cancels the effects of variations in the receiver clocks. The software incorporates final IGS (International GNSS Service) combination solutions for orbits (with accuracies of 1-2 cm) and Earth Orientation Parameters (EOP). Ionospheric and atmospheric corrections were applied during processing. Hydrostatic and water vapor delay are corrected using Vienna Mapping Functions (VMF). Solid Earth tide model (IERS03), ocean tidal loading (FES2004), tables for earth rotation values (nutation IAU2000, polar motion, universal time) and precession constant IAU76 are applied. The resulting GPS time series are calculated in the ITRF 2014 reference frame and then rotated with respect to the fixed North American plate using the rotation pole. Post-processing of daily position time series includes offset corrections and outlier removal that was performed with the help of python-based PYACS package developed by J.-M. Nocquet. Despite integrating all these considerations in the GPS data processing, it is important to notice that the remaining noise may be significant, as it has been recently analyzed in great detail in Guerrero (Maubant et al., 2020).

5.4.3 Template-matching seismicity analysis

To detect unreported seismicity within the Mw7.2 Pinotepa earthquake hypocentral region previous to the event, we applied two independent and complementary template matching (TM) techniques. In both cases, the waveform templates were earthquakes reported by the SSN with foci within 30 km from the Pinotepa earthquake hypocenter (Lat: 16.218°, Lon: -98.014°, 16 km depth). We used continuous velocity records in three broadband stations with epicentral distance smaller than 115 km during a one-year period preceding the earthquake, from March 1, 2017, to February 16, 2018 23:39 (UTC time of the Mw7.2 earthquake). The first technique (Liu et al., 2020) considers three permanent stations (PNIG, YOIG, TXIG) from the SSN network located in the state of Oaxaca (Fig. D.5A). We used a set of 394 events (templates) (previously identified as repeating earthquakes) reported in the SSN catalog and applied a bandpass Butterworth filter with corner frequencies of 1-8 Hz to reduce the noise, and to remove undesired regional and teleseismic events. For each template, we selected a cross-correlation window starting 1 seconds before the arrival of the S-wave and ending 5 seconds after, only one detection is allowed every 25 seconds (approximately the time needed for the P and S waves of an event to be recorded at all three stations, see Figure D.5C) to avoid duplicates of the same event. A detection was confirmed when the stacked correlation coefficient (scc) in the three stations (nine channels) was larger than 0.41 and the median average deviation larger than 25 (Fig. D.5C). These two values guarantee the best trade-off, with the highest number

of detections and the lowest number of false positives. To this end we performed a grid search in a plane of 4.5 km x 4.5 km around each template location (Fig. D.5A) and looked for the maximum spatial correlation coefficient value. For preventing detectability variations, we only processed those days with data for all components in the three stations. The second technique considers only the waveforms on the three channels of the station PNIG, the closest site to the earthquake epicenter (21 km, Fig. D.5B). For generating the templates, we selected 4,105 events from the catalog reported by the SSN in the period between March 1, 2017 and March 31, 2018. The waveforms were cut 0.2 seconds before the P-phase arrival and 0.5 seconds after the S-phase arrival, and filtered using a zero-phase Butterworth bandpass filter with corner frequencies at 3 Hz and 12 Hz. The template matching was performed using the Python package EQcorrscan (Chamberlain et al., 2018) and the detection threshold was set to 0.9 of the average cross-correlation value in the three channels, which guarantees not only that the detections come from the same place as the templates, but also that our local catalog do not include any false-positives. Single-station detections have proved to be a powerful tool to find earthquakes that are small and located close to certain stations, but that get too attenuated to be detected at farther stations given high cross-correlation thresholds (Garza Giron et al., 2020). Furthermore, a visual inspection of hundreds of waveforms helped us verify that the timing and the relative amplitudes of the ballistic P and S waves in the three components are very similar to the parent templates, guaranteeing that the detected signals are, indeed, earthquakes that share a common hypocentral location as the template events (Fig. D.5D). For this second matched filter technique we allow inter-event times to be greater or equal to 10 seconds, keeping only the best correlated detections. To assign a common magnitude to all detections, ML, we determined an attenuation relationship specific to PNIG using the LocMagInv code (Garza Giron et al., 2020) (Fig. D.6A). Instead of inverting for the magnitudes, we used the cataloged magnitudes from the SSN for events with SNR greater or equal to 5 and inverted only for the geometric spread, attenuation and station correction parameters from horizontal displacement records (mm) (i.e., their arithmetic mean). To obtain the displacements, we integrated velocity records in the bandwidth 3-12 Hz. We only used the available horizontal components for each event. We detected 3,156 events with the first technique (Fig. D.5A) and 5,064 with the second (Fig. D.5B), which represent a 180 % and 350 % detection increase, respectively, as compared with the 1,125 earthquakes reported by the SSN in the same period and within a 30 km hypocentral radius. Detections from both techniques were integrated into a single catalog avoiding duplicate events (Fig. 5.5D).Figure D.6C shows the frequency-magnitude histograms for both, our TM detections and the SSN catalog, where the cutoff completeness ML magnitudes correspond to 2.1, 2.4 and 3.2, for local detections (method two), regional detections (method one) and the SSE catalog, respectively. Since TM method one uses nine seismic channels (i.e., the three components of three stations) at a regional scale, its detections very likely correspond to events with hypocentral locations close to those of the templates that lie, all of them, within 30 km from the Pinotepa earthquake hypocenter. Thus, we used these detections for relatively large events to check how well method two, which only considers local records at PNIG (i.e., the three component), detected earthquakes within such hypocentral vicinity. Figure D.6D show a Venn diagram for all catalogs where we see that 72 % of regional detections were also found using only local records.

5.4.4 Dynamic Perturbations at the Plate Interface

From Strong Motion Records: For the Mw8.2 Tehuantepec event we used radial and vertical displacement records at 25 s period from strong motion stations in south-central Mexico (Fig. 5.5A and Fig. D.8C) to estimate the strain field produced by the Rayleigh waves fundamental mode at depth, and then the associated CFS (apparent friction coefficient of 0.5) over the 3D plate interface in the plate-convergence slip direction (Fig. D.9A). Values in Fig. 5.6A at sites without interface below correspond to a horizontal surface at 50 km depth. To estimate the surface-wave dynamic deformations (and tractions) at depth from observed ground displacements (i.e. double integration of single-station strong motion records) we followed a two-fold procedure: First, we estimated the displacement at depth (i.e., at the plate interface below each site, Fig. 5.6A) by modulating the field with the associated surface waves eigenfunctions for the chosen period within a four-layer regional model determined from the dispersion of surface waves (Campillo et al., 1996) (Fig. D.8D). Then, to estimate the whole strain tensor, we computed the horizontal deformations assuming a phase velocity of 3.5 km/s (Miyazawa and Brodsky, 2008), and the vertical deformations by deriving the eigenfunctions in that direction. Although Love waves can also have SSE triggering potential, in the analysis we only considered perturbations from Rayleigh waves, whose amplitudes differ from those of Love waves by less than a factor of two at distances where the O-SSE1 was developing when the Mw8.2 earthquake took place (420-520 km, Figure D.7), indicating that the stress perturbations at the interface induced by the two types of waves should not differ significantly. Figure D.9 shows, for the Mw8.2 Tehuantepec earthquake, the traction vector and CFS time series on the 3D plate interface along the plate-convergence slip-rate direction and dilation time series below some selected sites. To validate our procedure, we compared estimated (with our method) synthetic tractions with the exact solution for the Lamb's problem (i.e., for the wavefield excited by a single vertical force on top of a homogenous halfspace) at depth over a horizontal plane (Figs. D.8A and D.8B). The elastic properties of the medium are V_p = 5.6 km/s, V_p= 3.233 km/s, ρ = 2700 kg/m3, the surface station lies 300 km away from the source and the buried point is 20 km below the station. In this example, tractions were estimated for 10 s period. However similar, satisfactory results were obtained for different periods and depths. From 3D Numerical Simulations: To estimate the Mw7.2 Pinotepa earthquake (complete-wavefield) dynamic perturbations at the plate interface we performed a 3D kinematic-source numerical simulation by means of an hp-adaptive discontinuous Galerkin finite-element method (DGCrack) (Tago et al., 2012). The domain is discretized with a non-structured tetrahedral mesh considering a 3D crustal velocity model of the Guerrero-Oaxaca subduction zone (Spica et al., 2016) that incorporates the real topography and bathymetry, as well as the geometry of the plate interface (Fig. D.10A). The mesh size is 900 x 380 x 104 km in the along-trench, trench-perpendicular and vertical directions, respectively, with approximately 11 million elements to achieve a numerical accuracy up to 1 Hz. We run DGCrack in 512 cores on the UNAM supercomputer platform Miztli to complete 260 seconds of numerical simulation spending 12.5 hours of total computer elapsed time. To simulate the finite source, we first used the low-wavenumber slip solution of the Pinotepa earthquake estimated by the USGS (Fig. D.10B-up). Then, we discretized this solution into subfaults of 1 x 1 km and add high-wavenumber slip perturbations that are stochastically generated using a von Karman power spectral density (PSD) function to enhance the radiation of high frequencies following the methodology of Pulido et al. (2015) (Fig. D.10B-down).

The slip-rate of every subfault follows a regularized Yoffe function and the rupture evolution is described by the spatial distribution of the slip, rise time, rupture velocity and peak time (i.e., the time to reach the peak slip-rate in every subfault) (Fig. D.10C). These kinematic source parameters are heterogeneously distributed by means of a pseudo-dynamic rupture generator that considers the 1-point and 2-point statistics of each source parameter as well as their spatial interdependency extracted from dynamic rupture simulations. We validate the earthquake simulation by comparing the horizontal geometric mean of the observed and synthetic peak ground velocities (PGV) in different hard-site strong motion stations (Fig. D.10D). Since the resolution of the GPS time series does not allow distinguishing whether the Tehuantepec or Puebla-Morelos earthquakes (only eleven days in between them) produced the abrupt change of the crustal deformation pattern observed in Fig. 5.4A, we also estimated the dynamic perturbations on the plate interface due to the intraslab, normal-faulting, Mw7.1 Puebla-Morelos event using the same numerical procedure but taking a finite-source solution determined from the inversion of strong motions (Mirwald et al., 2019). Results are shown in Figure D.3F, where we appreciate that CFS peak values in the O-SSE1 region (apparent friction coefficient of 0.5) are smaller than those induced by the Tehuantepec earthquake (Fig. 5.6A) (i.e., <60 kPa). Considering also that the duration of intense shaking by the Mw7.1 is much shorter than that produced by the Mw8.2 Tehuantepec event (i.e. its SSE triggering potential is lower, Fig. D.11D) and that tremor activity in Oaxaca highly increased a few hours after the Tehuantepec earthquake (Husker et al., 2019), then we conclude that triggering of the O-SSE1 was produced by seismic waves from the Mw8.2 event.

5.4.5 Rate and State Friction SSE Model

Assuming a 6 cm yr-1 plate convergence (DeMets et al., 2010), we developed a R&S fault reference model for the Oaxaca region that spontaneously generates SSEs every 1.5 years with maximum slip of 10 cm (Fig. D.11C), which is a reasonable approximation of the SSE activity in that province (Graham et al., 2016). The model assumes a planar fault dipping 13 degrees in a 2D elastic half-space (Fig. 5.6A and Fig. D.11A). Following (Wei et al., 2018) and based on the SSEs slip distributions (Figs. 5.2C and 5.3A), the model is consisted of a velocity-weakening (VW) fault segment between 20 and 45 km depth where SSEs take place encompassed by stable, velocity-strengthening (VS) layers (Fig. D.11B). Uniform, dynamic stress perturbations from the 2017 Mw8.2 Tehuantepec earthquake and the 2018 Mw7.2 Pinotepa earthquake were inputted around the middle stage of a spontaneously initiated SSE at all depth with different scaling factors (Fig. 5.7) to consider the variations and uncertainties of both, the reference model and the CFS estimates throughout the SSE region.

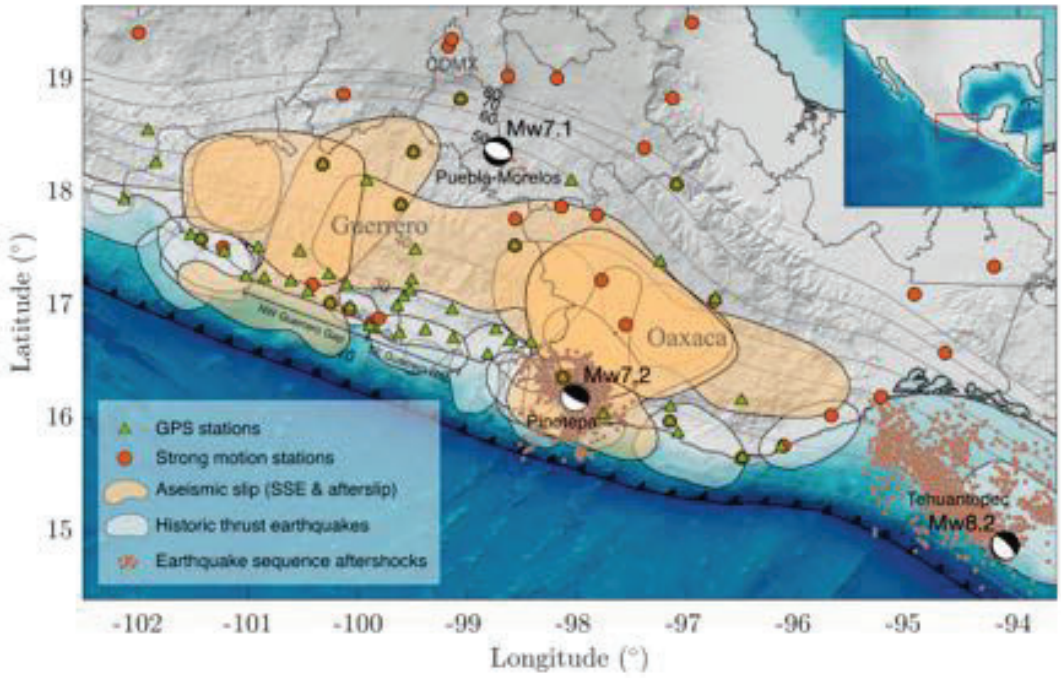

Figure 5.1. Study region and regional instrumentation around the Tehuantepec (Mw8.2), Puebla-Morelos (Mw7.1) and Pinotepa (Mw7.2) earthquake sequence. Orange shaded areas depict the 1 cm aseismic slip contours imaged between June 2017 and July 2019 in the plate interface. Green triangles and orange circles indicate GPS and strong motion sites, respectively. White shaded areas delineate rupture zones of historic thrust earthquakes. Orange dots show the 10-days aftershock sequences as reported by the SSN except for the Mw7.1 earthquake, for which three-months aftershocks are reported. Gray contours show iso-depths (in kilometers) of the 3D plate interface.

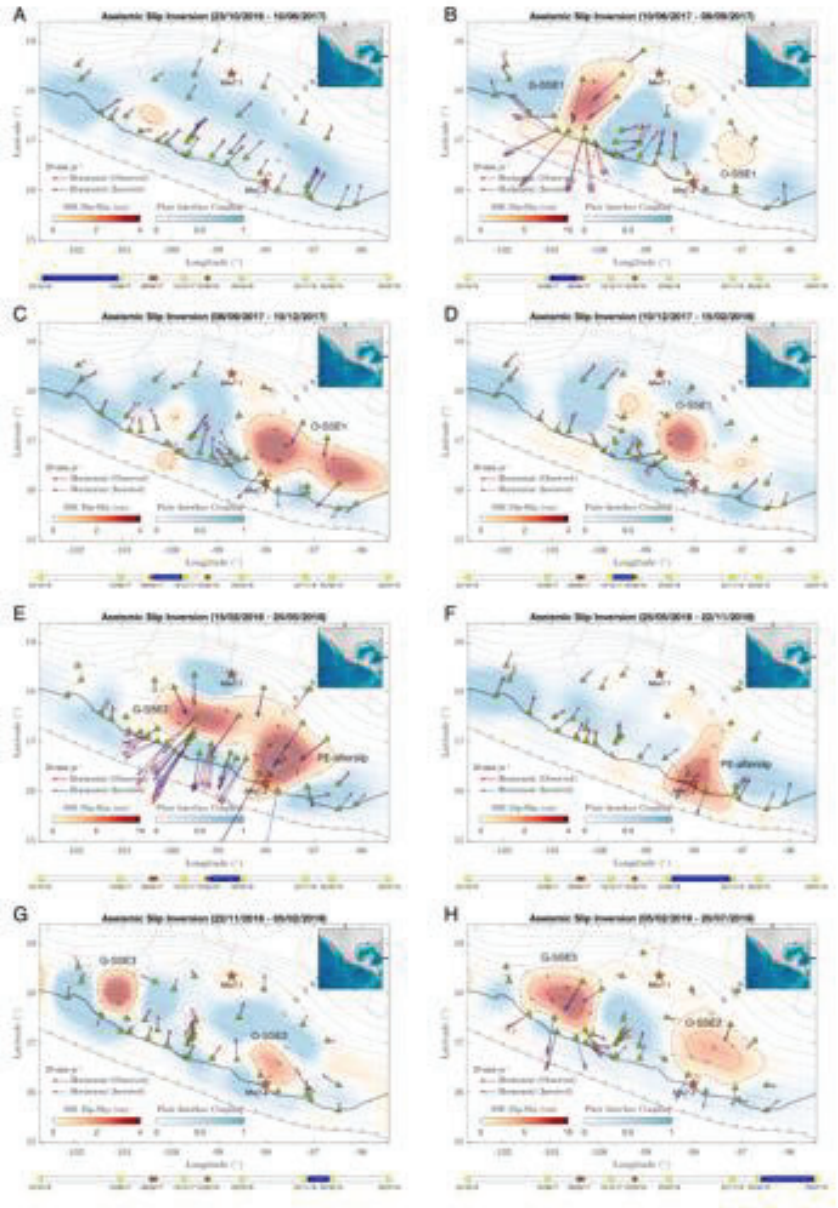

Figure 5.2. Aseismic slip inversions for the whole analyzed period across and after the earthquake sequence (see also Figure 5.3 and Supplementary Movie 1). We find (A) an almost typical interseismic deformation period; (B) the 2017 Guerrero SSE (G-SSE1) and the initiation of the 2017 Oaxaca SSE (O-SSE1); (B-D) the evolution of the O-SSE1; (E-F) the post-seismic slip of the Mw7.2 Pinotepa earthquake (PE-afterslip) together with a neighboring but separated SSE in Guerrero (G-SSE2, second one); and (G-H) the concomitant evolution of the 2019 Guerrero (G-SSE3, third one) and Oaxaca (O-SSE2, second one) SSEs (see Table 5.1). Dashed slip contours are in centimeters. Yellow circles encompassing the blue bar at the bottom of each panel indicate the dates of the associated inverted window, and red small stars, the Mw8.2 Tehuantepec, Mw7.1 Puebla-Morelos and Mw7.2 Pinotepa earthquakes timing, respectively, from left to right. Red and blue arrows show the observed and synthetic surface horizontal displacements, and the gray ellipses one standard deviation of the corresponding GPS data window.

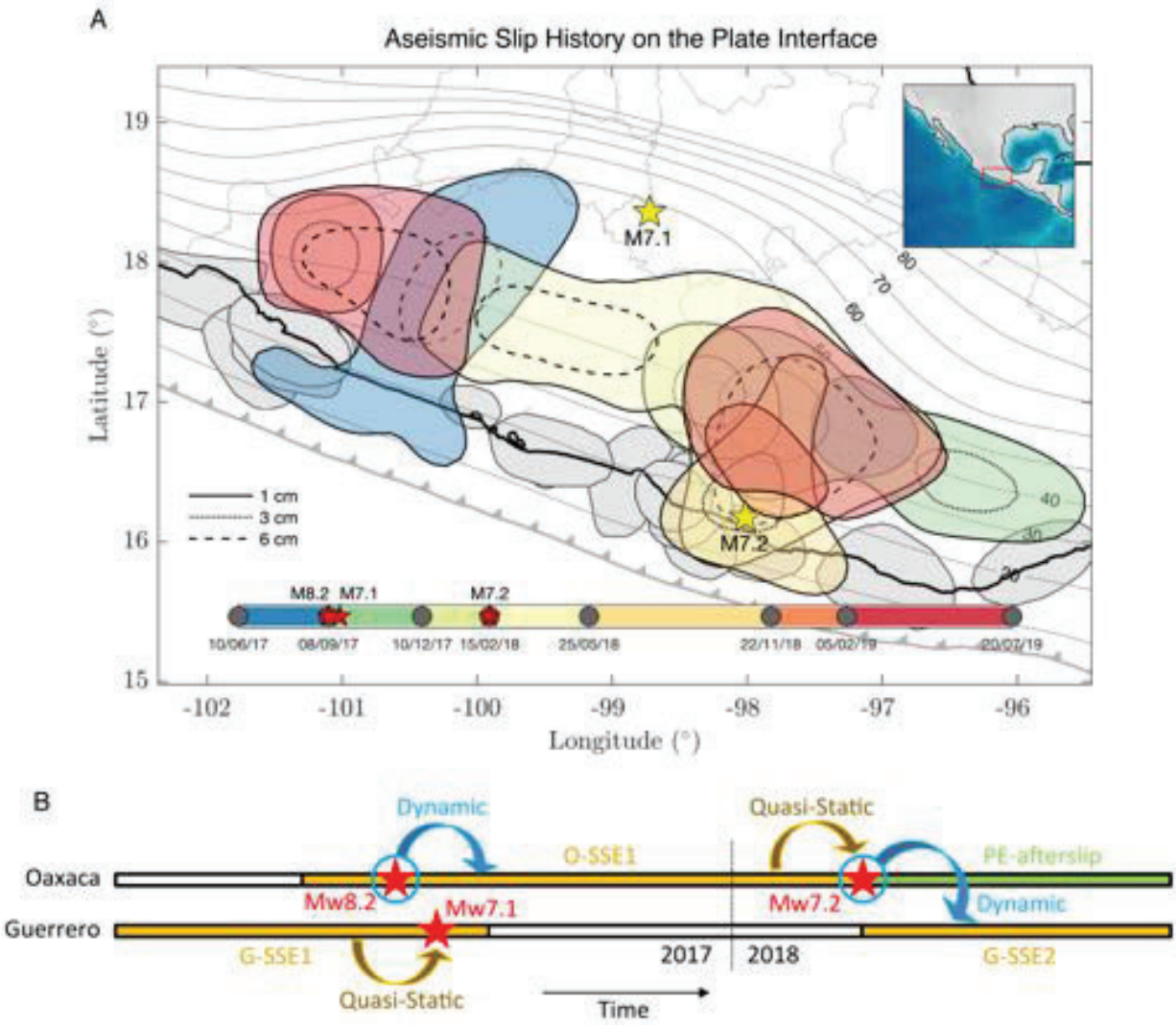

Figure 5.3. Evolution of the aseismic slip at the plate interface and types of interaction between the different events. (A) Colored patches are those of Figure 5.1 but indicating the timespan of each aseismic slip event (see colorbar). Slip contours are those reported in Figure 5.2 and gray contours show iso-depths (in kilometers) of the 3D plate interface. (B) Sketch showing the evolution of events across the earthquake sequence and the nature of the interaction between them in both states, Guerrero and Oaxaca, either dynamic or quasi-static. Evolution of the aseismic slip at the plate interface and types of interaction between the different events. (A) Colored patches are those of Figure 1 but indicating the timespan of each aseismic slip event (see colorbar). Slip contours are those reported in Figure 5.2 and gray contours show iso-depths (in kilometers) of the 3D plate interface. (B) Sketch showing the evolution of events across the earthquake sequence and the nature of the interaction between them in both states, Guerrero and Oaxaca, either dynamic or quasi-static.

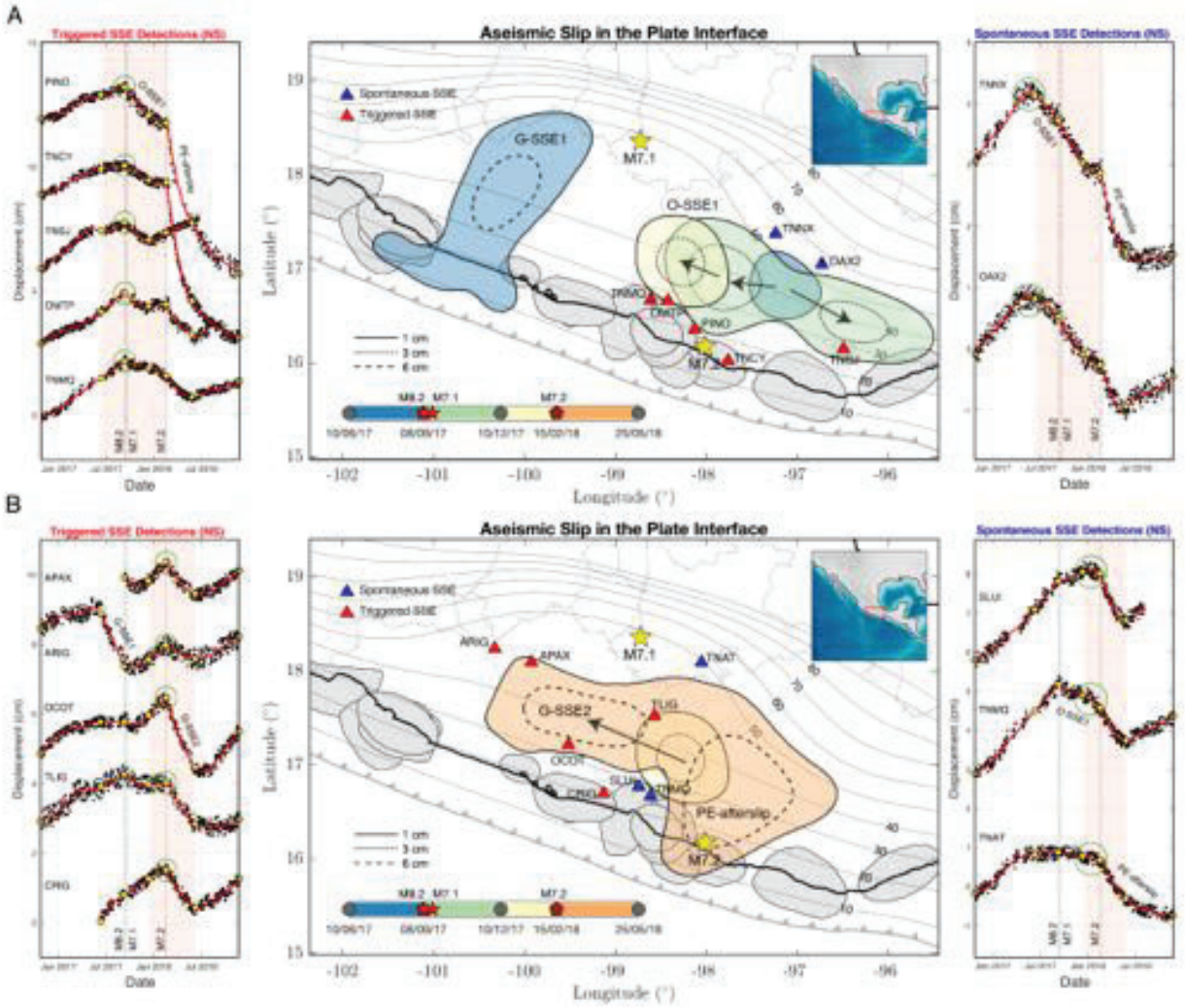

Figure 5.4. Evolution of the plate interface aseismic slip (SSEs and post-slip) during the earthquake sequence (separated in two parts) and representative GPS timeseries (north-south components). The first part before the M7.2 Pinotepa earthquake (A) and the other after the earthquake (B). Pink shaded rectangles encompass the GPS inverted windows (yellow dots) shown in the central maps for each panel. Blue triangles show GPS stations where we observe spontaneously initiated or preexistent SSEs (right panels, green circles), while red triangles show the stations where we observe triggered SSEs (left panels, green circles). Notice the abrupt reversal of the deformation pattern in the left panels (from north to south, green circles) right at the moment of the Mw8.2 Tehuantepec and Mw7.2 Pinotepa earthquakes. Gray contours show iso-depths (in kilometers) of the 3D plate interface.

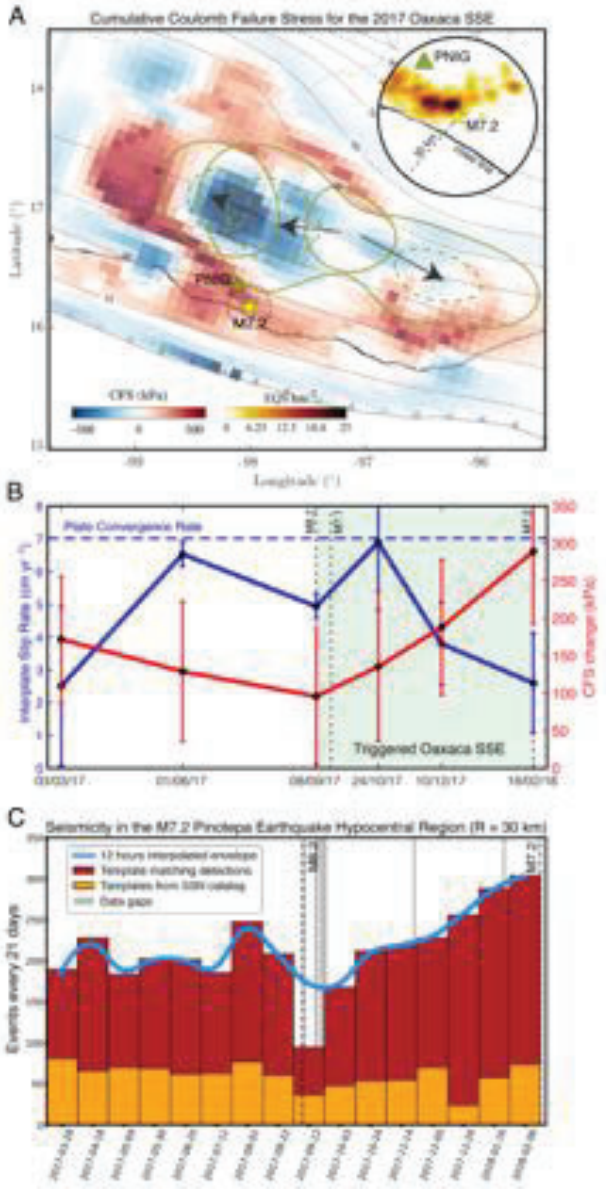

Figure 5.5. Coulomb Failure Stress (CFS), Plate Interface Coupling (PIC) and seismicity rate evolution before the Pinotepa earthquakes in the vicinity of its hypocenter. (A) 15-month cumulative CFS on the plate interface and spatial evolution of the O-SSE1 (1 cm slip solid contours and 3 cm slip dashed contours). Density of the template matching earthquake detections (i.e., of the precursor seismicity) (inset). Gray contours show iso-depths (in kilometers) of the 3D plate interface. (B) Temporal evolution of the CFS change and the interplate slip rate averaged within a 20 km radius from the Pinotepa earthquake hypocenter (dotted circle, panel A) along with the associated standard deviations (vertical bars). See also Supplementary Figure 5.4. (C) Seismicity rate evolution for template matched events (M >2.1) within 30 km from the Pinotepa earthquake hypocenter (see Figures D.5 and D.6).

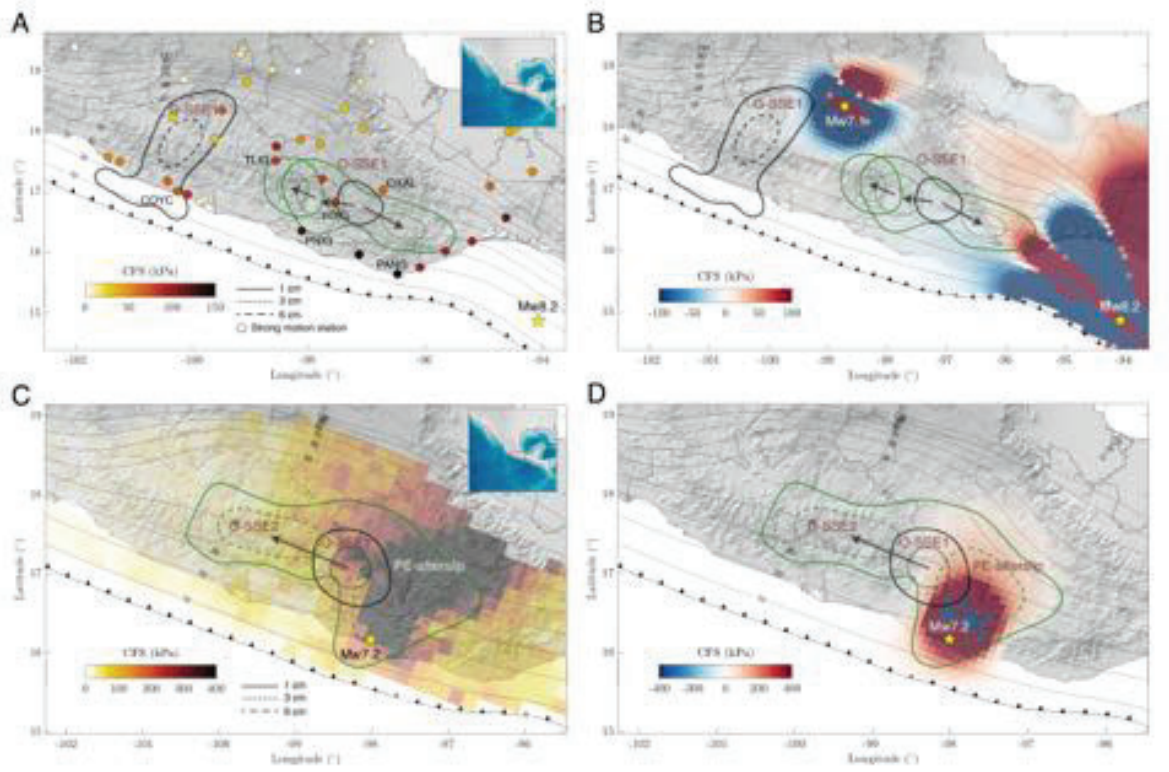

Figure 5.6. Dynamic (peak values) and static Coulomb Failure Stresses (CFS) on the 3D plate interface (gray contours in kilometers) produced by the Mw8.2 Tehuantepec (A and B, respectively) and Mw7.2 Pinotepa (C and D, respectively) earthquakes in the plate convergence direction for a friction coefficient of 0.5. Aseismic slip events right before the corresponding earthquake are shown with black contours, while those occurred immediately after the earthquake are shown with green contours. Dynamic stresses for the Tehuantepec event (A) where computed from actual strong motion records at different sites (colored circles, see Figure D.9A). Estimates for the Pinotepa event (C) where computed through a 3D finite-source numerical simulation of the earthquake (see Figure D.10).

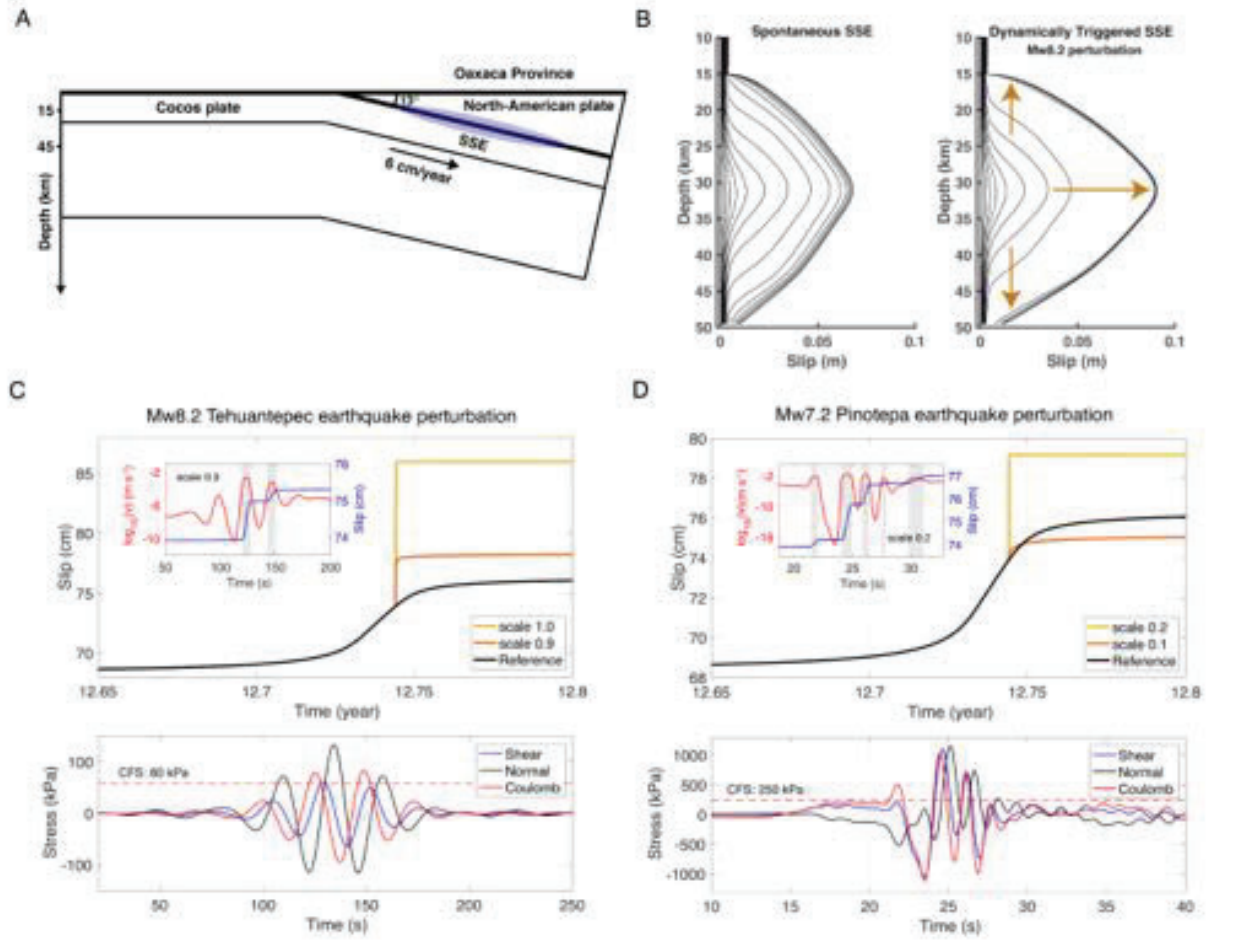

Figure 5.7. Rate-and-state fault models for SSE triggering by seismic-wave stress perturbations. (A) Synoptic 2D model of the subduction zone in the study area. (B) Slip evolution of a spontaneous SSE and a dynamically triggered SSE in the R&S friction model subject to the stress perturbations estimated under the YOIG station due to the Mw8.2 Tehuantepec earthquake (Fig. 5.6A and Fig. D.9). The contours time increment is about 2 days. (C) Top, slip evolution of the SSE reference model and two triggered events at 31 km depth for stress perturbations due to the Mw8.2 Tehuantepec earthquake with different scaling factors. The inset shows the slip velocity and slip at that depth with 0.9 scaled perturbation. Bottom, unscaled stress perturbation used in these simulations. (D) Same as (C) but for the Mw7.2 Pinotepa earthquake. Please note that the scaling factors are different.

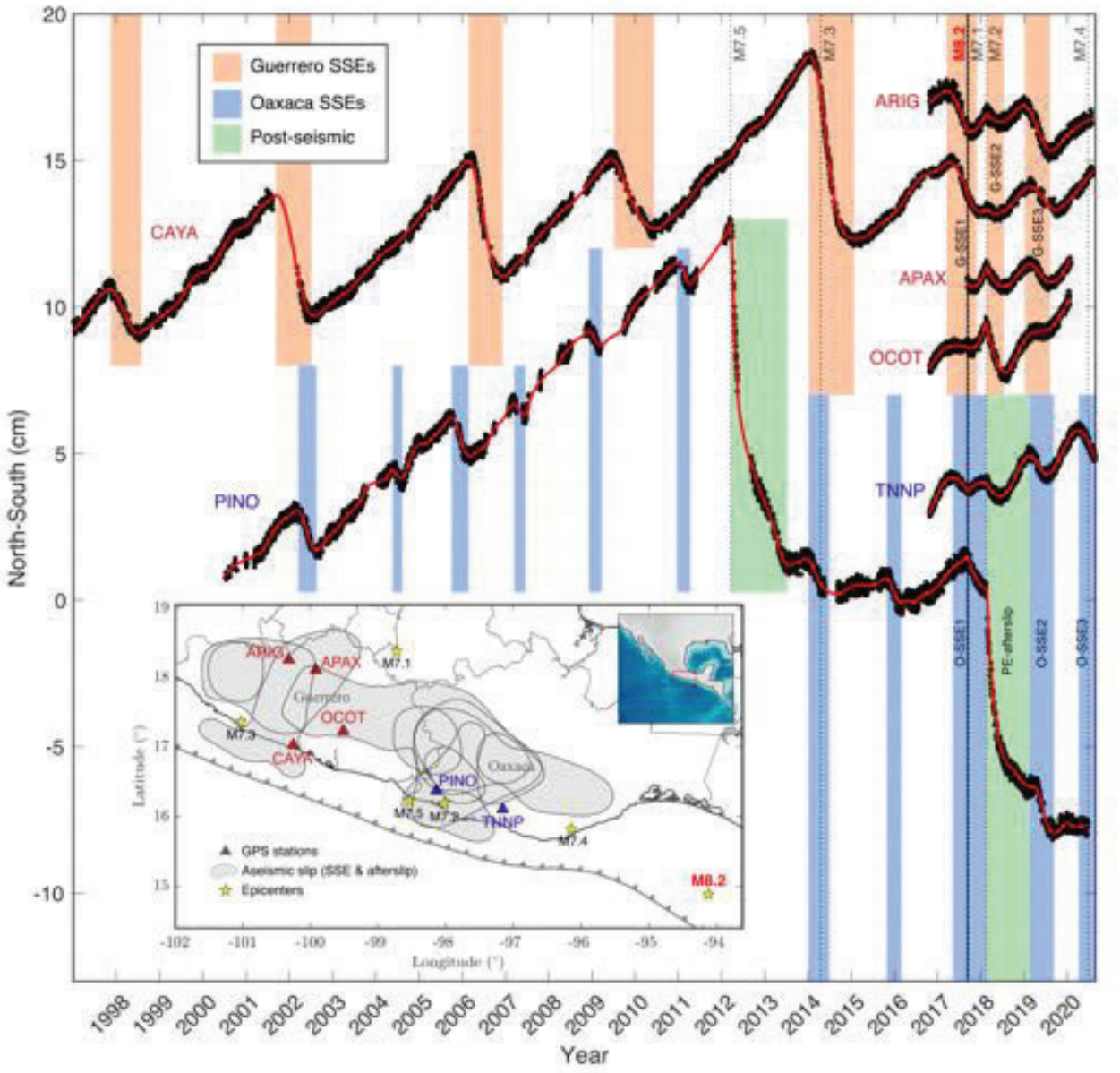

Figure 5.8. Displacement time series in Guerrero (red triangles) and Oaxaca (blue triangles) GPS stations. The map shows the epicenters of the thrust earthquakes occurred in the last 23 years in Mexico (M>7, yellow stars near the coast) and the intraslab Mw7.1 Puebla-Morelos event. Gray shapes delineate the areas of aseismic slip larger than 1 cm determined in this study between November 2016 and October 2019 (see Figure 5.3). All the aseismic events (SSEs and afterslip) observed in the time series since 1997 are indicated with vertical-colored bands. Note the great change in the temporal deformation patters throughout the entire region after the great Mw8.2 Tehuantepec earthquake. The O-SSE3, not studied here, initiated two months before the Mw7.4 Huatulco earthquake of June 23, 2020.

	Guerrero			**Oaxaca**	
Event	Dates	Mw	Event	Dates	Mw
G-SSE1	10/06/17 - 18/10/17	6.91	O-SSE1	01/06/17 - 15/02/18	6.93
G-SSE2	16/02/18 - 01/06/18	6.93	PE-afterslip	16/02/18 - 22/11/18	7.17
G-SSE3	22/11/18 - 20/07/19	6.99	O-SSE2	05/02/19 - 20/07/19	6.92

The prefixies G and O refer to the states of Guerrero and Oaxaca, respectively while PE refers to the Pinotepa earthquake.

s

Table 5.1. Dates (dd/mm/yy) and moment magnitudes (Mw) estimated from the 1 cm slip coontours of all aseismic slip events reported in this chapter

Chapter 6

Slow slip events and megathrust coupling changes reveal the earthquake potential before the 2020 Mw 7.4 Huatulco, Mexico event

Contents

This chapter has been modified from its associated article: **Villafuerte, C.**, Cruz-Atienza, V., Tago, J., Solano, D., Garza-Girón, R., Franco, S., Domínguez, L., and Kostoglodov, V. (2021). Slow slip events and megathrust coupling changes reveal the earthquake potential before the 2020 Mw 7.4 Huatulco, Mexico event. *Submitted to AGU Advances*.

Abstract

Stress accumulation on the plate interface of subduction zones is a key parameter that controls the location, timing and rupture characteristics of earthquakes. The diversity of slip processes occurring in the megathrust indicates that stress is highly variable in space and time. Based on GNSS and InSAR data, we study in depth the evolution of the interplate slip-rate along the Oaxaca subduction zone, Mexico, from October 2016 through August 2020, with particular emphasis on the pre-seismic, coseismic and post-seismic phases associated with the June 23, 2020 Mw 7.4 Huatulco earthquake, to understand how different slip processes contribute to the stress accumulation in the region. Unlike two long-term interplate coupling models previously proposed for the region, our results show that continuous changes in both the aseismic stress-releasing slip and the coupling produced a high stress concentration (i.e., Coulomb Failure Stress (CFS) of 800 $\pm$ 100 kPa) over the main asperity of the Huatulco earthquake and a stress shadow zone in the adjacent updip region (i.e., shallower than 17 km depth with CFS around -1.0 MPa). These findings may explain both the downdip rupture propagation of the Huatulco earthquake (between 17 and 30 km depth) and its rupture impediment to shallower, tsunamigenic interface regions, respectively. Time variations of the interplate coupling around the 1978 (Mw 7.8) Puerto Escondido rupture zones clearly correlate with the occurrence of the last three Slow Slip Events (SSEs) in Oaxaca far downdip of this zone, suggesting that SSEs are systematically accompanied by interplate coupling counterparts in the shallower seismogenic zone, which in turn have their own potentially-seismogenic stress and frictional implications. In the same period, the interface region of the 1978 event experienced a remarkably high CFS built-up of 800-1,500 kPa, half imparted by the co-seismic and early post-seismic slip of the neighboring Huatulco rupture, indicating large earthquake potential near Puerto Escondido. Continuous monitoring of the interplate slip-rate thus provides a better estimation of the stress accumulation in the seismogenic regions than those given by long-term, time-invariant coupling models and improves our understanding of the megathrust mechanics where future earthquakes are likely to occur.

6.1 Introduction

Large earthquakes occur along subduction zones in regions known as asperities (Lay and Kanamori, 1981), which represent locked areas of the interplate contact where frictional resistance allows elastic stress to build up during tens to hundreds of years as a consequence of the relative plate motion. Under the simple concept of Coulomb failure criterion, an earthquake occurs when the shear stress overcomes the strength of the fault. Both stressing-rate and fault strength are parameters that vary in time and space during the megathrust earthquake cycle (Moreno et al., 2011). Therefore, understanding the tectonic processes that cause these variations is essential to assess the seismic hazard in subduction zones.

Inter-seismic coupling maps obtained from geodetic observations have been widely used to identify heterogenous, highly locked segments of the plate interface where large earthquakes take place (Chlieh et al., 2008; Loveless and Meade, 2011; Moreno et al., 2010; Perfettini et al., 2010). Most of these estimations consider a steady-state long term deformation during the inter-seismic periods that results in a time invariant locking pattern. However, it has been observed that interplate coupling also varies with time (Heki and Mitsui, 2013; Melnick et al., 2017) and might be caused by different processes such as pore pressure transients (Cruz-Atienza et al., 2018b; Materna et al., 2019; Warren-Smith et al., 2019) or dynamic stresses from regional earthquakes (Cruz-Atienza et al., 2021; Delorey et al., 2015; Materna et al., 2019).

During the inter-seismic period, a broad spectrum of tectonic processes occurs on the plate interface with distinctive spatiotemporal characteristics that play an important role to accommodate the strain along the megathrust. Among these processes, short-term and long-term slow slip events (SSEs), which are aseismic slip transients lasting from days to months, release the strain accumulation in the deeper and shallower segments of the plate interface (Beroza and Ide, 2011; Saffer and Wallace, 2015). Since their discovery, observations and theoretical models have proposed that SSEs increase the stress in the adjacent seismogenic zone and may trigger damaging earthquakes (Obara and Kato, 2016; Segall and Bradley, 2012; Uchida et al., 2016; Voss et al., 2018). Moreover, it has been documented that major interplate earthquakes in different subduction zones are preceded by SSEs, although the actual mechanisms of their interaction remain under debate.

In the Mexican subduction zone, the recurrence of Mw 7+ interplate earthquakes is 30-50 years (Singh et al., 1981). In the deeper segment of the megathrust (30-50 km depth), long-term SSEs occur in Oaxaca and Guerrero with recurrence of 1.5 and 3.5 years, respectively (Cotte et al., 2009; Graham et al., 2016). The last four Mw 7+ interplate events in the Mexican subduction zone were preceded by SSEs in the downdip adjacent region: The 2014 Mw 7.4 Papanoa earthquake in Guerrero (Radiguet et al., 2016) and three more in Oaxaca, the 2012 Mw. 7.5 Ometepec earthquake (Graham et al., 2014a), the 2018 Mw 7.2 Pinotepa earthquake (Cruz-Atienza et al., 2021) and, as it will be shown later, the 2020 Mw 7.4 Huatulco earthquake. These observations suggest that the prevalent mechanism of the interaction between SSEs and unstable shallower regions in the Mexican subduction zone is the stress loading from adjacent slow slip processes. Although SSEs do not always trigger large earthquakes, they do interact periodically with the updip locked regions, thus contributing with the total stress built-up of the seismogenic zone.

Three years before the 2020 Huatulco earthquake, a complex sequence of SSEs and devastating earthquakes took place from June 2017 to July 2019 in central and southern Mexico, including the Mw 8.2 Tehuantepec and Mw 7.1 Puebla-Morelos earthquakes in 2017, and the Mw 7.2 Pinotepa earthquake in 2018, describing a cascade of events interacting with each other on a regional scale via quasi-static and/or dynamic perturbations (Cruz-Atienza et al., 2021). In Oaxaca, the plate interface slipped (aseismically) almost continuously for the whole two years period with at least two reactivations, one during the post-seismic relaxation of the Mw 7.2 Pinotepa earthquake, and the second one with the 2019 Oaxaca SSE.

Here we thoroughly study the evolution of the interplate slip-rate history in the Oaxaca segment during this unprecedented sequence including the pre-seismic, coseismic and post-seismic phases of the 2020 Huatulco earthquake with the aim of understanding how these processes contribute to the seismic potential in the region. We show that continuous and simultaneous monitoring of SSEs and the megathrust coupling provides a better estimation of the stress accumulation on the locked regions where future large earthquakes are expected to occur.

6.2 The 2020 Mw 7.4 Huatulco Earthquake

6.2.1 Coseismic slip inversion

On June 23, 2020, a shallow Mw 7.4 interplate thrust earthquake took place below the state of Oaxaca, Mexico (Fig. 6.1), with relocated hypocentral coordinates (15.822ž, -96.125ž, 17.2 km, determined from seismic records at the station HUAT of the Mexican Servicio Sismológico Nacional (SSN), which is 7 km south of the epicenter) within the aftershock area of the 1965 Mw 7.5 earthquake, the last interplate rupture in this region (Chael and Stewart, 1982).

We combined nearfield GNSS and Interferometric Synthetic Aperture Radar (InSAR) data to obtain the coseismic slip distribution by means of ELADIN, a newly developed adjoint inversion method (Tago et al., 2021) (see Appendix E). For the GNSS data we used high rate (1 s) time series to measure the coseismic static displacement at four stations near the epicenter (Figs. 6.1c and E.1c-f). The displacement in Huatulco (HUAT station), the closest epicentral site, was carefully and independently estimated using GNSS, tide gauge and strong motion data, yielding very consistent values of 49 cm uplift and 40 cm seaward displacement (Figs. E.1b and E.1c). The InSAR line-of-sight (LOS) displacement map (Figs. 6.1b and E.2) was generated from scenes taken before the earthquake, on June 19, and two days after the earthquake, on June 25, by the Sentinel satellite of the European Space Agency on ascending track 107. The InSAR data processing is described in the Appendix E. For all slip inversions presented in this work we assumed the 3D plate interface geometry introduced by Cruz-Atienza et al. (2021) and discretized it, for the coseismic solutions, into subfaults with square horizontal projections of 5 x 5 km2.

To determine the optimal data weights for the joint inversion of GNSS and InSAR data we first inverted each data set individually. Both independent solution models produced almost a perfect data fit but significantly different slip distributions, as shown in Figs. E.3a and E.3b. Numerous

joint inversion tests led us to optimal data weights (see Appendix E) producing a final solution that owns the most prominent features of both independent models and satisfactorily explains the whole set of observations, with average GNSS and InSAR data errors of 1.2 ± 1.0 cm and 0.2 ± 2.1cm, respectively (Figs. 6.1 and E.3c).

Figure 6.1a features our preferred coseismic slip solution with two main patches, the most prominent downdip the hypocenter, between 21 and 32 km depth with peak value of 3.4 m, and a second one 45 km east-northeast, almost below the coast (peak value of 1.8 m), which differs from a recently published solution (Melgar et al., 2021) that did not integrate the closest (GNSS and strong motion) data and estimated a static uplift in Huatulco 6 cm higher than ours. Our slip solution explains both the uplift and seaward displacement there, and shows that no significant slip (i.e., larger than 1 m) took place offshore (Fig. 6.1). Furthermore, it clearly suggests a rupture directivity towards the north-northeast, essentially downdip from the hypocenter. Two more features stand out from our model: 1) The rupture ends abruptly updip and very close to the nucleation point, and 2) the downdip slip limit might correspond to the end of the locked segment of the megathrust, as observed for the 2018 Pinotepa Earthquake (Li et al., 2020), the 2012 Ometepec Earthquake (de México Seismology et al., 2013) and the aftershocks areas of regional interplate earthquakes (white patches in Fig. 6.1). We performed resolution tests following Tago et al. (2021) for the joint GNSS and InSAR inversion by means of mobile checkerboards tests with patch sizes of 20 km and different correlation lengths (L) (see Appendix E). Our resolution analysis reveals that average restitution indexes (ARI, a metric that eliminates the resolution dependence on the checkerboard position) above 0.65 enclose the region where the two main slip patches are located (Fig. E.4), which means that our preferred slip model, including these features, has a nominal error below 35 % with respect to the actual slip distribution.

Whether the 2020 Huatulco earthquake is a repetition of two previous events that occurred in 1928 (Ms 7.6) and 1965 (Ms 7.4) is an important matter that goes beyond the scope of this work. However, since this question can be addressed by comparing far-field waveforms of the earthquakes, which are sensitive to the source depth (Chael and Stewart, 1982; Singh et al., 1984), we performed a supplementary inversion exercise where the interface was shifted 3.5 km upward to match our relocated hypocentral depth. The inversion yielded similar source characteristics as described above (Fig. E.5) with some differences discussed in the Appendix E that do not have a significant bearing on any subsequent analysis.

6.2.2 The 2020 Oaxaca SSE that preceded the earthquake

Two months before the Huatulco earthquake, on mid-April 2020, three GNSS stations in Oaxaca (TNNP, TNNX and OAXA) changed their typical interseismic motion from roughly northeast to southwest, indicating a transient deformation associated with a SSE (light blue section in Figs. 6.2a and S6a). We used continuous displacement records on 12 permanent GNSS stations in Oaxaca (Fig. 6.2b) belonging to the SSN and Tlalocnet (Cabral-Cano et al., 2018), between September 2019 and the Huatulco earthquake date (Fig. E.6) to simultaneously invert for the plate interface coupling (PIC,) and any stress-releasing slip episode (i.e., SSEs) in successive time windows using ELADIN (Fig. 6.2). To this end, we carefully corrected the displacement time series by fitting and removing

seasonal effects as explained in detail in the supplementary materials (Fig. E.14). For these and the next section inversions, the 3D plate interface was discretized with coarser subfaults of 10 x 10 km2. Given both the interface geometry and the distribution of the GNSS stations in Oaxaca, we adopted the optimal regularization length of 40 km determined by Tago et al. (2021), which guarantees an inversion error under 50 % (i.e., median restitution indexes higher than 0.5) for slip patches larger than 80 km length at most interface depths greater than 10 km (Fig. E.8).

Figure 6.2e shows the main slow slip patch downdip of the 1978 Puerto Escondido earthquake region, between 25 and 50 km depth, with an equivalent moment magnitude Mw 6.5 (Mo = 6.645 x 1018 N*m measured from the slip contour of 1 cm and assuming a shear modulus of 32 GPa). The location and magnitude of this SSE are consistent with previously reported SSEs in Oaxaca (Correa-Mora et al., 2008; Cruz-Atienza et al., 2021; Graham et al., 2016). It is also clear that the SSE did not penetrate the rupture area of the Huatulco earthquake. Instead, ňwe observe a remarkable PIC evolution previous to the event close to its hypocentral region, where the interface decoupled around February-March (Fig. 6.2d) before getting fully coupled just before the earthquake (i.e., during the strongest SSE phase, Fig. 6.2e). This can also be seen directly in the GNSS time series at the stations closest to the epicenter, such as OXUM and HUAT (Fig. 6.2a), where we do not observe the SSE southward rebound before the earthquake. Something similar occurred in the hypocentral region of the 2018 Pinotepa earthquake (Mw 7.2) 200 km west, where the seismicity rate also increased in the two months preceding the rupture (Cruz-Atienza et al., 2021). We carefully analyzed the foreshock seismicity starting from August 2016 in the hypocentral region of the Huatulco earthquake using the one-station template-matching procedure introduced by Cruz-Atienza et al. (2021) from continuous broadband records at the HUIG station (Fig. E.9). However, unlike the observations of the 2018 Pinotepa earthquake, we did not find significant increase in the seismicity rate prior to the event that could shed further light on the rupture initiation mechanism.

Although the transient deformation produced by the SSE is noticeable from mid-April, the inter-SSE displacement trends in some stations started changing well before, around mid-February as observed in Figure 6.2a (red dashed lines), suggesting a gradual ňplate interface decoupling process at a regional scale preceding the SSE-induced crustal relaxation, which can be observed in Figs. 6.2b-6.2d and 6.2f (see also Movie 2). Before such decoupling process began (Fig. 6.2b), the downdip segment of the plate interface, between 25-50 km, was fully coupled while small SSE episodes were taking place in both the 2018 (Mw 7.2) Pinotepa earthquake area and up-dip of the Huatulco earthquake rupture zone. In the following two months, there seems to have been an incipient downdip SSE propagation from south to north nearby Pinotepa (Movie 2 and Figs. 6.2b-6.2c). Then, in Figs. 6.2d and 6.2f we see how the segment downdip of the 1978 earthquake area is the last one to experience a PIC reduction (i.e., the interface slip starts accelerating but always below the plate convergence rate) leading to the main SSE patch occurrence in April-June, the months preceding the earthquake (Figs. 6.2e and 6.2f). All of these observations clearly demonstrate the regional-wide preparatory phase for the 2020 Oaxaca SSE.

A common practice to isolate the deformation associated with slow slip transients is to subtract the inter-SSE linear trend from the GNSS time series. The residual deformation is then assumed to correspond to the strain released by the SSE (e.g., Bartlow et al. (2011); Hirose et al. (2014); Radiguet et al. (2011)). When doing this to invert for the slip at the interface, the preparatory phase

of the SSE (i.e., the slow decoupling process preceding the SSE relaxation) is mapped/interpreted as aseismic slip resulting in an elastic crustal rebound (i.e., a stress drop). However, since this process instead reveals a gradual decrease in the upper crustal stressing rate, such an misleading practice leads to a systematic overestimation of the SSE-related surface displacements and, therefore, of the SSE equivalent seismic moment with relevant implications in the scaling properties of slow earthquakes and, more importantly, in the slip budget over several SSE cycles, which may be significantly underestimated.

6.2.3 Early post-seismic deformation

We inverted the early post-seismic GNSS displacements (i.e., the first 2 months following the earthquake discretized in 6 ten-day windows, Figs. 6.3a and E.7b) produced by the mainshock using the same parameterization for the ELADIN method as in the previous section. We then assumed that such displacements are only due to the afterslip on the plate interface, which is a reasonable approximation considering that the viscoelastic relaxation after a similar thrust event 260 km west, the 2012 (Mw 7.5) Ometepec earthquake, was negligible in a post-seismic period three times longer (Graham et al., 2014b).

Four main observations arise from the afterslip evolution of the Huatulco earthquake (Fig. 6.3b and Movie 2): (1) the largest afterslip concentrates between 20 and 50 km depth overlapping with the main SSE patch preceding the earthquake (i.e., downdip from the 1978 rupture area) and where previous SSEs have been identified (Fig. 6.4a); (2) the maximum postslip area completely overlaps with the coseismic rupture area; (3) the afterslip spreads offshore up to the oceanic trench where most of aftershocks concentrate; and (4) the afterslip rate reaches its maximum value of 390 cm/year during the first 10 days following the earthquake (Movie 2).

The complete overlap of coseismic and postseismic slip has been observed in the last three interplate thrust earthquakes (Mw >7) in Oaxaca, the 2012 (Mw 7.5) Ometepec (Graham et al., 2014b); the 2018 (Mw 7.2) Pinotepa (Cruz-Atienza et al., 2021) and the 2020 (Mw 7.4) Huatulco (this study) events, indicating that these seismogenic segments of the plate interface, with the depth range between 10 and 30 km, can release elastic strain energy both seismically and aseismically. However, the propagation of the Huatulco earthquake afterslip to the trench is an interesting feature that clearly differs from the Pinotepa earthquake, whose afterslip stopped under the coast (i.e., at 15 km depth and without offshore propagation) (Figs 6.4a and S10e-g). This observation suggests significant lateral variations in the mechanical and/or geo metrical properties along the Oaxaca subduction zone between the updip and downdip interface regions.

The cumulative aseismic moment released during the first two months following the earthquake was 1.808 x 1020 N*m, equivalent to a moment magnitude Mw 7.44, which is 24 % larger than the coseismic moment. The high postseismic/coseismic moment ratio is also a common feature of the three Oaxaca events mentioned above, that significantly differs from the much lower estimate for the 2014 (Mw 7.4) Papanoa thrust earthquake in Guerrero, where the aseismic postslip moment was 30 % smaller than the corresponding coseismic value (Gualandi et al., 2017).

One of the most noteworthy features of the postseismic process in the region is that the Huatulco

earthquake postslip did not penetrate the rupture area of the 1978 Puerto Escondido earthquake (dashed ellipse in Fig. 6.3b), which remained fully coupled during the two-month period. Unlike most of the preseismic phase (i.e., before April, Fig. 6.2e), the PIC in the 1978 rupture area remained fully locked after the earthquake (compare Figs. 6.2 and 6.3) suggesting significant dynamic implications for the accommodation of postseismic strain in the region.

6.3 Interplate slip-rate evolution in the Oaxaca subduction zone.

Before the occurrence of the Huatulco earthquake, a complex sequence of earthquakes and SSEs took place in an unusual way along the Mexican subduction zone from April 2017 to September 2019 due to the extremely large, unprecedented seismic waves from the Mw 8.2 Tehuantepec earthquake on September 8, 2017 (Cruz-Atienza et al., 2021). During this period, two large SSEs occurred in the downdip interface region of Oaxaca (namely the 2017 SSE (O-SSE1) and the 2019 SSE (O-SSE2)) where the recent 2020 SSE (O-SSE3) took also place (Figure 6.4a). Indeed, the plate interface slipped aseismically and continuously for two years from O-SSE1, experiencing two spontaneous reactivations in this period, one with the afterslip of the Pinotepa earthquake and the other with the O-SSE2 (Cruz-Atienza et al., 2021).

We corrected the GNSS displacement time series used by Cruz-Atienza et al. (2021) for seasonal effects from October 2016 to September 2019 as previously done in section 2.2 (Fig. E.14) and inverted them for the interplate aseismic slip in greater detail along the Oaxaca megathrust. The new inverted sequence is shown in Figure E.10 and Movie 2. During the sequence, the plate interface experienced remarkable changes of the PIC over time in the whole megathrust. To analyze the long-term evolution of the aseismic slip before the Huatulco earthquake, we integrated the new corrected slip sequence from October 2016 to September 2019 (Fig. E.10) and the subsequent sequence discussed in section 2.2 (from September 2019 to June 2020, Fig. 6.2), and linearly interpolated the complete slip history every 30 days. Following the same strategy to visualize our inversion results, we also disaggregated the total slip into relaxing and stressing interface regions (i.e., into SSEs and afterslip regions where the slip rate is greater than the plates convergence rate and, therefore, release elastic strain (e.g. red gradient zones in Figs. 6.2 and 6.3); and regions under coupling regime, where the velocity of the interplate creep is less than or equal to the plates convergence rate and, therefore, accumulate elastic strain (e.g. blue gradient zones in Figs. 6.2 and 6.3).

Figs. 6.4b and 6.4c show the evolution of the relaxing slip on the plate interface along the trench (i.e., projected into the green line of Figure 6.4a) averaged in two different depth ranges, between 10-20 km depth (Fig. 6.4b) and between 20-30 km depth (Fig. 6.4c), encompassing the rupture areas of the 2018 Pinotepa, 1978 Puerto Escondido and 2020 Huatulco earthquakes (Fig. 6.4a). Figures 6.4b and 4c show that the Pinotepa earthquake afterslip (yellow areas) dominates in the region for the analyzed period. However, there are other significant slip episodes (i.e., short-term SSEs) most often in the shallow zone (within the 10-20 km depth range) excluding the 1978 rupture zone.

To better analyze the interplate slip-rate variations we extracted the time series of the slip evolution at six places of the plate interface (dashed blue circles with radius of 20 km in Fig. 6.4a). Region

A, over the rupture area of the Huatulco earthquake; Region B, over the rupture area of the 1978 Puerto Escondido earthquake as estimated by Mikumo et al. (2002); Region C, downdip from the rupture area of the Puerto Escondido earthquake; Region D, updip from the Huatulco earthquake where most of its aftershocks are located; and Regions E and F, west and northwest of the Puerto Escondido earthquake. Figs. 6.5 and E.11 show the evolution of the mean total aseismic slip (black line), the creeping (yellow line), the relaxing slip (red line) and the PIC (blue line) within each of the six circular regions.

In the Huatulco rupture area (Region A, Fig. 6.5a), the largest contribution to the total slip is due to creeping except for a period after the Mw 8.2 Tehuantepec earthquake, when aseismic stress release occurred during the late phase of the O-SSE1 (see Figures 6.4a and E.10c). This phase of the O-SSE1 was indeed triggered by the quasistatic and dynamic stresses produced by the great Tehuantepec event as demonstrated by Cruz-Atienza et al. (2021). In this region, PIC is highly variable over time and there is no clear correlation with the occurrence of SSEs in Oaxaca that, except for the late phase of the O-SSE1 (Fig. E.10c), all occurred more than 100 km northwest from this region. We also find a gradual decrease of PIC down to values of 0.1-0.2 at the end of the afterslip period of the Pinotepa earthquake that eventually recovers during the O-SSE2 to remain high until the Huatulco earthquake occurs, with values ranging between 0.7-1.0.

In the 1978 rupture area (Region B, Fig. 6.5b) there is no significant evidence of aseismic stress release, so the total slip is only associated with creeping. In this region, PIC changes correlate remarkably well with the occurrence of downdip SSEs in Oaxaca even though these events did not penetrate the region. During the SSEs, PIC gradually increases to values of 0.7-0.8 in the initial stage of every SSE and then decreases in their final stage to remain relatively low, with values down to 0.2-0.4 observed during the inter-SSE periods. This remarkable behavior, which suggests a non-intuitive interaction between deep SSEs and the coupling regime in the shallower seismogenic zone, is also found in Region E (Fig. E.11c), west of the 1978 rupture area.

To the east and thus offshore (and updip) the Huatulco earthquake (Region D, Fig. E.11b) we find a different and more consistent low PIC value across the whole studied period with the exception of a prominent increase after the Tehuantepec earthquake, which might be associated with the stress shadow produced in this specific spot by the great Mw8.2 rupture (Suárez et al., 2019; Cruz-Atienza et al., 2021). The red curve indicates that there are small and persistent short-term, episodic SSEs in this offshore region over time that can also be appreciated in Figures 6.4b and E.10. Such a particular behavior is consistent with the significant afterslip that swept that area into the trench after the Huatulco earthquake (Fig. 6.3). These observations suggest that frictional properties of this offshore region are prone to release aseismically a fraction of the accumulated stress, as recently found in the Guerrero seismic gap (Plata-Martínez et al., 2021).

Finally, downdip from the 1978 rupture area (Regions C and F, Figs. E.11a and E.11d) we observe a complicated PIC evolution because of its proximity to the deep SSEs region. During the occurrence of SSEs, PIC reductions begin well before the silent events, meaning that creeping in some subfaults of these regions accelerates before the relaxing slip invades them (see how the blue curves start decreasing before the red curves start growing). These observations indicate that SSEs might partly penetrate these seismogenic depths (20 -30 km) (see also Figure 6.4a).

6.4 Implications of SSEs and PIC changes on the stress built-up

Variations in the interplate aseismic slip rate have important implications for both friction and the stress build-up along the megathrust. We estimated the Coulomb Failure Stress (CFS) changes (Nikkhoo and Walter (2015), see Appendix E) produced by the relaxing slip (SSEs and afterslip) and the interplate coupling to elucidate how the stress evolves along the Oaxaca segment. For this analysis we have also included the coseismic stresses imparted by the Tehuantepec (Cruz-Atienza et al., 2021), Pinotepa and Huatulco earthquakes. Figs. 6.6a and 6.6b show the average cumulative CFS every 30 days from October 2016 up to the moment of the Huatulco event along the trench (i.e., projected onto the green line in Figure 6.4a) for two different depth ranges encompassing the rupture areas of the 2020 Huatulco (between 20 and 30 km depth, Fig. 6.6a) and the 1978 Puerto Escondido (between 10 and 20 km depth, Fig. 6.6b) earthquakes. It is important to note that these estimates of the CFS are the result of stress contributions from the whole plate interface and not just from the sub-faults delimited by the depth ranges.

As expected, the CFS cumulative rate is highly variable over time and along the trench. For the deeper region (Fig. 6.6a), we observe that despite the great variations of the slip-rate on the megathrust, the CFS in Huatulco always increased up to values ranging from 600 to 800 kPa. We also observe a significant CFS contribution of 100 kPa induced by the Mw8.2 Tehuantepec earthquake in the eastern limit of the Huatulco rupture zone that exceeds 300 kPa further to the east. For the shallower region (Fig. 6.6b), the CFS systematically decreases and remains negative right updip of the Huatulco rupture reaching values of -900 kPa. Such large negative CFSs are associated with both the stress shadows produced by neighboring strong coupled segments (e.g., the 1978 earthquake area, Fig. 6.6c) and the periodic stress release by short-term SSEs in this offshore segment (Figs. 6.4b and 6.6d). To the west, in the 1978 rupture area (Fig. 6.6b), we find the opposite situation. The CFS always increased to values between 100 and 400 kPa, which are approximately half of the CFS estimates downdip of this segment (Fig. 6.6a).

Figure E.12 shows both the long-term and inter-SSE time-invariant interplate coupling models estimated by Radiguet et al. (2016)(personal communication) together with their associated CFS change rate. Both models produce large stressing rates mainly in the highly coupled segment of the 1978 earthquake region. However, they also produce large stress shadows in the adjacent, less coupled regions (both along-dip and along-strike) such as in the Pinotepa and Huatulco rupture zones. Although these time-invariant coupling models may lack some observational coverage compared to the present investigation, they share similar features (though not all) to those found by Rousset et al. (2016) for the inter-SSE regime, which incorporates all available GPS observations in the region (compare Figure E.12c and Figure 6.3B of Rousset et al. (2016)).

In contrast, our aseismic time-evolving slip model predicts a very different scenario. Figure 6.7a shows the cumulative CFS at the time of the Huatulco earthquake including contributions of all aseismic slip processes imaged in the megathrust during more than 3.5 years preceding the event (from October 2016 to June 23, 2020). A simple inspection reveals large differences in the stress build-up pattern with respect to the time-invariant models (Fig. E.12), especially in both the Huatulco and Pinotepa rupture areas, and east-southeast of the 1978 earthquake zone. The bottom

four panels of Figure 6.7 show the cumulative (trench-perpendicular average) CFS along the trench for the same two depth ranges analyzed earlier. The left column shows the cumulative CFS at the time of the Huatulco earthquake, while the right column shows the same quantity plus the coseismic and postseismic stress increments.

In the deeper region at the moment and within the rupture area of the Huatulco earthquake (Fig. 6.7b), the CFS from our time-evolving slip model (blue area) indicates more than double the CFS predicted by the inter-SSE coupling model by Radiguet et al. (2016) (yellow area), where their long-term coupling model (orange area) predicts even negative CFS values (i.e., no earthquake potential). Downdip of the 1978 rupture area, the CFS predicted by the three models are consistent (values ranging between 200 and 300 kPa), but to the west of this region our model again predicts very different stress concentrations, which are twice the CFS predicted by the inter-SSE coupling model. When adding the CFS imparted by the Huatulco earthquake and its postseismic afterslip (Fig. 6.7e), our estimate abruptly increases right downdip of the 1978 rupture area, from about 300 kPa to over 1.3 MPa. A significant fraction of this value is due to the persistently high coupling in this region throughout the post-seismic phase (Fig. 6.3). This large segment west of the Huatulco rupture (Region C in Fig. 6.4a) might be then very prone to a future earthquake, as has occurred in neighboring regions over the deep part of the locked zone where the last two interplate earthquakes in Oaxaca (the Pinotepa and Huatulco events) took place, with most of their seismic moment released below 20 km (Fig. 6.1a and Li et al. (2020)).

In the shallower region, the time-invariant coupling models predict higher CFS values over the 1978 rupture area than our time-evolving slip model before the Huatulco rupture (Fig. 6.7c). Only when adding the coseismic and postseismic stresses induced by the earthquake, the inter-SSE model prediction becomes similar to ours in the eastern part of the rupture area of the 1978 Puerto Escondido earthquake (Fig. 6.7f). Updip of the Huatulco rupture area (Fig. 6.7c), only our time-evolving model predicts a large CFS deficit, which is fully compensated (reaching positive values around 700 kPa) by the coseismic and postseismic deformations produced by the Huatulco earthquake (Fig. 6.7d).

We can therefore distinguish three major differences between our time-evolving CFS estimates and those from the time-invariant coupling models introduced by Radiguet et al. (2016): (1) very high stress concentration over the rupture area of the Huatulco earthquake before the event predicted only by our model, (2) absolute CFS values between 20 and 30 km depth at least twice as high in our model, and (3) a large stress shadow zone updip the Huatulco rupture before the event that is absent in both time-invariant models.

We now analyze in depth the CFS evolution in the Huatulco and 1978 rupture areas produced by our time-evolving interplate slip-rate model. Figures E.13a and E.13b show the total CFS evolution in both regions (black curves, Regions A and B in Figure 6.4a) together with the linear predictions given by the time-invariant coupling models of Radiguet et al. (2016) (green lines). To assess which slip regime dominates the stress evolution, we also disaggregated the total CFS into the stress contributions produced by slip regions under coupling (creeping) regime only (yellow curves) and by regions undergoing relaxing slip only (red curves).

In the Huatulco rupture zone (Region A, Fig. E.13a) our model shows a sustained growth of the total CFS during more than 3.5 years prior to the rupture, reaching values close to 800 kPa and

where 75 % of the stress contribution comes from regions in coupling regime. The remaining 25 % is mainly associated with the SSE occurred following the 2017 Tehuantepec earthquake. In contrast, the long-term time-invariant model predicts a sustained decrease of CFS that implies a continuous reduction of the earthquake potential. On the other hand, while the inter-SSE time-invariant model predicts a growth of the CFS, the final value is about one fourth of what our model yields. This can also be seen in top view by comparing our estimates of CFS in the hypocentral region at the time of the earthquake (Movie 2 and Fig. 6.7a) with those produced by the time-invariant models (Fig. E.12). Since the Huatulco earthquake took place, it seems that our time-evolving slip-rate model and its associated CFS represents a more realistic description of the actual megathrust processes than any of the time-invariant coupling models analyzed here.

Considering the 1978 rupture zone (Region B, Fig. E.13b), our model reveals significant temporal variations primarily controlled by the stress contributions from regions in under coupling regime. The cumulative stress produced by SSEs at the time of the Huatulco earthquake is 100 kPa and, therefore, the main responsible for the accumulated positive CFS in this region. For this specific region, both inter-SSE and long-term time-invariant models predict a much higher cumulative stress. When integrating the stress contributions from the coseismic and postseismic slip of the Huatulco earthquake, then our stress estimate becomes similar to the long-term estimation and closer (but still much smaller) to the inter-SSE prediction with CFS values around 700 kPa.

Figures 6.8a and 6.8b show separately the regional contributions to the CFS of both the relaxing and the creeping (i.e., under coupling regime) slip, respectively, during the whole analyzed period before the Huatulco earthquake. Although in very different proportions, both stress contributions promote an increase in earthquake potential in the rupture areas of the Huatulco and 1978 earthquakes. Figures 6.8c and 6.8d show the percentages of these contributions with respect to the total CFS only where the latter is positive in Figure 6.7a (i.e., where there is an effective increase of the earthquake potential).

Between 20-30 km depth, where regions A and C are located, we observe that most of the accumulated stress (65-80 %) was generated by coupled interface regions and the remaining 20-35 % by the relaxing slip (i.e., long- and short-term SSEs, and the Pinotepa earthquake afterslip) that occurred in the region during more than 3.5 years (Figs. E.13a and E.13c). Given its proximity with the Pinotepa earthquake, Region F differs significantly from this stress partitioning because it is strongly affected by the stresses produced during the coseismic slip and afterslip of the Pinotepa earthquake (Fig. E.13f).

For shallower depths, offshore Region D, which has no prestress earthquake potential, experienced a sustained reduction of CFS due to both coupling-related stress shadows (Fig. 6.8a) and short-term SSEs (Fig. 6.8b) in similar proportions (Fig. E.13d). In contrast, although the stress partitioning between them is not very consistent, Regions B and E do show an increase in earthquake potential. In region B (Fig. E.13b), due to the high variability of the PIC, the regions in coupling regime produce a stress release there, i.e., a negative stress contribution. However, the total stress accumulation in this region during the analyzed period is positive. This is because the stress produced by the relaxing slip overcame the stress deficit produced by the coupled portions of the interface and, therefore, its contribution is 170 % of the final CFS. In region E (Fig. E.13e), both stress contributions are very

similar, with 45 % due to regions under coupling regime and the other 55 % associated with relaxing slip. These estimations show the highly heterogeneous stress accumulation and partitioning along the plate interface in the Oaxaca segment.

6.5 Discussion

Previous M7 class interplate earthquakes such as those of 1965 and 1928 occurred in close proximity of the 2020 Huatulco rupture, suggesting a possible reactivation of the same asperity over time (Chael and Stewart, 1982; Singh et al., 1984). Historical data also suggest that two older, probably thrust earthquakes with magnitude larger than 7 occurred nearby in 1870 and 1801 (Suárez et al., 2020). Assuming that all these events broke the same plate interface patch, their average return period would be 55 +/- 13 years.

In this Oaxaca region, the great Mw 8.6 San Sixto earthquake ruptured a 300 km along-strike segment in 1787 producing a very large tsunami offshore Oaxaca (Suárez and Albini, 2009; Ramírez-Herrera et al., 2020). Such event must have involved several locked segments along the Oaxaca megathrust, including offshore shallow portions of the plate interface to generate the mega-tsunami. Whether M8+ events may repeat depends, among other factors, on the interplate mechanical properties and constructive stress interaction between different locked and unlocked fault segments (Kaneko et al., 2010, 2018), which evolve with time and may escape from the quantitative analysis of known seismicity over the last century (Nocquet et al., 2017). Recent laboratory experiments and theoretical fault models strongly suggest that friction is a very sensitive function of the interplate slip velocity where SSEs take place (Im et al., 2020). Therefore, since the slip velocity changes over time, as shown in this study, such variations should play an important role in the dynamic stability of the megathrust because of both their frictional counterparts and the associated stress changes documented here for the Oaxaca subduction zone. To have an insight into the actual megathrust earthquake potential (i.e., to assess whether adjacent locked segments are likely to break jointly to produce a much larger event) it is thus necessary a proper and continuous quantification of the stress accumulation as proposed here. Monitoring the interplate slip-rate continuously might also allow us to constrain the evolution of the frictional parameters that control the slip stability conditions on the megathrust.

An interesting feature of the Huatulco earthquake is that rupture did not propagate into the adjacent updip segment (above 17 km depth). Impeding rupture into this shallower segment might be partly explained with the existence of the large stress barrier produced by both the stress shadow from nearby strongly coupled zones and persistent short-term SSEs updip (i.e., offshore, see Figures 6.4b and 6.7a). However, other factors such as the geometry of the interface (e.g. subducted plate reliefs in the region, as recently proposed in the Guerrero seismic gap (Plata-Martínez et al., 2021)) and frictional variations could also contribute to the explanation of this particular rupture pattern. The spatial concentration of aftershocks during the first 50 days following the Huatulco event is clearly shifted updip (about 30 km) from the rupture area, where the afterslip developed and the CFS strongly increased (Fig. 6.7d). Only very few aftershocks lie within the main slip patch, indicating an effective stress release in most of the rupture area, which is consistent with other M7 class

earthquakes observed worldwide (Wetzler et al., 2018). Also interesting is the earthquake initiation at the shallowest extremity of the rupture zone and its northward propagation. The nucleation point lies in the very limit between a highly stressed (downdip) and a highly relaxed (updip) interface regions (Fig. 6.7a), which means on a place with relatively large stress gradient and, therefore, strain field. The initiation of the earthquake at this point is therefore well explained by our model, as is its propagation towards the most loaded, downdip interface region.

Our results also suggest that the interplate coupling in Oaxaca is variable in space and time (Figs. 6.5, E.10 and E.11). Such remarkable PIC variations might certainly be associated with changes in the mechanical properties of the fault zone materials induced by the dynamic perturbations of seismic waves from recent significant regional earthquakes (Cruz-Atienza et al., 2021; Materna et al., 2019; Delorey et al., 2015). However, PIC variations in the shallow, seismogenic zone (i.e., between 10 and 20 km depth) are somehow linked to the occurrence of long-term deeper SSEs (Figs. 6.5b and E.11c). To explain these variations at shallow depths we favor the idea involving transient fluctuations of fluid pressure, as proposed for the long-term SSEs in the Guerrero (Cruz-Atienza et al., 2018b), southern Cascadia (Materna et al., 2019), Japan (Bedford et al., 2020) and Hikurangi (Warren-Smith et al., 2019) subduction zones. Recent models evoking the fault-valving concept show that overpressure fluid pulses migrate upward as the permeability evolves in the fault zone due to slow deformation processes (Cruz-Atienza et al., 2018b; Shapiro et al., 2018; Zhu et al., 2020). These transient changes in pore pressure may lead to large variations of the fault strength as high as 10-20 MPa (Zhu et al., 2020), which makes this mechanism a plausible candidate to explain the strong and systematic PIC variations we found in the shallow seismogenic zone of Oaxaca during the occurrence of SSEs.

Earthquake potential depends on the state of stress along the subduction zone which, as shown here, is a function of different evolving processes taking place from the trench to its deep portion, where the mechanical interaction between the plates ceases. The stress build-up therefore changes over time and space in a complex way, so does the earthquake potential. Time-invariant estimates of the interplate coupling are often used to identify seismogenic segments prone to large earthquakes (Chlieh et al., 2008; Loveless and Meade, 2011; Moreno et al., 2010; Perfettini et al., 2010). However, while these estimates are certainly useful on a large spatial and temporal scale, they do not provide a reliable picture of the earthquake potential associated with smaller ($7 < M < 8.5$) but potentially devastating ruptures that occur more frequently, as shown in this work for the Oaxaca megathrust.

Our results indicate that continuous and systematic monitoring of the interplate slip velocity, incorporating simultaneously in a continuum the stressing (i.e., coupled) and relaxing (i.e., slow, coseismic and postseismic) slip regions, provides a more reliable reconstruction of the short-term stress evolution over the megathrust and, probably also, of the long-term evolution, which could provide significant insights into the M8+ earthquake supercycles. Proceeding this way may thus be relevant to evaluate theoretical predictions of the interface dynamics, which is our leading approach to understand the underlying physics in subduction systems.

6.6 Conclusions

We analyzed the interplate slip-rate evolution during more than 3.5 years in the Oaxaca subduction zone including the pre-seismic, coseismic and post-seismic phases associated with the June 23, 2020 Mw 7.4 Huatulco earthquake to understand how the different slip processes contribute to the plate-interface stress accumulation in the region. We found that the main rupture area of the Huatulco earthquake extents between 20 and 30 km depth with two main and compact slip patches, the most prominent north the hypocenter and the other close to the coast, east-northeast of the hypocenter. The 2020 SSE that occurred before the earthquake did not penetrate the rupture area and was preceded by a gradual interface decoupling process at a regional scale, including the maximum SSE slip area. During the two months preceding the earthquake, when the 2020 SSE developed, the Huatulco earthquake rupture area became fully locked. Our slip inversions indicate that the two-month earthquake afterslip overlapped the whole coseismic rupture area and propagated both to the trench and downdip to the northwest, where most of aftershocks happened and where the 2020 SSE was developing, respectively. During the post-seismic phase, the rupture area of the 1978 Puerto Escondido earthquake became and remained fully coupled. The interplate slip-rate evolution in Oaxaca during the 3.5 years preceding the Huatulco earthquake shows that PIC in the megathrust seismogenic region is highly variable in time and space. One prominent feature of such variations is a clear correlation between PIC increments at shallow depths (10-20 km, including the 1978 rupture area) and the occurrence of three successive SSEs far downdip, suggesting a physical interaction between aseismic slip processes in nearby regions that simultaneously relax and load the plate interface.

We also found that both relaxing aseismic slip events and megathrust coupling changes during those 3.5 years produced a high stress concentration (800 kPa) over the main asperities of the Huatulco earthquake, as well as a large and shallow (offshore) stress reduction (-900 kPa) that may have impeded (along with other possible factors) the updip propagation of the earthquake. Our results indicate that continuous monitoring of the interplate aseismic slip-rate and its CFS counterpart provide a better estimation of M7+ earthquake potential over seismogenic regions than predictions detached from time-independent interplate coupling models. Finally, the stress imparted during the coseismic and postseismic phases of the Huatulco earthquake on the 1978 Puerto Escondido rupture area (and its downdip portion between 20 and 30 km depth) makes it a region prone to the next earthquake in the near future, a prediction that is consistent with the 50 years earthquake return period in the Oaxaca region.

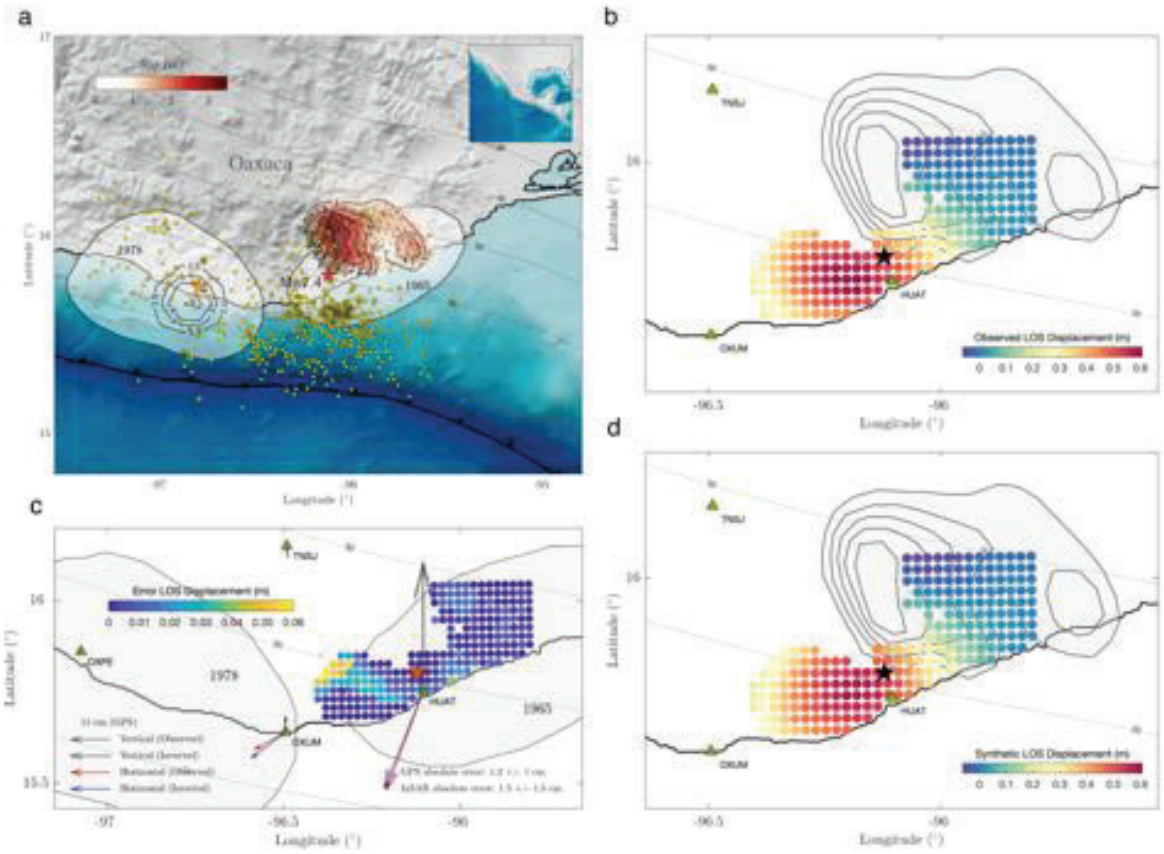

Figure 6.1. Coseismic slip inversion of the 2020 Mw 7.4 Huatulco earthquake. a Red colored region with black contours indicates the slip on the plate interface for our preferred joint GPS and InSAR slip inversion. Red and orange stars indicate the epicenters of the Huatulco and the 1978 Puerto Escondido earthquakes, respectively. Black contours around the 1978 Puerto Escondido epicenter represent the 1.5, 3, 4 and 6 m slip isolines determined by Mikumo et al. (2002). White shaded patches show the aftershock areas of the historic thrust earthquakes of 1965 and 1978. Yellow dots depict the first 50 days Huatulco earthquake aftershocks reported by the SSN. Gray contours indicate the iso-depths of the 3D plate interface used for the slip inversions in this study. b and d show the observed and synthetic line-of-sight (LOS) InSAR displacements, respectively (see Figure S2). c Misfit between observed and predicted LOS and GNSS surface displacements for our preferred slip model show in a (see Figure S3).

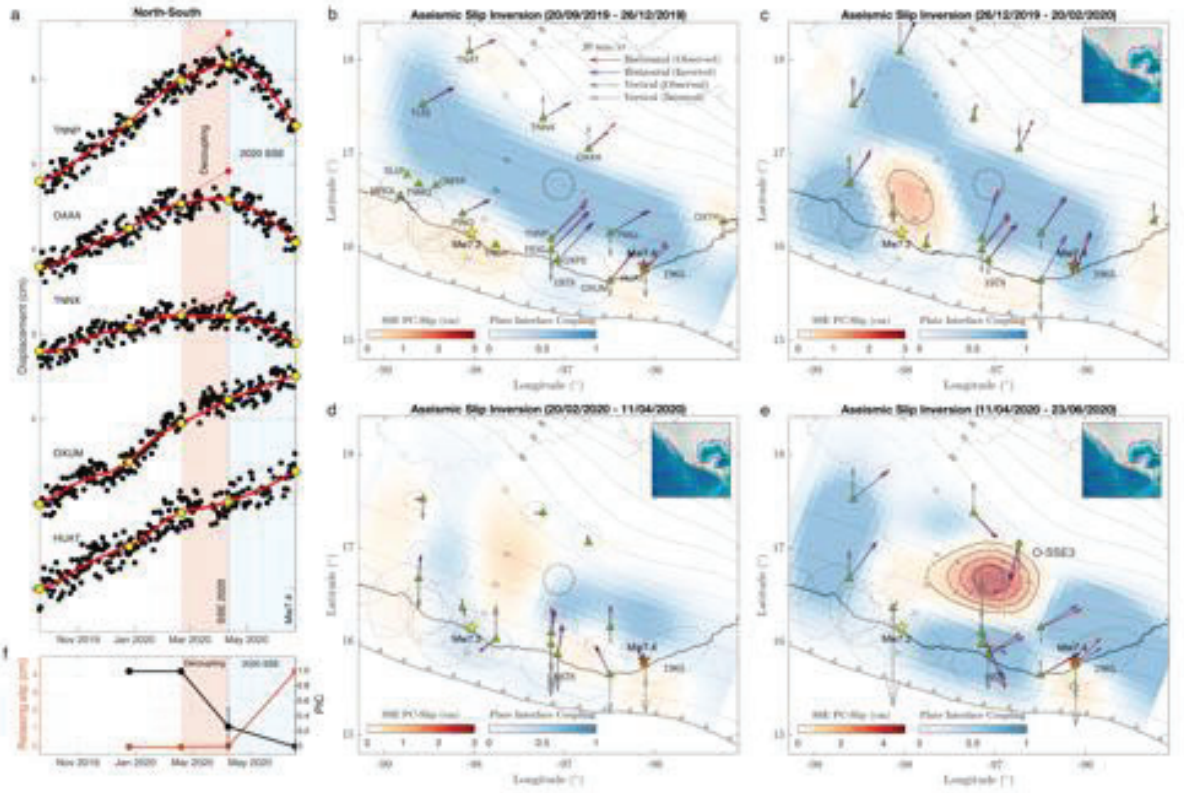

Figure 6.2. GNSS inversions of the 9-month deformation period prior to the June 23, 2020, Mw 7.4 Huatulco earthquake. a North-south GNSS time series in 5 selected stations. Yellow dots indicate the beginning and end of the four time-windows used for the slip inversions shown in b-e, and red dashed lines depict the inter-SSE displacement trend during the interface decoupling phase. b-e Inverted slip in the plate-convergence (PC) direction for all time windows. Slip contours are in centimeters. Red and yellow stars indicate the epicenters of the Huatulco and 2018 Pinotepa (Mw 7.2) earthquakes, respectively. Dashed regions are the aftershock areas of historic interplate earthquakes. Gray ellipses around the arrow tips are represent one standard deviations of the observed displacements. f Average and standard deviation (vertical bars) of the plate interface coupling (PIC) and relaxing slip in the region where the 2020 SSE developed (i.e., within the dotted black circle in b-e).

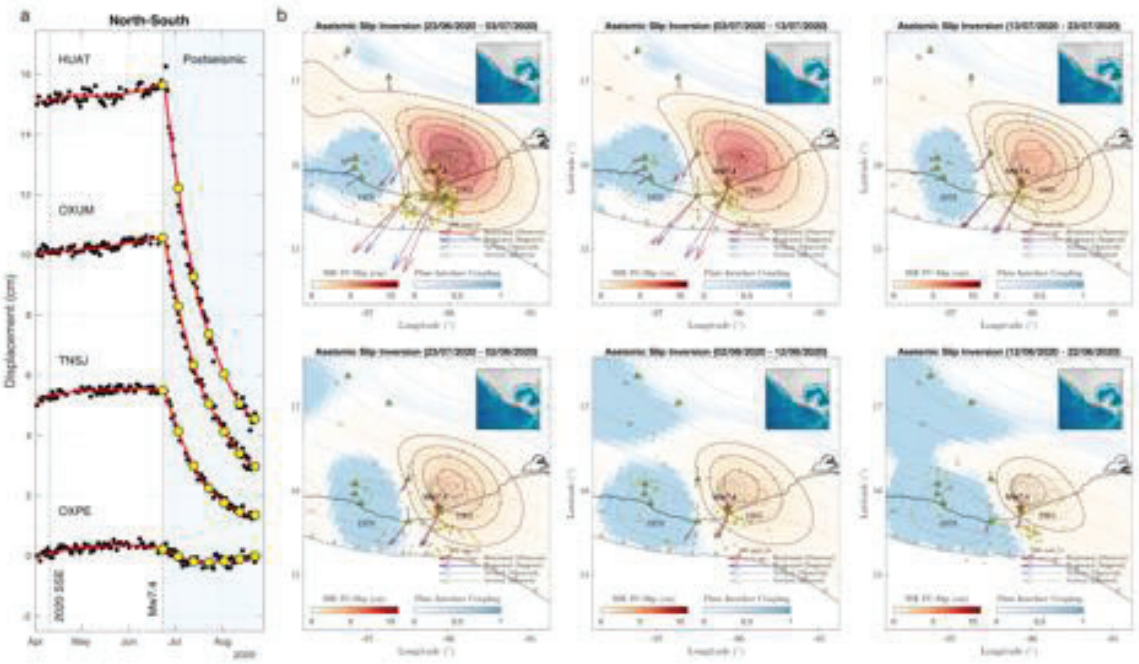

Figure 6.3. GNSS inversion of the postseismic deformation of the Huatulco earthquake. a North-south displacement GNSS time series in 4 selected stations. Yellow dots indicate the start and the end of the six 10-day windows used for the slip inversions shown in b. b Aseismic slip inversion for the two months following the Huatulco earthquake.Thick light gray contours are the coseismic slip shown in figure 1a.

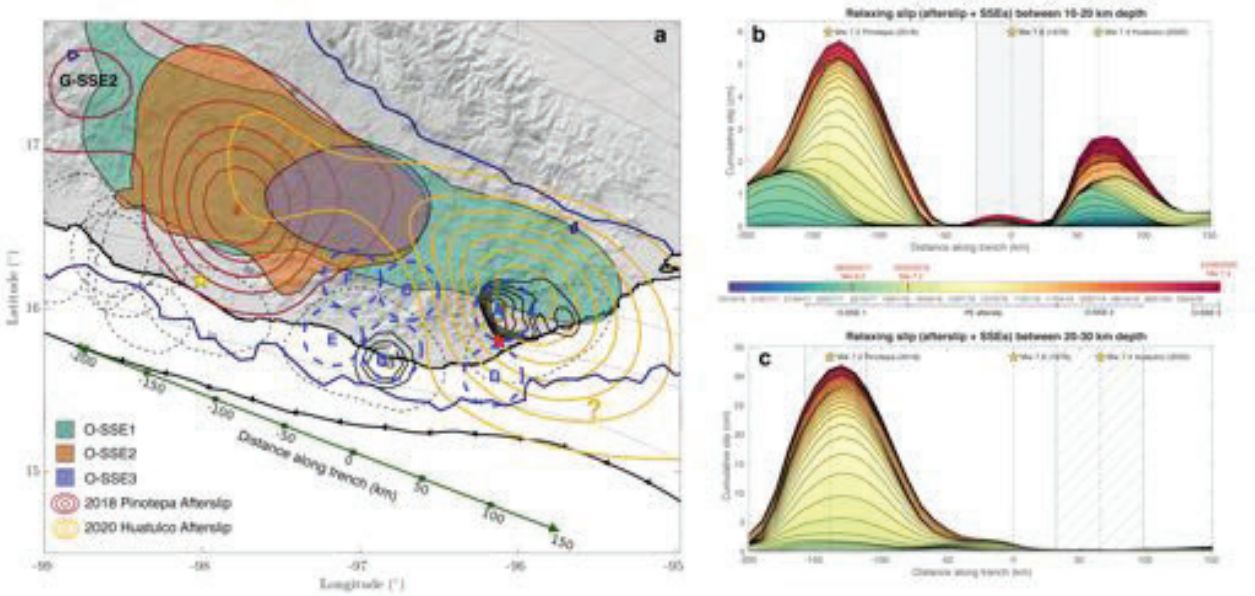

Figure 6.4. Aseismic slip at the plate interface in Oaxaca. a Summary of the aseismic slip processes (SSEs and afterslip) occurring from October 2016 to August 2020 in Oaxaca. Colored patches indicate the SSEs regions with slip values higher than 1.5 cm. Colored contours depict the afterslip of the Pinotepa and Huatulco earthquakes with slip isolines every 5 cm beginning with 1.5 cm. Dark blue contour indicates the region with restitution indexes higher than 0.5 from Figure S8b. Red, orange and yellow stars indicate the hypocenter of the Huatulco, the 1978 Puerto Escondido and the Pinotepa earthquakes, respectively. Dashed blue circles represents the areas where we analyze the evolution of the interplate slip rate and the CFS shown in Figs. 5 and S13. Green line indicates the along-trench profile where the evolution of the aseismic slip and CFS on the plate interface is analyzed in b and c and Figs. 6 and 7. b and c show the evolution of the relaxing aseismic slip (SSEs and afterslip) along the trench within the seismogenic zone averaged between 20-30 and 10-20 km depth, respectively. Hatched regions show the interplate segments with the highest moment release of the 2018 Pinotepa, 1978 Puerto Escondido and 2020 Huatulco earthquakes. Stars and dashed black lines indicate the along-trench coordinate of the hypocenters.

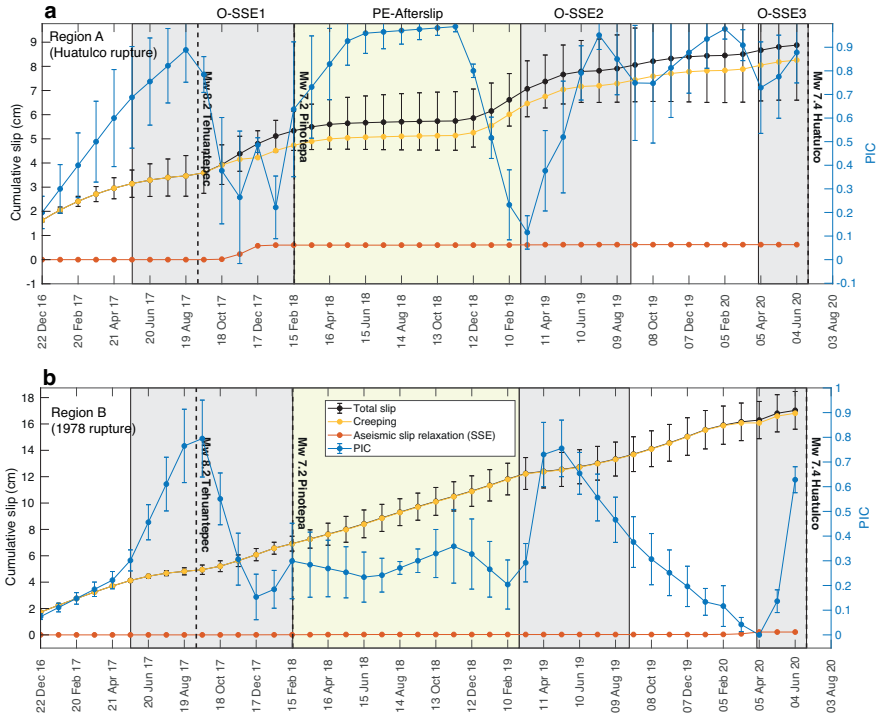

Figure 6.5. Detailed evolution of the aseismic slip in the seismogenic segment of Oaxaca. Time series show the cumulative total slip, creeping (slip under coupling regime), relaxing slip (SSEs) and plate interface coupling (PIC) in (a) Region A (the Huatulco rupture area) and (b) Region B (the 1978 Puerto Escondido rupture area) (see Figure 4). Gray rectangles indicate the time windows of the downdip SSEs in Oaxaca. The light-yellow rectangle depicts the timespan of the 2018 Pinotepa earthquake afterslip in the region.

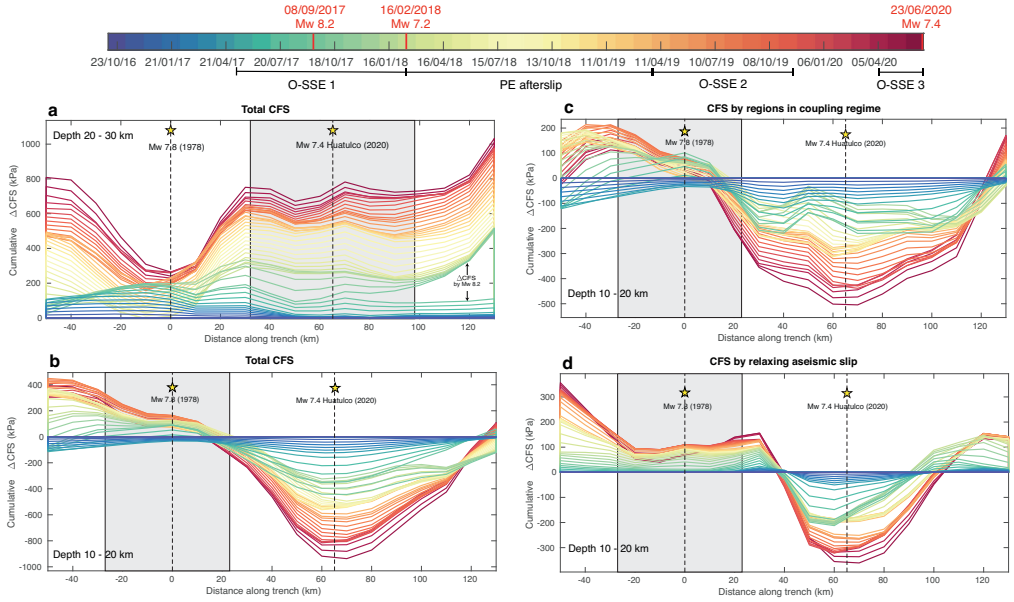

Figure 6.6. Evolution of the CFS in the seismogenic segment of Oaxaca. Evolution of the total CFS along the trench for every 30 days averaged between a 20-30 km and b 10-20 km depth. Gray rectangles show the interplate segments with the highest moment release of the 2020 Huatulco earthquake and the 1978 Puerto Escondido event (Mikumo et al., 2002). c and d show the evolution of the CFS for the band between 10-20 km depth split into the contributions from regions in coupling regime and the relaxing aseismic slip, respectively.

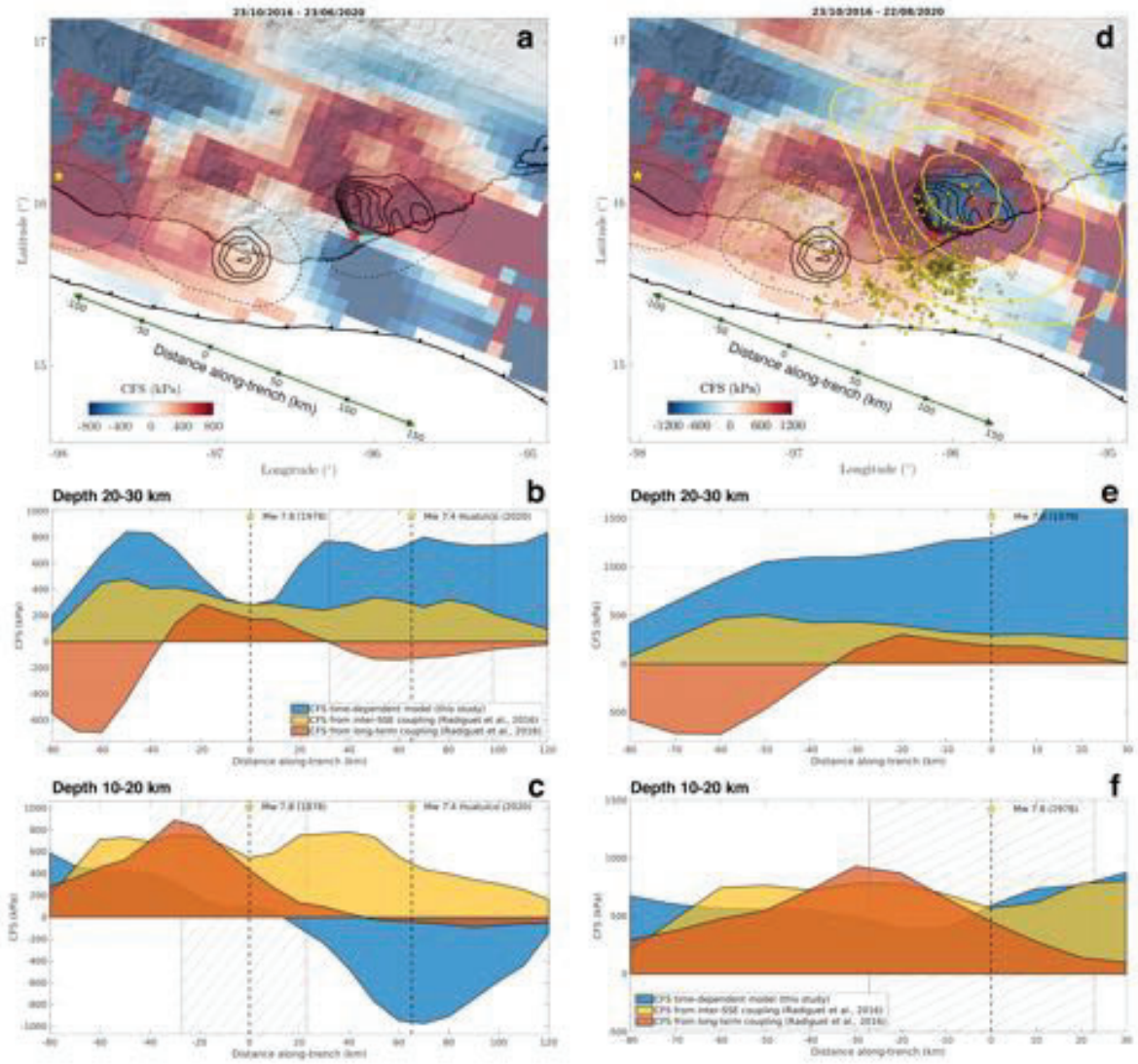

Figure 6.7. Cumulative CFS from the time-variant model and its comparison with the stress built up predicted by time-invariant coupling models. a Cumulative CFS in the plate interface between October 2016 and the date of the 2020 Huatulco earthquake. Black contours represent the isoslip values for the 2020 Huatulco and 1978 Puerto Escondido (Mikumo et al., 2002) earthquakes. Black dashed lines delimit the aftershock areas of historic interplate earthquakes. White dashed circles represent the regions where we analyze the evolution of the interplate slip rate and the CFS shown in figures 6, 7c and 7d. b, c Comparison between our cumulative CFS time-variant model and the CFS predicted by time-invariant coupling models of the region (Radiguet et al., 2016) between October 2016 and the date of the 2020 Huatulco earthquake for two depth bands, between 20-30 km depth and between 10-20 km depth, respectively. d Same than a but including the stress contributions from the coseismic and postseismic phases of the Huatulco earthquake. Yellow contours are the 5,10,20 and 30 cm slip isolines of the two months cumulative afterslip. Yellow dots depict the 50 days aftershocks after the Huatulco Earthquake reported by the SSN. e,f Same as b,c but including the stress contribution from the coseismic and postseismic phases of the Huatulco earthquake focused only in the 1978 rupture segment.

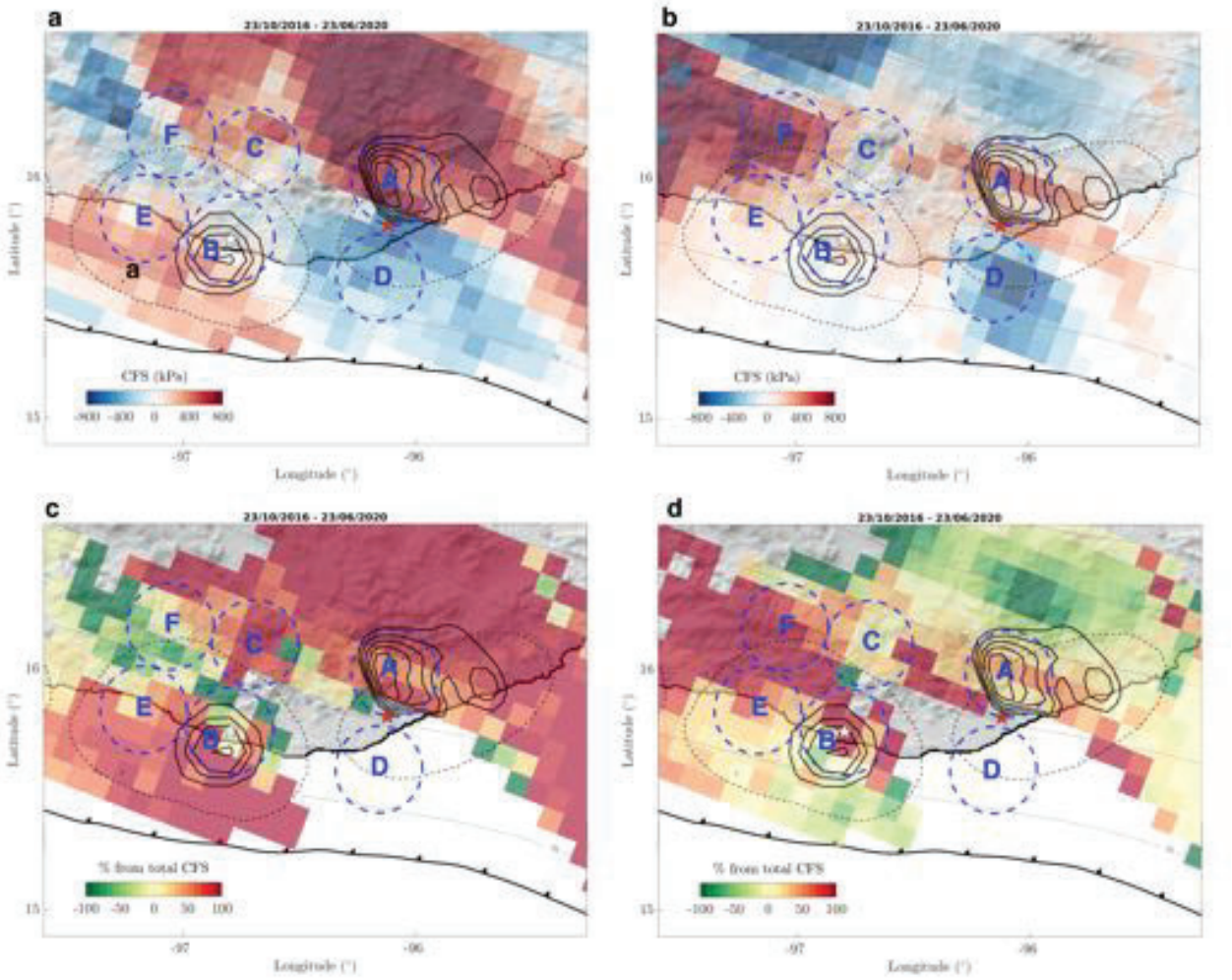

Figure 6.8. CFS contributions by regions in coupling regime and relaxing slip. a and b show the cumulative CFS contributions in the plate interface between October 2016 and the date of the 2020 Huatulco earthquake associated with regions in coupling regime and relaxing slip, respectively. c and d show the CFS contributions (in %) on the plate interface where the total CFS is positive (see figure 7a) by regions in coupling regime and relaxing slip, respectively

Chapter 7

Conclusions

With this dissertation we contribute to the understanding of the underlying processes that are responsible of different interplate slip phenomena and their spatiotemporal interaction during the seismic cycle by means of both observational and modeling approaches. We investigated the different aseismic slip processes taking place along the Mexican subduction zone, their causal relationship with tectonic tremor and, more importantly, their interaction with large earthquakes. The results of this investigation are presented in 5 published/submitted research articles which correspond to each of the main chapters of the manuscript.

In Chapter 2 we provide insights into the causal relationship linking TTs and SSEs in Guerrero by analyzing the evolution of the elastic fields induced by the long-term 2006 SSE together with independent new locations of TTs we determined using the TREP method (Cruz-Atienza et al., 2015) and a catalog of low-frequency earthquakes in the region. We found that the SSE slip rate modulates the TT and LFE occurrence rate in the whole tremor region, suggesting that the driving force of TT radiation is the stressing rate history of the locked asperities that are surrounded by the SSE and modulated by its slip rate. Based on these results we estimated that the frictional strength of the asperities radiating tremor downdip (i.e., in the so-called sweet spot) is around 3 kPa, which is 2.2 times smaller than the corresponding value updip (i.e., in the so-called transient zone), partly explaining the overwhelming tremor activity of the sweet spot despite that the slow slip there is almost three times smaller. Based on the LFEs occurrence rate history during the inter-SSE period we also determined that the short-term SSEs in Guerrero take place further downdip (i.e., about 35 km farther from the coast) than previously estimated by (Frank et al., 2015a), overlapping the sweet spot.

In Chapter 3, we investigate more complex fault-zone processes on the plate interface that are manifested as rapid tremor migrations (RTM). Based on multiple RTMs found in Guerrero from our TT locations and the conditions of overpressured fluids at the interface where SSEs and TT take place, we introduced a non-linear fluid diffusion model that explains the existance of secondary slow slip pulses (SSP) during SSEs, which are believed to generate the RTMs in different subduction zones. Our model shows that the origin of SSPs is likely to be solitary pore-pressure waves in the plate interface, propagating with speeds and pathways similar to those observed for RTMs across the globe, including Guerrero. We demonstrate that these waves may explain the whole hierarchy of RTM patterns (e.g., rapid tremor reversals and slip-parallel streaks) by producing transient reductions of the fault strength and thus SSPs in the observed RTM directions during slow earthquakes. This model is valid for the conditions expected in different subduction zones such as Cascadia and provide a physical explanation of this phenomenon in Guerrero. The model we

propose may help to better understand the fault system in different geophysical conditions, such as geothermal fields, volcanic systems and production wells with induced seismicity, where the seismic hazard is high and should be assessed by means of physics-based modeling considerations.

In Chapter 4, we introduce the ELADIN (ELastostatic ADjoint INversion) method, a new fault-slip inversion technique that uses the adjoint elastostatic equations under a constrained optimization framework. The ELADIN method allows determining the aseismic slip on any 3D plate interface (or any fault surface) from geodetic observations by simultaneously inverting the relaxing slip (i.e., SSEs, and/or co- and post-seismic slips) and the coupled fault areas with a spectral control of the solutions (i.e., their wavenumber content). This is achieved by means of a von Karman regularization function and a gradient projection method to guarantee that physically-consistent slip constraints are met. For estimating the resolution of the inverse problem, we introduced a mobile checkerboard analysis that allows to determine lower-bound fault resolution zones for an expected slip-patch size and a given stations array. We applied this analysis considering both the 3D plate interface geometry and the distribution of the GNSS stations in Guerrero and Oaxaca and found that the optimal regularization length (L) of 40 km in this region guarantees an inversion error under 50 % (i.e., median restitution indexes higher than 0.5) for slip patches larger than 80 km length at most interface depths greater than 10 km. We then inverted the 2006 Guerrero SSE and found that our preferred slip model has the most reliable features of two previously published slip models (Radiguet et al., 2011; Cavalié et al., 2013). However, although the three solutions predict an SSE shallow penetration along a large part of the northwest Guerrero seismic gap, our resolution analysis clearly shows that this penetration might not be a reliable feature of the 2006 SSE.

In the last two chapters, we analyze the four most recent and significant earthquakes in Mexico, namely, the 2017 (Mw 8.2) Tehuantepec and (Mw 7.1) Puebla-Morelos earthquakes, the 2018 (Mw 7.2) Pinotepa earthquake and the 2020 (Mw 7.4) Huatulco event, along with an unprecedented sequence of SSEs in Guerrero and Oaxaca to shed light on the physical processes leading to the interaction between these phenomena.

In Chapter 5, we reconstruct the history of both the interplate slip velocity (using the ELADIN method) and the Coulomb Failure Stress (CFS) across the Mexican megathrust from 2016 to 2019 (where five large SSEs and one post-slip relaxation took place in 2.8 years) and found that the 2017 intraslab Puebla-Morelos and 2018 interplate Pinotepa earthquakes, both devastating events, are likely related to SSEs and/or changes in the plate interface coupling (PIC), describing a cascade of events interacting (most of them) with each other on a regional scale via quasi-static and/or dynamic perturbations. Such interaction seems to be conditioned by the transient memory of Earth materials subject to the unprecedented dynamic deformations produced by seismic waves of the great 2017 (Mw 8.2) Tehuantepec earthquake, which strongly disturbed the SSE cycles over the Guerrero and Oaxaca segments of the subduction plate interface. The interaction among all these events can be summarized as follows:

1. SSEs in Guerrero (G-SSE1) and Oaxaca (O-SSE1) begun in 2017 before the 2017 Tehuantepec earthquake. 2. The transient stress/strain perturbations by the seismic waves of the great Tehuantepec event modified the mechanical conditions of both the plate interface and the 2017 Puebla-Morelos earthquake fault (i.e., a material modulus softening due to the fault-gouge non-linear elas-

tic response), and dynamically enhanced the along-strike bilateral development of the O-SSE1. 3. The downdip PIC changes associated with the G-SSE1 increased the CFS in the Puebla-Morelos earthquake fault, which was softened eleven days earlier by waves of the Tehuantepec earthquake, promoting the initiation of this event. 4. The downdip evolution of the O-SSE1 triggered the 2018 Mw 7.2 Pinotepa earthquake by increasing the CFS right in the earthquake nucleation zone. 5. The dynamic stress perturbations produced by the seismic waves of the 2018 Pinotepa earthquake triggered a second SSE in Guerrero (G-SSE2) west to the afterslip of this earthquake. 6. The third (G-SSE3) and second (O-SSE2) SSEs in Guerrero and Oaxaca, respectively, initiated almost simultaneously in 2019 just a few months after the preceding SSEs in each region.

In Chapter 6, we analyze the interplate slip-rate evolution during more than 3.8 years in the Oaxaca subduction zone before the June 23, 2020 Mw 7.4 Huatulco earthquake, including the pre-seismic, co-seismic and post-seismic phases associated with this earthquake (from October 2016 to August 2020). From the simultaneous inversion of GNSS and InSAR data using of the ELADIN method, we found that the main rupture area of the Huatulco earthquake extents between 20 and 33 km depth with two main and compact slip patches, the largest downdip from the hypocenter and the second to the east, below the coast. The 2020 SSE (O-SSE3) that occurred before the earthquake did not penetrate the rupture area and was preceded by a gradual interface decoupling process at a regional scale, including the maximum SSE slip area. Our aseismic slip inversions from GNSS data indicate that the first two-month earthquake afterslip overlapped the whole coseismic rupture area and spread downdip and northwestward where the 2020 SSE was developing. In addition, and probably more interesting, the afterslip rose offshore to the trench where most of the aftershocks occurred. The interplate slip-rate evolution in Oaxaca during the 3.5 years preceding the Huatulco earthquake shows that PIC in the megathrust seismogenic region is highly variable in time and space. One prominent feature of such variations is a clear correlation between PIC increments at shallow depths (10-20 km, including the 1978 Puerto Escondido rupture area) and the occurrence of three successive SSEs far downdip, suggesting a physical interaction between aseismic slip processes in nearby regions that simultaneously relax and load the plate interface. Based on very recent investigations, we speculate that this possible interaction could happen due to fluid migration at the plate interface induced by the SSEs strain-field pumping.

We also found that both relaxing aseismic slip events and megathrust coupling changes during those 3.5 years produced a high stress concentration of 750 kPa (7.5 bar) all over the main asperities of the Huatulco earthquake, as well as a large and shallow (offshore) stress reduction (i.e., a stress shadow) that may have impeded (along with other possible factors) the updip propagation of the earthquake. Finally, the stress imparted during the coseismic and postseismic phases of the Huatulco earthquake on the 1978 Puerto Escondido rupture area (and its downdip portion between 20 and 30 km depth with CFS increments higher than 1,100 kPa) makes it a region prone to the next earthquake in the near future, a prediction that is consistent with the 50-years earthquake return period in the Oaxaca region.

The results presented in this thesis indicate that a continuous and systematic monitoring of the interplate slip velocity incorporating simultaneously (in a continuum) the stressing (i.e., coupled) and relaxing (i.e., slow, coseismic and postseismic) slip regions, together with the tectonic tremor activity is necessary to generate more reliable reconstructions of the short-term stress evolution over

the megathrust, and thus, to provide a better estimation of the earthquake potential. Proceeding this way may thus be relevant to evaluate theoretical predictions of the interface dynamics, which is our leading approach to understand the underlying physics in subduction systems.

Appendix A

A.1 Supplementary information for Chapter 2

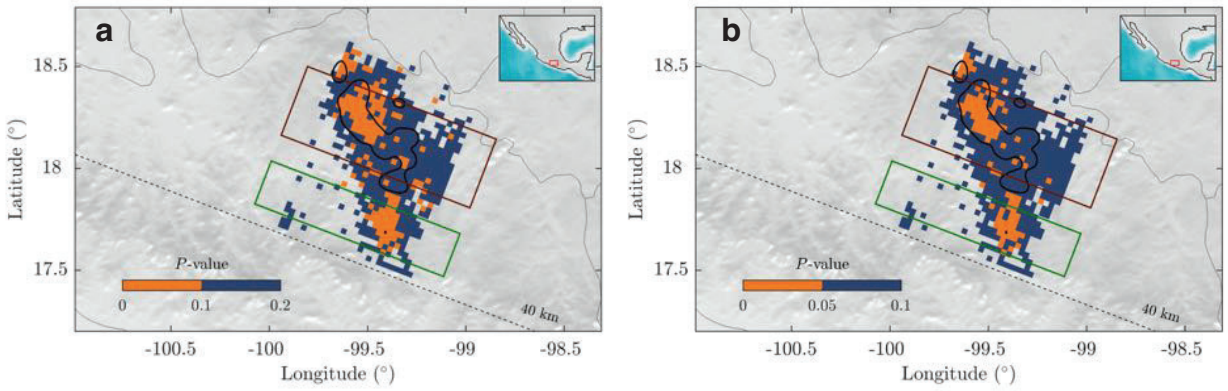

Figure A.1. p-value distribution determined under the null hypothesis that the activity of TTs and the evolution of the slip rate are not correlated. Orange bins indicate the regions where the null hypothesis is rejected at the 90 % (a) and 95 % (b) confidence level. The black contours represent the regions with the highest occurrence of TTs. The green and maroon rectangles indicate the Transient Zone and the Sweet Spot, respectively

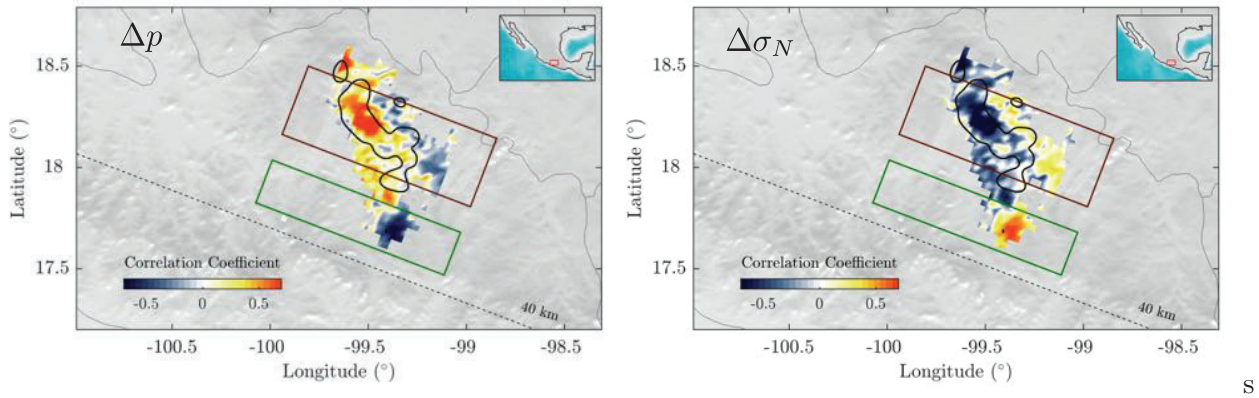

s

Figure A.2. Correlation coefficient distribution between the activity of TTs and the evolution of the pore pressure change $\triangle p$ (left) and the normal stress change $\triangle\sigma_N$ (right) during the 2006 SSE. The black contours indicate the regions with the highest occurrence of TTs. Green and maroon boxes insdicate the transient zone and the sweet spot, respectively. Note that in the Sweet spot exist a highly positive correlation between the activity of TT and the $\triangle p$, which is counteracted by a high anticorrelation between the activity of TT and the $\triangle\sigma_N$

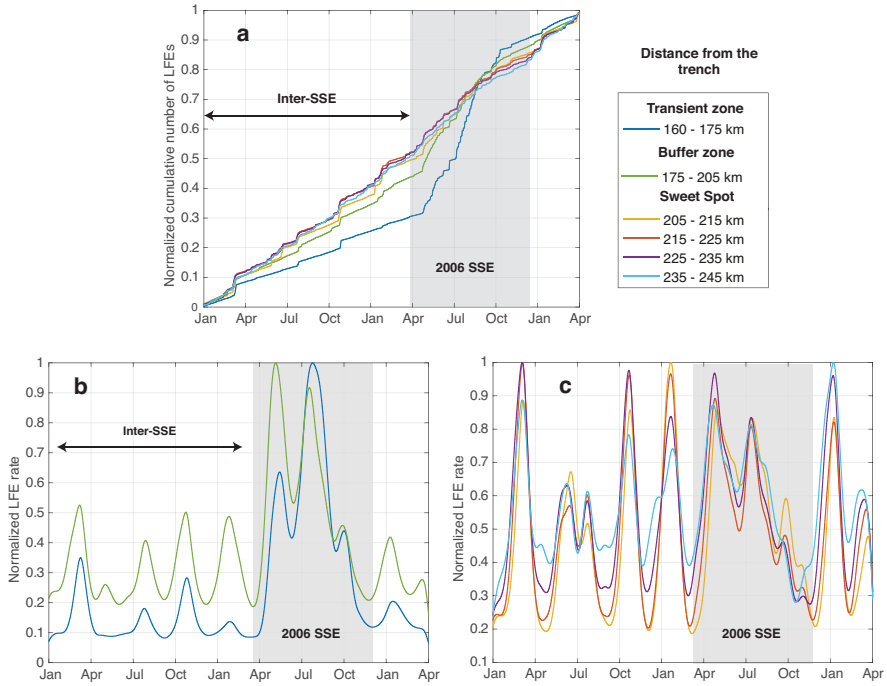

Figure A.3. LFE occurrence-rate in Guerrero during the 2006 SSE (gray box) and the inter-SSE period. (a) Normalized cumulative number of LFEs sorted by their distance from the trench. LFE occurrence-rate in the transient zone and the buffer zone (Bb), and in the sweet spot (c) filtered for periods longer than 40 days.

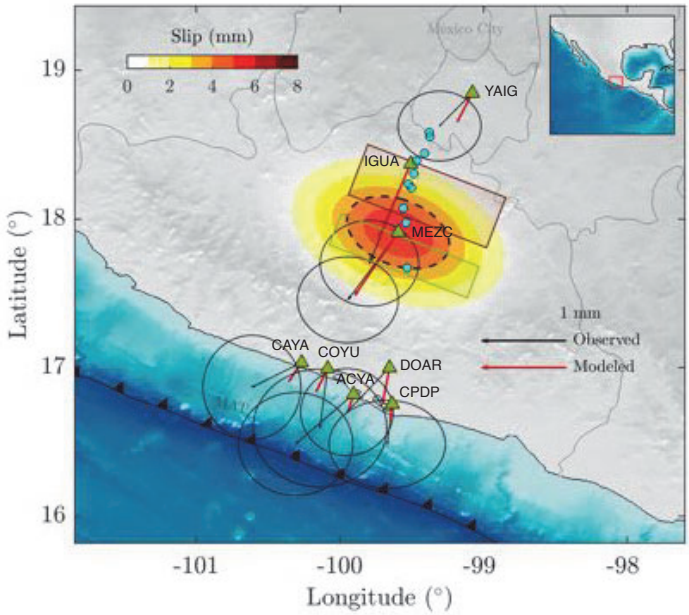

Figure A.4. Gaussian-like slip distribution considered to represent the small short-term SSE found by Frank et al. (2015b). The dashed black ellipse approximates the 4mm isoslip contour of the short-term SSE. As a reference, the cyan circles indicate the MASE stations shown in Figure 1 of Frank et al. (2015b). Green triangles represent the local GPS stations. The observed surface displacements are shown in black arrows with their corresponded 1σ error ellipses and red arrows represent the predicted surface displacement by our slip approximation. The maximum of 6 mm lies between the two TT source region (i.e., in the buffer zone).

Appendix B

B.1 Supplementary information for Chapter 3

B.1.1 Verification of the 2D Finite Volume Method

To verify the implementation of our 2D FV solver for the diffusion equation (1), in this section we compare numerical predictions yielded by the FV approach with an analytical solution for a given problem with constant k in space and time. We had to make this assumption because, to our knowledge, there is no analytical solution for Equation (1) given the exponential form of $k(P_e)$ of the Equation (2), both of the main text. To approximate constant k in our approach we simply set parameter γ to zero.

For setting the pore pressure initial conditions of the problem, we chose de following function

$$p(x, z, t) = \exp(-2Kt)\cos(x)\cos(z), \tag{B.1}$$

which is a solution of Equation (1) of the main text for constant k and the no-flux Neumann boundary conditions introduced in the section of Methods (Oñeil, 2011). From this function we can built the initial conditions for p simply by making t=0. As shown in Supplementary Figure B.8a.

To complete the benchmark problem we assumed a constant diffusivity $K = \zeta k = 2m/s$ in the whole arbitrary domain defined by $[0, 2\pi]$ in each direction.

Supplementary Figure B.8b presents the comparison of both solutions for $t = 0.5$ and 2.0 s. The red solid lines represent the analytical solution, while the blue dashed lines show the numerical solution yielded by our FV approach. Solutions correspond to p values along the diagonal dashed line of Supplementary Figure B.8a. As a reference, the black curve shows the initial conditions along the same line. The excellent match between both predictions proves that the FV approach converges and produces accurate enough solutions.

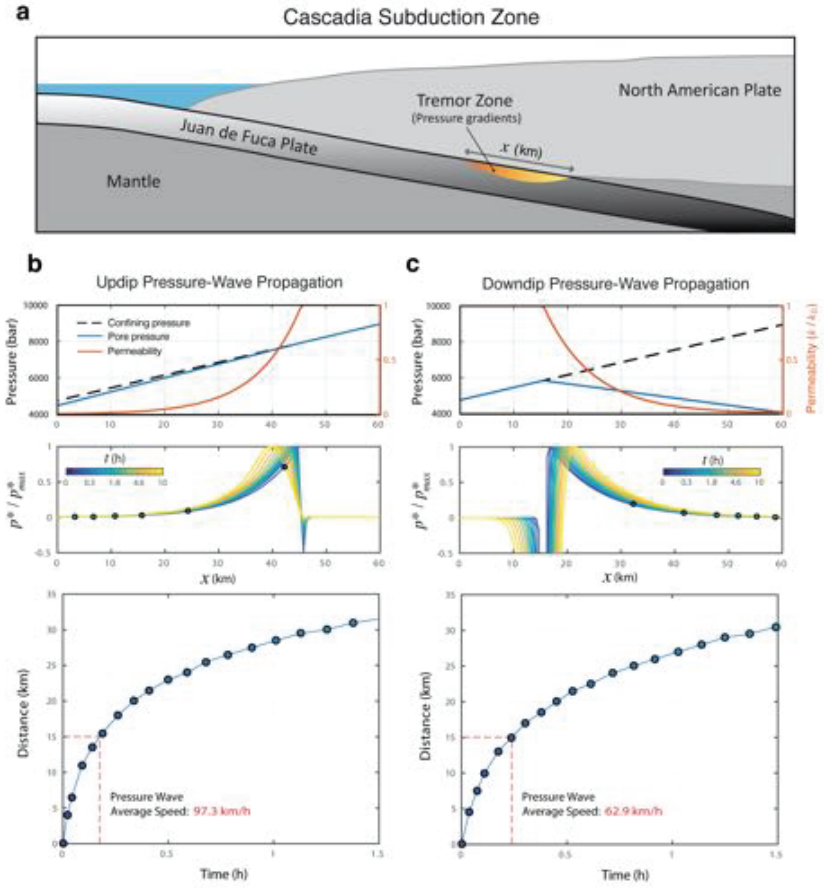

Figure B.1. RTM in Nankai and Cascadia exhibit a wide diversity of behaviors. For instance, most of the so-called streaks propagate in both the down-dip and up-dip opposite directions (Shelly et al., 2007a; Ghosh et al., 2010; Bletery et al., 2017). In contrast with the horizontal configuration of the slab in Guerrero (Figures 2 and 5a), in these subduction zones the OC sinks into the earth producing P_c gradients in the slip-parallel direction. This supplementary condition along with localized dehydration pulses and local variations of the plate-interface geometry may induce complex pore-pressure gradients likely to produce pressure waves in both directions within the active SSE front. In this figure we show the simulation results for two non-exhaustive examples considering the interface geometry in Cascadia, where pressure waves propagate in both opposite along-dip directions. (a) Cartoon showing the geometry of the Juan de Fuca plate under the continent. Gradient of gray colors illustrate the lithostatic pressure in the subducted slab, while the color gradient illustrate local pore pressure changes where RTMs are observed. (b) and (c) show, from top to bottom, the simulation initial conditions (for constant k_0 = 1e-13 m^2), the pressure-waves propagation (where $p^* = p - p_0$) and the wave-front speed (p threshold of 3 kPa) for both updip and downdip propagation directions, respectively. The purpose of these simulations is just to illustrate that even in the presence of a downdip lithostatic pressure gradient, pressure-waves can propagate in both opposite directions with speeds similar to those observed in Cascadia. Although plausible, these Cascadia-like models should certainly be explored in future investigations.

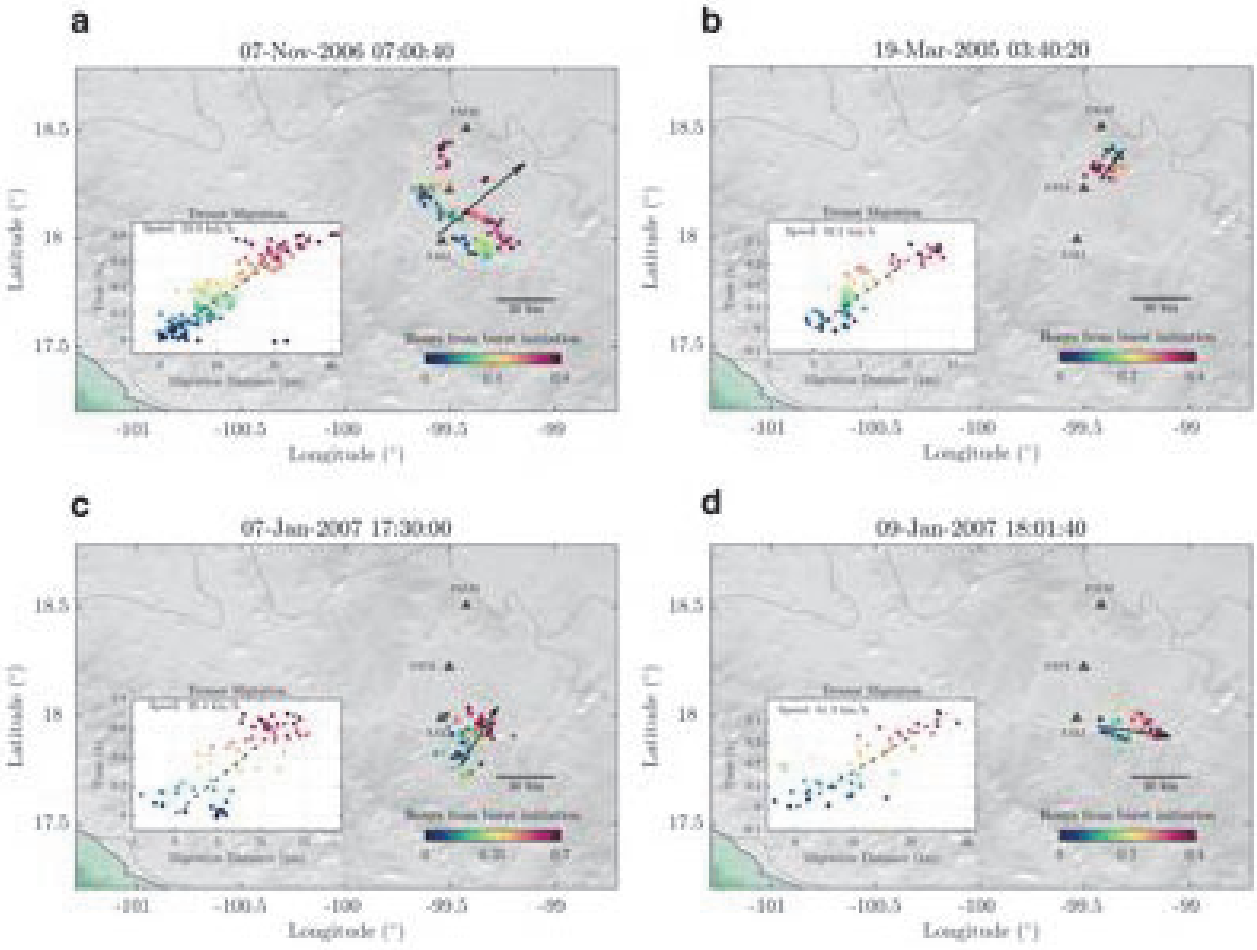

Figure B.2. Four examples of RTMs in Guerrero determined with the TREP method (Cruz-Atienza et al., 2015) (panels a to d). Tremor hypocenters were determined from one-minute moving windows with 20 s overlap. Hypocentral projections onto migration directions (black arrows) are show in the insets, where migration speeds are reported. The basemaps were created using SRTM15+ data.

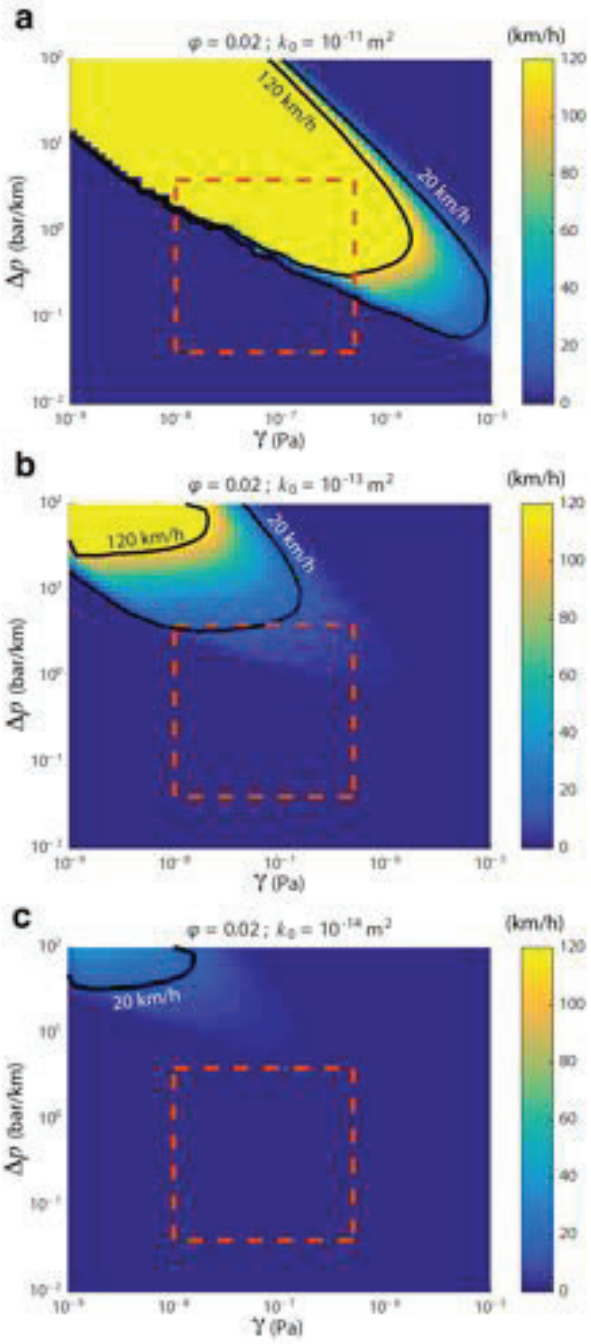

Figure B.3. Results from the parametric analysis of Equation 2 (main text) in terms of pressure-wave speeds (color shaded) for three different permeabilities k_0 (panels a to c) and a wave-front threshold of 3 kPa. Pressure-waves speed values between the black curves include those observed for RTMs in Guerrero. Red square delineates γ values observed in laboratory experiments (Evans et al., 1997) and the maximum pore-pressure gradient induced by the 2006 SSE (lower limit) and an arbitrary upper limit.

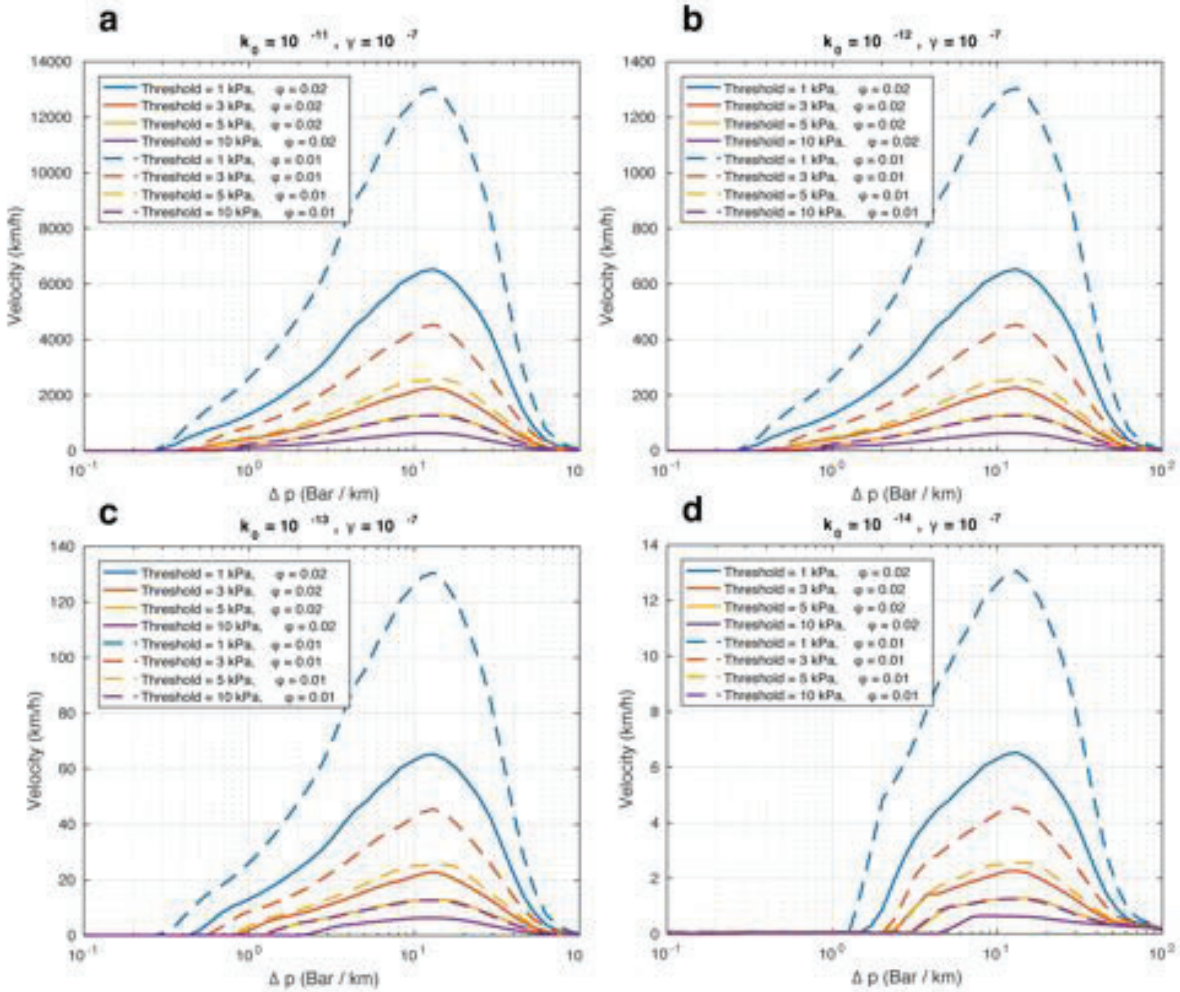

Figure B.4. Pore-pressure wave speeds (vertical axes) as a function of the pore-pressure gradient for four different permeabilities k_0 (panels a to d) detached from the parametric analysis of Equation 2 (main text). In each panel, we report wave speeds for four different values of the wave-front threshold and two values of porosity (i.e. 1 % and 2 %).

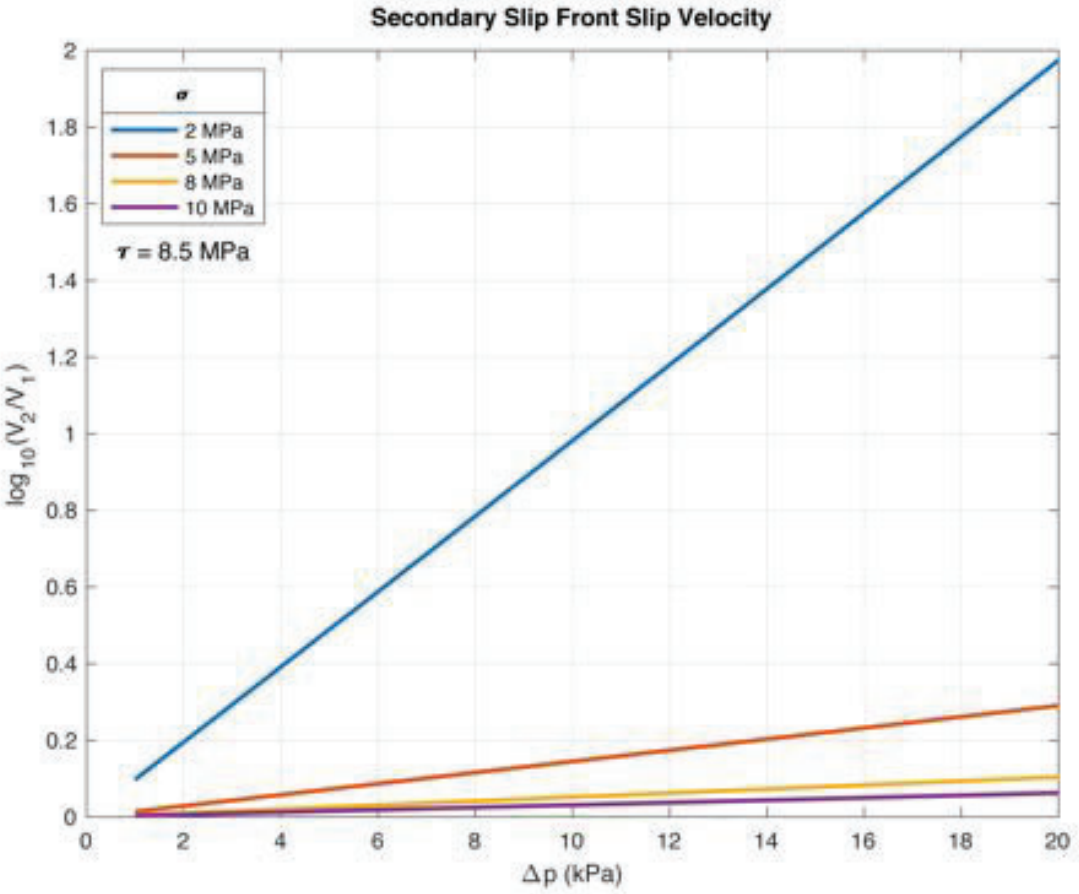

Figure B.5. Exponential growth of Secondary Slip Fronts (SSF) slip velocity (V_2) relative to the SSE slip velocity (V_1) under stable conditions in a R&S friction framework (i.e. velocity strengthening parameters) as a function of the pore pressure increment (Δp) in the fault. V_1 and V_2 represent the slip rates before and after the pore pressure increment has been applied, respectively, with constant shear (τ) and normal (σ) fault tractions. These curves have been generated using Equation 3 of the main text, which has been introduced by (Liu and Rice, 2007) for modeling SSEs.

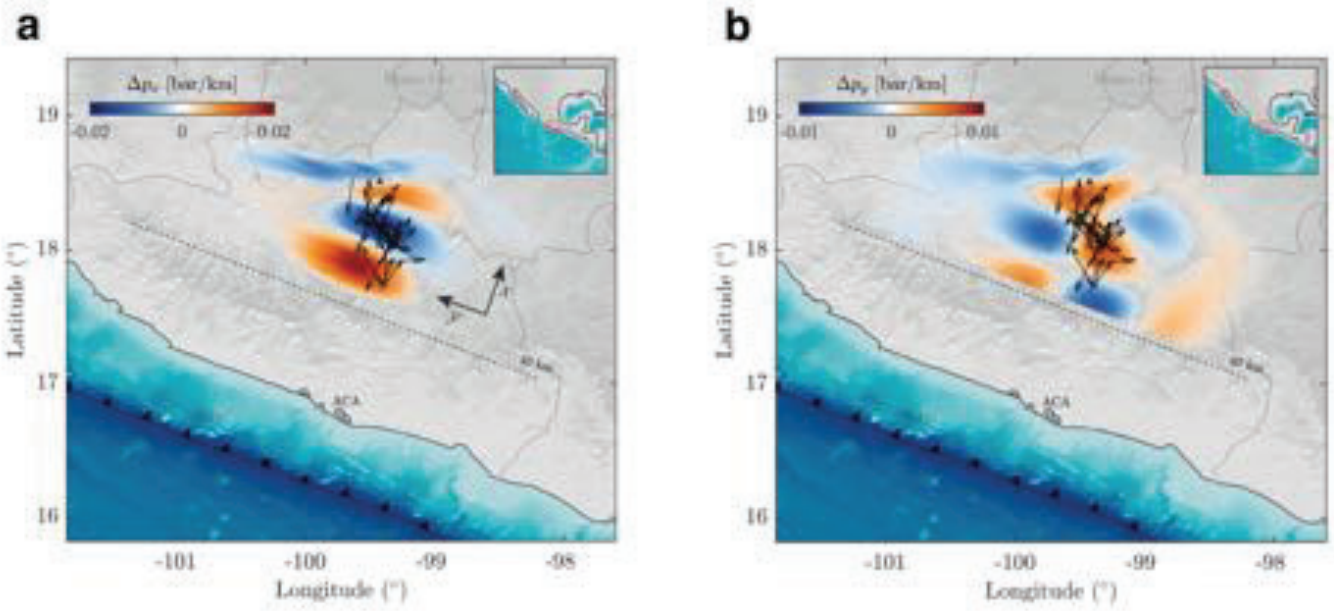

Figure B.6. Final pore-pressure gradient components (blue-red colors) induced by the 2006 SSE in the along-dip (a) and trench-parallel (b) directions (see main text). Blue colors indicate pressure reduction away from the trench in (a), and along the northwest trench-parallel direction in (b). Black arrows show the locations and propagation directions of the 54 RTMs found in the catalog. To calculate the gradient we simply estimated the change in p from the change in P_c assuming undrained conditions with a Skempton coefficient $B = 0.8$ (i.e. $p = B * Pc$) (Villafuerte and Cruz-Atienza, 2017). Two things stand out from the left figure: (1) most of RTMs in the down-dip direction lie within the minimum of the p gradient (blue colors), and (2) the minimum p gradient indicates a pore-pressure reduction with distance from the trench (i.e. in the RTM direction). This seems consistent with Equation 2, which predicts the propagation of pore-pressure waves towards depressurised regions (Figures 1a and S3). However, the maximum gradient values induced by the SSE (0.02 bar/km) are significantly smaller that those required to produce waves with the expected speeds (Table S2). Although the residual strain field from past SSEs may probably lead to larger pressure gradients, an additional preexistent gradient seems necessary in Guerrero to meet the conditions for rapid pressure-waves propagation. The basemaps and inset maps were created using SRTM15+ data.

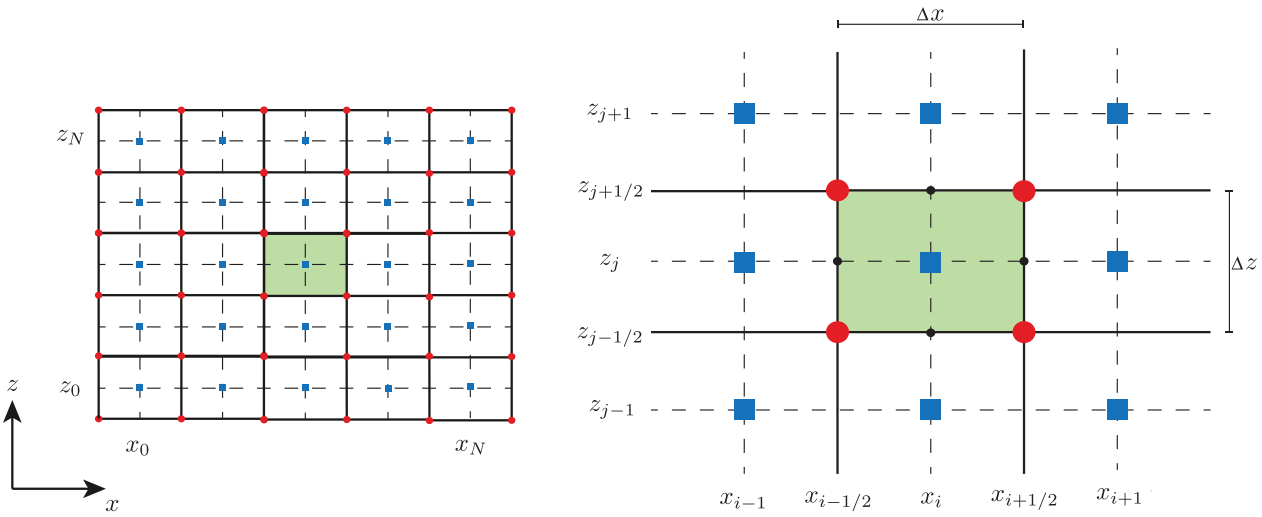

Figure B.7. Discretization of the 2D domain and representation of a cell volume $\triangle V$ (green cell). Values of the cell volumes are represented by blue squares in the center of each cell and the corner values by red circles. The black dots represent values over the faces of each cell. For this example $N = M$.

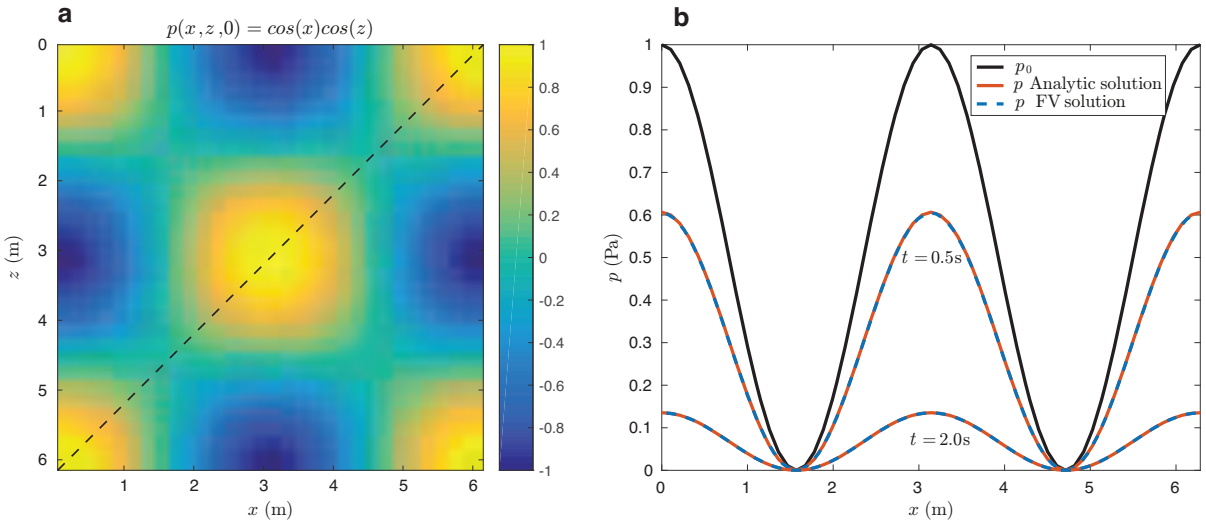

Figure B.8. (a) Initial conditions for p in 2D given by Equation B.1 for $t = 0$.(b) Verification between the analytical (red) and the FV (dashed blue) solution over a diagonal section (black dashed line in a) for two different times at 0.5 and 2.0 seconds over the section. The black curve represent the initial condition of p over the dashed diagonal in a).

Appendix C

C.1 Computation of the projection matrix

The projection matrix, $\underline{\underline{F}}$, can be computed with any correlation function and with different strategies. For reproducibility purposes, we explain in the following algorithm how we compute it.

Algorithm 2: Computation of the projection matrix: $\underline{\underline{F}}$

---

1. With the von Karman autocorrelation function, eq. (4.7), compute the Von Karman mask, $\underline{\underline{V}} \in \mathbb{R}^{M_p \times M_c}$, which has the same dimensions as the fault domain with M_p and M_c the number of subfaults along p- and c-directions, respectively.
2. Build the convolution matrix, $\underline{\underline{C}} \in \mathbb{R}^{M \times M}$, with replication and the Von Karman mask, $\underline{\underline{V}}$. $\underline{\underline{C}}$ is a square matrix with dimension $M = M_p \cdot M_c$. For the arithmetic details, we recommend Dumoulin and Visin (2016).
3. Build an split operator, $\underline{\underline{S}} \in \mathbb{R}^{2M \times 2M}$, such that

$$\underline{\underline{S}}\underline{D} = \begin{bmatrix} \underline{D}_p \\ \underline{D}_c \end{bmatrix}, \tag{C.1}$$

   where $\underline{D}_p, \underline{D}_c \in \mathbb{R}^M$ are the p- and c-slip components ordered according to the subfaults enumaration of the fault domain used for the von Karman mask, $\underline{\underline{V}}$.
4. Ensamble the two-components convolution matrix, $\underline{\underline{B}} \in \mathbb{R}^{2M \times 2M}$, as

$$\underline{\underline{B}} = \begin{bmatrix} \underline{\underline{C}} & \underline{0} \\ \underline{0} & \underline{\underline{C}} \end{bmatrix}, \tag{C.2}$$

   where $\underline{0} \in \mathbb{R}^M$ is a null matrix.
5. Compute the projection matrix, $\underline{\underline{F}} \in \mathbb{R}^{2M \times 2M}$, as

$$\underline{\underline{F}} = \underline{\underline{S}}^T \underline{\underline{B}}\,\underline{\underline{S}}. \tag{C.3}$$

C.2 Gradient projection method: Cauchy point calculation

The Cauchy point is an optimal state computed with a descent direction that respects the feasible solution region. We begin by reformulating our inverse problem, eqs. (4.9-4.11), as the quadratic problem

$$\frac{1}{2}\underline{D}^T\underline{\underline{G}}\underline{D} + \underline{c}^T\underline{D}, \tag{C.4}$$

subject to

$$D_i^{j,l} \leq (\underline{\underline{F}}\underline{D})_i \leq D_i^{j,u}, \qquad i \in \{p, c\} \wedge j \in \{\text{SSE, Coupling}\}\,\text{regime}, \tag{C.5}$$

where

$$\underline{\underline{G}} = \underline{\underline{F}}^T\underline{\underline{\mathcal{T}}}^T\underline{\underline{C}}_d^{-1}\underline{\underline{\mathcal{T}}}\underline{\underline{F}} + \beta\underline{\underline{F}}^T\underline{\underline{W}}^T\underline{\underline{W}}\underline{\underline{F}}, \tag{C.6}$$

$$\underline{c} = -\left[\underline{U}_o^T\underline{\underline{C}}_d^{-1}\underline{\underline{\mathcal{T}}}\underline{\underline{F}} + \underline{D}_p^T\underline{\underline{W}}^T\underline{\underline{W}}\underline{\underline{F}}\right]. \tag{C.7}$$

The gradient without considering the inequality contraint, eq. (C.5),is

$$\underline{g} = \underline{\underline{G}}\underline{D} + c, \tag{C.8}$$

First, we need to identify the step lengths for which each slip component reaches its bound along the direction $-\underline{g}$ and store them in $\underline{\bar{t}}$. Then, we eliminate duplicates and zero values of $\underline{\bar{t}}$ to obtain a sorted reduced set of breakpoints $\{t_1, t_2, \ldots, t_l\}$ such that $t_i < t_{i+1}$ for $i \in \{1, 2, \ldots, l-1\}$. With this set, we construct a set of intervals like $\{[0, t_1], [t_1, t_2], \ldots, [t_{l-1}, t_l]\}$. Suppose that we have not found the minimizer up to the interval $[t_{j-1}, t_j]$, then we can model the slip along that interval as

$$\underline{D}(t) = \underline{D}(t_{j-1}) + (\Delta t)\underline{p}^{j-1}, \tag{C.9}$$

where

$$\Delta t = t - t_{j-1} \in [0, t_j - t_{j-1}], \tag{C.10}$$

$$p_i^{j-1} = \begin{cases} -g_i & \text{if } t_{j-1} < \bar{t}_i, \\ 0 & \text{otherwise.} \end{cases} \tag{C.11}$$

If we substitute eq. (C.9) in the quadratic cost function (C.4), we leave it as a function of Δt

$$q(\Delta t) = \frac{1}{2}\left(\underline{D}(t_{j-1}) + (\Delta t)\underline{p}^{j-1}\right)^T\underline{\underline{G}}\left(\underline{D}(t_{j-1}) + (\Delta t)\underline{p}^{j-1}\right) + c^T\left((\Delta t)\underline{p}^{j-1}\right), \tag{C.12}$$

which can be reformulated as

$$q(\Delta t) = f_{j-1} + g_{j-1}\Delta t + \frac{1}{2}h_{j-1}(\Delta t)^2, \tag{C.13}$$

where

$$f_{j-1} = \frac{1}{2}D(t_{j-1})^T\underline{\underline{G}}D(t_{j-1}) + \underline{c}^T\underline{D}(t_j - 1), \tag{C.14}$$

$$g_{j-1} = D(t_{j-1})^T\underline{\underline{G}}\underline{p}^{j-1} + \underline{c}^T\underline{p}^{j-1}, \tag{C.15}$$

$$h_{j-1} = \left(\underline{p}^{j-1}\right)^T\underline{\underline{G}}\underline{p}^{j-1}. \tag{C.16}$$

The solution of this problem is

$$\Delta t^* = -\frac{g_{j-1}}{h_{j-1}}. \tag{C.17}$$

Only one of the following three cases can occur

(i) If $g_{j-1} > 0$ the minimizer is at $\Delta t* = 0$ with $t^* = t_{j-1}$ and $p^* = p_{j-1}$.

(ii) If $\Delta t^* \in [0, t_j - t_{j-1})$ the minimizer is in the interval with $t^* = t_{j-1}$ and $p^* = p_{j-1}$.

(iii) If $\Delta t^* > t_j - t_{j-1}$ then try the next interval.

Once the optimal step has been found, Δt^*, the Cauchy point is evaluated as

$$\underline{D}^c = \underline{D}(t^*) + \Delta t^* p^*. \tag{C.18}$$

C.3 Gaussian slip inversions

Figures S1 and S2 show the synthetic data inversions and restitution indexes with and without noise of the Gaussian-like pulses shown in Figures 4.4A and 4.4B, respectively.

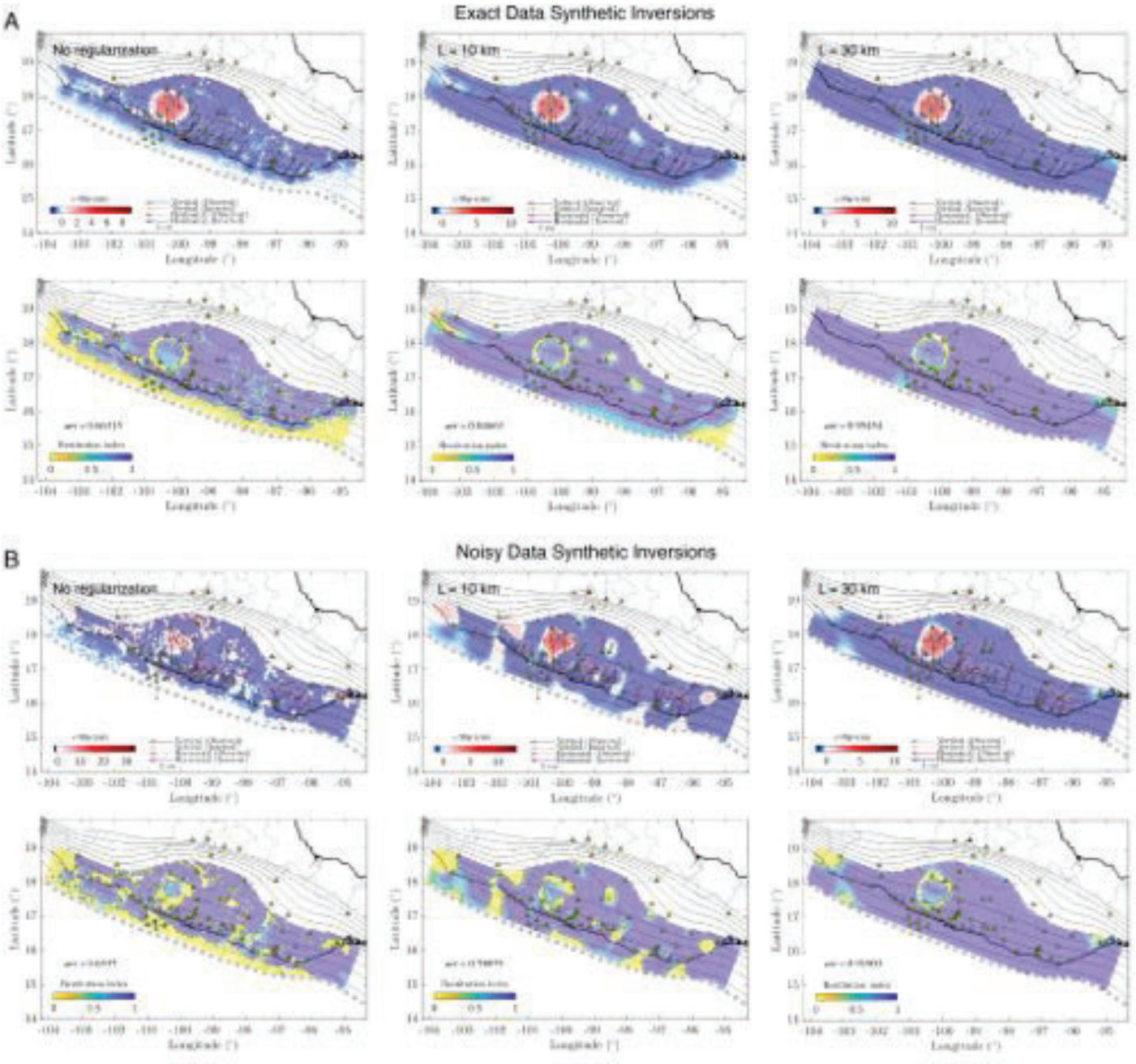

Figure S1: Synthetic inversion results along the *c*-direction for the Gaussian-like slip model shown in Figure 4.4A from the exact target displacements (panel A) and from the perturbed displacements (panel B). The second row of each panel shows the distribution of the restitution index over the plate interface without regularization and for different values of the correlation length, L.

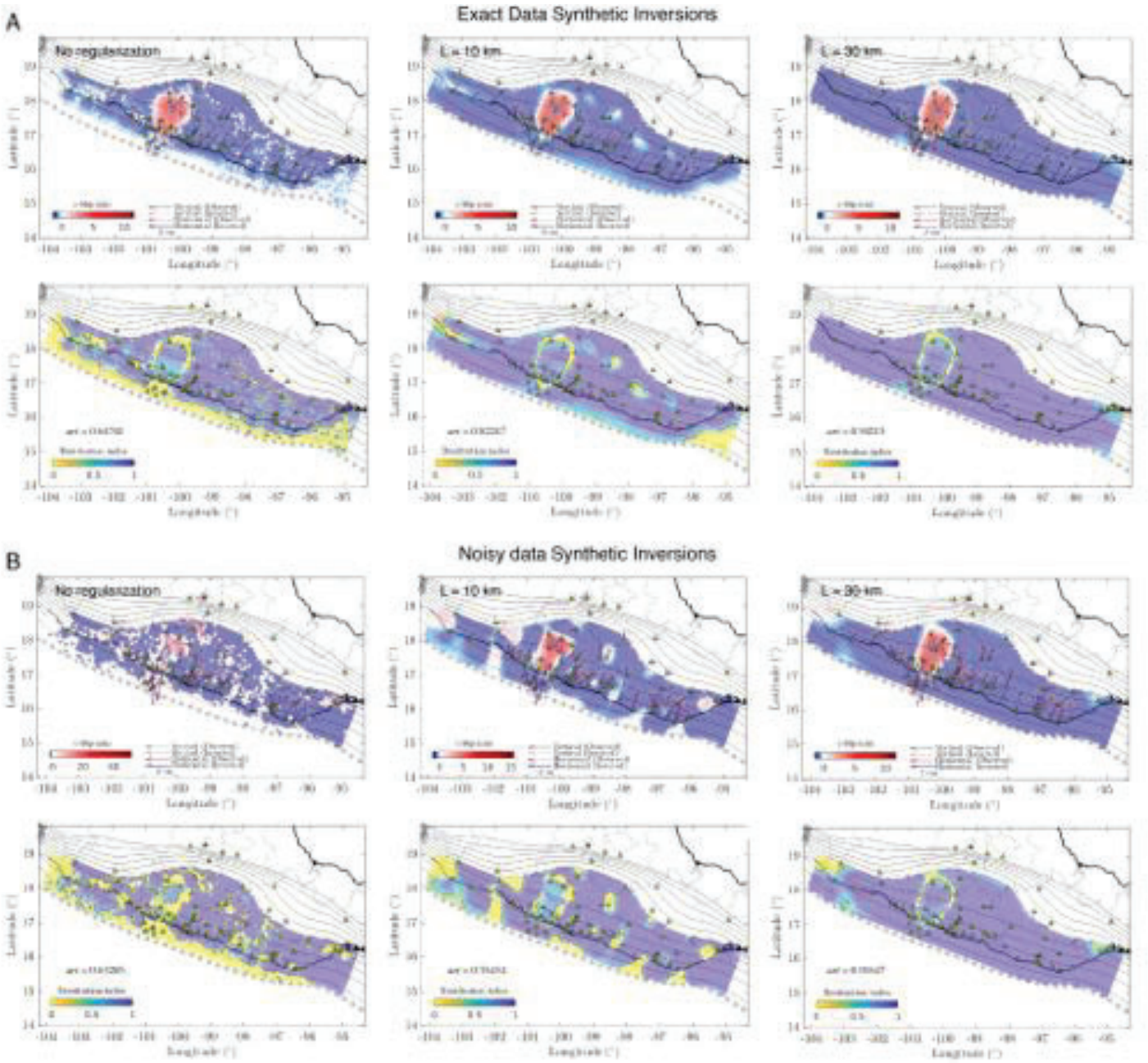

Figure S2: Synthetic inversion results along the *c*-direction for the Gaussian-like slip model shown in Figure 4.4B from the exact target displacements (panel A) and from the perturbed displacements (panel B). The second row of each panel shows the distribution of the restitution index over the plate interface without regularization and for different values of the correlation length, L.

Appendix D

D.1 Supplementary information for Chapter 5

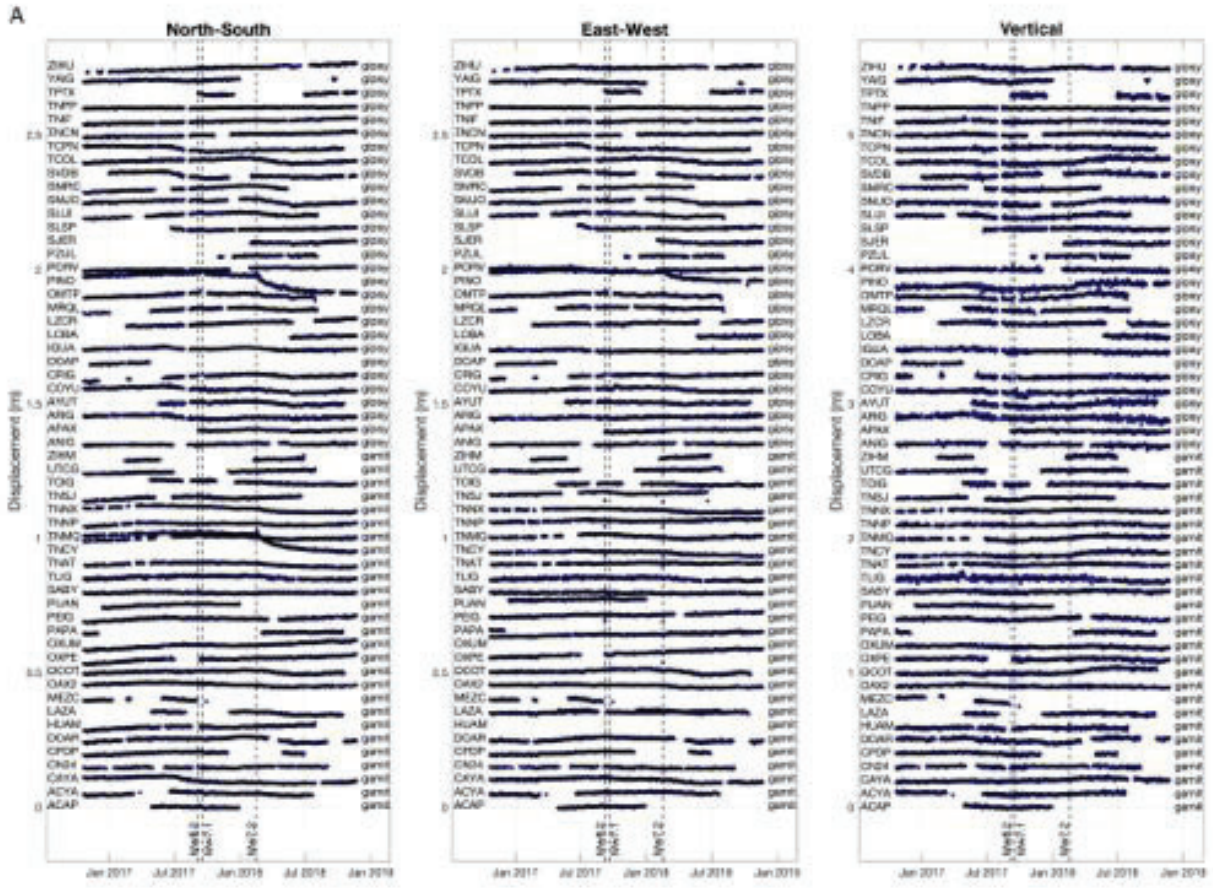

Figure D.1. Displacement GPS time series used in the study. 57 selected stations (A) from October 23 (2016) to November 22 (2018) and (B) from November 22 (2018) to October 8 (2019). To the right of each series is indicated the data processing method selected for the inversions. Vertical dashed lines indicate the occurrence of the three earthquakes of the sequence.

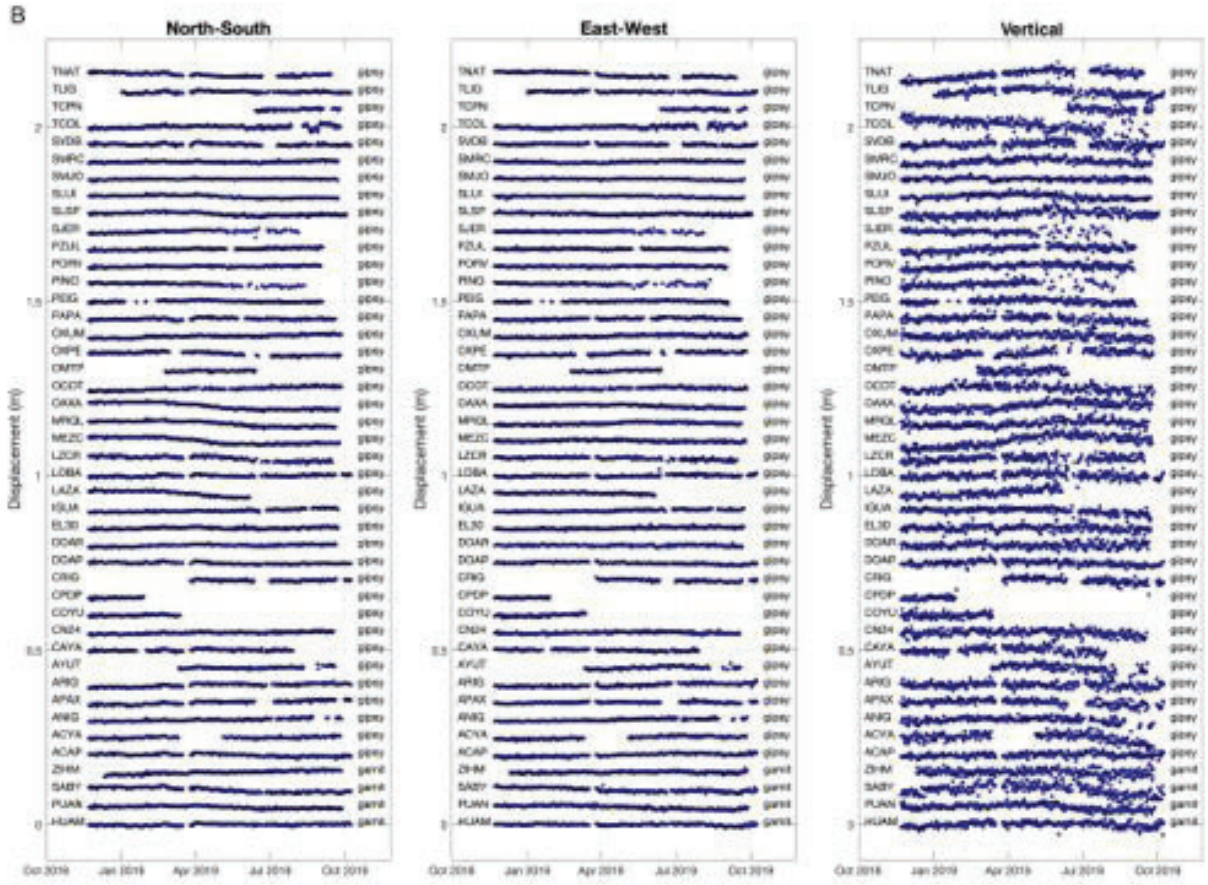

Figure D.1 (continuation)

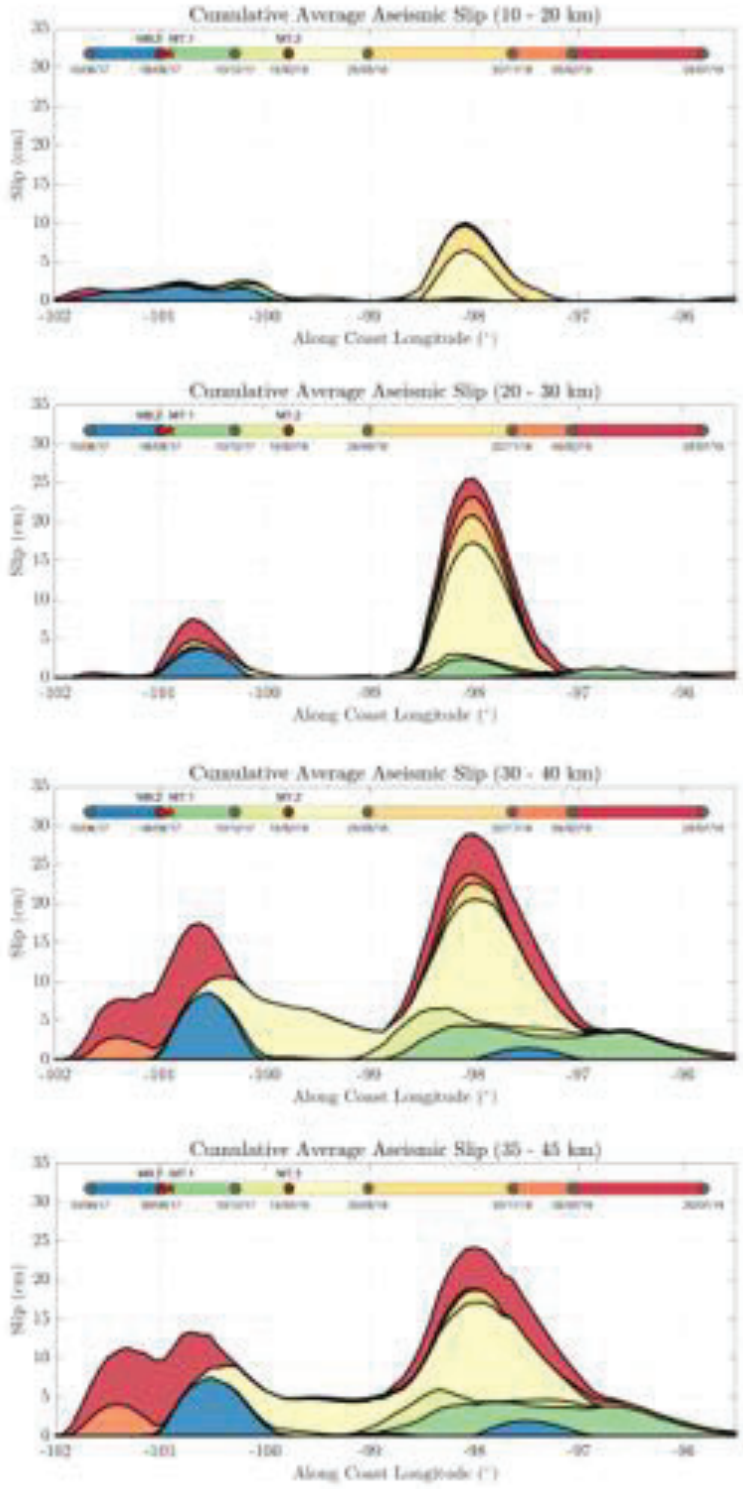

Figure D.2. Cumulative aseismic slip evolution over different plate-interface depth ranges (see panel titles). Average values per depth range were obtained from solutions shown in Figure 5.3A. Between 10 and 20 km depth (i.e., mainly offshore), only the G-SSE1 and the PE-afterslip are significant, with maximum slip of 2.0 and 6.5 cm, respectively. The largest SSE activity concentrates between 20 and 45 km depth.

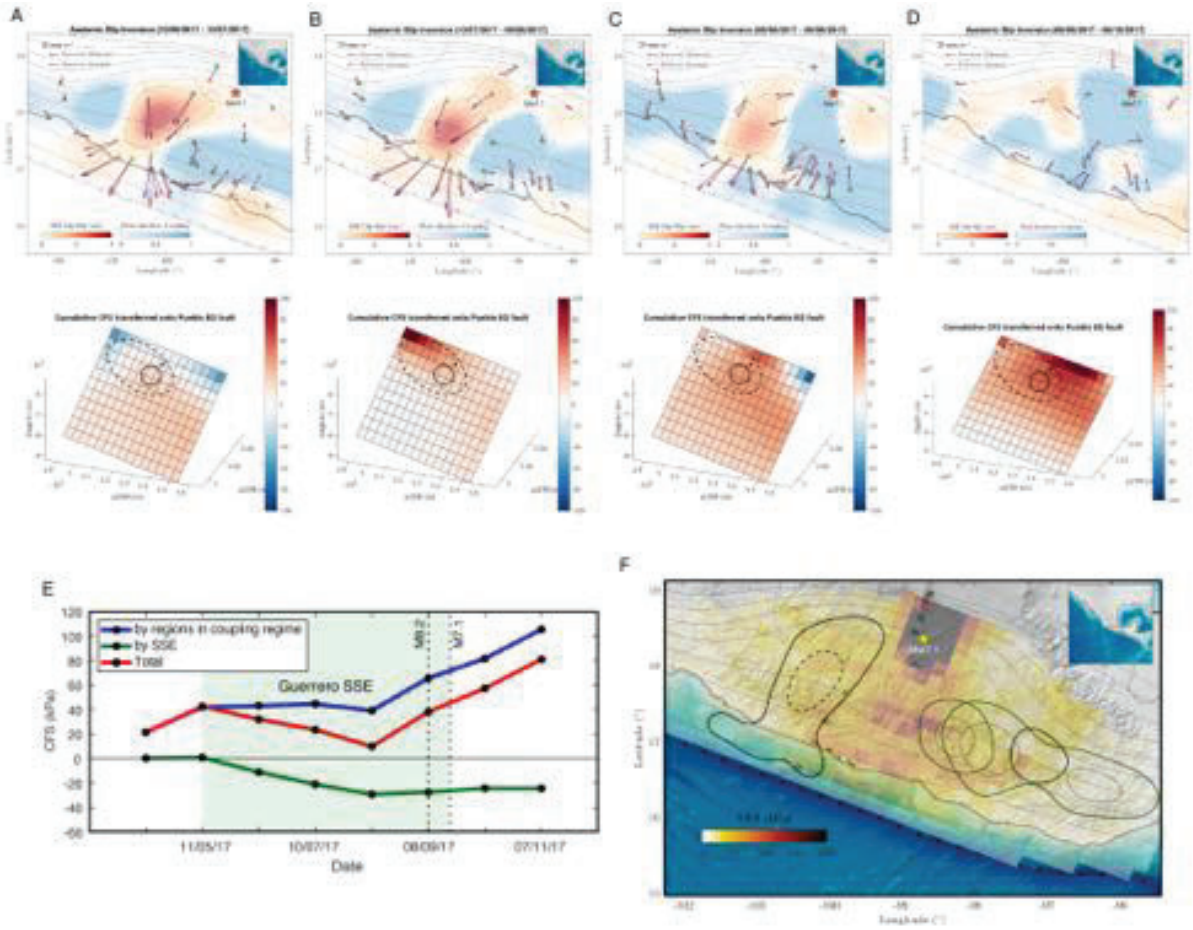

Figure D.3. Interaction between the GSSE-1 and the Puebla-Morelos earthquake. (A-D) 30-day time windows aseismic slip inversions of the G-SSE1 (up) and the associated cumulative total CFS over the intermediate-depth normal fault where the Mw7.1 Puebla-Morelos earthquake took place on September 19, 2017 (down). The inverted time windows are shorter than those shown in Figure 5.2. (E) CFS evolution within a 20 km radius from the Puebla-Morelos hypocenter. Notice the CFS sustained growth induced by the PIC in the later SSE stage. (F) Dynamic CFS maximum values on the plate interface induced by the Puebla-Morelos earthquake seismic waves. They were estimated with a 3D finite source simulation (see Fig. D.10) similar to that performed for the Pinotepa earthquake (Fig. 5.6C) but using the finite-source solution determined by Mirwald et al. (1). Aseismic slip events right before the earthquake are shown with black contours, while those occurred immediately after the earthquake are shown with green contours.

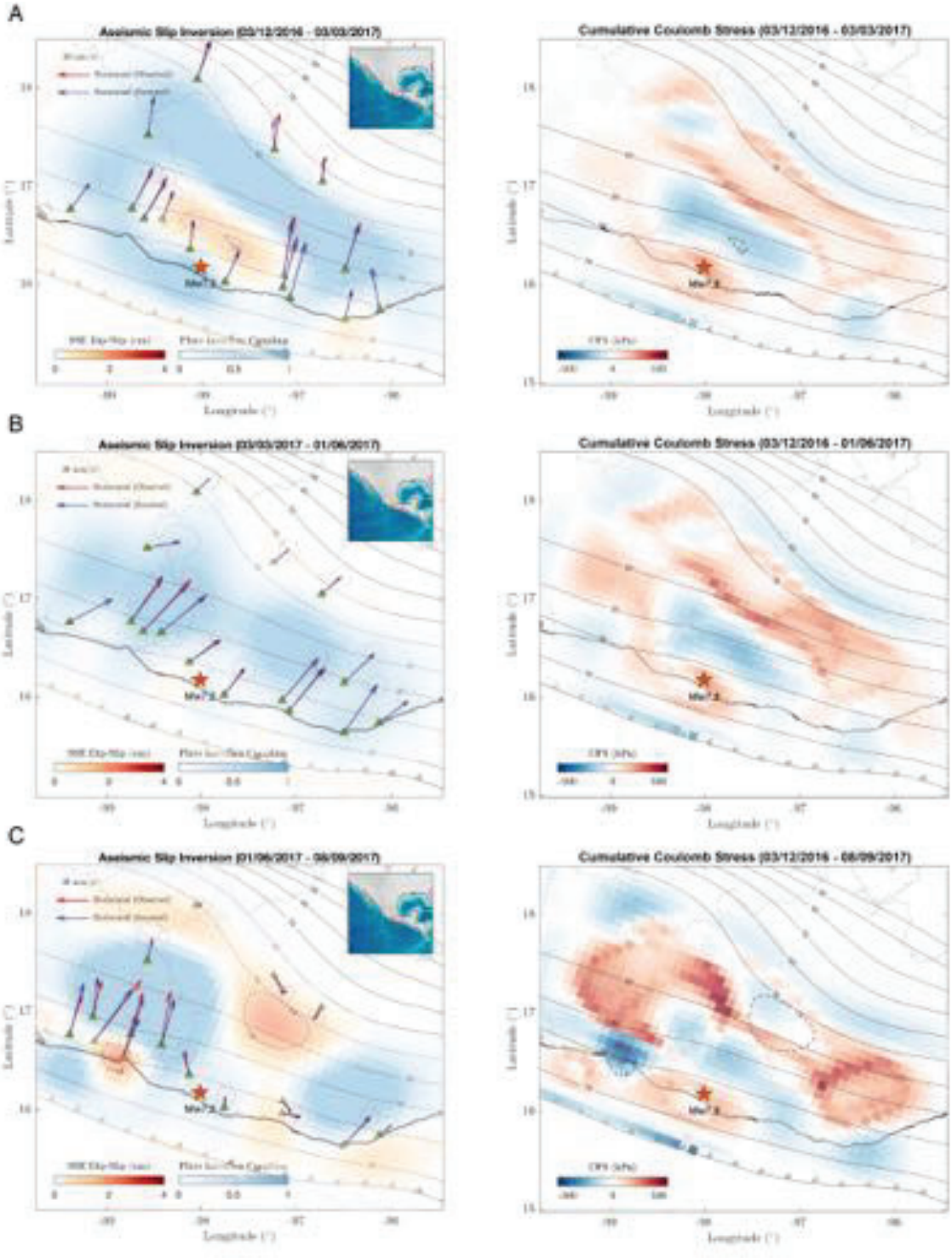

Figure D.4. Aseismic slip inversions preceding the Mw7.2 Pinotepa earthquake during the O-SSE1 (left column) and the associated cumulative CFS on the plate interface (right column). Dashed contours in the right column show the aseismic slip contours of the associated time window. Notice that the inverted time windows are shorter than those shown in Fig. 5.2. Cumulative CFSs from these higher time-resolution inversions are shown in Fig. 5.5a.

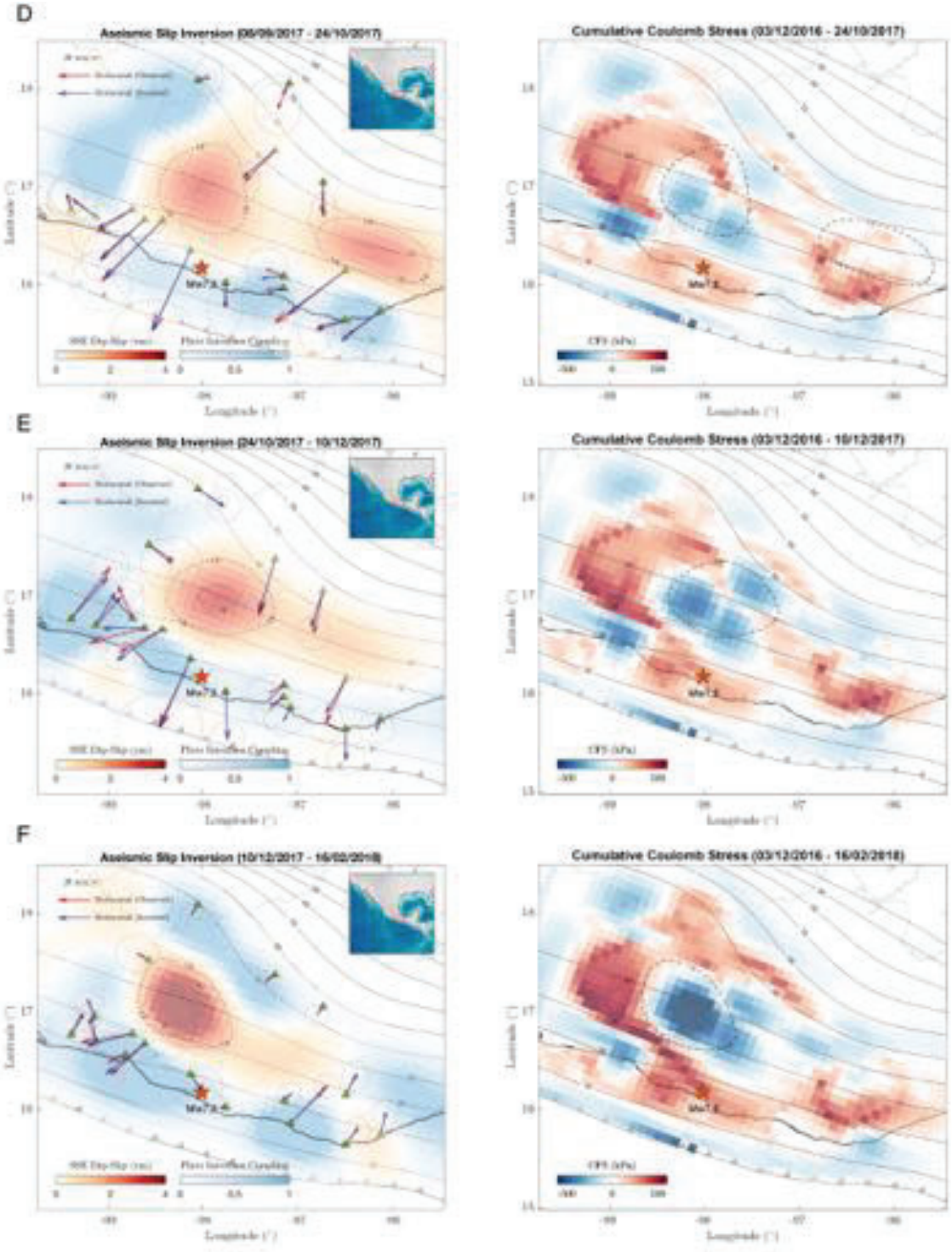

Figure D.4 (continuation)

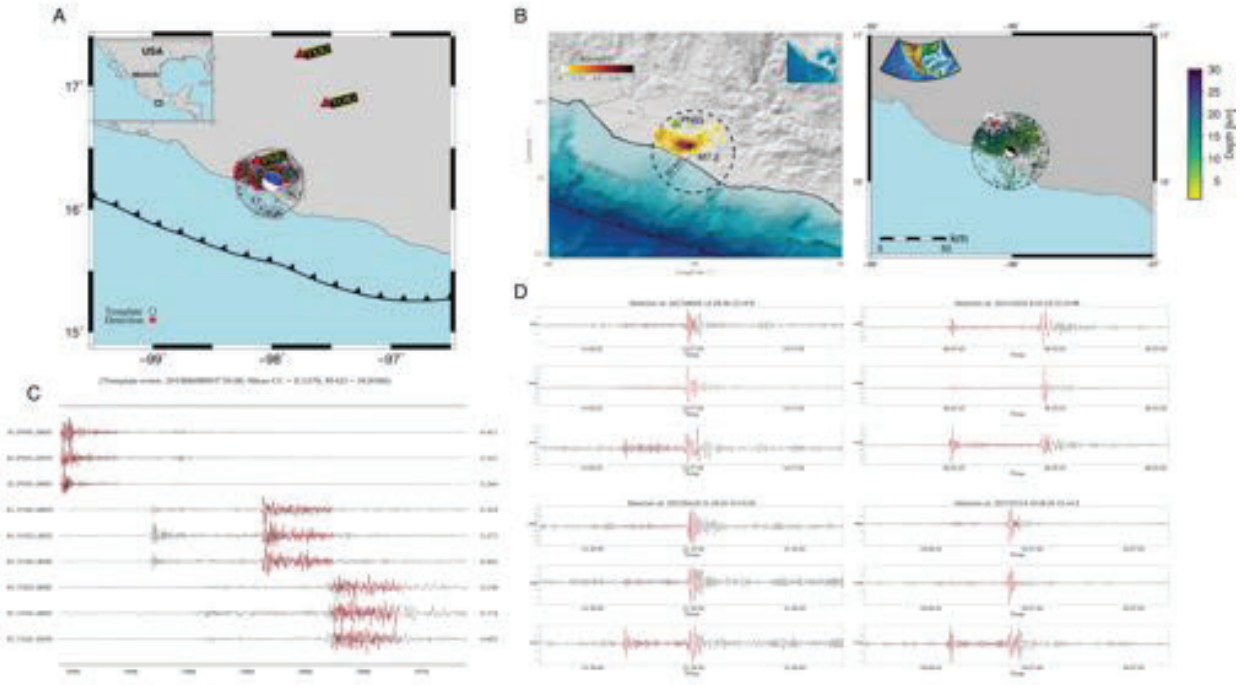

Figure D.5. Template matching results using two different methods during the year preceding the Pinotepa earthquake. (A) Map of events detected by method 1 using three stations at a regional scale. (B) Density map for the template events used by method 2 (left) and their spatial distribution (right). (C) Example of a regional detection made at stations PNIG, YOIG and TXIG using method 1 for the direct S wave and its coda. (D) Examples of local detections made at station PNIG using method 2. Fits of the templates with both the P and S direct waves along with the coda of the P waves guarantee that detections come from the same hypocentral locations as the template events. See Figure 5.5c of the main text.

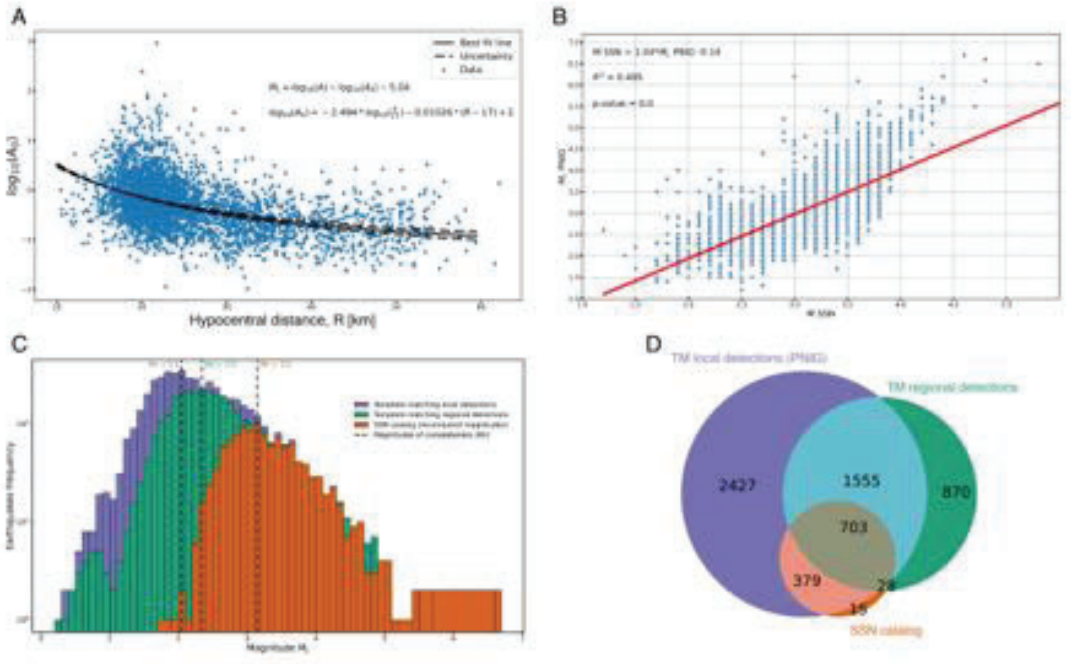

Figure D.6. Magnitude estimation for the template-matching detected earthquakes and final catalogs comparison. (A) Attenuation relationship calculated on the horizontal components (geometric mean) of PNIG and magnitude scale ML. (B) Correlation between recomputed ML magnitudes using the PNIG station and the magnitudes reported by the SSN. (C) Earthquake frequency distributions for the template matched catalogs using the closest station PNIG (blue), three stations of the regional network (green) and the catalog provided by the SSN (orange). (D) Venn diagram showing the relationship of the number of events of each catalog. The intersections are calculated by finding common events in time (events within 10 seconds of each other).

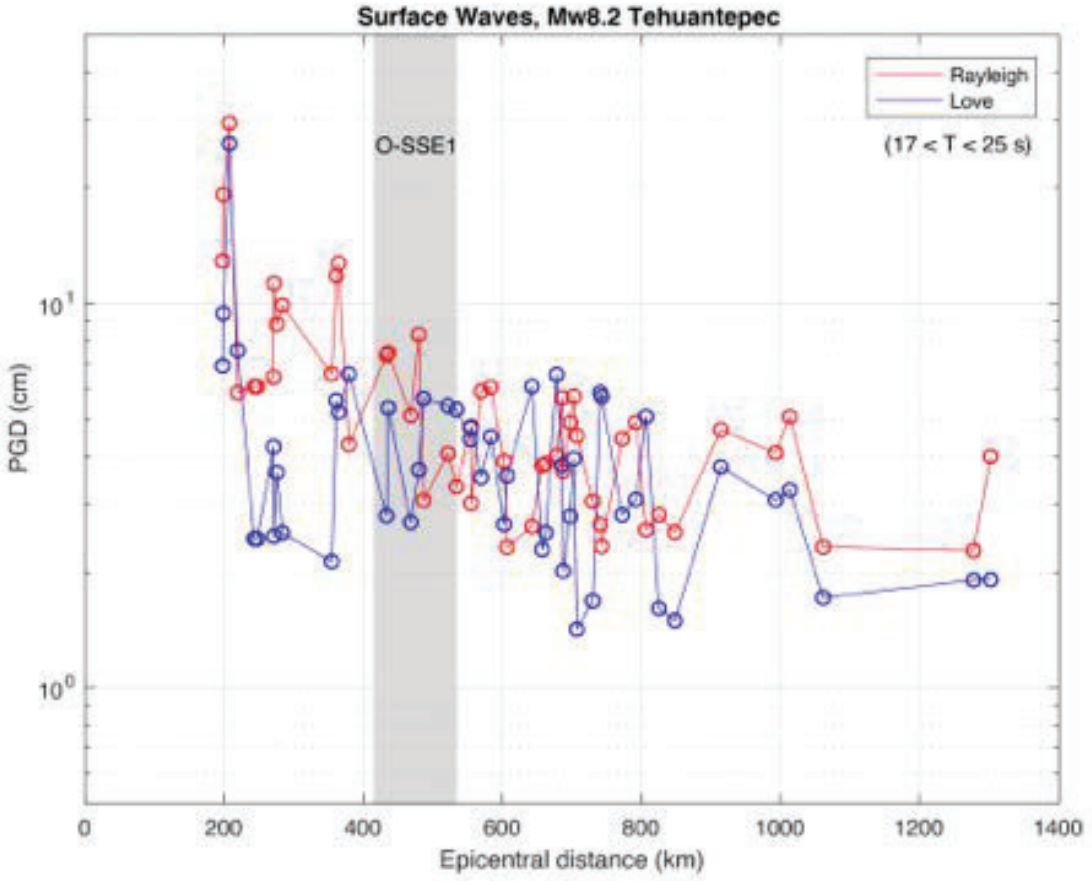

Figure D.7. Attenuation of peak ground displacements for Rayleigh and Love waves produced by the Mw8.2 Tehuantepec earthquake. Peak values of both types of surface waves differ in less than a factor of two at distances where the O-SSE1 was developing at the moment of the earthquake.

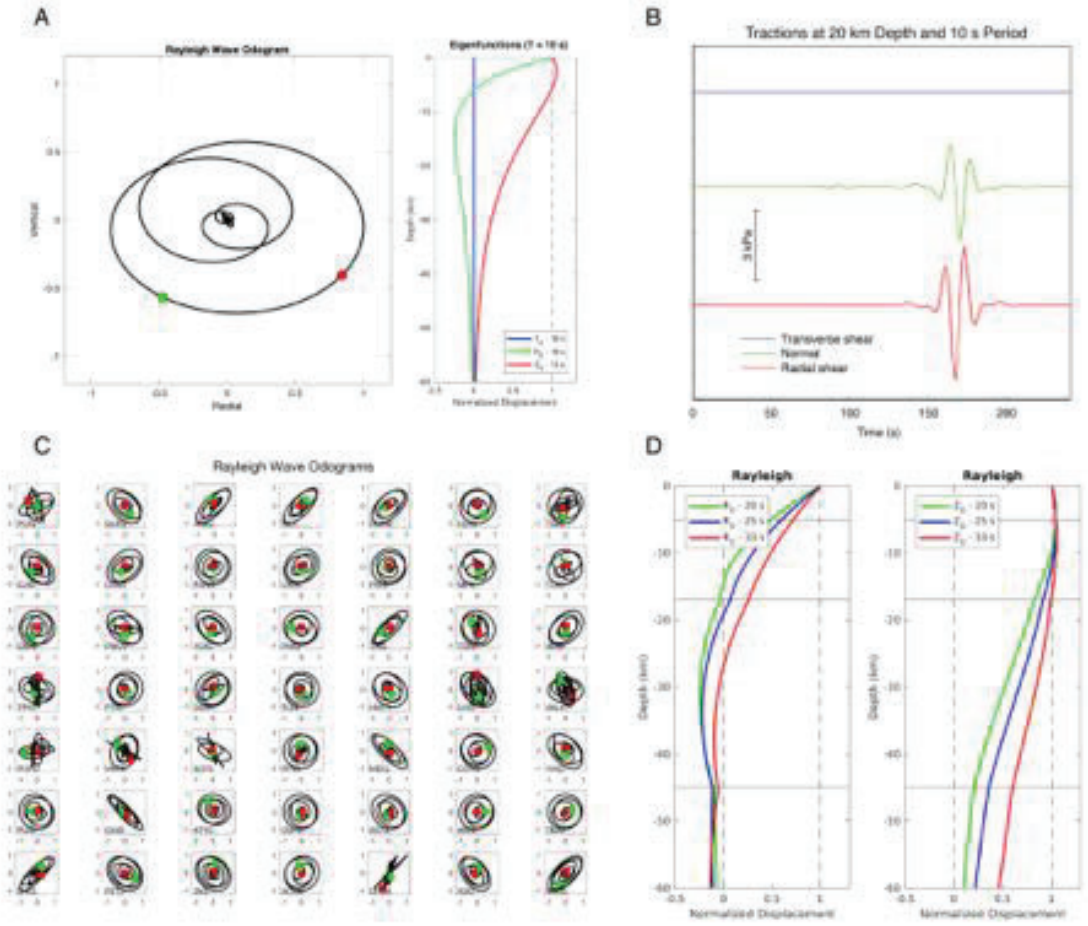

Figure D.8. Validation of the procedure to estimate dynamic perturbations on the plate interface from actual strong motion records. (A) Odogram of a Lamb pulse (i.e., of the wavefield produced by a vertical force applied at the free surface of a homogeneous halfspace) (left), and corresponding eigenfunctions for the Rayleigh wave fundamental mode at 10 s period (right). (B) Comparison at 20 km depth (horizontal plane) and 10 s period of the exact traction evolution (solid) and the estimated traction following the procedure described in Methods (dashed). (C) Odograms for the radial and vertical displacement components around 25 s period from actual records of the Mw8.2 Tehuantepec earthquake on 49 strong motion station (see Fig. D.9). (D) Eigenfunctions of the Rayleigh waves fundamental mode in a crustal 1D velocity model (2) used to estimate beneath each station the traction, CFS and dilation evolution on the 3D plate interface shown in Fig. 5.6A and Fig. D.9.

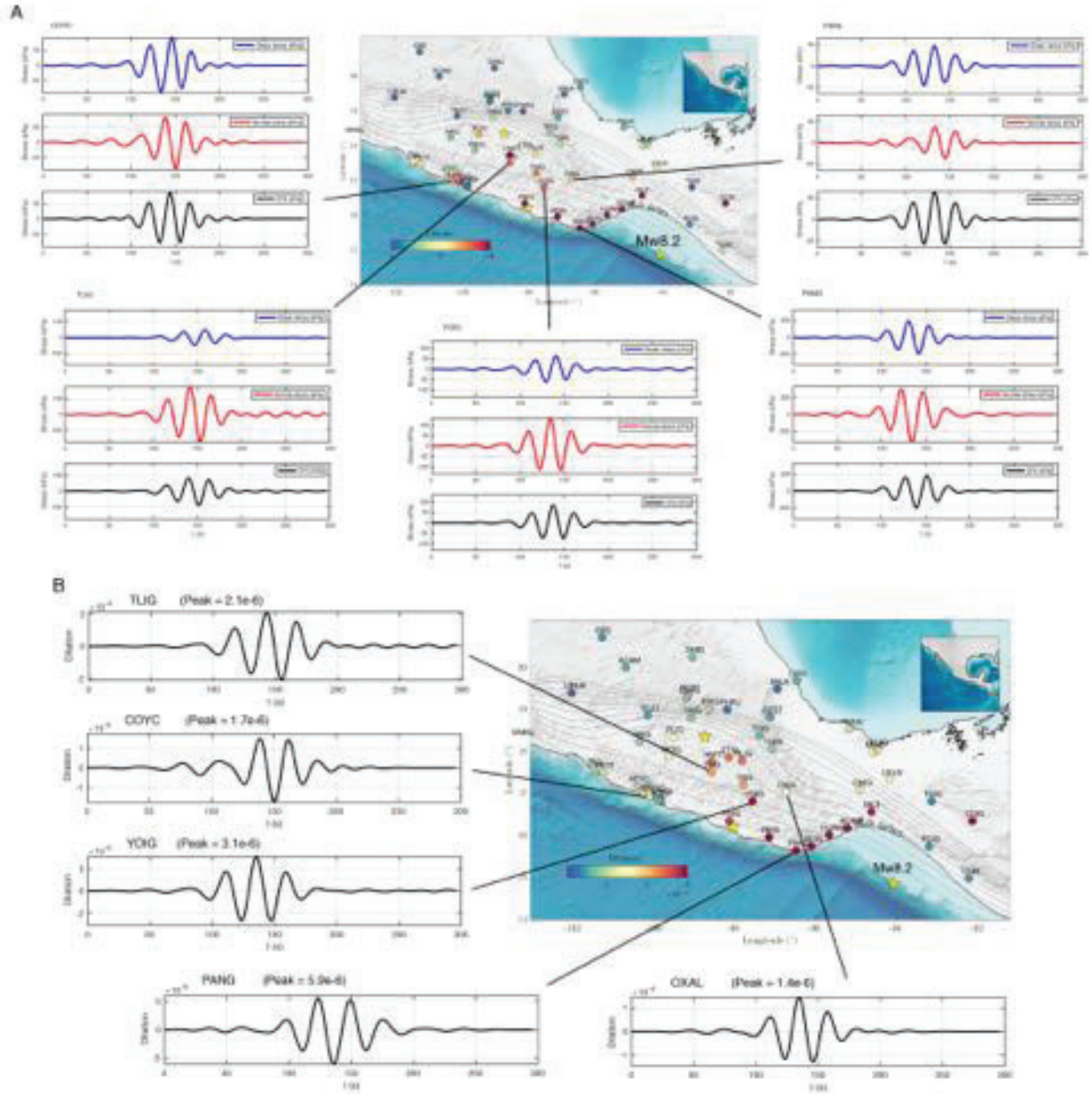

Figure D.9. Dynamic perturbations at the plate interface produced by the Mw8.2 Tehuantepec earthquake. 25 s period dynamic-stress (A) and dilation (B) perturbations over the 3D plate interface (gray contours) estimated from actual strong motion records of the earthquake below different seismic stations (circles). CFSs (computed in the plate-convergence slip direction) and dilations peak values are color-coded in each site. Values where there is no plate interface below correspond to 50 km depth over a horizontal surface.

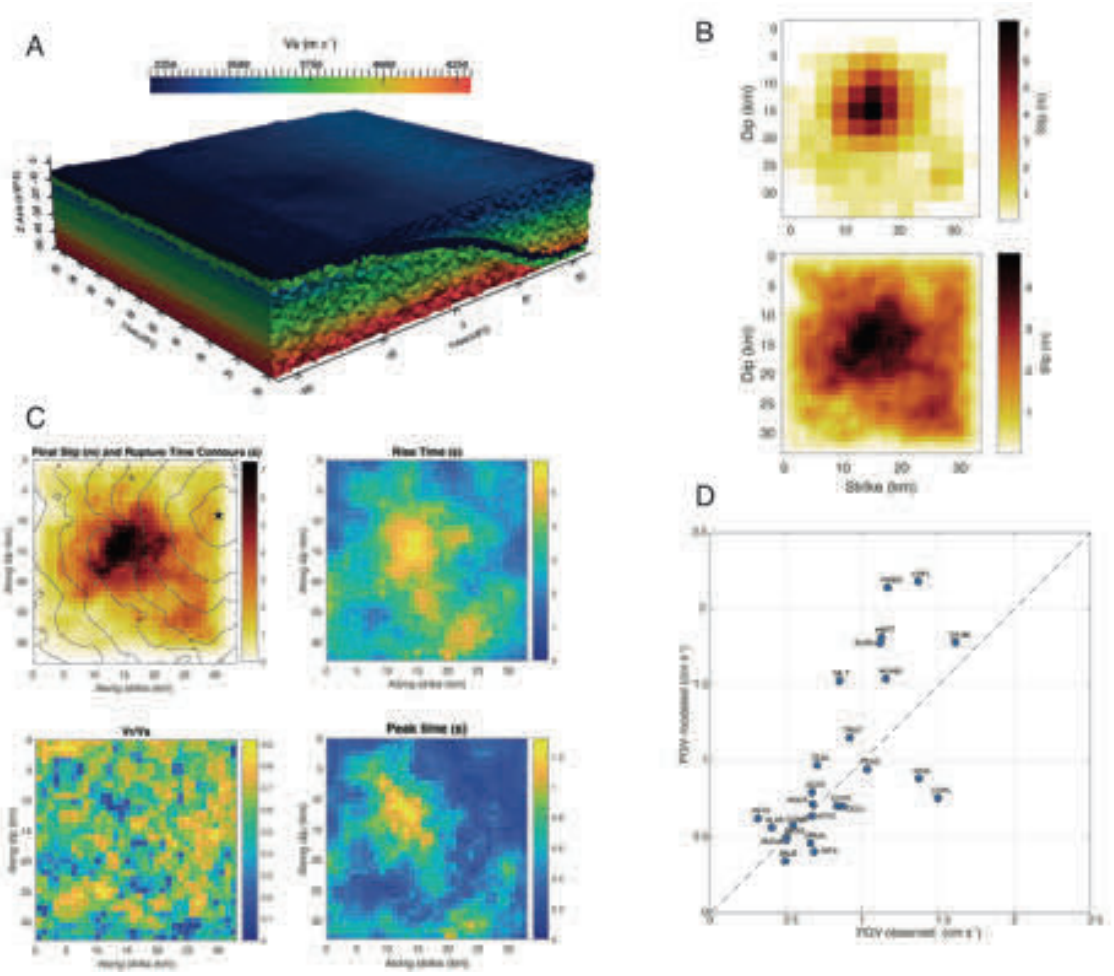

Figure D.10. 3D kinematic finite-source numerical simulation of the Mw7.2 Pinotepa earthquake. (A) Non-structured tetrahedral discretization of the Oaxaca subduction zone. (B) Initial USGS finite source inversion (up) and broad-band wavelength finite slip model (bottom). (C) Spatial distribution of the slip, the rise time, the rupture velocity and the peak time used to describe the kinematic rupture evolution. (D) Comparison between modeled and observed horizontal PGV for different hard-site strong motion stations (see Supplementary Fig. D.9 for site locations).

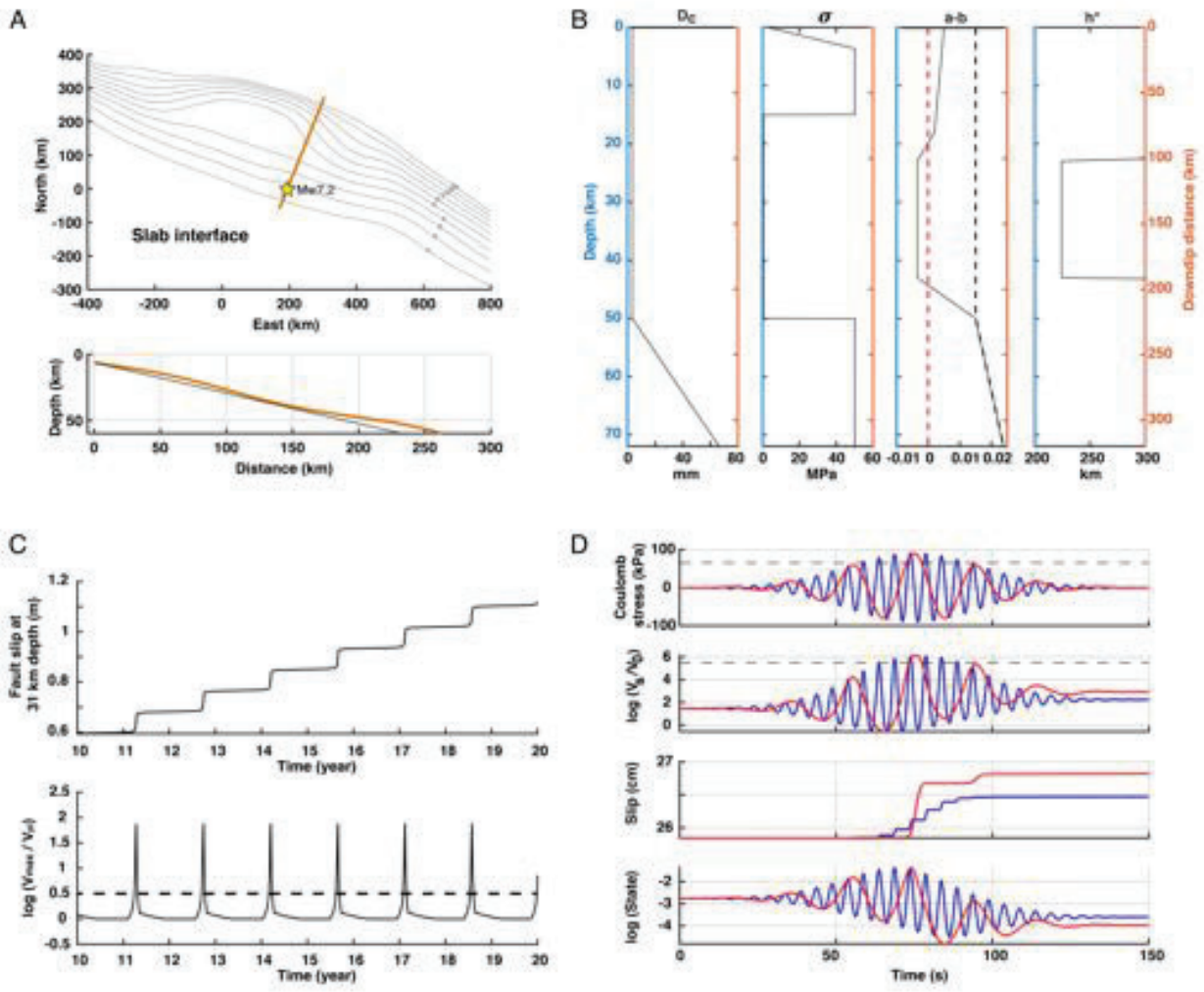

Figure D.11. Rate-and-state friction SSE model for the Oaxaca state. (A) Top, slab geometry in the study area across the 2018 Mw7.2 Pinotepa earthquake epicenter. The orange solid line shows the profile of our 2D model over the 3D plate interface geometry. Bottom, the black solid line shows the planar fault model and the orange line shows the slab geometry. (B) Rate-and-state parameters used in our 2D reference model. *Dc* above 50 km is 3.5 mm. The effective normal stress in the low stress zone is 0.45 MPa. (C) Slip at 31 km depth and the maximum slip rate on the fault for the reference model. (D) Evolution of key model parameters with two different perturbations with different characteristic periods (5 s and 20 s periods) and same 60 kPa CFS peak values. Notice that longer period waves have significantly larger SSE triggering potential, i.e., 40 % larger final slip and much larger (effective) slip acceleration.

Appendix E

E.1 Supplementary information for Chapter 6

E.1.1 GNSS time series processing

The GNSS displacement times series are estimated using the GIPSY 6.4 software package (Lagler et al., 2013), which follows a Precise Point Positioning strategy. The station positions are defined in the International Terrestrial Reference Frame, year 2014 (ITRF 2014). For daily processing we used the Jet Propulsion Laboratory final and non-fiducial products (orbits and clocks). We generated observables using 2 model categories: (1) Earth models and (2) observation models. The Earth models include tidal effects (i.e., solid tides, ocean loading and tide created by polar motion), Earth rotation (UT1), polar motion, nutation and precession. Observation models, on the other hand, are related with phase center offsets, tropospheric effects and timing errors (i.e., relativistic effects). The troposphere delay is estimated like as random walk process. This effect is broken into wet and dry components. The azimuthal gradient and the dry component are estimated using GPT2 model and mapping function (TGIPSY1). The antennas phase center variations are considered through antenna calibration files. For receiver antennas, the correction is estimated taking the International GNSS Service (IGS) Antex file. We also applied a wide-lane phase bias to account for the ambiguity resolution.

To remove the outliers and then estimate the displacement vectors per time window, we first determine the data variance for each component and time window from the differences between daily displacement values and a moving, locally weighted LOESS function (i.e., 2nd order polynomial regressions with a half-window time support, Figs. 6.2a, 6.3a and E.6). Then, all data points in a time window with differences larger than two standard deviations were dismissed. Once the outliers are removed, a new regression is performed to estimate the final displacement vectors.

E.1.2 Correction of seasonal effects

To properly associate the displacement time series with the deformation produced by slip processes on the plate interface its necessary to identify and remove the signals associated with seasonal oscillations. We assume that these signals can be modeled as a linear combination of two annual and two semi-annual trigonometric terms excluding inter-annual variations (Bevis and Brown, 2014):

$$S(t_i) = b_1 \sin(2\pi t_i) + b_2 \cos(2\pi t_i) + c_1 \sin(4\pi t_i) + c_2 \cos(4\pi t_i) \tag{E.1}$$

where $S(t_i)$ is the seasonal displacement at time t_i in years units, b_1 and b_2 are the coefficients for the annual terms and c_1 and c_2 the coefficients for the semi-annual terms. We use only inter-SSE time windows of the actual data to identify the contribution of these periodic oscillations to the observed displacements. Thus, we assume that the GNSS time series during an inter-SSE window can be modeled as the sum of their secular inter-SSE displacement and the seasonal contributions as:

$$U(t_i) = a_i + vt_i + S(t_i) \tag{E.2}$$

where $U(t_i)$ represents the GNSS displacement at time t_i in years units, a is the intercept and v the constant secular velocity in the inter-SSE periods. Removing the seasonal contribution in Oaxaca is challenging because the amplitude and recurrence of the annual and semi-annual terms are comparable to those of the SSEs in the region (from 1-2 years). Since the seasonal effects are much stronger in the vertical component than in the horizontal components, we first determined the coefficients of equation 1 for the vertical component by means of a simple least squares approach. In many stations the length of the inter-SSE windows is no longer than one year, preventing a reliable seasonal-noise characterization in such restrictive time windows. To overcome this problem, we use as many inter-SSE windows as possible in the longest GNSS time series available per station to obtain both the four coefficients of the seasonal function (i.e., the same coefficients for all inter-SSE windows) and the individual secular contribution per window. The inter-SSE windows were manually selected by excluding those periods where clear SSEs and earthquakes afterslip were present (Fig. E.14). Then, the displacement time series for the vertical component during inter-SSE periods can be expressed as

$$\alpha(x) = \begin{cases} a_1 + v_1 t_i + S_v(t_i) if {T_1}^l < t_i < {T_1}^l \\ a_2 + v_2 t_i + S_v(t_i) if {T_2}^l < t_i < {T_2}^l \\ \vdots \\ a_k + v_k t_i + S_v(t_i) if {T_k}^l < t_i < {T_k}^l \end{cases} \tag{E.3}$$

where a_k and v_k are the intercept and the constant secular velocity during the k inter-SSE window, respectively, S_v is the seasonal function for the vertical component, and $[{T_k}^l, {T_k}^u]$ are the lower- and upper-time limits of the k inter-SSE window. For the treatment of the horizontal displacement components, where the amplitude of the seasonal noise is usually smaller than that of the transient tectonic deformations, we assumed that the seasonal effects on the three components are all proportional. This is a reasonable hypothesis since most of these contributions are related to the earth's elastic response due to hydrological processes ocurring on the surface (Heki, 2001). Therefore, the displacement for every horizontal component in the inter-SSE periods, U_h, can be represented as

$$\alpha(x) = \begin{cases} a_1 + v_1 t_i + \alpha_h S_v(t_i) if {T_1}^l < t_i < {T_1}^l \\ a_2 + v_2 t_i + \alpha_h S_v(t_i) if {T_2}^l < t_i < {T_2}^l \\ \vdots \\ a_k + v_k t_i + \alpha_h S_v(t_i) if {T_k}^l < t_i < {T_k}^l \end{cases} \tag{E.4}$$

where α_h is the proportionality factor determined also by means of the multi-window least square method, and h stands for the north-south or east-west component. We decided to proceed in this way because when determining the seasonal functions independently per component (i.e., by independently applying the procedure described for vertical displacements to all components) we realized that the horizontal SSE signals (consistently found at several stations) were in some cases eliminated by applying the correction. Several examples illustrating our approach are shown in Figure E.14.

E.1.3 InSAR images processing

We calculate a coseismic interferogram of the Huatulco Earthquake using two single look complex Synthetic Aperture Radar (SAR) scenes acquired by the Sentinel-1 satellites in the Interferometric Wide Swath acquisition mode, ascending pass, track 107 (Fig. E.2a). The selected scenes were acquired on June 19th and June 25th, 2020, which correspond to the pair with the shortest-possible acquisition span (6 days). The pass and track were selected to provide the best-possible coverage of the coseismic signal. We use the processing chain provided in the InSAR Scientific Computing Environment (ISCE) (Rosen et al., 2012) to calculate the interferometric phase between the two SAR scenes, which includes a coarse co-registration assisted by a digital elevation model (DEM), a coarse inteferogram calculation, a fine coregistration, a fine inteferogram calculation, and basic phase corrections. Accordingly, we additionally use a 1 arc-second DEM from the Shuttle Radar Topography Mission (Farr et al., 2007) to complete the interferogram formation and topographic phase correction. Subsequently, we filter the interferometric phase using a Goldstein filter (Goldstein and Werner, 1998) to later perform phase unwrapping using SNAPHU (Chen and Zebker, 2000). We finally geocode the unwrapped interferogram, convert it to displacement in meters in line of sight (LOS) geometry and mask out water bodies and areas with spatial coherence lower than 0.4 (Fig. E.2b).

Geodetic measurements from GNSS and InSAR have different reference frames, which requires converting one into the other to make a fair comparison of the displacements obtained by each technique. GNSS measurements are referenced in East, North and Up components, whereas satellite InSAR have a pixel-wise reference frame in terms of incidence (θ) and azimuth (α) angles, which vary pixel by pixel and define the relative LOS direction towards the SAR satellite. GNSS displacements can be projected onto the satellite's LOS direction following the expression (Hanssen, 2001):

$$GPS_{LOS} = -\sin(\alpha - \frac{3\pi}{2})\sin(\theta d_e) - \cos(\alpha - \frac{3\pi}{2})\sin(\theta d_n) + \cos(\theta d_u) \tag{E.5}$$

where GPS_{LOS} is the projection of the GNSS displacement vector onto the LOS vector, and d_e, d_n and d_u are the GNSS displacement components in the East, North and Up directions, respectively. Based on this transformation we adapted the ELADIN inversion method (see next section) so that the Somigliana tensor used to generate the synthetic displacements was projected into the individual LOS unit vectors per InSAR data point to perform the simultaneous GNSS and InSAR data inversion.

E.1.4 Slip inversion method

The ELADIN (ELastostatic ADjoint INversion) method (Tago et al., 2021) solves a constrained optimization problem based on the adjoint elastostatic equations with Tikhonov regularization terms, a von Karman autocorrelation function and a gradient projection method to guarantee physically-consistent slip restrictions. The method simultaneously determines the distribution of PIC and relaxing slip (i.e., SSEs and afterslip) in the plate interface to explain the surface displacements. Its precision matrix, which corresponds to the inverse of the data variance matrix (see Section 1), allows to minimize the effect of data errors (i.e., cumulative processing errors and non-tectonic physical signals) by weighting the observations. For the pre-seismic and post-seismic GNSS inversions (Figs. 6.2 and 6.3), the weights are directly based on the data variance matrix per time window and displacement component (i.e., ellipses around the tips of the horizontal displacement vectors in Figures 6.2 and 6.3) (Tago et al., 2021).

For the coseismic analysis, where GNSS and InSAR displacements are simultaneously inverted (Figs. 6.1 and E.3c), we first inverted each data set independently. The solution using only GNSS data (Fig. E.3a) describes a very simple and concentrated slip patch downdip the hypocenter with a maximum value of 4.2 m and a marginally lower than expected moment magnitude Mw 7.32 with average GNSS data error of 0.2 ± 0.2 cm (Fig. E.3a). The resulting model using only InSAR data (Fig. E.3b) describes a more heterogeneous slip distribution with maximum value of 2.5 m and a slightly higher moment magnitude of 7.34 with average InSAR data error of 0.0 ± 1.2 cm (Fig. E.3b). To combine both data sets in a single joint inversion, the data weights were determined by trial and error until reaching a satisfactory slip solution (Fig. E.3c), with maximum value of 3.4 m and average GNSS and InSAR data errors of 1.2 ± 1.0 cm and 0.2 ± 2.1cm, respectively. The optimal set of weighting factors are such that all InSAR data (i.e., the 221 LOS displacements, Figs. 6.1b and E.2c) were attributed a value equal to one, while the GNSS data (i.e., 12 displacement components) were attributed according to the epicentral distance of each station as follows. The HUAT and OXUM sites weighed 25, the TNSJ site weighed 15, and the OXPE site weighed 5, with these values being the same in all three components per site.

In these inversions we assumed a von Karman Hurst exponent of 0.75 and restricted the slip component perpendicular to the plate convergence direction to be smaller than 0.6 m (for details see Tago et al. (2021)). To determine the optimal von Karman correlation length L for the coseismic joint inversion, we analyzed the problem resolution by means of several mobile checkerboards (MOC) tests (Tago et al., 2021) for a patch size of 20 km and 2.4 m of slip. Each MOC resolution test implies 64 independent checkerboard inversions. For each test we assumed a different L ranging between 5 and 15 km. Figure E.4 shows the MOC test results for the optimal correlation length L = 7 km,

which maximizes the average restitution index (ARI) in the 2020 Huatulco earthquake rupture zone and minimizes the data error. An example of a checkerboard inversion with such parameterization is also shown in the figure. Our optimal model parameterization guarantees that the coseismic slip inversion has a nominal error smaller than 35 % (i.e., with restitution indexes higher than 0.65) over most of the recovered rupture area for slip patches with characteristic lengths greater than or equal to 20 km (Fig. S4).

Following Tago et al. (2021) and Cruz-Atienza et al. (2021), to guarantee slip restitution indexes higher than 0.5 in the whole Oaxaca region for slip patch sizes larger than 80 km (Fig. E.8), we assumed also a Hurst exponent of 0.75 and the optimal correlation length (L) of 40 km (parameters of the von Karman function controlling the inverse-problem regularization) for the pre- and post-seismic slip inversions. Also following these works, the slip rake angle could only vary 30o with respect to the plate convergence direction.

As for the inversion exercise mentioned in the main text with a 3.5 km shallower plate interface to match the relocated hypocentral depth of 17.2 km, the slip model (Fig. E.5) significantly improved the data fit (i.e., average errors of 0.7 ± 0.6 cm and 0.1 ± 1.4 cm for GNSS and InSAR data, respectively) while reproducing similar source characteristics to those of our preferred solution (Figs. 6.1a and E.3c). However, it is worth noting some differences: (1) the maximum slip is significantly larger (4.3 m), (2) the moment magnitude is smaller (Mw 7.3) as determined from the 1 m slip contour, and (3) the rupture is more concentrated in the main patch north of the hypocenter, between 18 and 30 km deep. For consistency throughout the manuscript (i.e., to assume the same interface geometry in all presented exercises), we keep the deeper solution shown in Figure 6.1 for subsequent analysis.

E.1.5 Coulomb Failure Stress estimation

The total static stress change on the plate interface is the sum of the stress contributions from plate interface regions that slip, producing either a stress relaxation of the continental crust (i.e., due to SSEs, coseismic slip and afterslip) or a stress built-up (due to regions in coupling regime that we modeled as backslip, Savage (1983)). To estimate the stress tensor, following (Cruz-Atienza et al., 2021) we discretized the 3D plate interface into triangular subfaults and used the artefact-free triangular dislocation method introduced by Nikkhoo and Walter (2015) for a half-space to compute the Coulomb Failure Stress change ($\triangle CFS$) on the plate interface by assuming a locally-consistent thrust mechanism, so that:

$$\triangle CFS = \triangle\tau + \mu\triangle\sigma_n, \tag{E.6}$$

where $\triangle\tau$ represents the change of the shear stress in the direction of the fault slip (assumed to be parallel to the plate convergence direction following DeMets et al. (2010)); $\triangle\sigma_n$ is the change of the fault normal stress (positive for tension); and μ is the apparent coefficient of friction assumed to be 0.5.

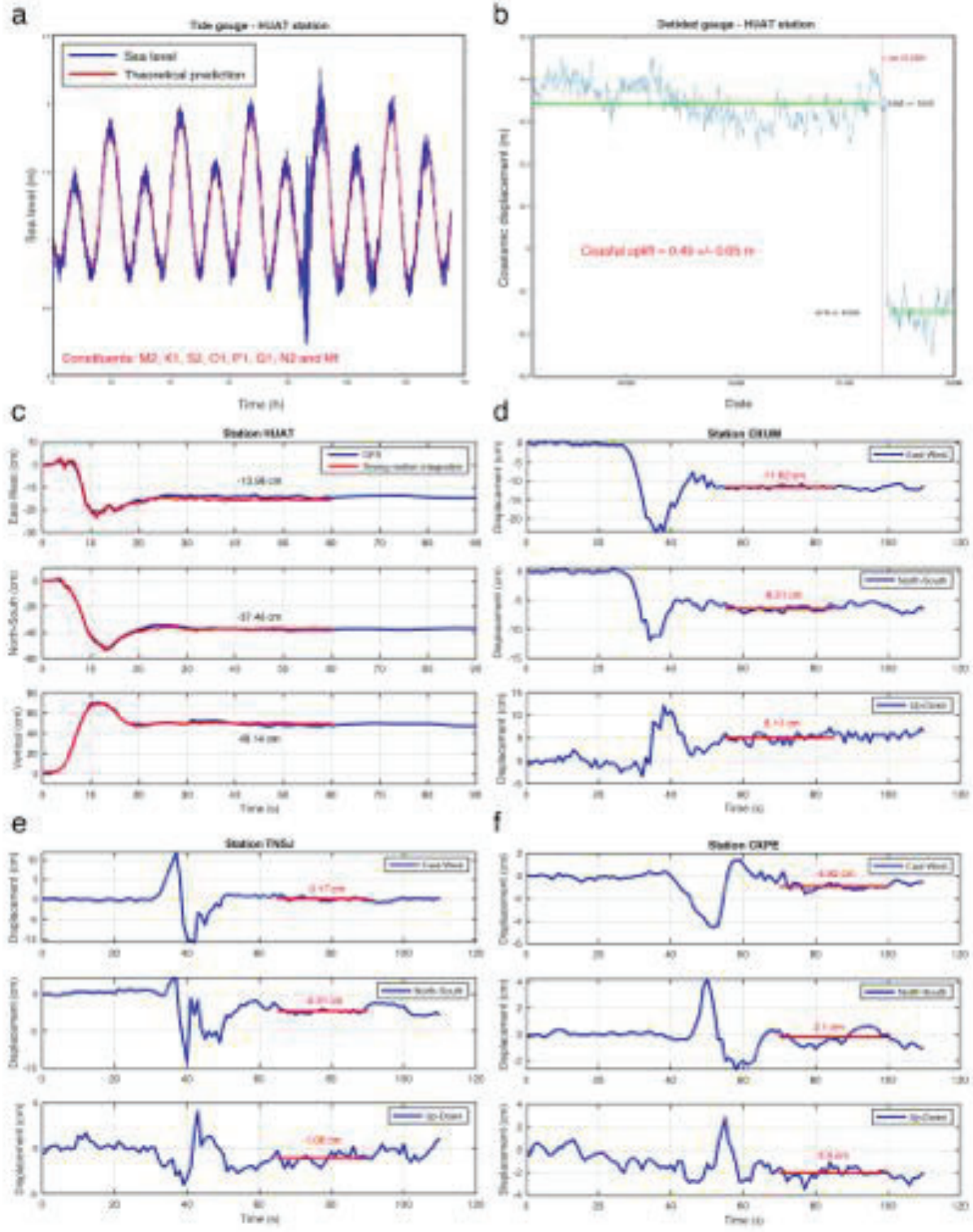

Figure E.1. Huatulco earthquake co-seismic displacements estimated from the HUAT tide gauge (a and b); high-rate GNSS time series at stations HUAT (c), OXUM (d), TNSJ (e) and OXPE (f); and double integration of a strong motion record following the procedure of Wang et al. (2011)(red curve in c).

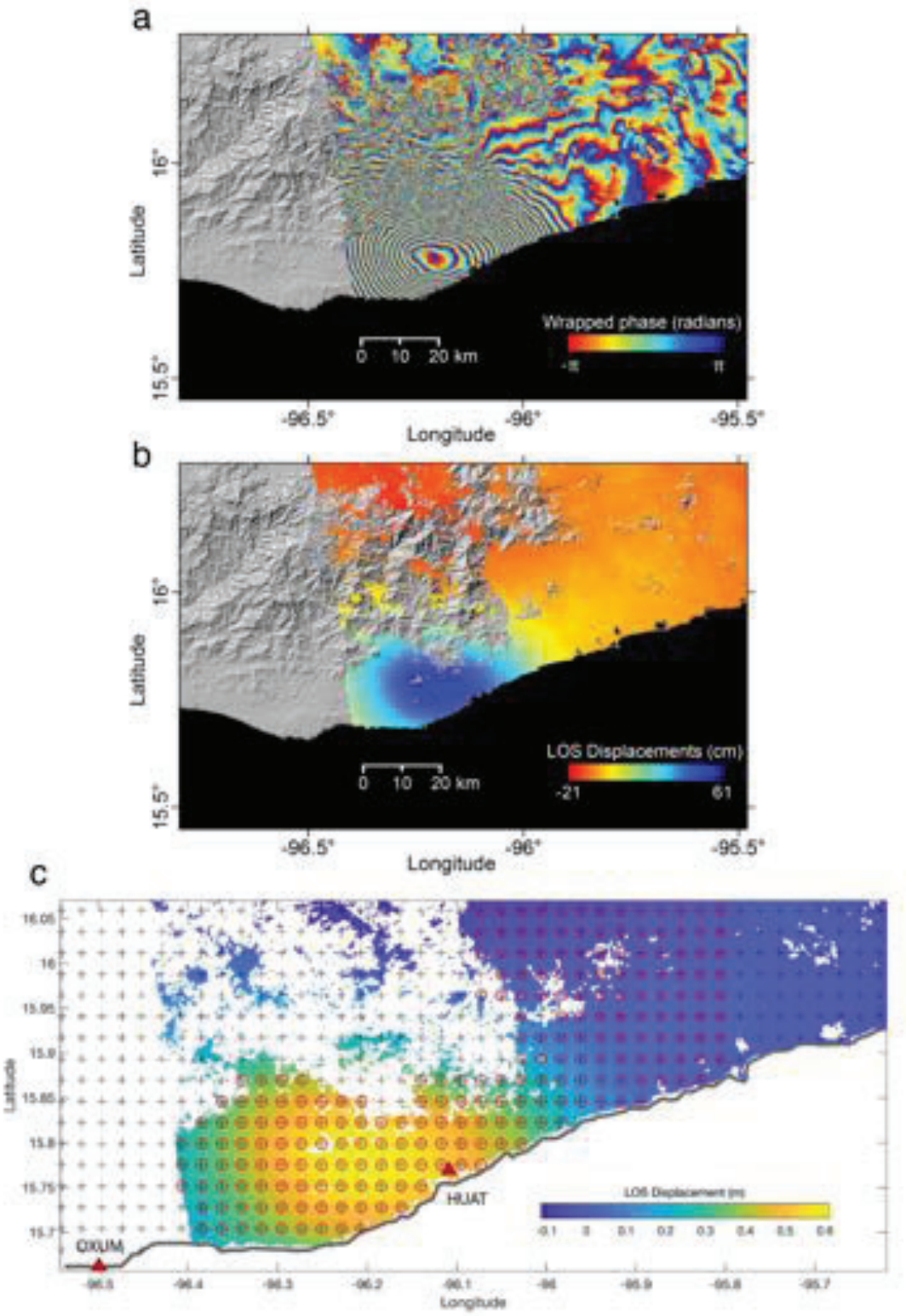

Figure E.2. Huatulco earthquake InSAR displacements estimated from Sentinel satellite images on Track 107 Ascending for scenes on June 19 and 25, 2020. a Wrapped phase ascending interferogram. b Line of sight (LOS) displacement from ascending track, positive values correspond to motion towards the satellite. c Same than b but showing the data (circles with crosses) used for the coseismic inversion.

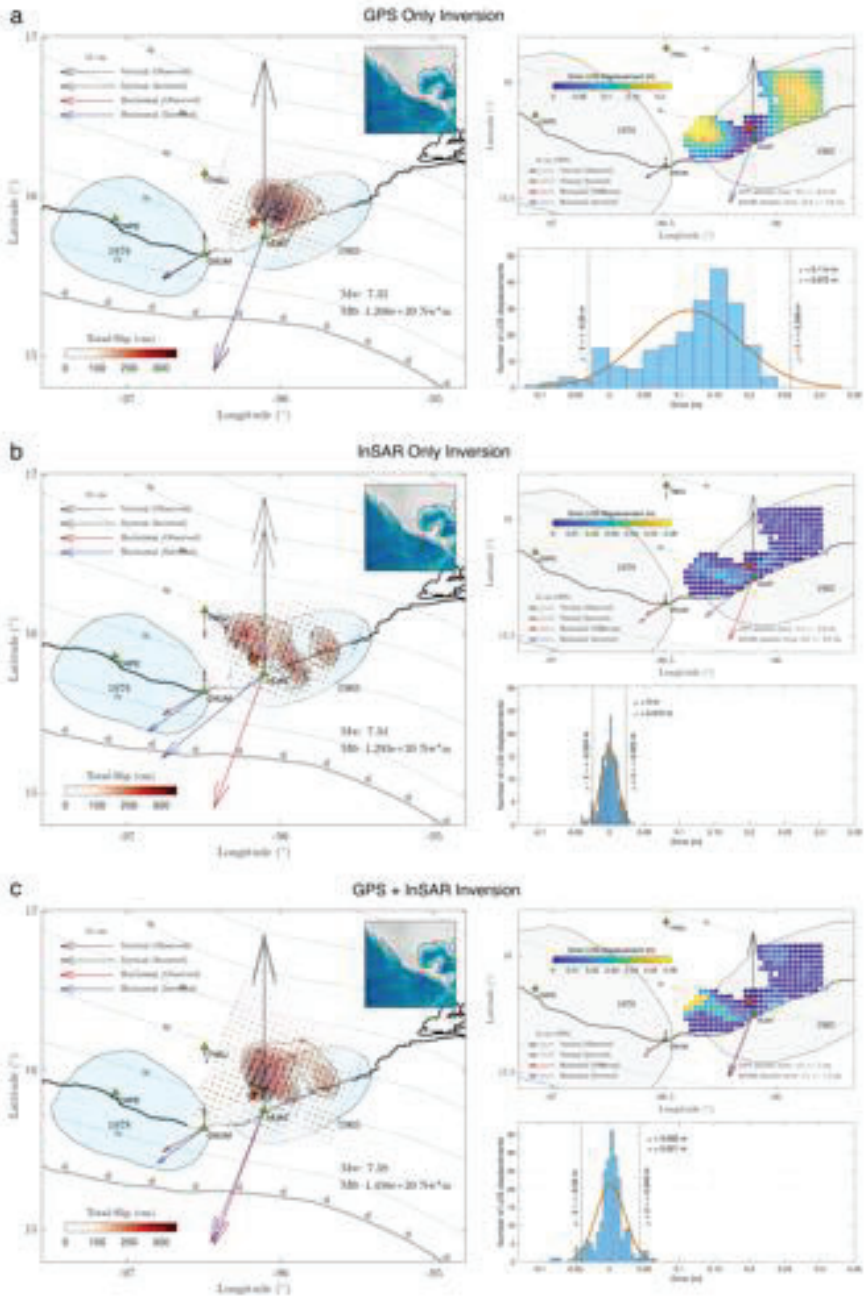

Figure E.3. Coseismic slip inversions for the Huatulco earthquake using different data sets. Coseismic slip inversion (left panel) and their associated misfit GNSS and LOS displacements errors (right panels) using (a) only GNSS data, (b) only InSAR data and (c) both GNSS and InSAR data.

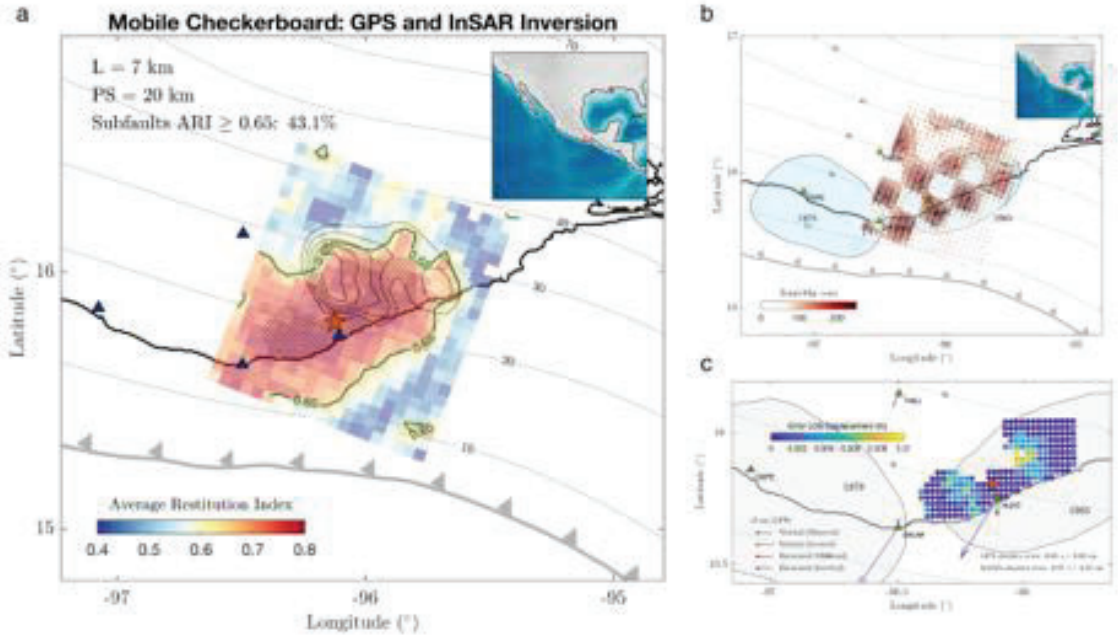

Figure E.4. Resolution analysis for the coseismic GNSS+InSAR joint inversion. a Average restitution index (ARI) obtained from a mobile checkerboard (MOC) analysis that integrates 64 independent checkerboard inversions with patch size (PS) of 20 km and correlation length (L) of 7 km. Blue triangles are the GNSS stations, small gray circles the InSAR data sites, gray contours our preferred slip model for the 2020 Huatulco earthquake and the red star its epicenter. b Example of a single checkerboard slip inversion of the MOC test. c) GNSS and InSAR displacement errors associated with the checkerboard test shown in b.

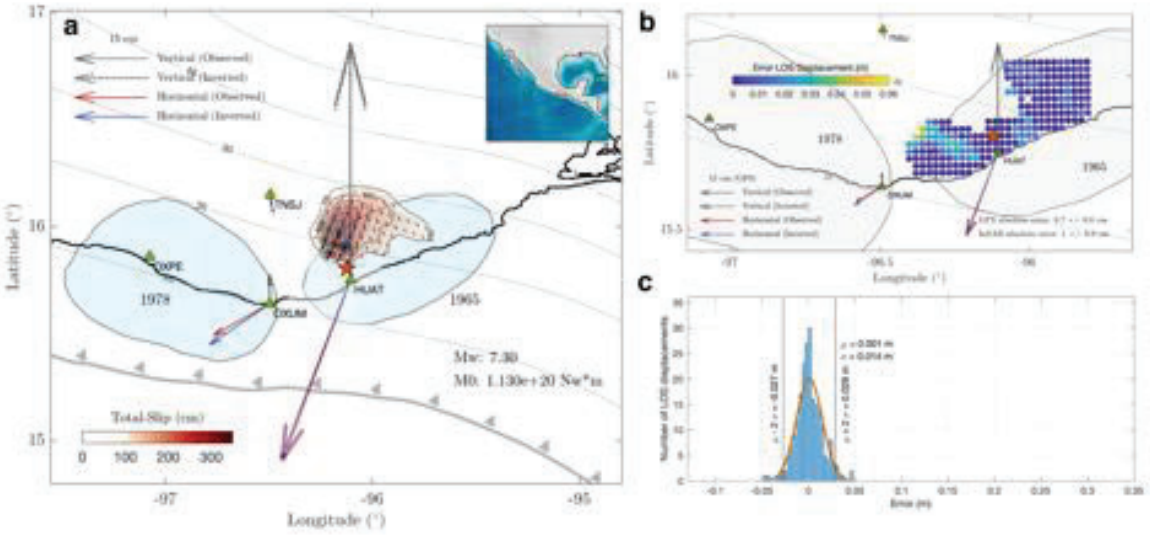

Figure E.5. Huatulco earthquake joint inversion (GNSS and InSAR) assuming that the plate interface has a depth of 17.2 km at the epicenter (i.e., shifted 3.5 km upwards with respect to the interface shown in Figure E.3). Coseismic slip inversion (a) and their associated misfit GNSS and LOS displacements errors (b and c).

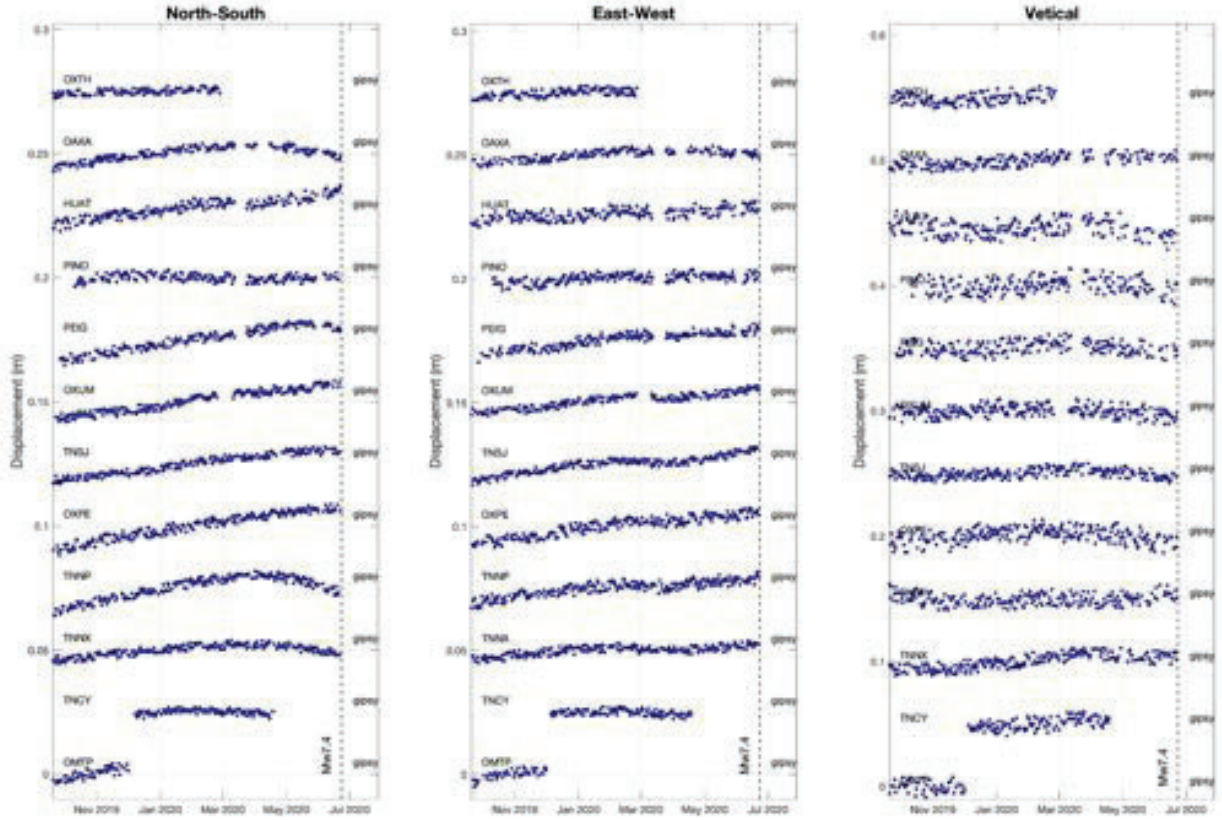

Figure E.6. GNSS displacement time series estimated with the Gipsy-Oasis (v6.4) software for the pre-seismic period in the 12 stations and the three components. See Figures 6.2 and E.6

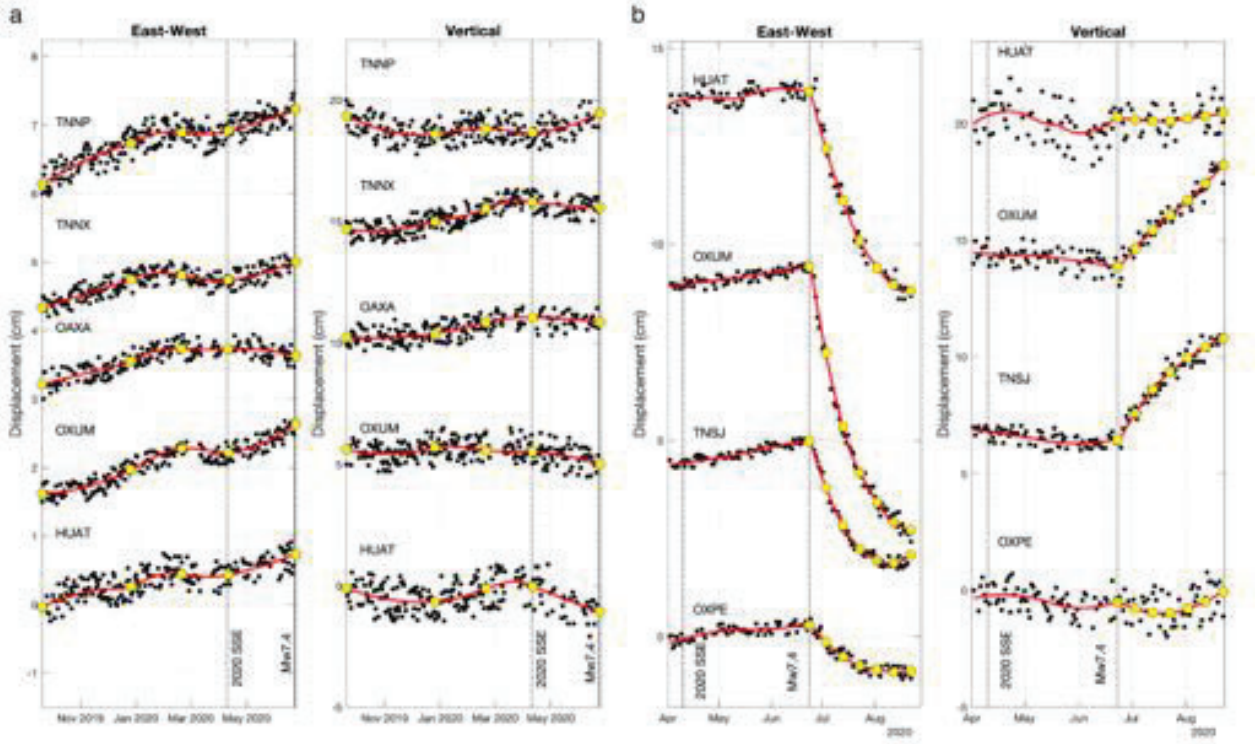

Figure E.7. East-west and vertical GNSS displacement time series estimated with the Gipsy-Oasis software for the pre-seismic and post-seismic periods in selected stations shown in figures 6.2 and 6.3.

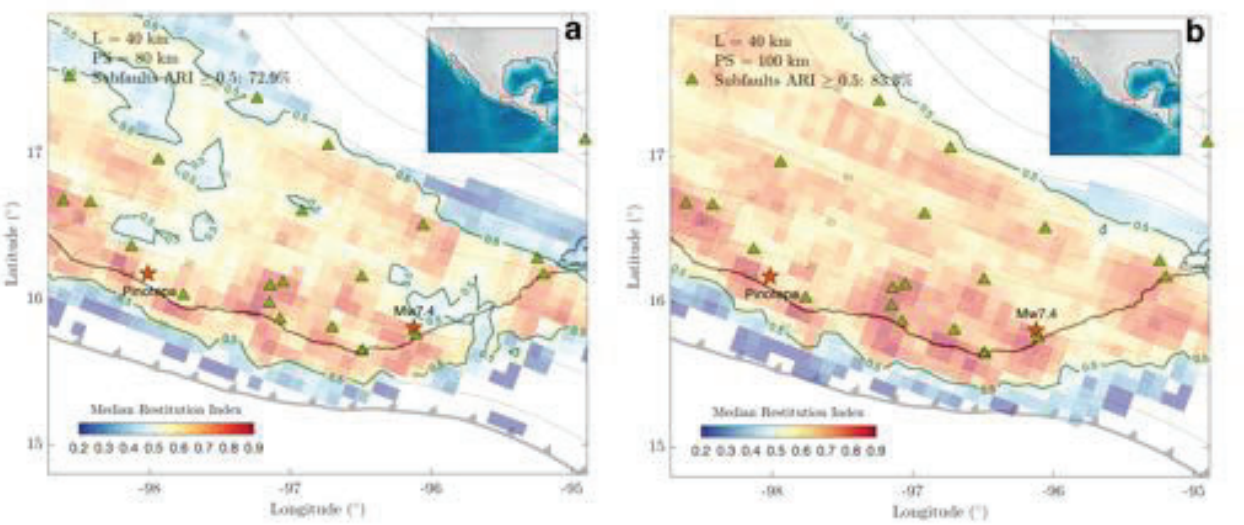

Figure E.8. Resolution analysis for the aseismic slip inversions in Oaxaca. a Distribution of the median restitution index obtained from the mobile checkerboard inversion tests considering slip patches sizes of 80 km. b Same than a but with slip patches sizes of 100 km. Notice how well resolved are the plate interface regions with depths greater than 10 km.

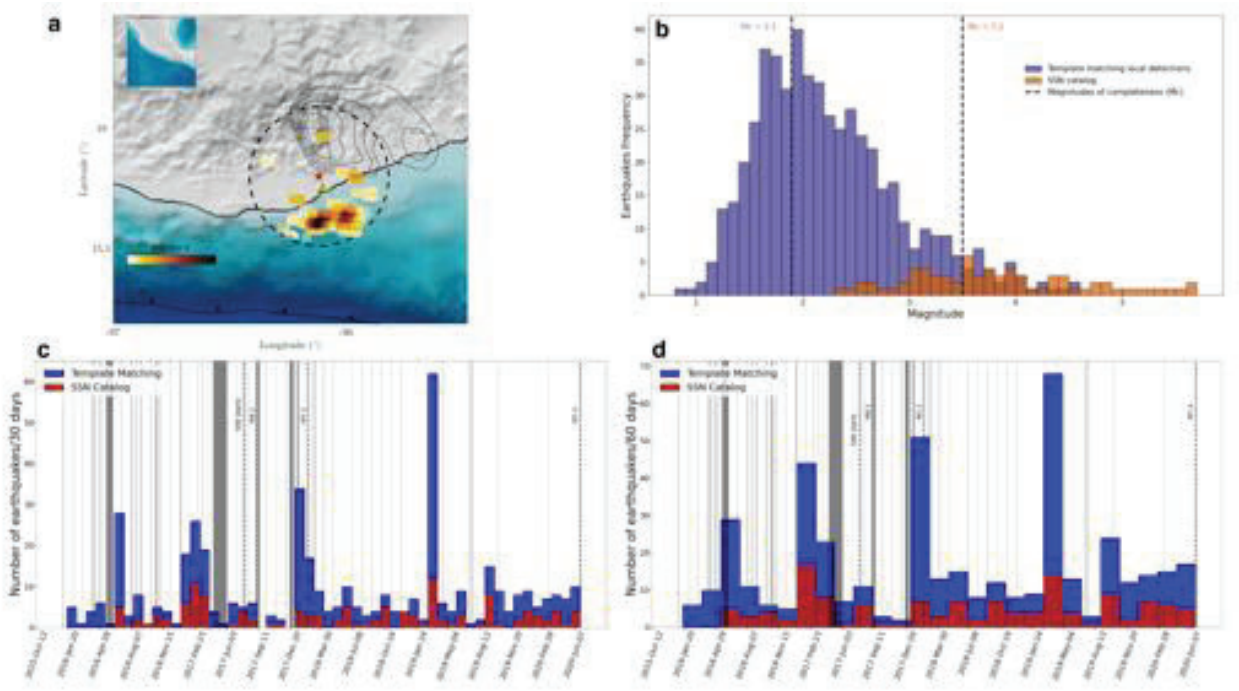

Figure E.9. Illustration of template matching (TM) results using the one station method (Cruz-Atienza et al., 2021). a Density map of precursor TM detections using the closest station HUIG (green triangle) within 30 km from the Huatulco earthquake hypocenter (red star) and M >2.1. Notice how almost all the detections are concentrated updip of the hypocenter due to the scarcity of templates located in the Huatulco rupture area. b Frequency distributions for the TM and SSN catalogs and their associated magnitude of completeness. c,d Seismicity rate evolution for the TM and SSN for two different earthquake rates. Gray sections indicate data gaps.

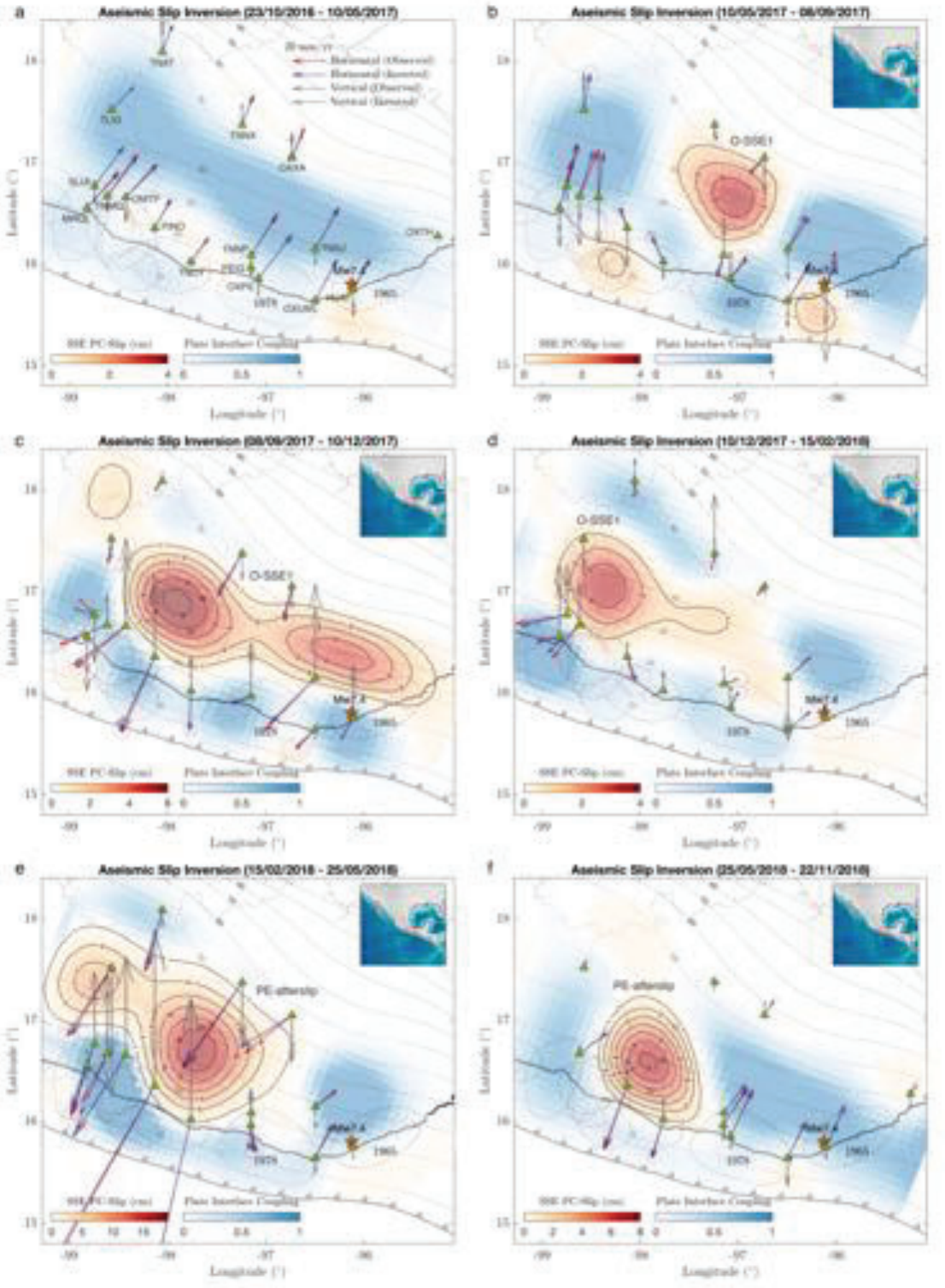

Figure E.10. Detailed evolution aseismic slip inversions in Oaxaca from October 2016 to September 2019 including the 2017 Oaxaca SSE (O-SSE1), the Pinotepa earthquake afterslip (PE-afterslip) and the 2019 Oaxaca SSE (O-SSE2)(see also Movie 2).

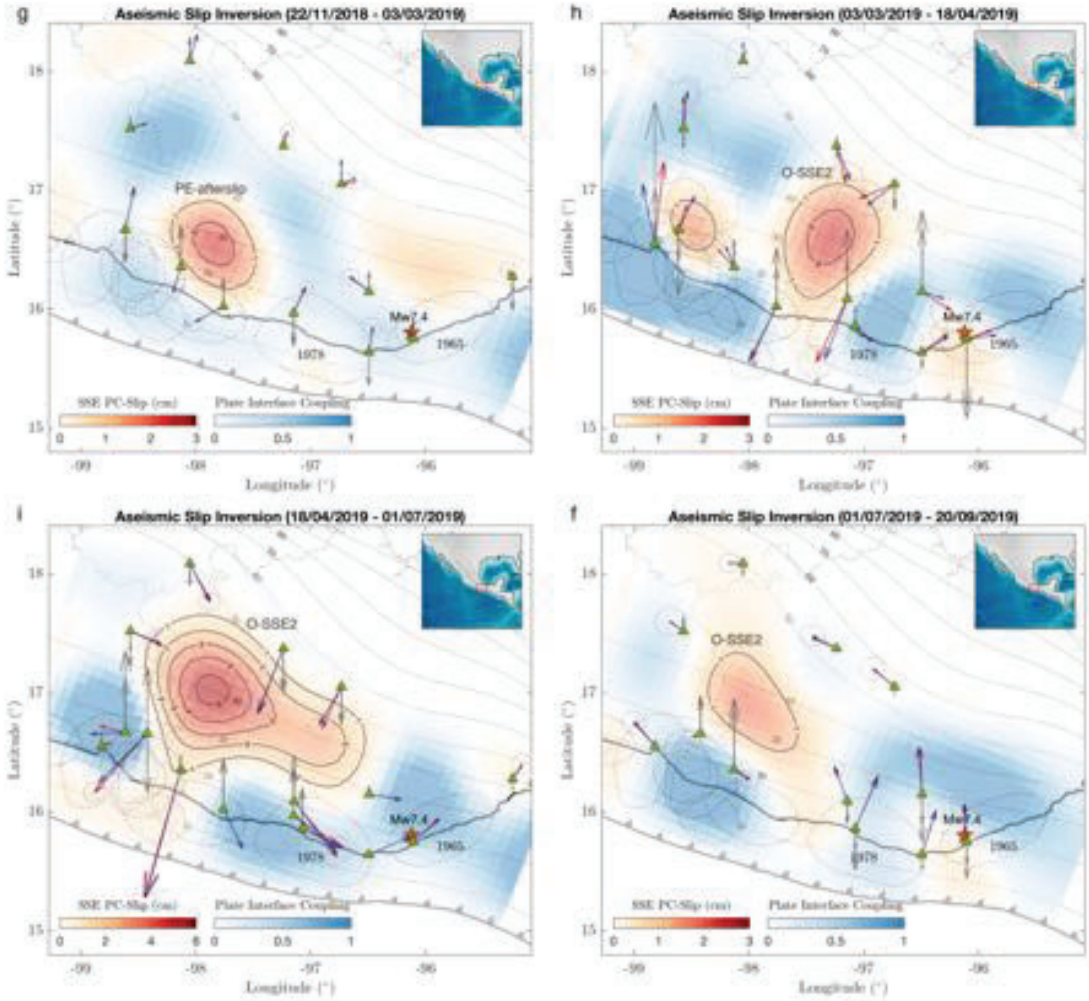

Figure E.10 (continuation)

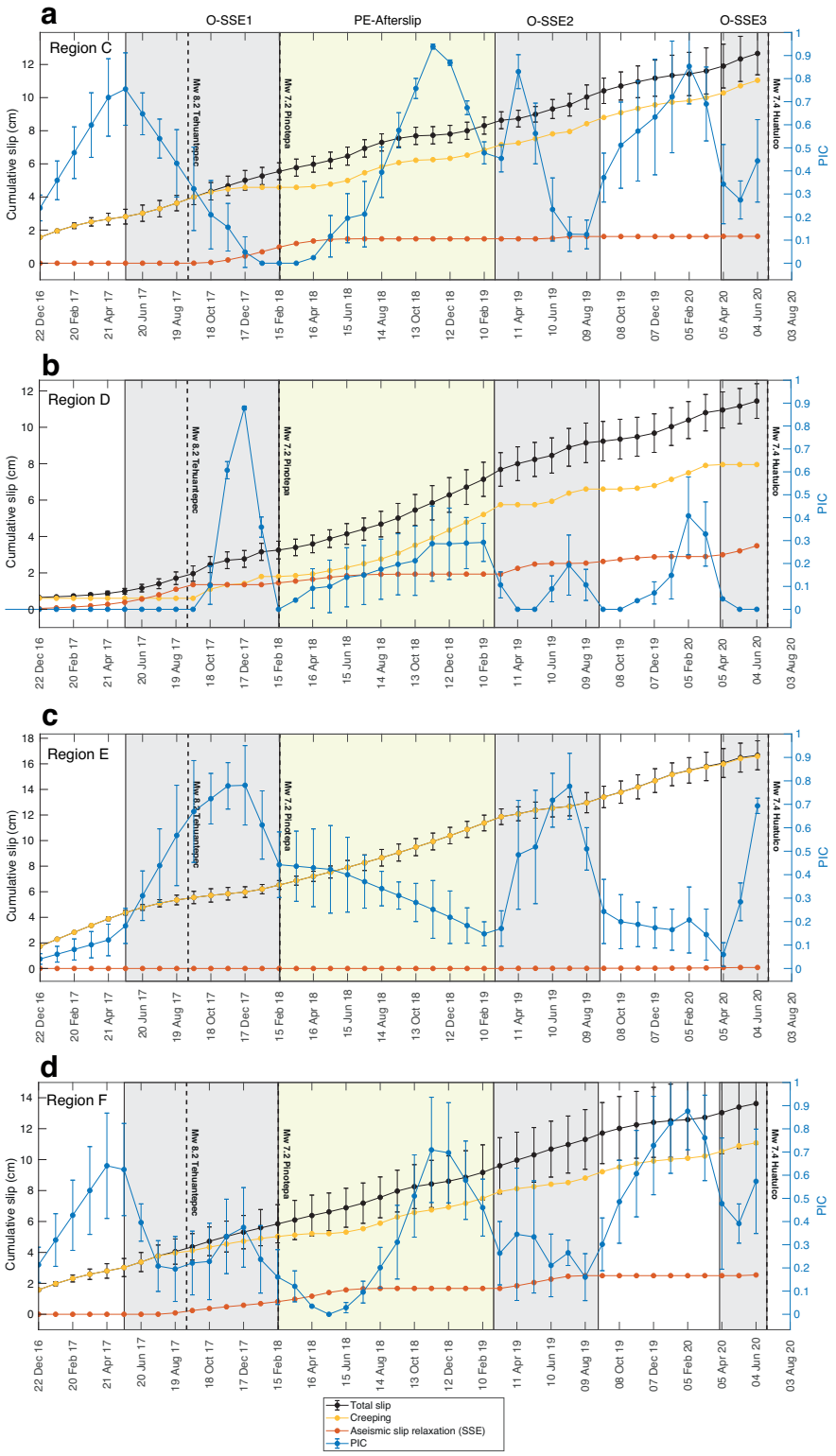

Figure E.11. Evolution of the cumulative total slip, creeping (slip under coupling regime), relaxing aseismic slip (SSEs and afterslip) and plate interface coupling (PIC) in regions C, D, E and F (see Figure 6.4)

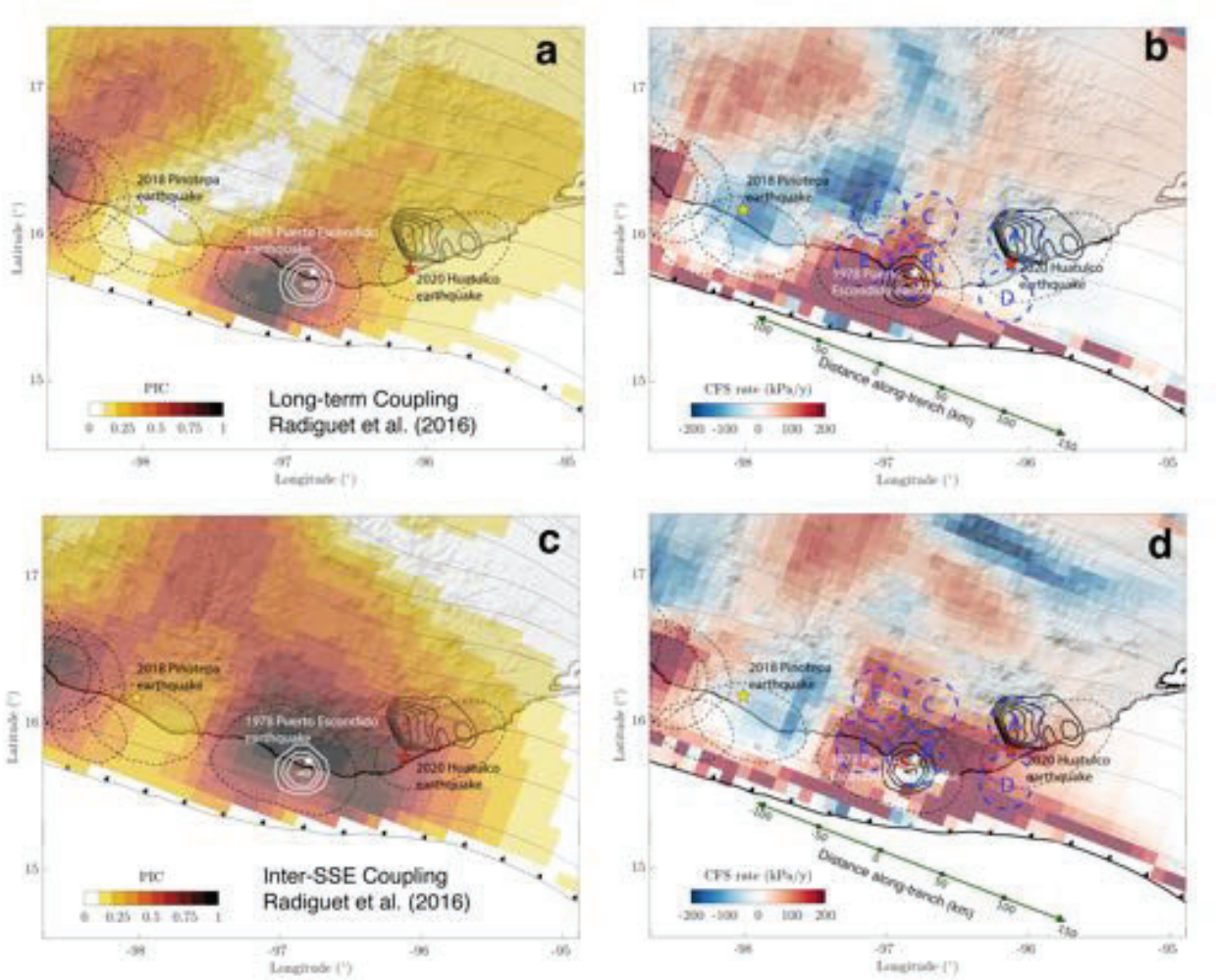

Figure E.12. Long-term and inter-SSE time-invariant interplate coupling models estimated by Radiguet et al. (2016) for the Oaxaca subduction zone and their associated CFS rates.

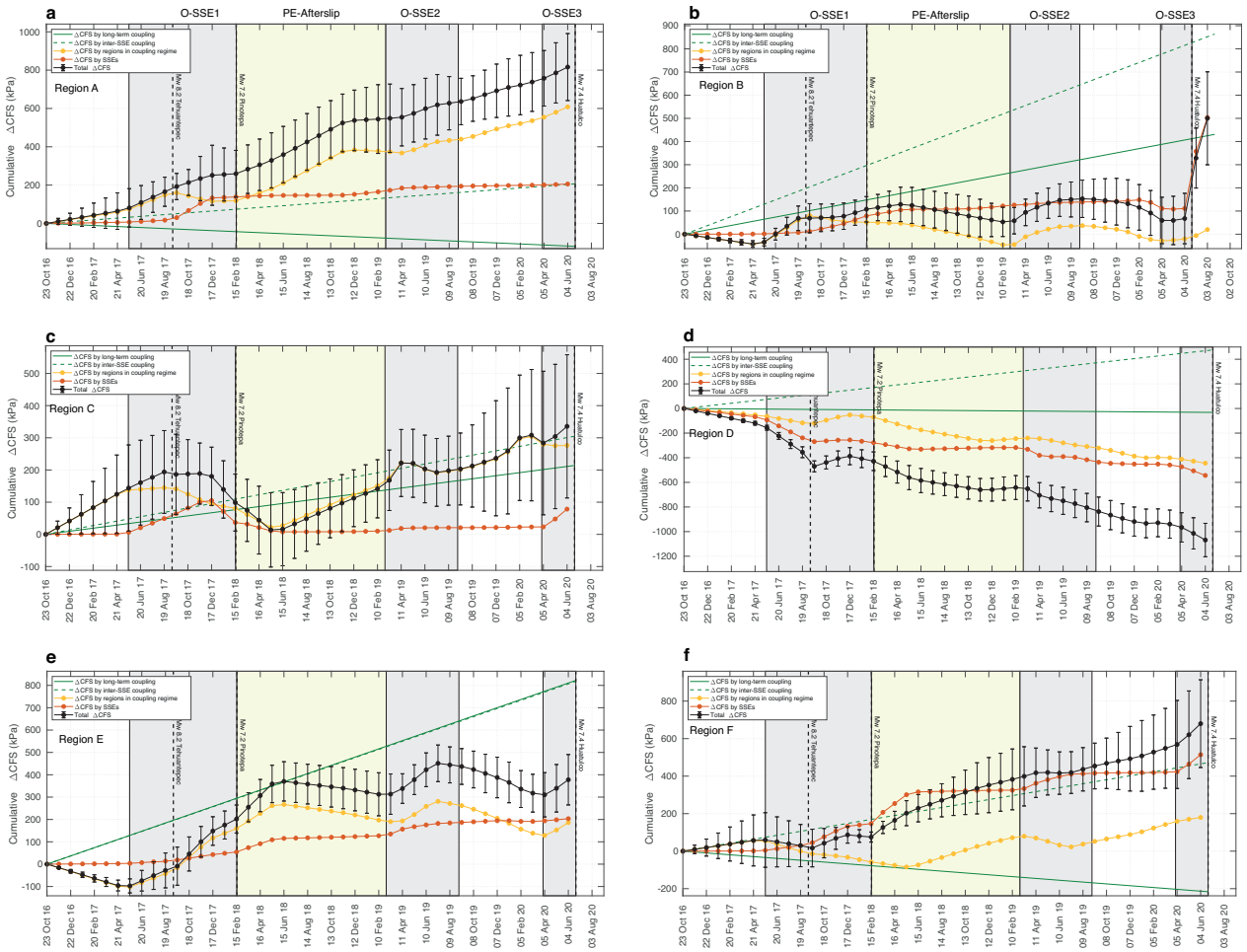

Figure E.13. Evolution of the stress partitioning in the seismogenic zone in Oaxaca. Every panel show the evolution of the total CFS (black curves) and their contributions from the relaxing aseismic slip (red curve) and coupled regions (yellow curve), for Regions A-F. Gray rectangles indicate the occurrence of SSEs in the region. The light-yellow rectangle shows the period when the postseismic afterslip of the 2018 Pinotepa and 2020 Huatulco earthquakes developed in the region.

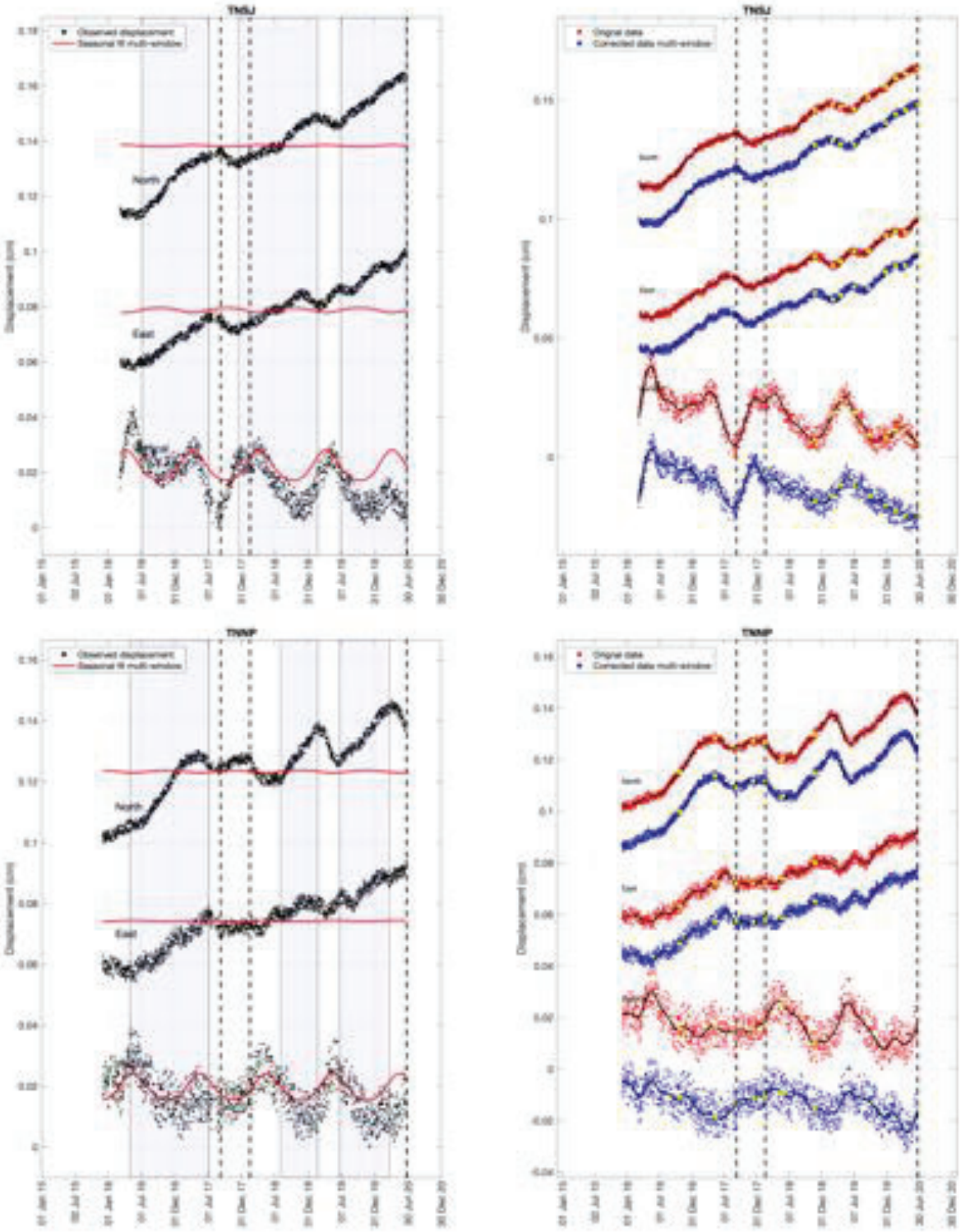

Figure E.14. Example of the correction of displacement time series in station TNSJ for seasonal effects. a Pre-processed GNSS time series (black dots) and seasonal functions for every component (red curves) estimated from the multi-window fit procedure. b Original (red dots) and corrected (blue dots) displacement time series.

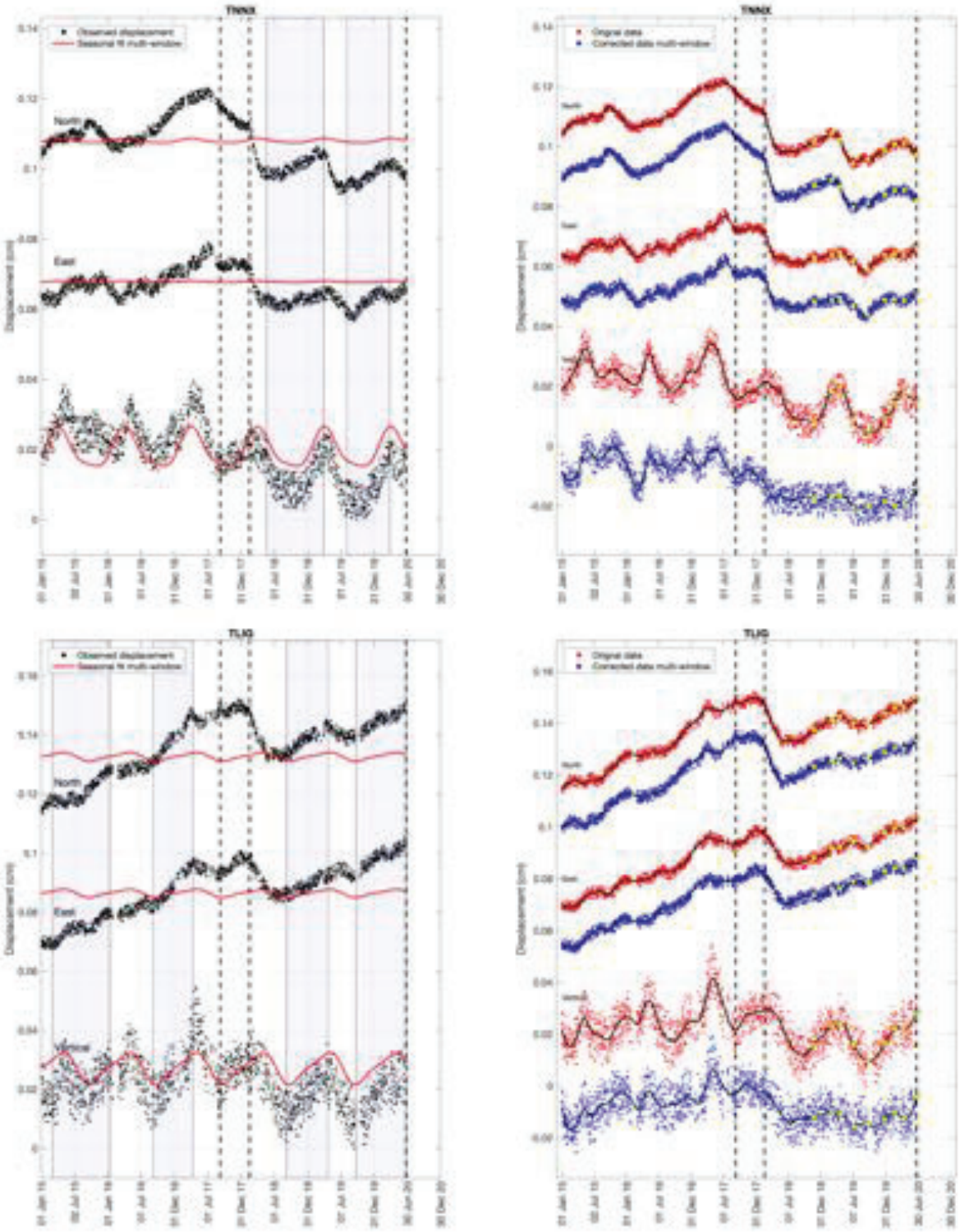

Figure E.14 (continuation)

Bibliography

Amey, R. M. J., Hooper, A., and Walters, R. J. (2018). A Bayesian Method for Incorporating Self-Similarity Into Earthquake Slip Inversions. Journal of Geophysical Research: Solid Earth, 123(7):6052–6071.

Ando, R., Takeda, N., and Yamashita, T. (2012). Propagation dynamics of seismic and aseismic slip governed by fault heterogeneity and newtonian rheology. Journal of Geophysical Research: Solid Earth, 117(B11).

Angiboust, S., Kirsch, J., Oncken, O., Glodny, J., Monié, P., and Rybacki, E. (2015). Probing the transition between seismically coupled and decoupled segments along an ancient subduction interface. Geochemistry, Geophysics, Geosystems, 16(6):1905–1922.

Angiboust, S., Pettke, T., De Hoog, J. C., Caron, B., and Oncken, O. (2014). Channelized fluid flow and eclogite-facies metasomatism along the subduction shear zone. Journal of petrology, 55(5):883–916.

Arzate-Flores, J. A., Molina-Garza, R., Corbo-Camargo, F., and Márquez-Ramírez, V. (2016). Low angle contact between the oaxaca and juárez terranes deduced from magnetotelluric data. In Geodynamics of the Latin American Pacific Margin, pages 3357–3371. Springer.

Askan, A., Akcelik, V., Bielak, J., and Ghattas, O. (2007). Full Waveform Inversion for Seismic Velocity and Anelastic Losses in Heterogeneous Structures. Bulletin of the Seismological Society of America, 97(6):1990–2008.

Asnaashari, A., Brossier, R., Garambois, S., Audebert, F., Thore, P., and Virieux, J. (2013). Regularized seismic full waveform inversion with prior model information. Geophysics, 78(2):R25–R36.

Audet, P., Bostock, M. G., Christensen, N. I., and Peacock, S. M. (2009). Seismic evidence for overpressured subducted oceanic crust and megathrust fault sealing. Nature, 457(7225):76–78.

Audet, P. and Kim, Y. (2016). Teleseismic constraints on the geological environment of deep episodic slow earthquakes in subduction zone forearcs: A review. Tectonophysics, 670:1–15.

Bartlow, N. M., Miyazaki, S., Bradley, A. M., and Segall, P. (2011). Space-time correlation of slip and tremor during the 2009 cascadia slow slip event. Geophysical Research Letters, 38(18).

Bartlow, N. M., Wallace, L. M., Beavan, R. J., Bannister, S., and Segall, P. (2014). Time-dependent modeling of slow slip events and associated seismicity and tremor at the hikurangi subduction zone, new zealand. Journal of Geophysical Research: Solid Earth, 119(1):734–753.

Bedford, J. R., Moreno, M., Deng, Z., Oncken, O., Schurr, B., John, T., Báez, J. C., and Bevis,

M. (2020). Months-long thousand-kilometre-scale wobbling before great subduction earthquakes. Nature, 580(7805):628–635.

Bekaert, D. P. S., Hooper, A., and Wright, T. J. (2015). Reassessing the 2006 Guerrero slow-slip event, Mexico: Implications for large earthquakes in the Guerrero Gap. Journal of Geophysical Research: Solid Earth, 120(2):1357–1375.

Benavente, R., Dettmer, J., Cummins, P. R., and Sambridge, M. (2019). Efficient Bayesian uncertainty estimation in linear finite fault inversion with positivity constraints by employing a log-normal prior. Geophysical Journal International, 217(1):469–484.

Beroza, G. C. and Ide, S. (2011). Slow earthquakes and nonvolcanic tremor. Annual review of Earth and planetary sciences, 39:271–296.

Bevis, M. and Brown, A. (2014). Trajectory models and reference frames for crustal motion geodesy. Journal of Geodesy, 88(3):283–311.

Bletery, Q., Thomas, A. M., Hawthorne, J. C., Skarbek, R. M., Rempel, A. W., and Krogstad, R. D. (2017). Characteristics of secondary slip fronts associated with slow earthquakes in cascadia. Earth and Planetary Science Letters, 463:212–220.

Bouchon, M. and Aki, K. (1977). Discrete wave-number representation of seismic-source wave fields. Bulletin of the Seismological Society of America, 67(2):259–277.

Bourlange, S. and Henry, P. (2007). Numerical model of fluid pressure solitary wave propagation along the décollement of an accretionary wedge: application to the nankai wedge. Geofluids, 7(3):323–334.

Brenguier, F., Campillo, M., Hadziioannou, C., Shapiro, N. M., Nadeau, R. M., and Larose, E. (2008). Postseismic relaxation along the san andreas fault at parkfield from continuous seismological observations. science, 321(5895):1478–1481.

Brown, J. R., Beroza, G. C., Ide, S., Ohta, K., Shelly, D. R., Schwartz, S. Y., Rabbel, W., Thorwart, M., and Kao, H. (2009). Deep low-frequency earthquakes in tremor localize to the plate interface in multiple subduction zones. Geophysical Research Letters, 36(19).

Brudzinski, M. R., Hinojosa-Prieto, H. R., Schlanser, K. M., Cabral-Cano, E., Arciniega-Ceballos, A., Diaz-Molina, O., and DeMets, C. (2010). Nonvolcanic tremor along the oaxaca segment of the middle america subduction zone. Journal of Geophysical Research: Solid Earth, 115(B8).

Cabral-Cano, E., Pérez-Campos, X., Márquez-Azúa, B., Sergeeva, M., Salazar-Tlaczani, L., DeMets, C., Adams, D., Galetzka, J., Hodgkinson, K., Feaux, K., et al. (2018). Tlalocnet: A continuous gps-met backbone in mexico for seismotectonic and atmospheric research. Seismological Research Letters, 89(2A):373–381.

Caltech (2007). Meso-america subduction experiment (mase). caltech, http://web.gps.caltech.edu/ clay/mexweb/mexsubduction.html.

Calvetti, D., Morigi, S., Reichel, L., and Sgallari, F. (2000). Tikhonov regularization and the L-

curve for large discrete ill-posed problems. Journal of computational and applied mathematics, 123(1-2):423–446.

Campillo, M., Singh, S., Shapiro, N., Pacheco, J., and Hermann, R. (1996). Crustal structure south of the mexican volcanic belt, base don group velocity dispersion. Geofísica Internacional, 35(4).

Cavalié, O., Pathier, E., Radiguet, M., Vergnolle, M., Cotte, N., Walpersdorf, A., Kostoglodov, V., and Cotton, F. (2013). Slow slip event in the mexican subduction zone: Evidence of shallower slip in the guerrero seismic gap for the 2006 event revealed by the joint inversion of insar and gps data. Earth and Planetary Science Letters, 367:52–60.

Chael, E. P. and Stewart, G. S. (1982). Recent large earthquakes along the middle american trench and their implications for the subduction process. Journal of Geophysical Research: Solid Earth, 87(B1):329–338.

Chamberlain, C. J., Hopp, C. J., Boese, C. M., Warren-Smith, E., Chambers, D., Chu, S. X., Michailos, K., and Townend, J. (2018). Eqcorrscan: Repeating and near-repeating earthquake detection and analysis in python. Seismological Research Letters, 89(1):173–181.

Chao, K., Peng, Z., Frank, W. B., Prieto, G. A., and Obara, K. (2019). Isolated triggered tremor spots in south america and implications for global tremor activity. Seismological Research Letters, 90(5):1726–1739.

Chen, C. W. and Zebker, H. A. (2000). Network approaches to two-dimensional phase unwrapping: intractability and two new algorithms. JOSA A, 17(3):401–414.

Chlieh, M., Avouac, J.-P., Sieh, K., Natawidjaja, D. H., and Galetzka, J. (2008). Heterogeneous coupling of the sumatran megathrust constrained by geodetic and paleogeodetic measurements. Journal of Geophysical Research: Solid Earth, 113(B5).

Colella, H. V., Dieterich, J. H., Richards-Dinger, K., and Rubin, A. M. (2012). Complex characteristics of slow slip events in subduction zones reproduced in multi-cycle simulations. Geophysical Research Letters, 39(20).

Correa-Mora, F., DeMets, C., Cabral-Cano, E., Marquez-Azua, B., and Diaz-Molina, O. (2008). Interplate coupling and transient slip along the subduction interface beneath oaxaca, mexico. Geophysical Journal International, 175(1):269–290.

Cotte, N., Walpersdorf, A., Kostoglodov, V., Vergnolle, M., Santiago, J.-A., and Campillo, M. (2009). Anticipating the next large silent earthquake in mexico. Eos, Transactions American Geophysical Union, 90(21):181–182.

Coutant, O. (1990). Programme de Simulation numérique AXITRA. Rapport LGIT, Université Joseph Fourier, Grenoble, France.

Cruz-Atienza, V., Tago, J., Villafuerte, C., Wei, M., Garza-Girón, R., Dominguez, L., Kostoglodov, V., Nishimura, T., Franco, S., and Real, J. (2021). Short-term interaction between silent and devastating earthquakes in mexico. Nature communications.

Cruz-Atienza, V. M., Husker, A., Legrand, D., Caballero, E., and Kostoglodov, V. (2015). Non-volcanic tremor locations and mechanisms in guerrero, mexico, from energy-based and particle motion polarization analysis. Journal of Geophysical Research: Solid Earth, 120(1):275–289.

Cruz-Atienza, V. M., Ito, Y., Kostoglodov, V., Hjörleifsdóttir, V., Iglesias, A., Tago, J., Calò, M., Real, J., Husker, A., Ide, S., et al. (2018a). A seismogeodetic amphibious network in the guerrero seismic gap, mexico. Seismological Research Letters, 89(4):1435–1449.

Cruz-Atienza, V. M., Villafuerte, C., and Bhat, H. S. (2018b). Rapid tremor migration and pore-pressure waves in subduction zones. Nature communications, 9(1):1–13.

de México Seismology, U. N. A. et al. (2013). Ometepec-pinotepa nacional, mexico earthquake of 20 march 2012 (mw 7.5): A preliminary report. Geofísica Internacional, 52(2):173–196.

Delorey, A. A., Chao, K., Obara, K., and Johnson, P. A. (2015). Cascading elastic perturbation in japan due to the 2012 mw 8.6 indian ocean earthquake. Science advances, 1(9):e1500468.

DeMets, C., Gordon, R. G., and Argus, D. F. (2010). Geologically current plate motions. Geophysical Journal International, 181(1):1–80.

Dettmer, J., Benavente, R., Cummins, P. R., and Sambridge, M. (2014). Trans-dimensional finite-fault inversion. Geophysical Journal International, 199(2):735–751.

Dieterich, J. (1994). A constitutive law for rate of earthquake production and its application to earthquake clustering. Journal of Geophysical Research: Solid Earth, 99(B2):2601–2618.

Dragert, H., Wang, K., and James, T. S. (2001). A silent slip event on the deeper cascadia subduction interface. Science, 292(5521):1525–1528.

Dumoulin, V. and Visin, F. (2016). A guide to convolution arithmetic for deep learning. arXiv preprint arXiv:1603.07285.

Dunham, E. M., Thomas, A., Becker, T. W., Cattania, C., Hawthorne, J., Hubbard, J., Lotto, G. C., Olive, J.-A., and Platt, J. (2020). Megathrust modeling workshop report.

Evans, J. P., Forster, C. B., and Goddard, J. V. (1997). Permeability of fault-related rocks, and implications for hydraulic structure of fault zones. Journal of Structural Geology, 19(11):1393–1404.

Faccenda, M., Gerya, T. V., and Burlini, L. (2009). Deep slab hydration induced by bending-related variations in tectonic pressure. Nature Geoscience, 2(11):790–793.

Fagereng, Å., Hillary, G. W., and Diener, J. F. (2014). Brittle-viscous deformation, slow slip, and tremor. Geophysical Research Letters, 41(12):4159–4167.

Farr, T. G., Rosen, P. A., Caro, E., Crippen, R., Duren, R., Hensley, S., Kobrick, M., Paller, M., Rodriguez, E., Roth, L., et al. (2007). The shuttle radar topography mission. Reviews of geophysics, 45(2).

Ferrari, L., Orozco-Esquivel, T., Manea, V., and Manea, M. (2012). The dynamic history of the trans-mexican volcanic belt and the mexico subduction zone. Tectonophysics, 522:122–149.

Fichtner, A., Bunge, H.-P., and Igel, H. (2006). The adjoint method in seismology: I. Theory. Physics of the Earth and Planetary Interiors, 157:86–104.

Fichtner, A., Kennett, B., Igel, H., and Bunge, H.-P. (2010). Full waveform tomography for radially anisotropic structure: New insights into present and past states of the Australasian upper mantle. Earth and Planetary Science Letters, 290:270–280.

Fisher, A. T. (1998). Permeability within basaltic oceanic crust. Reviews of Geophysics, 36(2):143–182.

Frank, W., Shapiro, N., Husker, A., Kostoglodov, V., Bhat, H., and Campillo, M. (2015a). Along-fault pore-pressure evolution during a slow-slip event in guerrero, mexico. Earth and Planetary Science Letters, 413:135–143.

Frank, W. B. (2016). Slow slip hidden in the noise: The intermittence of tectonic release. Geophysical Research Letters, 43(19):10–125.

Frank, W. B., Radiguet, M., Rousset, B., Shapiro, N. M., Husker, A. L., Kostoglodov, V., Cotte, N., and Campillo, M. (2015b). Uncovering the geodetic signature of silent slip through repeating earthquakes. Geophysical Research Letters, 42(8):2774–2779.

Frank, W. B., Shapiro, N. M., Husker, A. L., Kostoglodov, V., Romanenko, A., and Campillo, M. (2014). Using systematically characterized low-frequency earthquakes as a fault probe in guerrero, mexico. Journal of Geophysical Research: Solid Earth, 119(10):7686–7700.

Frank, W. B., Shapiro, N. M., Kostoglodov, V., Husker, A. L., Campillo, M., Payero, J. S., and Prieto, G. A. (2013). Low-frequency earthquakes in the mexican sweet spot. Geophysical Research Letters, 40(11):2661–2666.

Fukuda, J. and Johnson, K. M. (2008). A fully Bayesian inversion for spatial distribution of fault slip with objective smoothing. Bulletin of the Seismological Society of America, 98(3):1128–1146.

García, D., Singh, S. K., Herráiz, M., Pacheco, J. F., and Ordaz, M. (2004). Inslab earthquakes of central mexico: Q, source spectra, and stress drop. Bulletin of the Seismological Society of America, 94(3):789–802.

Garza Giron, R., Brodsky, E. E., Spica, Z. J., and Haney, M. M. (2020). Clog and crack: Opening and closing behavior during a sustained explosive eruption as recorded by its hidden earthquakes. ESSOAR.

Gauthier, O., Virieux, J., and Tarantola, A. (1986). Two-dimensional nonlinear inversion of seismic waveforms: Numerical results. Geophysics, 51(7):1341–1519.

Ghosh, A., Vidale, J. E., Sweet, J. R., Creager, K. C., Wech, A. G., Houston, H., and Brodsky, E. E. (2010). Rapid, continuous streaking of tremor in cascadia. Geochemistry, Geophysics, Geosystems, 11(12).

Goldstein, R. M. and Werner, C. L. (1998). Radar interferogram filtering for geophysical applications. Geophysical research letters, 25(21):4035–4038.

Graham, S., DeMets, C., Cabral-Cano, E., Kostoglodov, V., Rousset, B., Walpersdorf, A., Cotte, N., Lasserre, C., McCaffrey, R., and Salazar-Tlaczani, L. (2016). Slow slip history for the mexico subduction zone: 2005 through 2011. In Geodynamics of the Latin American Pacific Margin, pages 3445–3465. Springer.

Graham, S. E., DeMets, C., Cabral-Cano, E., Kostoglodov, V., Walpersdorf, A., Cotte, N., Brudzinski, M., McCaffrey, R., and Salazar-Tlaczani, L. (2014a). Gps constraints on the 2011–2012 oaxaca slow slip event that preceded the 2012 march 20 ometepec earthquake, southern mexico. Geophysical Journal International, 197(3):1593–1607.

Graham, S. E., DeMets, C., Cabral-Cano, E., Kostoglodov, V., Walpersdorf, A., Cotte, N., Brudzinski, M., McCaffrey, R., and Salazar-Tlaczani, L. (2014b). Gps constraints on the m w= 7.5 ometepec earthquake sequence, southern mexico: Coseismic and post-seismic deformation. Geophysical Journal International, 199(1):200–218.

Gualandi, A., Perfettini, H., Radiguet, M., Cotte, N., and Kostoglodov, V. (2017). Gps deformation related to the mw 7.3, 2014, papanoa earthquake (mexico) reveals the aseismic behavior of the guerrero seismic gap. Geophysical Research Letters, 44(12):6039–6047.

Hanssen, R. F. (2001). Radar interferometry: data interpretation and error analysis, volume 2. Springer Science & Business Media.

Hawthorne, J. and Rubin, A. (2013). Tidal modulation and back-propagating fronts in slow slip events simulated with a velocity-weakening to velocity-strengthening friction law. Journal of Geophysical Research: Solid Earth, 118(3):1216–1239.

Hawthorne, J. C., Bostock, M. G., Royer, A. A., and Thomas, A. M. (2016). Variations in slow slip moment rate associated with rapid tremor reversals in cascadia. Geochemistry, Geophysics, Geosystems, 17(12):4899–4919.

Heki, K. (2001). Seasonal modulation of interseismic strain buildup in northeastern japan driven by snow loads. Science, 293(5527):89–92.

Heki, K. and Mitsui, Y. (2013). Accelerated pacific plate subduction following interplate thrust earthquakes at the japan trench. Earth and Planetary Science Letters, 363:44–49.

Herring, T., King, R., McClusky, S., et al. (2010). Introduction to gamit/globk. Massachusetts Institute of Technology, Cambridge, Massachusetts.

Hirose, H., Asano, Y., Obara, K., Kimura, T., Matsuzawa, T., Tanaka, S., and Maeda, T. (2010). Slow earthquakes linked along dip in the nankai subduction zone. Science, 330(6010):1502–1502.

Hirose, H., Matsuzawa, T., Kimura, T., and Kimura, H. (2014). The boso slow slip events in 2007 and 2011 as a driving process for the accompanying earthquake swarm. Geophysical Research Letters, 41(8):2778–2785.

Hirose, H. and Obara, K. (2010). Recurrence behavior of short-term slow slip and correlated nonvolcanic tremor episodes in western shikoku, southwest japan. Journal of Geophysical Research: Solid Earth, 115(B6).

Houston, H. (2015). Low friction and fault weakening revealed by rising sensitivity of tremor to tidal stress. Nature Geoscience, 8(5):409–415.

Houston, H., Delbridge, B. G., Wech, A. G., and Creager, K. C. (2011). Rapid tremor reversals in cascadia generated by a weakened plate interface. Nature Geoscience, 4(6):404–409.

Husker, A., Frank, W. B., Gonzalez, G., Avila, L., Kostoglodov, V., and Kazachkina, E. (2019). Characteristic tectonic tremor activity observed over multiple slow slip cycles in the mexican subduction zone. Journal of Geophysical Research: Solid Earth, 124(1):599–608.

Husker, A., Peyrat, S., Shapiro, N., and Kostoglodov, V. (2010). Automatic non-volcanic tremor detection in the mexican subduction zone. Geofísica internacional, 49(1):17–25.

Husker, A. L., Kostoglodov, V., Cruz-Atienza, V. M., Legrand, D., Shapiro, N. M., Payero, J. S., Campillo, M., and Huesca-Pérez, E. (2012). Temporal variations of non-volcanic tremor (nvt) locations in the mexican subduction zone: Finding the nvt sweet spot. Geochemistry, Geophysics, Geosystems, 13(3).

Ida, Y. (1973). The maximum acceleration of seismic ground motion. Bulletin of the Seismological Society of America, 63(3):959–968.

Ide, S., Shelly, D. R., and Beroza, G. C. (2007). Mechanism of deep low frequency earthquakes: Further evidence that deep non-volcanic tremor is generated by shear slip on the plate interface. Geophysical Research Letters, 34(3).

Iglesias, A., Clayton, R., Pérez-Campos, X., Singh, S., Pacheco, J., García, D., and Valdés-González, C. (2010). S wave velocity structure below central mexico using high-resolution surface wave tomography. Journal of Geophysical Research: Solid Earth, 115(B6).

Ikari, M. J. and Saffer, D. M. (2011). Comparison of frictional strength and velocity dependence between fault zones in the nankai accretionary complex. Geochemistry, Geophysics, Geosystems, 12(4).

Im, K., Saffer, D., Marone, C., and Avouac, J.-P. (2020). Slip-rate-dependent friction as a universal mechanism for slow slip events. Nature Geoscience, 13(10):705–710.

Ito, Y., Hino, R., Kido, M., Fujimoto, H., Osada, Y., Inazu, D., Ohta, Y., Iinuma, T., Ohzono, M., Miura, S., et al. (2013). Episodic slow slip events in the japan subduction zone before the 2011 tohoku-oki earthquake. Tectonophysics, 600:14–26.

Ito, Y., Obara, K., Shiomi, K., Sekine, S., and Hirose, H. (2007). Slow earthquakes coincident with episodic tremors and slow slip events. Science, 315(5811):503–506.

Johnson, P., Carpenter, B., Knuth, M., Kaproth, B., Le Bas, P.-Y., Daub, E., and Marone, C. (2012). Nonlinear dynamical triggering of slow slip on simulated earthquake faults with implications to earth. Journal of Geophysical Research: Solid Earth, 117(B4).

Johnson, P. A. and Jia, X. (2005). Nonlinear dynamics, granular media and dynamic earthquake triggering. Nature, 437(7060):871–874.

Kaneko, Y., Avouac, J.-P., and Lapusta, N. (2010). Towards inferring earthquake patterns from geodetic observations of interseismic coupling. Nature Geoscience, 3(5):363–369.

Kaneko, Y., Wallace, L. M., Hamling, I. J., and Gerstenberger, M. C. (2018). Simple physical model for the probability of a subduction-zone earthquake following slow slip events and earthquakes: Application to the hikurangi megathrust, new zealand. Geophysical Research Letters, 45(9):3932–3941.

Kano, M., Miyazaki, S., Ishikawa, Y., Hiyoshi, Y., Ito, K., and Hirahara, K. (2015). Real data assimilation for optimization of frictional parameters and prediction of afterslip in the 2003 Tokachi-oki earthquake inferred from slip velocity by an adjoint method. Geophysical Journal International, 203(1):646–663.

Katayama, I., Terada, T., Okazaki, K., and Tanikawa, W. (2012). Episodic tremor and slow slip potentially linked to permeability contrasts at the moho. Nature Geoscience, 5(10):731–734.

Kato, A., Obara, K., Igarashi, T., Tsuruoka, H., Nakagawa, S., and Hirata, N. (2012). Propagation of slow slip leading up to the 2011 mw 9.0 tohoku-oki earthquake. Science, 335(6069):705–708.

Kawano, S., Katayama, I., and Okazaki, K. (2011). Permeability anisotropy of serpentinite and fluid pathways in a subduction zone. Geology, 39(10):939–942.

Kim, Y., Clayton, R., and Jackson, J. (2010). Geometry and seismic properties of the subducting cocos plate in central mexico. Journal of Geophysical Research: Solid Earth, 115(B6).

Kostoglodov, V., Husker, A., Shapiro, N. M., Payero, J. S., Campillo, M., Cotte, N., and Clayton, R. (2010). The 2006 slow slip event and nonvolcanic tremor in the mexican subduction zone. Geophysical Research Letters, 37(24).

Kostoglodov, V., Singh, S. K., Santiago, J. A., Franco, S. I., Larson, K. M., Lowry, A. R., and Bilham, R. (2003). A large silent earthquake in the guerrero seismic gap, mexico. Geophysical Research Letters, 30(15).

Krischer, L., Fichtner, A., Boehm, C., and Igel, H. (2018). Automated Large-Scale Full Seismic Waveform Inversion for North America and the North Atlantic. Journal of Geophysical Research: Solid Earth, 123(7):5902–5928.

Lagler, K., Schindelegger, M., Böhm, J., Krásná, H., and Nilsson, T. (2013). Gpt2: Empirical slant delay model for radio space geodetic techniques. Geophysical research letters, 40(6):1069–1073.

Lay, T. and Kanamori, H. (1981). An asperity model of large earthquake sequences.

Li, Y., Shan, X., Zhu, C., Qiao, X., Zhao, L., and Qu, C. (2020). Geodetic model of the 2018 m w 7.2 pinotepa, mexico, earthquake inferred from insar and gps data. Bulletin of the Seismological Society of America, 110(3):1115–1124.

Liu, M., Li, H., Zhang, M., and Wang, T. (2020). Graphics processing unit-based match and locate (gpu-m&l): An improved match and locate method and its application. Seismological Research Letters, 91(2A):1019–1029.

Liu, Y. and Rice, J. R. (2007). Spontaneous and triggered aseismic deformation transients in a subduction fault model. Journal of Geophysical Research: Solid Earth, 112(B9).

Liu, Y. and Rubin, A. M. (2010). Role of fault gouge dilatancy on aseismic deformation transients. Journal of Geophysical Research: Solid Earth, 115(B10).

Loveless, J. P. and Meade, B. J. (2011). Spatial correlation of interseismic coupling and coseismic rupture extent of the 2011 mw= 9.0 tohoku-oki earthquake. Geophysical Research Letters, 38(17).

Lui, S. K. and Lapusta, N. (2016). Repeating microearthquake sequences interact predominantly through postseismic slip. Nature communications, 7(1):1–7.

Mai, P. M. and Beroza, G. C. (2002). A spatial random field model to characterize complexity in earthquake slip. Journal of Geophysical Research: Solid Earth, 107(B11):ESE 10–1–ESE 10–21.

Manea, V. C. and Manea, M. (2011). Flat-slab thermal structure and evolution beneath central mexico. Pure and Applied Geophysics, 168(8-9):1475–1487.

Marone, C., Raleigh, C. B., and Scholz, C. (1990). Frictional behavior and constitutive modeling of simulated fault gouge. Journal of Geophysical Research: Solid Earth, 95(B5):7007–7025.

Materna, K., Bartlow, N., Wech, A., Williams, C., and Bürgmann, R. (2019). Dynamically triggered changes of plate interface coupling in southern cascadia. Geophysical Research Letters, 46(22):12890–12899.

Matsuzawa, T., Hirose, H., Shibazaki, B., and Obara, K. (2010). Modeling short-and long-term slow slip events in the seismic cycles of large subduction earthquakes. Journal of Geophysical Research: Solid Earth, 115(B12).

Maubant, L., Pathier, E., Daout, S., Radiguet, M., Doin, M.-P., Kazachkina, E., Kostoglodov, V., Cotte, N., and Walpersdorf, A. (2020). Independent component analysis and parametric approach for source separation in insar time series at regional scale: application to the 2017–2018 slow slip event in guerrero (mexico). Journal of Geophysical Research: Solid Earth, 125(3):e2019JB018187.

Maury, J., Ide, S., Cruz-Atienza, V., Kostoglodov, V., González-Molina, G., and Pérez-Campos, X. (2016). Comparative study of tectonic tremor locations: Characterization of slow earthquakes in guerrero, mexico. Journal of Geophysical Research: Solid Earth.

McCaffrey, R., Qamar, A., King, R., Wells, R., Khazaradze, G., Williams, C., Stevens, C., Vollick, J., and Zwick, P. (2007). Fault locking, block rotation and crustal deformation in the Pacific Northwest. Geophysical Journal International, 169:1315–1340.

Melgar, D., Ruiz-Angulo, A., Garcia, E. S., Manea, M., Manea, V. C., Xu, X., Ramirez-Herrera, M. T., Zavala-Hidalgo, J., Geng, J., Corona, N., et al. (2018). Deep embrittlement and complete rupture of the lithosphere during the m w 8.2 tehuantepec earthquake. Nature Geoscience, 11(12):955–960.

Melgar, D., Ruiz-Angulo, A., Pérez-Campos, X., Crowell, B. W., Xu, X., Cabral-Cano, E., Brudzinski, M. R., and Rodriguez-Abreu, L. (2021). Energetic rupture and tsunamigenesis during the 2020 m w 7.4 la crucecita, mexico earthquake. Seismological Society of America, 92(1):140–150.

Melnick, D., Moreno, M., Quinteros, J., Baez, J. C., Deng, Z., Li, S., and Oncken, O. (2017). The super-interseismic phase of the megathrust earthquake cycle in chile. Geophysical Research Letters, 44(2):784–791.

Métivier, L. and Brossier, R. (2016). The SEISCOPE optimization toolbox: A large-scale nonlinear optimization library based on reverse communication. Geophysics, 81(2):F1–F15.

Mikumo, T., Yagi, Y., Singh, S. K., and Santoyo, M. A. (2002). Coseismic and postseismic stress changes in a subducting plate: Possible stress interactions between large interplate thrust and intraplate normal-faulting earthquakes. Journal of Geophysical Research: Solid Earth, 107(B1):ESE–5.

Miller, S. A. (2013). The role of fluids in tectonic and earthquake processes. In Advances in geophysics, volume 54, pages 1–46. Elsevier.

Miller, S. A. (2015). Modeling enhanced geothermal systems and the essential nature of large-scale changes in permeability at the onset of slip. Geofluids, 15(1-2):338–349.

Miller, S. A., Collettini, C., Chiaraluce, L., Cocco, M., Barchi, M., and Kaus, B. J. (2004). Aftershocks driven by a high-pressure co2 source at depth. Nature, 427(6976):724–727.

Minson, S. E., Simons, M., and Beck, J. L. (2013). Bayesian inversion for finite fault earthquake source models IâĂŤtheory and algorithm. Geophysical Journal International, 194(3):1701–1726.

Mirwald, A., Cruz-Atienza, V. M., Díaz-Mojica, J., Iglesias, A., Singh, S. K., Villafuerte, C., and Tago, J. (2019). The 19 september 2017 (m w 7.1) intermediate-depth mexican earthquake: A slow and energetically inefficient deadly shock. Geophysical Research Letters, 46(4):2054–2064.

Miyazaki, S., Segall, P., McGuire, J. J., Kato, T., and Hatanaka, Y. (2006). Spatial and temporal evolution of stress and slip rate during the 2000 Tokai slow earthquake. Journal of Geophysical Research: Solid Earth, 111(B3).

Miyazawa, M. and Brodsky, E. E. (2008). Deep low-frequency tremor that correlates with passing surface waves. Journal of Geophysical Research: Solid Earth, 113(B1).

Miyazawa, M. and Mori, J. (2006). Evidence suggesting fluid flow beneath japan due to periodic seismic triggering from the 2004 sumatra-andaman earthquake. Geophysical Research Letters, 33(5).

Moreno, M., Melnick, D., Rosenau, M., Bolte, J., Klotz, J., Echtler, H., Baez, J., Bataille, K., Chen, J., Bevis, M., et al. (2011). Heterogeneous plate locking in the south–central chile subduction zone: Building up the next great earthquake. Earth and Planetary Science Letters, 305(3-4):413–424.

Moreno, M., Rosenau, M., and Oncken, O. (2010). 2010 maule earthquake slip correlates with pre-seismic locking of andean subduction zone. Nature, 467(7312):198–202.

Nakata, R., Suda, N., and Tsuruoka, H. (2008). Non-volcanic tremor resulting from the combined effect of earth tides and slow slip events. Nature Geoscience, 1(10):676–678.

Nikkhoo, M. and Walter, T. R. (2015). Triangular dislocation: an analytical, artefact-free solution. Geophysical Journal International, 201(2):1119–1141.

Nishimura, T., Hirasawa, T., Miyazaki, S., Sagiya, T., Tada, T., Miura, S., and Tanaka, K. (2004). Temporal change of interplate coupling in northeastern Japan during 1995-2002 estimated from continuous GPS observations. Geophysical Journal International, 157(2):901–916.

Nocedal, J. and Wright, S. J. (2006). Numerical Optimization. Springer, 2nd edition.

Nocquet, J. (2018). Stochastic static fault slip inversion from geodetic data with non-negativity and bound constraints. Geophysical Journal International, 214(1):366–385.

Nocquet, J., Villegas-Lanza, J., Chlieh, M., Mothes, P., Rolandone, F., Jarrin, P., Cisneros, D., Alvarado, A., Audin, L., Bondoux, F., Martin, X., Font, Y., Régnier, M., Vallée, M., Tran, T., Beauval, C., Maguiña Mendoza, J., Martinez, W., Tavera, H., and Yepes, H. (2014). Motion of continental slivers and creeping subduction in the northern Andes. Nature Geoscience, 214(7).

Nocquet, J.-M., Jarrin, P., Vallée, M., Mothes, P., Grandin, R., Rolandone, F., Delouis, B., Yepes, H., Font, Y., Fuentes, D., et al. (2017). Supercycle at the ecuadorian subduction zone revealed after the 2016 pedernales earthquake. Nature Geoscience, 10(2):145–149.

Nur, A. and Booker, J. R. (1972). Aftershocks caused by pore fluid flow? Science, 175(4024):885–887.

Obara, K. (2002). Nonvolcanic deep tremor associated with subduction in southwest japan. Science, 296(5573):1679–1681.

Obara, K. (2010). Phenomenology of deep slow earthquake family in southwest japan: Spatiotemporal characteristics and segmentation. Journal of Geophysical Research: Solid Earth, 115(B8).

Obara, K. (2011). Characteristics and interactions between non-volcanic tremor and related slow earthquakes in the nankai subduction zone, southwest japan. Journal of Geodynamics, 52(3-4):229–248.

Obara, K. and Hirose, H. (2006). Non-volcanic deep low-frequency tremors accompanying slow slips in the southwest japan subduction zone. Tectonophysics, 417(1-2):33–51.

Obara, K., Hirose, H., Yamamizu, F., and Kasahara, K. (2004). Episodic slow slip events accompanied by non-volcanic tremors in southwest japan subduction zone. Geophysical Research Letters, 31(23).

Obara, K. and Kato, A. (2016). Connecting slow earthquakes to huge earthquakes. Science, 353(6296):253–257.

Obara, K., Matsuzawa, T., Tanaka, S., and Maeda, T. (2012). Depth-dependent mode of tremor migration beneath kii peninsula, nankai subduction zone. Geophysical Research Letters, 39(10).

Okubo, K. (2014). The effect of waste water injection on earthquake nucleation in damaged fault zones. MSc thesis, 1(1).

Olsen, K., Day, S., Dalguer, L., Mayhew, J., Cui, Y., Zhu, J., Cruz-Atienza, V., Roten, D., Maechling, P., Jordan, T., et al. (2009). Shakeout-d: Ground motion estimates using an ensemble of large

earthquakes on the southern san andreas fault with spontaneous rupture propagation. Geophysical Research Letters, 36(4).

Oñeil, P. V. (2011). Advanced engineering mathematics. Cengage learning.

Payero, J. S., Kostoglodov, V., Shapiro, N., Mikumo, T., Iglesias, A., Pérez-Campos, X., and Clayton, R. W. (2008). Nonvolcanic tremor observed in the mexican subduction zone. Geophysical Research Letters, 35(7).

Peacock, S. M., Christensen, N. I., Bostock, M. G., and Audet, P. (2011). High pore pressures and porosity at 35 km depth in the cascadia subduction zone. Geology, 39(5):471–474.

Peng, Y. and Rubin, A. M. (2016). High-resolution images of tremor migrations beneath the o lympic p eninsula from stacked array of arrays seismic data. Geochemistry, Geophysics, Geosystems, 17(2):587–601.

Peng, Y. and Rubin, A. M. (2017). Intermittent tremor migrations beneath guerrero, mexico, and implications for fault healing within the slow slip zone. Geophysical Research Letters, 44(2):760–770.

Peng, Y., Rubin, A. M., Bostock, M. G., and Armbruster, J. G. (2015). High-resolution imaging of rapid tremor migrations beneath southern vancouver island using cross-station cross correlations. Journal of Geophysical Research: Solid Earth, 120(6):4317–4332.

Peng, Z. and Chao, K. (2008). Non-volcanic tremor beneath the central range in taiwan triggered by the 2001 m w 7.8 kunlun earthquake. Geophysical Journal International, 175(2):825–829.

Peng, Z. and Gomberg, J. (2010). An integrated perspective of the continuum between earthquakes and slow-slip phenomena. Nature geoscience, 3(9):599–607.

Pérez-Campos, X., Kim, Y., Husker, A., Davis, P. M., Clayton, R. W., Iglesias, A., Pacheco, J. F., Singh, S. K., Manea, V. C., and Gurnis, M. (2008). Horizontal subduction and truncation of the cocos plate beneath central mexico. Geophysical Research Letters, 35(18).

Perfettini, H., Avouac, J.-P., Tavera, H., Kositsky, A., Nocquet, J.-M., Bondoux, F., Chlieh, M., Sladen, A., Audin, L., Farber, D. L., et al. (2010). Seismic and aseismic slip on the central peru megathrust. Nature, 465(7294):78–81.

Perry, M., Spinelli, G. A., Wada, I., and He, J. (2016). Modeled temperatures and fluid source distributions for the mexican subduction zone: Effects of hydrothermal circulation and implications for plate boundary seismic processes. Geochemistry, Geophysics, Geosystems.

Plata-Martínez, R., Ide, S., Shinohara, M., Mortel, E. S. G., Mizuno, N., Ramirez, L. A. D., Taira, T., Yamashita, Y., Toh, A., and Yamada, T. (2021). Shallow slow earthquakes to decipher future catastrophic earthquakes in the guerrero seismic gap. Accepted at Nature Communications.

Plümper, O., John, T., Podladchikov, Y. Y., Vrijmoed, J. C., and Scambelluri, M. (2017). Fluid escape from subduction zones controlled by channel-forming reactive porosity. Nature Geoscience, 10(2):150–156.

Pulido, N., Aguilar, Z., Tavera, H., Chlieh, M., Calderón, D., Sekiguchi, T., Nakai, S., and Yamazaki, F. (2015). Scenario source models and strong ground motion for future mega-earthquakes: Application to lima, central peru. Bulletin of the Seismological Society of America, 105(1):368–386.

Radiguet, M., Cotton, F., Vergnolle, M., Campillo, M., Valette, B., Kostoglodov, V., and Cotte, N. (2011). Spatial and temporal evolution of a long term slow slip event: the 2006 guerrero slow slip event. Geophysical Journal International, 184(2):816–828.

Radiguet, M., Cotton, F., Vergnolle, M., Campillo, M., Walpersdorf, A., Cotte, N., and Kostoglodov, V. (2012). Slow slip events and strain accumulation in the guerrero gap, mexico. Journal of Geophysical Research: Solid Earth, 117(B4).

Radiguet, M., Perfettini, H., Cotte, N., Gualandi, A., Valette, B., Kostoglodov, V., Lhomme, T., Walpersdorf, A., Cano, E. C., and Campillo, M. (2016). Triggering of the 2014 m w 7.3 papanoa earthquake by a slow slip event in guerrero, mexico. Nature Geoscience, 9(11):829–833.

Ramírez-Herrera, M.-T., Corona, N., Cerny, J., Castillo-Aja, R., Melgar, D., Lagos, M., Goguitchaichvili, A., Machain, M. L., Vazquez-Caamal, M. L., Ortuño, M., et al. (2020). Sand deposits reveal great earthquakes and tsunamis at mexican pacific coast. Scientific Reports, 10(1):1–10.

Rice, J. R. (1992). Fault stress states, pore pressure distributions, and the weakness of the san andreas fault. International Geophysics, 51:475–503.

Rivet, D., Campillo, M., Radiguet, M., Zigone, D., Cruz-Atienza, V., Shapiro, N. M., Kostoglodov, V., Cotte, N., Cougoulat, G., Walpersdorf, A., and Daub, E. (2013). Seismic velocity changes, strain rate and non-volcanic tremors during the 2009âĂŞ2010 slow slip event in Guerrero, Mexico. Geophysical Journal International, 196(1):447–460.

Rivet, D., Campillo, M., Shapiro, N. M., Cruz-Atienza, V., Radiguet, M., Cotte, N., and Kostoglodov, V. (2011). Seismic evidence of nonlinear crustal deformation during a large slow slip event in mexico. Geophysical Research Letters, 38(8).

Rodríguez-Domínguez, M., Pérez-Campos, X., Montealegre-Cázares, C., Clayton, R. W., and Cabral-Cano, E. (2019). Crustal structure variations in south-central mexico from receiver functions. Geophysical Journal International, 219(3):2174–2186.

Rogers, G. and Dragert, H. (2003). Episodic tremor and slip on the cascadia subduction zone: The chatter of silent slip. Science, 300(5627):1942–1943.

Rosen, P. A., Gurrola, E., Sacco, G. F., and Zebker, H. (2012). The insar scientific computing environment. In EUSAR 2012; 9th European Conference on Synthetic Aperture Radar, pages 730–733. VDE.

Rousset, B., Lasserre, C., Cubas, N., Graham, S., Radiguet, M., DeMets, C., Socquet, A., Campillo, M., Kostoglodov, V., Cabral-Cano, E., et al. (2016). Lateral variations of interplate coupling along the mexican subduction interface: Relationships with long-term morphology and fault zone mechanical properties. Pure and Applied Geophysics, 173(10):3467–3486.

Royer, A., Thomas, A., and Bostock, M. (2015). Tidal modulation and triggering of low-frequency earthquakes in northern cascadia. Journal of Geophysical Research: Solid Earth, 120(1):384–405.

Rubin, A. M. (2011). Designer friction laws for bimodal slow slip propagation speeds. Geochemistry, Geophysics, Geosystems, 12(4).

Rubin, A. M. and Ampuero, J.-P. (2005). Earthquake nucleation on (aging) rate and state faults. Journal of Geophysical Research: Solid Earth, 110(B11).

Rubin, A. M. and Ampuero, J.-P. (2009). Self-similar slip pulses during rate-and-state earthquake nucleation. Journal of Geophysical Research: Solid Earth, 114(B11).

Rubin, A. M. and Armbruster, J. G. (2013). Imaging slow slip fronts in cascadia with high precision cross-station tremor locations. Geochemistry, Geophysics, Geosystems, 14(12):5371–5392.

Rubinstein, J. L., Gomberg, J., Vidale, J. E., Wech, A. G., Kao, H., Creager, K. C., and Rogers, G. (2009). Seismic wave triggering of nonvolcanic tremor, episodic tremor and slip, and earthquakes on vancouver island. Journal of Geophysical Research: Solid Earth, 114(B2).

Ruiz, S., Metois, M., Fuenzalida, A., Ruiz, J., Leyton, F., Grandin, R., Vigny, C., Madariaga, R., and Campos, J. (2014). Intense foreshocks and a slow slip event preceded the 2014 iquique mw 8.1 earthquake. Science, 345(6201):1165–1169.

Saffer, D. M. and Tobin, H. J. (2011). Hydrogeology and mechanics of subduction zone forearcs: Fluid flow and pore pressure. Annual Review of Earth and Planetary Sciences, 39:157–186.

Saffer, D. M. and Wallace, L. M. (2015). The frictional, hydrologic, metamorphic and thermal habitat of shallow slow earthquakes. Nature Geoscience.

Sánchez-Reyes, H. S., Tago, J., Métivier, L., Cruz-Atienza, V., and Virieux, J. (2018). An evolutive linear kinematic source inversion. Journal of Geophysical Research: Solid Earth, 123(6):4859–4885.

Savage, J. C. (1983). A dislocation model of strain accumulation and release at a subduction zone. Journal of Geophysical Research: Solid Earth, 88(B6):4984–4996.

Schurr, B., Asch, G., Hainzl, S., Bedford, J., Hoechner, A., Palo, M., Wang, R., Moreno, M., Bartsch, M., Zhang, Y., et al. (2014). Gradual unlocking of plate boundary controlled initiation of the 2014 iquique earthquake. Nature, 512(7514):299–302.

Schwartz, S. Y. and Rokosky, J. M. (2007). Slow slip events and seismic tremor at circum-pacific subduction zones. Reviews of Geophysics, 45(3).

Segall, P. and Bradley, A. M. (2012). Slow-slip evolves into megathrust earthquakes in 2d numerical simulations. Geophysical Research Letters, 39(18).

Segall, P. and Rice, J. R. (1995). Dilatancy, compaction, and slip instability of a fluid-infiltrated fault. Journal of Geophysical Research: Solid Earth, 100(B11):22155–22171.

Segall, P., Rubin, A. M., Bradley, A. M., and Rice, J. R. (2010). Dilatant strengthening as a mechanism for slow slip events. Journal of Geophysical Research: Solid Earth, 115(B12).

Shapiro, N. M., Campillo, M., Kaminski, E., Vilotte, J.-P., and Jaupart, C. (2018). Low-frequency earthquakes and pore pressure transients in subduction zones. Geophysical Research Letters, 45(20):11–083.

Shapiro, S. A., Rothert, E., Rath, V., and Rindschwentner, J. (2002). Characterization of fluid transport properties of reservoirs using induced microseismicity. Geophysics, 67(1):212–220.

Shelly, D. R., Beroza, G. C., and Ide, S. (2007a). Complex evolution of transient slip derived from precise tremor locations in western shikoku, japan. Geochemistry, Geophysics, Geosystems, 8(10).

Shelly, D. R., Beroza, G. C., and Ide, S. (2007b). Non-volcanic tremor and low-frequency earthquake swarms. Nature, 446(7133):305–307.

Shelly, D. R., Beroza, G. C., Ide, S., and Nakamula, S. (2006). Low-frequency earthquakes in shikoku, japan, and their relationship to episodic tremor and slip. Nature, 442(7099):188–191.

Shibazaki, B. and Shimamoto, T. (2007). Modelling of short-interval silent slip events in deeper subduction interfaces considering the frictional properties at the unstable?stable transition regime. Geophysical Journal International, 171(1):191–205.

Simpson, R., Schulz, S., Dietz, L., and Burford, R. (1988). The response of creeping parts of the San Andreas fault to earthquakes on nearby faults: Two examples. Pure and Applied Geophysics, 126(2-4):665–685.

Singh, S., Astiz, L., and Havskov, J. (1981). Seismic gaps and recurrence periods of large earthquakes along the mexican subduction zone: A reexamination. Bulletin of the seismological Society of America, 71(3):827–843.

Singh, S., Dominguez, T., Castro, R., and Rodriguez, M. (1984). P waveform of large, shallow earthquakes along the mexican subduction zone. bulletin of the seismological society of america. Bulletin of the seismological Society of America, 74(6):2135–2156.

Singh, S., Reinoso, E., Arroyo, D., Ordaz, M., Cruz-Atienza, V., Perez-Campos, X., Iglesias, A., and Hjorleifsdottir, V. (2018). Deadly intraslab mexico earthquake of 19 september 2017 (m w 7.1): Ground motion and damage pattern in mexico city. Seismological Research Letters, 89(6):2193–2203.

Socquet, A., Valdes, J. P., Jara, J., Cotton, F., Walpersdorf, A., Cotte, N., Specht, S., Ortega-Culaciati, F., Carrizo, D., and Norabuena, E. (2017). An 8 month slow slip event triggers progressive nucleation of the 2014 chile megathrust. Geophysical Research Letters, 44(9):4046–4053.

Somala, S. N., Ampuero, J.-P., and Lapusta, N. (2018). Finite-fault source inversion using adjoint methods in 3-D heterogeneous media. Geophysical Journal International, 214(1):402–420.

Song, T.-R. A., Helmberger, D. V., Brudzinski, M. R., Clayton, R. W., Davis, P., Pérez-Campos, X., and Singh, S. K. (2009). Subducting slab ultra-slow velocity layer coincident with silent earthquakes in southern mexico. Science, 324(5926):502–506.

Spica, Z., Perton, M., Calò, M., Legrand, D., Córdoba-Montiel, F., and Iglesias, A. (2016). 3-d shear wave velocity model of mexico and south us: bridging seismic networks with ambient noise cross-

correlations (c1) and correlation of coda of correlations (c3). Geophysical Journal International, 206(3):1795–1813.

Stein, R. S. (1999). The role of stress transfer in earthquake occurrence. Nature, 402(6762):605–609.

Suárez, G. and Albini, P. (2009). Evidence for great tsunamigenic earthquakes (m 8.6) along the mexican subduction zone. Bulletin of the Seismological Society of America, 99(2A):892–896.

Suárez, G., Ruiz-Barón, D., Chico-Hernández, C., and Zúñiga, F. R. (2020). Catalog of preinstrumental earthquakes in central mexico: epicentral and magnitude estimations based on macroseismic data. Bulletin of the Seismological Society of America, 110(6):3021–3036.

Suárez, G., Santoyo, M. A., Hjorleifsdottir, V., Iglesias, A., Villafuerte, C., and Cruz-Atienza, V. M. (2019). Large scale lithospheric detachment of the downgoing cocos plate: The 8 september 2017 earthquake (mw 8.2). Earth and Planetary Science Letters, 509:9–14.

Tago, J., Cruz-Atienza, V. M., Villafuerte, C., Nishimura, T., Kostoglodov, V., Real, J., and Ito, Y. (2021). Adjoint slip inversion under a constrained optimization framework: Revisiting the 2006 guerrero slow slip event. Accepted at Geophysical Journal International.

Tago, J., Cruz-Atienza, V. M., Virieux, J., Etienne, V., and Sánchez-Sesma, F. J. (2012). A 3d hp-adaptive discontinuous galerkin method for modeling earthquake dynamics. Journal of Geophysical Research: Solid Earth, 117(B9).

Tarantola, A. (1984). Inversion of seismic reflection data in the acoustic approximation. Geophysics, 49(8):1259–1266.

Tarantola, A. and Valette, B. (1982). Generalized nonlinear inverse problems solved using the least squares criterion. Reviews of Geophysics, 20(2):219–232.

Thomas, A., Bürgmann, R., Shelly, D., Beeler, N., and Rudolph, M. L. (2012). Tidal triggering of low frequency earthquakes near parkfield, california: Implications for fault mechanics within the brittle-ductile transition. Journal of Geophysical Research: Solid Earth, 117(B5).

Thomas, A. M., Nadeau, R. M., and Bürgmann, R. (2009). Tremor-tide correlations and near-lithostatic pore pressure on the deep san andreas fault. Nature, 462(7276):1048–1051.

Tromp, J., Tape, C., and Liu, Q. (2005). Seismic tomography, adjoint methods, time reversal and banana-doughnut kernels. Geophysical Journal International, 160(1):195–216.

Tsuji, T., Kamei, R., and Pratt, R. G. (2014). Pore pressure distribution of a mega-splay fault system in the nankai trough subduction zone: Insight into up-dip extent of the seismogenic zone. Earth and Planetary Science Letters, 396:165–178.

Tymofyeyeva, E., Fialko, Y., Jiang, J., Xu, X., Sandwell, D., Bilham, R., Rockwell, T. K., Blanton, C., Burkett, F., Gontz, A., et al. (2019). Slow slip event on the southern san andreas fault triggered by the 2017 m w 8.2 chiapas (mexico) earthquake. Journal of Geophysical Research: Solid Earth, 124(9):9956–9975.

Uchida, N., Iinuma, T., Nadeau, R. M., Bürgmann, R., and Hino, R. (2016). Periodic slow slip triggers megathrust zone earthquakes in northeastern japan. Science, 351(6272):488–492.

UNAM, S. (2015). Papanoa, Mexico earthquake of 18 April 2014 (Mw7.3). Geofisica Internacional, 54:363–386.

Van Den Abeele, K.-A., Johnson, P. A., and Sutin, A. (2000). Nonlinear elastic wave spectroscopy (news) techniques to discern material damage, part i: nonlinear wave modulation spectroscopy (nwms). Journal of Research in Nondestructive Evaluation, 12(1):17–30.

Vergnolle, M., Walpersdorf, A., Kostoglodov, V., Tregoning, P., Santiago, J., Cotte, N., and Franco, S. (2010). Slow slip events in mexico revised from the processing of 11 year gps observations. Journal of Geophysical Research: Solid Earth, 115(B8).

Villafuerte, C. and Cruz-Atienza, V. M. (2017). Insights into the causal relationship between slow slip and tectonic tremor in guerrero, mexico. Journal of Geophysical Research: Solid Earth, 122(8):6642–6656.

Villafuerte, C.and Cruz-Atienza, V., Tago, J., Solano, D., Garza-Girón, R., Franco, S., Domínguez, L., and Kostoglodov, V. (2021). Slow slip events and megathrust coupling changes reveal the earthquake potential before the 2020 Mw 7.4 Huatulco, Mexico, event. Submitted to AGU Advances.

Voss, N., Dixon, T. H., Liu, Z., Malservisi, R., Protti, M., and Schwartz, S. (2018). Do slow slip events trigger large and great megathrust earthquakes? Science advances, 4(10):eaat8472.

Wallace, L. M. and Beavan, J. (2010). Diverse slow slip behavior at the Hikurangi subduction margin, New Zealand. Journal of Geophysical Research: Solid Earth, 115(B12).

Wallace, L. M., Kaneko, Y., Hreinsdóttir, S., Hamling, I., Peng, Z., Bartlow, N., D?Anastasio, E., and Fry, B. (2017). Large-scale dynamic triggering of shallow slow slip enhanced by overlying sedimentary wedge. Nature Geoscience, 10(10):765–770.

Wang, Q.-Y., Campillo, M., Brenguier, F., Lecointre, A., Takeda, T., and Hashima, A. (2019). Evidence of changes of seismic properties in the entire crust beneath japan after the m w 9.0, 2011 tohoku-oki earthquake. Journal of Geophysical Research: Solid Earth, 124(8):8924–8941.

Wang, R., Schurr, B., Milkereit, C., Shao, Z., and Jin, M. (2011). An improved automatic scheme for empirical baseline correction of digital strong-motion records. Bulletin of the Seismological Society of America, 101(5):2029–2044.

Warren-Smith, E., Fry, B., Wallace, L., Chon, E., Henrys, S., Sheehan, A., Mochizuki, K., Schwartz, S., Webb, S., and Lebedev, S. (2019). Episodic stress and fluid pressure cycling in subducting oceanic crust during slow slip. Nature Geoscience, 12(6):475–481.

Wech, A. G. and Bartlow, N. M. (2014). Slip rate and tremor genesis in cascadia. Geophysical Research Letters, 41(2):392–398.

Wech, A. G., Creager, K. C., and Melbourne, T. I. (2009). Seismic and geodetic constraints on cascadia slow slip. Journal of Geophysical Research: Solid Earth, 114(B10).

Wei, M., Kaneko, Y., Shi, P., and Liu, Y. (2018). Numerical modeling of dynamically triggered shallow slow slip events in new zealand by the 2016 mw 7.8 kaikoura earthquake. Geophysical Research Letters, 45(10):4764–4772.

Wetzler, N., Lay, T., Brodsky, E. E., and Kanamori, H. (2018). Systematic deficiency of aftershocks in areas of high coseismic slip for large subduction zone earthquakes. Science advances, 4(2):eaao3225.

Williams, C. A. and Wallace, L. M. (2015). Effects of material property variations on slip estimates for subduction interface slow-slip events. Geophysical Research Letters, 42(4):1113–1121.

Yabe, S. and Ide, S. (2014). Spatial distribution of seismic energy rate of tectonic tremors in subduction zones. Journal of Geophysical Research: Solid Earth, 119(11):8171–8185.

Yabe, S. and Ide, S. (2017). Slip-behavior transitions of a heterogeneous linear fault. Journal of Geophysical Research: Solid Earth, 122(1):387–410.

Yabe, S., Tanaka, Y., Houston, H., and Ide, S. (2015). Tidal sensitivity of tectonic tremors in nankai and cascadia subduction zones. Journal of Geophysical Research: Solid Earth, 120(11):7587–7605.

Yabuki, T. and MatsuÚra, M. (1992). Geodetic data inversion using a Bayesian information criterion for spatial distribution of fault slip. Geophysical Journal International, 109(2):363–375.

Yingdi, L. and Ampuero, J.-P. (2017). Preprint: Tremor migration patterns and the collective behavior of deep asperities mediated by creep.

Zhu, W., Allison, K. L., Dunham, E. M., and Yang, Y. (2020). Fault valving and pore pressure evolution in simulations of earthquake sequences and aseismic slip. Nature communications, 11(1):1–11.

Zigone, D., Rivet, D., Radiguet, M., Campillo, M., Voisin, C., Cotte, N., Walpersdorf, A., Shapiro, N. M., Cougoulat, G., Roux, P., et al. (2012). Triggering of tremors and slow slip event in guerrero, mexico, by the 2010 mw 8.8 maule, chile, earthquake. Journal of Geophysical Research: Solid Earth, 117(B9).

List of figures